

Mineral Replacements in Flooding Experiments Linked to Enhanced Oil Recovery in Chalk

by

Mona Wetrhus Minde

Thesis submitted in fulfilment of
the requirements for the degree of
PHILOSOPHIAE DOCTOR
(PhD)



Faculty of Science and Technology
Institute of Energy Resources
2018

University of Stavanger
NO-4036 Stavanger
NORWAY
www.uis.no

©2018 Mona Wetrhus Minde

ISBN: 978-82-7644-799-6

ISSN: 1890-1387

PhD: Thesis UiS No. 419

*To my parents,
Anne Lise & Per Gunnar,
and my family,
Pål, Espen & Maren*

Acknowledgements

The quote “dwarfs standing on the shoulders of giants” has been traced back to the 12th century, but is certainly also valid in the 21st century. I feel lucky to have been able to work with the group of researchers at UiS studying chalk. Not only have I been able to learn from the best, building on the work performed over the last decades, I have also had the opportunity to study samples from so many experiments, performed by others and myself, enabling me to work with a wide range of research questions over the last three years.

I would like to thank my supervisors Professor Merete Vadla Madland and Professor Udo Zimmermann for the guidance they have given me, the trust they have put in me and for providing me with chances to work with different people, equipment and in different places around the world I would not have experienced without them. I am truly thankful, this could not have been done without you!

I would also like to thank the engineers at UiS who are always there to help and especially Reidar Inge Korsnes for his sharing of knowledge, his help, patience and good mood, helping me keep the faith. In addition, I want to thank Professor Aksel Hiorth for all his help in modelling and understanding the geochemical theory behind rock-fluid interaction, as well as fruitful discussions on many questions. Among all the colleagues who have helped me on my way, I also want to thank Vidar Folke Hansen for his help in electron microscopy and for support the last years.

I would like to thank the National IOR Centre of Norway and UiS for employing me and all my former and current colleagues and friends at UiS, especially Ema Kallestén, Nina Egeland and Irene Ringen for good companionship and collaboration, as well as Tania Hildebrand-Habel and Ingunn Cecilie Olsen for introducing me to the wonderful world of electron

microscopy. The list of people to thank at UiS, and IRIS, includes many more! Working with the group of PhDs in the National IOR Centre of Norway and at the Faculty of Science and Technology has been wonderful, with good scientific discussions, sharing of knowledge and ideas and lots of fun. The Centre has also been an arena for meeting other researchers and representatives from the industry with the possibility to present our work, discussions and receive valuable feedback.

I also like to thank the many institutions around the world I have had the opportunity to visit during my PhD years. I have learned so much from your work and our discussions. A special thanks to Bernhard Schulz and Sabine Gilbricht in Freiberg and the team in Misasa, Japan.

I would like to thank my parents, Anne Lise and Per Gunnar for their support and making me believe in myself. I would like to thank Maren, Espen and Pål and the rest of my family and friends for all the help, support and cheering on the way. Gry, thank you for cheering and motivating me through numerous coffee-breaks and lunches.

Mona Wetrhus Minde

Summary

Seawater injection into chalk-reservoirs on the Norwegian Continental Shelf has increased the oil recovery and reduced seabed subsidence. In the research-field of Improved Oil Recovery (IOR) the effects of injection of seawater-like brines into chalk have been studied for decades. Particular ions in brines seem to have the power to change the wetting conditions of the rock as well as affecting the strength of chalk. Therefore, when optimizing brines to enhance the production of oil, it is paramount to understand how the injected brine impose alterations in geo-mechanical properties, which in turn affect the strength of the rock. These effects are referred to as “water weakening of chalk” and should be controlled to avoid undesired compaction effects and loss in well stabilities, affecting both safety and costs.

This thesis aims to describe the “the which, the how and the where” of mineralogical alterations in chalk when flooded with reactive brines, with special focus on the Mg^{2+} -ion. The produced changes may directly impact mechanical properties of the rock, and can often only be observed at micron- and sub-micron-scale. The study of these alterations therefore requires methods with possibilities to image and quantify the chemical composition of the rock with resolution below pore-scale, often at nano-scale. The analytical tools used in this study are, on one hand, well-known in terms of their application to rocks and partly on chalk, but on the other hand, this research has developed new methodological approaches for the study of mineralogical changes in Enhanced Oil Recovery (EOR) experiments. This work has resulted in the design of a toolbox which holds the possibility to sufficiently investigate the mineralogical effects of EOR-fluids.

Tests have been performed on several types of outcrop chalk, flooded with different brines, at different stresses and temperatures, and for different periods

of time. In addition, similar experiments on “artificial chalk cores”, made from pure calcite powder, have been completed. The tests were performed on cylindrical core samples and analysed by scanning and transmission electron microscopy, Mineral Liberation Analyzer, electron microprobe analysis, whole-rock geochemistry, stable isotope analyses, nano secondary ion mass spectrometry, X-ray diffraction, along with measurements of the specific surface area, density and porosity, and quantification of the composition of the effluent water.

Thorough core- pore- and nano-scale investigation has been conducted and the results from all scales match. The combination of scales supplement each other to an improved understanding of the data and the following results can be highlighted:

Analyses after flooding with NaCl show very few mineralogical reactions in chalk, however, in silica-rich chalk, the distribution of silicate minerals may be significantly altered. After flooding with MgCl₂, the results show dissolution of calcite and precipitation of magnesite. The occurrence and shape of new-grown crystals depend on flooding time and distance from the flooding inlet of the sample cores, together with the primary mineralogy of the chalk and its diagenetic history. Crystals vary in size, from a few nanometres up to over 10 µm and may crystallize as single grains or in clusters. Additionally, non-carbonate phases dissolve and precipitate during flooding, altering the distribution of these minerals within the cores. The type of chalk, with different contents and types of non-carbonate minerals, is found to play a role for the strength of the chalk and is also reflected in the precipitated mineral phases during flooding. These new-formed minerals may alter the permeability, porosity and the reactive surface of the flooded chalk.

All tests show pronounced alteration of texture and mineralogy at the flow-inlet side of the core, along with a decreasing trend in magnesium content towards

the outlet. With longer duration of flooding, the alterations move like a front further into the cores, and for a three year long test, the whole core is altered from the primary mineralogy to newly formed minerals. When studied at core- and pore-scale, the newly formed crystals are found to be magnesite with minor calcium impurities, together with clay minerals. In two slightly shorter tests, flooded for one and a half and two years, respectively, the alteration front is still observable. On the outlet side of the cores, the mineralogy still mainly consists of calcite, primary clay minerals and other non-carbonate minerals together with occurrences of newly formed magnesite and secondary clay minerals. On the inlet side of the cores, the mineralogy consists of magnesite and clay minerals, as observed in the experiment flooded for three years. Dolomite or low to high Mg-calcite, are not observed.

An interesting observation in long-term flooded chalk, is the abrupt transition between the two mineral regimes found on each side of the alteration front. These transition zones have higher porosity than other parts of the cores, a pattern similar to what is observed in single-crystal experiments, where the alterations happen through dissolution and precipitation, driven by the progression of high porosity-zones and the state of equilibrium at the boundary between the primary and secondary mineral phases.

In long-term flooded chalk, the texture of larger macrofossils is often preserved, while their mineralogy is altered. Such pseudomorphism is observed at centimetre- and micrometre-scale, but not at nanometre-scale, pointing to the precipitation rate of magnesite being the rate-limiting factor, found to result in micrometre-scale pseudomorphism. Severe signs of dissolution on calcite grains and high-resolution analyses of precipitation on grain-scale confirm that the formation of new mineral phases is controlled by dissolution and precipitation, and not by molecular solid state diffusion.

Saturation indices modelled along the flooding axis of chalk cores, during flooding with reactive brines, do, in general, not match the form and size of crystals and aggregates observed in these experiments. It seems that smaller crystals precipitate in the fluid-phase at the inlet where nucleation rates are high, and subsequently aggregate and settle downstream in the core, towards the outlet. As such, the crystal shapes and sizes are dictated by a function of nucleation, growth and transport rates within the core. Moreover, the transport includes both transport of ions and nanometre-sized crystals in the fluid-phase. The fluid-flow may also be affected by the primary texture and fractures in chalk, which in turn also concern the mineralogical alterations due to rock-fluid interactions when injecting MgCl_2 as well as seawater. Preliminary studies show that mineralogical changes in outcrop chalk from the Niobrara Fm (USA) are similar in water wet and mixed wet systems, suggesting that the observations made in water wet chalk may be used to interpret mixed wet chalk and to understand hydrocarbon reservoir behaviour.

All these points are important input parameters to models and simulators which are used at all scales to predict effects of any EOR fluids. The interaction between laboratory experiments and modelling as well as simulation is essential to understand the underlying mechanisms at play when flooding chalk with non-equilibrium brines as well as to constrain and validate models and simulation of fluid-injection.

These studies have tested numerous analytical methods and the experiences have shown that through application of basic analysis tools such as electron microscopy, X-ray diffraction, whole-rock and stable isotope geochemistry, the major mineralogical changes in flooded chalk-cores may be identified and sufficiently quantified. More detailed information on nano-scale can be provided, as shown, by e.g. transmission electron microscopy on focused ion beam lamellas. For core-scale mapping, scanning electron microscopy mapping

tools, such as Mineral Liberation Analyser or QEMSCAN, can provide helpful results. Together, these tools provide a toolbox for researchers and industry, which may help to understand the effects of injection of reactive brines and how the rocks depositional facies and diagenetic history impact the effects of EOR-fluids in laboratory experiments, pilot projects and field implementations.

List of publications

Paper I:

Minde, M.W., Zimmermann, U., Madland, M.V., Korsnes, R.I., Schulz, B., Gilbricht, S. (In review)

Mineral Replacement in Long-Term Flooded Porous Carbonate Rocks.
Geochimica et Cosmochimica Acta.

Paper II:

Minde, M.W., Madland, M.V., Zimmermann, U., Egeland, N., Korsnes, R.I., Nakamura, E., Kobayashi, K., Ota, T. (In review)

Mineralogical alterations in calcite powder flooded with MgCl₂ to study Enhanced Oil Recovery (EOR) mechanisms at pore scale.

Microporous and mesoporous materials.

Paper III:

Minde, M.W., Zimmermann, U., Madland, M.V., Korsnes, R.I., Schulz, B. and Audinot, J.-N. (2016)

Fluid-flow during EOR experiments in chalk: insights using SEM-MLA, EMPA and nanoSIMS applications.

SCA annual symposium, Snowmass Colorado.

Paper IV:

Minde, M.W., Wang, W., Madland, M.V., Zimmermann, U., Korsnes, R.I., Bertolino, S.R.A. and Andersen, P.Ø. (2018)

Temperature effects on rock engineering properties and rock-fluid chemistry in opal-CT-bearing chalk.

Journal of Petroleum Science and Engineering 169, 454-470.

Paper V:

Andersen, P.Ø., Wang, W., Madland, M.V., Zimmermann, U., Korsnes, R.I., Bertolino, S.R.A., Minde, M.W., Schulz, B. and Gilbricht, S. (2017)
Comparative Study of Five Outcrop Chalks Flooded at Reservoir Conditions: Chemo-mechanical Behaviour and Profiles of Compositional Alteration. *Transport in Porous Media* 121, 135–181.

Paper VI:

Zimmermann, U., Madland, M.V., Minde, M.W., Borromeo, L. and Egeland, N. (2017)
Tools to Determine and Quantify Mineralogical Changes During EOR Flooding Experiments on Chalk,
Abu Dhabi International Petroleum Exhibition & Conference. Society of Petroleum Engineers, Abu Dhabi, UAE.

Paper VII:

Borromeo, L., Egeland, N., Minde, M.W., Zimmermann, U., Andò, S., Madland, M.V. and Korsnes, R.I. (2018)
Quick, Easy, and Economic Mineralogical Studies of Flooded Chalk for EOR Experiments Using Raman Spectroscopy. *Minerals* 8 (6).

List of additional papers

Borromeo, L., Minde, M.W., Zimmermann, U., Andò, S., Toccafondi, C. and Ossikovski, R. (2017)

A new frontier technique for nano-analysis on flooded chalk: TERS (Tip Enhanced Raman Spectroscopy).

EAGE - 19th European Symposium on Improved Oil Recovery/IOR Norway 2017, Stavanger.

Borromeo, L., Zimmermann, U., Andò, S., Minde, M.W., Egeland, N., Toccafondi, C. and Ossikovski, R. (In press)

Application of Tip-Enhanced Raman Spectroscopy for the nanoscale characterization of flooded chalk.

Journal of Applied Physics.

Egeland, N., Minde, M.W., Kobayashi, K., Ota, T., Nakamura, E., Zimmermann, U., Madland, M.V. and Korsnes, R.I. (2017)

Quantification of Mineralogical Changes in Flooded Carbonate under Reservoir Conditions.

EAGE - 19th European Symposium on Improved Oil Recovery/IOR Norway 2017, Stavanger.

Kallesten, E.I., Zimmermann, U., Minde, M.W. and Madland, M.V. (2017)

Petrological, Mineralogical and Geochemical Constraints on Hydrocarbon Bearing North Sea Reservoir Chalk.

EAGE - 19th European Symposium on Improved Oil Recovery/IOR Norway 2017, Stavanger.

Kjøller, C., Sigalas, L., Christensen, H.F. and Minde, M.W. (2016)

A Fast Method for Homogenous Dissolution of Chalk Specimens for Laboratory Experiments – Documentation by X-ray CT Scanning and Scanning Electron Microscopy.

SCA Annual Symposium, Snowmass, Colorado.

Minde, M.W., Haser, S., Korsnes, R.I., Zimmermann, U. and Madland, M.V. (2017)

Comparative Studies of Mineralogical Alterations of Three Ultra-long-term Tests of Onshore Chalk at Reservoir Conditions.

EAGE - 19th European Symposium on Improved Oil Recovery/IOR Norway 2017, Stavanger.

Neuville, A., Renaud, L., Luu, T.T., Minde, M.W., Jettestuen, E., Vinningland, J.L., Hiorth, A. and Dysthe, D.K. (2017)

Xurography for microfluidics on a reactive solid.

Lab on a Chip 17, 293-303.

Hansen, V., Echevarria-Bonet, C., Minde, M.W., Taftø, J. (In review)

Determination of atomic positions and polar direction in the half-Heusler $Sb_{1-x}Sn_xTi_{1-y-z}Hf_yZr_zCo$ using Electron channeling.

Journal of Applied physics.

Conference contributions

2018

Korsnes, R.I., Minde, M.W., Madland, M.V., Zimmermann, U. Can we control water induced compaction in chalk reservoirs? Experiences from in-situ core and pore scale studies. *DHRTC – Modified Salinity Water Flooding Workshop*, 2018.

Minde, M.W., Korsnes, R.I., Egeland, N., Madland, M.V., Zimmermann, U. Mineralogical alterations in calcite powder flooded with MgCl₂ to study underlying Enhanced Oil Recovery (EOR) mechanisms. *CPM 8*, 2018.

Bredal, T.V., Minde, M.W., Zimmermann, U., Madland, M.V., Korsnes, R.I., Ruud, C. Micro- and nano-analyses of fracture-filling after flooding on-shore chalk with different IOR fluids. *IOR NORWAY 2018*.

Gjersdal, S.G., Minde, M.W., Zimmermann, U., Madland, M.V., Hiorth, A., Giske, N.H., Stavland, A. Polymer-injection for IOR purposes at the Norwegian Continental shelf – micro- and nanoanalytical approach for the understanding of phase-formation and its implication for upscaling. *IOR NORWAY 2018*.

Kavli, E., Minde, M.W., Zimmermann, U., Madland, M.V., Korsnes, R.I., Erba, E. The impact of paleontological components on IOR experiments and upscaling from pore to core and larger scales. *IOR NORWAY 2018*.

Minde, M.W., Sachdeva, J.S., Zimmermann, U., Madland, M.V., Korsnes, R.I., Nermoen, A. Mineral alterations in water wet and mixed wet chalk due to flooding of seawater-like brines. *IOR NORWAY 2018*.

Thu, R.S.W.S., Minde, M.W., Zimmermann, U., Madland, M.V., Korsnes, R.I., Kalai, D.Y. Systematic specific surface area analyses on rocks to implement as a necessary, quick and informative method to understand geomechanical parameter in IOR experiments. *IOR NORWAY 2018*.

2017

Zimmermann, U., Madland, M.V., Minde, M.W., Borromeo, L. and Egeland, N. (2017) Tools to Determine and Quantify Mineralogical Changes During EOR Flooding Experiments on Chalk, *Abu Dhabi International Petroleum Exhibition & Conference. Society of Petroleum Engineers, Abu Dhabi, UAE.*

Egeland, N., Minde, M.W., Kobayashi, K., Ota, T., Nakamura, E., Zimmermann, U., Madland, M.V., Korsnes, R.I. Quantification of Mineralogical Changes in Flooded Carbonate under Reservoir Conditions. *2nd Reservoir Characterization Conference; 2017.*

Minde, M.W., Madland, M.V., Zimmermann, U. From Core to Pore to Field. *NFiP annual one day seminar 2017.*

Minde, M.W., Zimmermann, U., Madland, M.V. Understanding EOR mechanisms. *Lunch and Learn ConocoPhillips; 2017.*

Borromeo, L., Zimmermann, U., Andò, S., Minde, M.W., Egeland, N., Toccafondi, C., Ossikovski, R. Micro-Raman spectroscopy and TERS (Tip Enhanced Raman Spectroscopy) applied to Enhanced Oil Recovery. *Nano Innovation 2017.*

Borromeo, L., Minde, M.W., Zimmermann, U., Andò, S., Toccafondi, C., Ossikovski, R. A new frontier technique for nano-analysis on flooded chalk: TERS (Tip Enhanced Raman Spectroscopy). *EAGE - 19th European Symposium on Improved Oil Recovery/IOR Norway 2017.*

Egeland, N., Minde, M.W., Kobayashi, K., Ota, T., Nakamura, E., Zimmermann, U., Madland, M.V., Korsnes, R.I. Quantification of Mineralogical Changes in Flooded Carbonate under Reservoir Conditions. *EAGE - 19th European Symposium on Improved Oil Recovery/IOR Norway 2017.*

Kallestén, E.I., Zimmermann, U., Minde, M.W., Madland, M.V. Petrological, Mineralogical and Geochemical Constraints on Hydrocarbon Bearing North Sea Reservoir Chalk. *EAGE - 19th European Symposium on Improved Oil Recovery/IOR Norway 2017.*

Minde, M.W., Haser, S., Korsnes, R.I., Zimmermann, U., Madland, M.V. Comparative Studies of Mineralogical Alterations of Three Ultra-long-term Tests of Onshore Chalk at Reservoir Conditions. *EAGE - 19th European Symposium on Improved Oil Recovery/IOR Norway 2017*.

Neuville, A., Renaud, L., Minde, M.W., Vinningland, J.L., Hiorth, A., Dysthe, D.K. Can we get a better knowledge on dissolution processes in chalk by using microfluidic chips? *EGU General Assembly 2017*.

2016

Kjøller, C., Sigalas, L., Christensen, H.F., Minde, M.W. A Fast Method for Homogenous Dissolution of Chalk Specimens for Laboratory Experiments – Documentation by X-ray CT Scanning and Scanning Electron Microscopy. *SCA Annual Symposium; 2016*.

Nermoen, A., Jettestuen, E., Minde, M.W., Madland, M.V. Quantifying the microscopic morphology of SEM images. *Annual IEA-EOR; 2016*.

Egeland, N., Zimmermann, U., Borromeo, L., Andò, S., Madland, M.V., Minde, M.W., Korsnes, R.I. Raman spectroscopy applied to enhanced oil recovery research. *Goldschmidt conference 2016*.

Minde, M.W., Zimmermann, U., Madland, M.V., Korsnes, R.I. Studies of Mineralogical Changes for the Understanding of Enhanced Oil Recovery Mechanisms at Porescale. *Goldschmidt Conference 2016*.

Borromeo, L., Egeland, N., Minde, M.W., Zimmermann, U., Andò, S., Toccafondi, C., Ossikovski, R. Micro- and Nano- Raman analyses of chalk. *IOR NORWAY 2016*.

Minde, M.W., Zimmermann, U., Madland, M.V., Korsnes, R.I. Micron and submicron investigation - what can we learn? *IOR NORWAY 2016*.

Minde, M.W., Zimmermann, U., Madland, M.V., Korsnes, R.I. "Understanding EOR mechanisms at pore-scale". *IOR NORWAY 2016*.

Egeland, N., Madland, M.V., Zimmermann, U., Kobayashi, K., Nakamura, E., Ota, T., Minde, M.W., Korsnes, R.I. Mineralogical and chemical alteration of calcite by MgCl₂ injection. *Misasa International Symposium 2016*.

Minde, M.W., Zimmermann, U., Madland, M.V., Korsnes, R.I., Schulz, B., Audinot, J-N. Fluid-flow during EOR experiments in chalk: insights using SEM-MLA, EMPA and nanoSIMS applications. *SCA annual symposium; 2016*.

Nermoen, A., Jettestuen, E., Minde, M.W., Madland, M.V. Quantifying the microscopic morphology of SEM microscopy images. *ENI Workshop; 2016*.

Table of Contents

Acknowledgements.....	v
Summary.....	vii
List of publications	xiii
List of additional papers	xv
Conference contributions.....	xvii
Table of Contents.....	xxi
Table of Figures.....	xxiii
Part 1.....	xxix
1 Introduction.....	1
2 Material and methods.....	9
2.1 Material	9
2.1.1 Chalk.....	9
2.1.2 Fractures in chalk reservoirs.....	12
2.2 Outcrop chalks in this study.....	13
2.2.2 Calcite powder.....	16
2.3 Methods.....	16
2.3.1 Triaxial tests	17
2.3.2 Electron microscopy	20
2.3.3 Nano Secondary Ion Mass spectrometry (NanoSIMS).....	29
2.3.4 Carbon and Oxygen Isotopes.....	31
2.3.5 Whole-rock geochemistry (Inductive Coupled Plasma Mass Spectrometry, ICP-MS)	32
2.3.6 Analyses of effluent water.....	33
2.3.7 X-ray Diffraction (XRD).....	34
2.3.8 Specific Surface Area (SSA), Brunauer–Emmett–Teller (BET) theory.....	35
2.3.9 Pycnometry.....	36
2.3.10 Raman spectroscopy.....	36
3 Main results and discussion	39

3.1	Core-scale alterations	40
3.1.1	Two fronts of alterations.....	40
3.1.2	A porous transition zone with sharp boundaries.....	53
3.2	Pore-scale alterations	62
3.3	Scales of pseudomorphism.....	67
3.4	Fractures and texture	69
3.5	Effects of primary mineralogy	73
3.6	Mechanisms controlling crystal shape and distribution of new-grown minerals.....	75
3.7	The effect of wettability	79
3.8	A toolbox to analyse EOR experiments	81
3.9	Implications for the industry	82
4	Conclusion and future work.....	85
4.1	Conclusions.....	85
4.2	Future work.....	89
	References.....	92
	Part 2.....	101
	Paper I: Mineral Replacement in Long-Term Flooded Porous Carbonate Rocks	
	Paper II: Mineralogical alterations in calcite powder flooded with MgCl ₂ to study Enhanced Oil Recovery (EOR) mechanisms at pore scale	
	Paper III: Fluid-flow during EOR experiments in chalk: insights using SEM-MLA, EMPA and nanoSIMS applications	
	Paper IV: Temperature effects on rock engineering properties and rock-fluid chemistry in opal-CT-bearing chalk	
	Paper V: Comparative Study of Five Outcrop Chalks Flooded at Reservoir Conditions: Chemo-mechanical Behaviour and Profiles of Compositional Alteration	
	Paper VI: Tools to Determine and Quantify Mineralogical Changes During EOR Flooding Experiments on Chalk	
	Paper VII: Quick, Easy, and Economic Mineralogical Studies of Flooded Chalk for EOR Experiments Using Raman Spectroscopy	

Table of Figures

Figure 1: SEM micrograph of Liège chalk showing typical components of chalk; skeletal debris of coccolithophores and other microfossils along with minor occurrences of clay minerals.	10
Figure 2: Sketch of a typical core for testing and how it is cut for analyses after ended experiment.	19
Figure 3: SEM micrograph taken by the use of a SE-detector. The imaged object is an opal-CT lepisphere found in Aalborg chalk.	22
Figure 4: SEM micrograph of a foraminifera fossil found in MgCl ₂ -flooded outcrop chalk from Liège using backscattered electrons (BSE). The difference in grey-scale reflects the average atomic number of each phase, thereby separating different mineralogies from each other. Here, clay minerals accumulated inside the fossil walls have a brighter shade of grey than the surrounding magnesite, because of a higher AAN. The black areas are pore-spaces filled with epoxy with a low AAN.	23
Figure 5: Production of FIB-lamella of MgCl ₂ -flooded chalk. a) cut-out of lamella from the sample surface. b) Thinned lamella welded to the copper grid (white arrow).	27
Figure 6: MLA scans of a) unflooded material b), the LTT, slice 4, c) MLTT, Slice 4 and d) the ULTT (slice 5). Legend below. The LTT and MLTT show small abundances of precipitated magnesite (blue) inside the original calcite (red) mineralogy, not observed ion unflooded material (a). The ULTT consist only of magnesite (blue) and clay minerals (green).	41
Figure 7: FEG-SEM micrographs of unflooded Liège chalk. a): Recognizable rings (coccoliths) from coccolithophores along with fragments and decoupled grains from micro- and nano-fossils. b): Occurrences of clay minerals (black arrows) and authigenic calcite crystals (white arrow).	41
Figure 8: Examples of precipitation of magnesite in a) inside a foraminifera in the LTT, b) Close-up of magnesite crystal found at the inlet of outcrop chalk from Stevns Klint flooded with MgCl ₂ for 61	

	days. c) Polycrystalline aggregates of magnesite found in chalk from Kansas flooded for 75 days with MgCl ₂	42
Figure 9:	Example of authigenic inorganic calcite (black arrow) found inside a foraminifera shell in unflooded outcrop chalk from Kansas. .	43
Figure 10:	Material from completely altered area in the ULTT. a) Typical texture of the newly formed crystals with rhombic shape and sizes mostly between 100 nm and 1 μm. b) Close-up of crystals in a). c) Spectrum and semi-quantitative analyses of the elemental composition of the area in a). The sample is coated with palladium (Pd), hence the Pd-peak in the spectrum.	44
Figure 11:	FEG-SEM micrograph of unflooded calcite powder. Grainsize varies between ~4 and 33 μm, with partially interlocking grains.	45
Figure 12:	FEG-SEM micrographs of crystals with high magnesium content growing on existing calcite grains at the inlet of an artificial chalk core after 27 days of flooding, marked with black arrows. Original calcite grains are marked with Cc.	45
Figure 13:	FEG-SEM micrographs of polycrystalline aggregates of new-grown crystals with high magnesium content found after 289 days of flooding with MgCl ₂ . Original calcite grains are marked with Cc. a) Observations are made halfway along the flooding-axis and at the outlet (b) Similar observations made at the outlet of the same core, with smaller aggregates of magnesite. c) EDS spectrum of the clusters of new-grown minerals with main contents of C, O and Mg and only minor content of Ca, corresponding to clusters in a).	46
Figure 14:	Severe defects on crystal faces found in long-term flooded calcite powder, halfway between the inlet and the outlet of the cylinder. White boxes show partly dissolved surfaces, while the white arrow points to polycrystalline magnesium aggregates inside one of the defects.	47
Figure 15:	FEG-SEM micrograph of the strongest mineralogical alteration in flooded calcite powder. a) A distribution of crystals of different sizes and shapes is observed. All grains show minimal content of Ca, c) typical EDS spectrum for the crystals. Samples coated with palladium (Pd).....	47

Figure 16: Combination of MLA mapping, ICP-MS analyses and oxygen isotopes measured along the centre of the flooding axis of the three long-term tests. CaO, MgO and $\delta^{18}\text{O}$ isotopes vary along the flooding axis, and match the MLA maps. MLA legend in Figure 6.	49
Figure 17: Results of ICP-MS analyses of the two flooded artificial chalk cores, along with the values for unflooded powder. Only the wt% for MgO and CaO are presented. MgO is higher in the inlet of the two cores, and generally higher after longer flooding period (Core 2). Please observe differences in scale of MgO wt% for the two graphs.....	52
Figure 18: FEG-SEM-micrograph of the transition-zone in the LTT with increased porosity, below the white dashed line, compared to the area still dominated by the original calcite mineralogy to the top of the image.....	54
Figure 19: High magnification FEG-SEM micrograph of clay minerals found inside the transition zone of the LTT.	55
Figure 20: FEG-SEM-EDS mapping of new grown magnesite in a hollow cylinder chalk core flooded with MgCl_2 . Red pixels = magnesium, blue pixels = calcium. Cortesey of Tine Vigdel Bredal.	56
Figure 21: MLA scan of the transition zone in LTT. Legend in Figure 6. Blue pixels = magnesite, red = calcite and green = clay minerals. .	57
Figure 22: FEG-SEM-BSE micrograph from inside the transition zone of LTT. Lighter mineral phases with lower AAN yield less electrons and are therefore darker in the image.	57
Figure 23: SEM-EDS mapping and analysis of the transition zone in MLTT. a) The three slices closest to the inlet of the core. Black box indicates mapped area b) FEG-SEM micrograph of the mapped area. c) EDS map showing the distribution of calcium and magnesium in the area of interest. d) EDS spectrum and quantification from the dolomitic part of the sample. The sample was coated with Au and Pd, hence the peaks.....	58
Figure 24: XRD analyses of the transition zone in slice 2 of MLTT, marked with major peaks. Only calcite (red asterisks) and magnesite (blue asterisk) were observed together with possible	

	observations of clay minerals. No dolomite could be observed.	59
Figure 25:	XRD analysis of slice 2 in the artificial chalk core flooded for 289 days with MgCl ₂ , marked with major peaks. Only calcite (red asterisks) and magnesite (blue asterisk) were observed together with possible observations of clay minerals. No dolomite could be observed.	60
Figure 26:	Raman spectra collected on the first slice of the LTT showing the presence of calcite and the presence of recrystallized magnesite. Calcite peaks are reported in blue/bold, magnesite peaks in red/italic. * represent the neon lamp emission line at 476.8 cm ⁻¹ used for calibration with the Horiba XploRA spectrometer. Peak positions are reported without decimals.	61
Figure 27:	Bright field-STEM image of the primary front in the MLTT, slice 2. Original calcite grains (blue) are rounded (white arrows) and the structure resembles the form of coccolithophore rings. To the right of the image, partly dissolved grains are observed (black arrow). Newly precipitated magnesite grains (red) have a more angular shape and contain small impurities of calcium.	63
Figure 28:	a) Bright field-STEM-EDS image inside the secondary front in the MLTT, slice 2. Newly precipitated magnesite grains (red) with an angular shape, containing small impurities of calcium (blue). b) The distribution of magnesium (red) and calcium (blue) in the crystals c) Typical spectrum and non-standard quantification of the magnesite found in the three long-term flooded cores. The FIB-lamellas are glued to a copper grid (Cu), hence the peak.....	64
Figure 29:	TERS mapping acquired on the MLTT. a) 1 μm x 1 μm topography acquired with tuning-fork based AFM. b) Magnitude signal acquired in the same 1 μm x 1 μm area. c) typical TERS spectrum obtained on a single point, showing peaks at 1086 cm ⁻¹ (calcite), 1094 cm ⁻¹ (magnesite) and 1112 cm ⁻¹ (bicarbonate ion). d) TERS mapping showing the distribution of the 1086 cm ⁻¹ calcite ν ₁ peak. e) TERS mapping showing the distribution of the 1094 cm ⁻¹ magnesite ν ₁ peak. f)	

	Superimposition of the TERS mappings of calcite and magnesite, following the colour code used in the previous panels; g) superimposition of the TERS mappings of calcite and magnesite and of the topography image in a).....	65
Figure 30:	a) Bright field image of adjacent crystals. b) STEM mapping of crystal growing on top of original calcite crystal. Ca = calcium = blue, Mg = magnesium = yellow. c) The position of the line-scan profiles for the crystals in a). d) Chemical analysis along the line scan in c) with X-ray intensities for Mg and Ca. Ca = calcium = blue, Mg = magnesium = red. The white pattern behind the crystals is the copper grid the slice is attached to.	66
Figure 31:	SEM-BSE micrograph of a shell of a foraminifera preserved in the ULTT, ~0.5 cm from the outlet (see Figure 2). The shape of the fossil is preserved, but the mineralogy consists of magnesite with calcium impurities. b) Newly formed crystals of magnesite observed in slice 2 of the ULTT, resembling the shape and size of a coccolithophore ring.	68
Figure 32:	FEG-SEM-BSE micrograph of the fracture after flooding with SSW for 34 days. The flooding direction was horizontally in the images that show approximately one cm of the fracture, split into two images. The lighter phases in the SEM-BSE image are remnants of the fracture, seem denser and have an increase in lighter mineral phases.	70
Figure 33:	SEM-BSE micrograph (a) and MLA scan (b) of the same area of the fracture. The Mg-content is higher on the concave side (below) of the shell than on the convex side (above). Legend below. White areas relate to pore space.	71
Figure 34:	Oxide values measured by EMPA along the profile A - A' in Figure 33. Dotted lines are average values.	71
Figure 35:	NanoSIMS images showing relative concentrations of elements between a shell-fragment and the surrounding matrix in fractured Liège chalk flooded with synthetic seawater (SSW). Notice the enrichment of Mg in the surrounding matrix compared to the concentration of Mg in the shell-fragment and the opposite pattern for Ca.	72

Figure 36: FEG-SEM image of outcrop chalk from Liège flooded at 130 °C for 115 days with MgCl₂ (slice 6, near the outlet), showing pore surfaces and throats covered by newly formed Si-Mg-bearing minerals (orange dashed circle)..... 74

Figure 37: Saturation index of magnesite in the flooded calcite powder after a) 10 days b) 50 days and c) 289 days. After 289 days, magnesite no longer precipitates at the inlet, and may possibly even dissolve, due to changes in e.g. pH. Courtesy of Aksel Hiorth. 77

Figure 38: FEG-SEM micrographs of water wet and mixed wet Kansas chalk. At the inlet (a and b), small grains or crystals of magnesite precipitate on top of original calcite grains, while further into the core (c and d), polycrystalline magnesite aggregates precipitate..... 80

Part 1

1 Introduction

On the Norwegian Continental Shelf (NCS) many of the producing hydrocarbon fields are mature with a declining production trend. A large amount of resources cannot be produced with the current technologies or strategies, and the potential is enormous for creating additional values through improving the recovery from these fields. The time is ripe to implement measures which can improve the recovery of oil, as well as providing better solutions to produce hydrocarbons from future reservoirs in an effective way, with regards to recovery rate, produced water, finances and minimizing the environmental footprint.

Carbonate reservoirs hold over 50% of the world's hydrocarbon reserves (Flügel, 2004; Roehl et al., 1985), and research on carbonate mineralogy is therefore important. In the Norwegian, British and Danish sectors of the southern North Sea, one of the major reservoir rocks is the very fine-grained carbonate rock chalk, containing significant hydrocarbon deposits in formations such as the Ekofisk (Danian), Tor (Campanian to Maastrichtian) and Hod (Turonian to Campanian) Formations.

Injection of seawater is a well-proven Improved Oil Recovery (IOR) measure to maintain pore-pressure and production of hydrocarbons from reservoirs. During the 1980's the chalk field at Ekofisk experienced significant compaction accompanied by seabed subsidence due to depletion of the reservoir (Hermansen et al., 2000; Hermansen et al., 1997; Maury et al., 1996; Nagel, 1998; Sulak et al., 1989; Teufel et al., 1991). To reduce compaction and re-pressurize the reservoir, injection of seawater was introduced in 1987. The injection program succeeded to build up pore-pressure, however, reservoir compaction continued even after re-pressurization (Delage et al., 1996). This phenomenon was explained by interactions between ions in the seawater and

Introduction

the rock itself, and is referred to as “water weakening of chalk”. Since this discovery, understanding the interactions between non-equilibrium brines and reservoir rock has been of major interest both in scientific research and to the industry.

Compaction is an important driving mechanism to increase the recovery of oil, and injection of non-equilibrium brines has proven to also affect the wetting state of the rock, thus the possibility to release more of the immobile oil from the rock surface. Injection of fluids with specific compositions is referred to as Enhanced Oil Recovery (EOR), and is concerned with optimizing the injection fluid to produce the immobile oil, thus maximising the recovery of hydrocarbons.

Over the last decades, large amounts of experiments have been carried out to understand how ions in non-equilibrium brines interact with the rock in which it is injected into, in particular with chalk. Spontaneous imbibition experiments have shown that certain ions in e.g. seawater are more active in rock-fluid interaction than others affecting the recovery of oil, and that both temperature and primary mineralogy may be important factors in this interplay (Austad et al., 2008; Fathi et al., 2011; Fernø et al., 2011; Generosi et al., 2017; Milter et al., 1996; Puntervold et al., 2008; Sakuma et al., 2014; Strand et al., 2006; Zhang et al., 2007). Ions in the seawater may alter the mineral surfaces from oil or mixed wet to more water wet, especially at elevated temperatures. Of particular interest are Mg^{2+} , Ca^{2+} , and SO_4^{2-} , and the composition of the pore-fluid and injected water are also found to be important factors in water weakening of chalk e.g. (Andersen et al., 2017; Carles et al., 2005; Delage et al., 1996; Gutierrez et al., 2000; Heggheim et al., 2005; Hellmann et al., 2002; Hiorth et al., 2013; Korsnes et al., 2008a; Korsnes et al., 2008b; Madland et al., 2011; Megawati et al., 2013; Megawati et al., 2015; Nerموen et al., 2015; Nerموen et al., 2018; Newman, 1983; Piau et al., 1994; Rhatt et al., 2001;

Introduction

Risnes et al., 2005; Schroeder et al., 1998; Tucker et al., 1990). There are multiple processes affecting the rock during flooding with reactive brines. This includes changes in surface-complexation, -charge and -potential along with alterations of mineralogy and ion-exchange (e.g. (Andersen et al., 2017; Austad et al., 2008; Borchardt et al., 1989; Flügel, 2004; Heggheim et al., 2005; Hiorth et al., 2010; Hiorth et al., 2013; Jackson et al., 2016; Korsnes et al., 2008b; Madland et al., 2011; Megawati et al., 2013; Nermoen et al., 2015; Sakuma et al., 2014; Strand et al., 2006; Tucker et al., 1990; Zhang et al., 2007; Zimmermann et al., 2015)). Chalk is a rock, which due to its very fine-grained character, has a high specific surface area (often between 1.5 and 7 m²/g, (Hjuler et al., 2009)), up to 10 times the value of sandstones. The injected seawater therefore interacts with the rock along extended mineral surface areas, which increase the effect of rock-fluid interactions, hence the fluid sensitivity of the rock (Heggheim et al., 2005). Changes in the mineralogic composition affect compaction, specific surface area, mineral surface charges, porosity and permeability of chalk, as well as the wettability of the grain surfaces. Therefore, when the brine composition is optimized for EOR purposes, it is important to study its effect on mechanical properties.

Understanding the underlying mechanisms of water weakening of chalk is important to predict and control hydrocarbon-reservoir behaviour, through modelling and simulation at all scales. Additionally, water weakening also plays a role in carbonate aquifers and erosion of costal carbonate cliff formations (Lawrence et al., 2013; Mortimore et al., 2004).

In this study, the main objective has been to investigate which, how and where mineralogical alterations take place in a rock sample when flooded with specific fluids under specific conditions, and link those mineralogical alterations to the mentioned changes in mechanical properties of the rock. Previous studies have shown that mineralogical alterations first and foremost

Introduction

take place at micro- and nano-scale (**Paper IV** and **V** (referring to “List of publications”, page xiii and part 2 of the thesis) and e.g. (Madland et al., 2011; Minde et al., 2017; Minde et al., 2016; Zimmermann et al., 2015)). Mineralogical alterations or incorporation of ions can even on grain-scale and below change the adsorption energy of the surface, thus altering the wettability (Andersson et al., 2016; Sakuma et al., 2014). The foci of the research in this study are, on one hand, therefore to understand the mineralogical alterations at core- and pore-scale, down to submicron resolution, and, on the other hand, to create a “toolbox” that is equipped with a set of methods that provide informative and effective analyses of mineral replacement reactions in rocks, related to EOR research as discussed in **Paper VI**.

This approach delivers explanations in regard of the which, the how and the where:

- 1) **Which** mineralogical alterations take place? **Which** shape and structure do the precipitated minerals have?
- 2) **How** do the mineral replacements take place?
- 3) **Where** do the changes take place? Is the preferred place related to texture, original mineralogy and distance from the fluid injection site?

Studies of mineral replacements encompass a wide range of disciplines. Research carried out to understand the kinetics and reactions associated with mineral replacements, whether these are linked to metamorphism, metasomatism, diagenesis and/or weathering, is of importance not only as basic knowledge of rock-fluid interactions, but also to “...quantify and predict the response of Earth’s surface and crust to the disequilibria caused by the various natural and anthropic input of energy to our planet.” (Oelkers et al., 2009). Carbonate sedimentary rocks are common on Earth and limestone and dolomite are two major rock-types found in sedimentary rock successions. Limestones are important contributors in the global carbon and geochemical cycles.

Introduction

Additionally, carbonate mineral kinetics dictate a wide range of processes in our world like preservation of large monuments and buildings as well as the characteristics of petroleum reservoirs (Morse et al., 2002), and are important for the development of fauna and algae in the marine environments. Understanding carbonate dissolution and precipitation kinetics are therefore paramount for numerous important processes in nature.

In the field of mineral replacements most of the experiments are carried out on single crystals or on powdered material in fluid-suspension. A thorough review of such experiments is given in Putnis et al. (2009), concluding that in fluid-induced mineral replacements, the transition from one mineral to another progresses from the surface and towards the centre of a crystal by the formation of a porous reaction front where the driver is the state of equilibrium at the reaction interface, not the equilibrium state of the bulk fluid. None of the discussed examples show evidence of solid state diffusion through crystal lattices. The alterations are driven by a front of dissolution and precipitation progressing into the crystal with a sharp reaction rim. The alteration products show different scales of pseudomorphism, dictated by the rate-limiting factor being either the dissolution rate, resulting in nanometre-scale pseudomorphism, or being the precipitation rate, resulting in micrometre-scale pseudomorphism (Xia et al., 2009).

Over the years, in the studies of water weakening of chalk and related EOR research, a need to simplify the system has become apparent. Numerous factors, like brine composition, temperature, pressure, and mineralogical aspects are interdependent, hence it is difficult to separate the effects of each parameter. Seawater has been replaced by simpler aqueous brines, such as MgCl_2 , to study the effects of specific ions, in this case Mg^{2+} , which is very reactive towards calcite even after short periods of flooding. Additionally, even though chalk largely consists of calcite, differences in primary mineralogy and arguably the

Introduction

depositional environment seem to dictate many of the alterations during mechanical flow-through experiments (**Paper III**), revealing extraordinary complex rock-fluid interactions. Those aspects are central parts of this thesis, including performing EOR experiments on “artificial chalk cores”, (see chapter “2.2.2 Calcite powder” and **Paper II** on this topic) and analysing the mineralogical alterations when calcium is replaced by magnesium. The materials that form the basis of this work are different types of chalk sampled in quarries from Denmark, Belgium and USA (see chapter “2.2 Outcrop chalks in this study” for detailed information about the used sample material) and calcite powder, all tested in triaxial cells (see chapter “2.3.1 Triaxial tests” for detailed experiment description) and compared with untested material or sample material flooded with less reactive brines such as NaCl (**Paper IV and V**).

The analytical tools used in this study are on one hand well-known in terms of their application to rocks and partly on chalk and on the other hand this research presented here developed new methodological approaches for the study of mineralogical changes in EOR experiments. The methods used in this project have been:

- Field Emission Gun Scanning Electron Microscopy (FEG-SEM) with Energy Dispersive X-ray Spectroscopy (EDS)
- Mineral Liberation Analyzer (MLA)
- Focused Ion Beam (FIB)-SEM
- Transmission Electron Microscopy (TEM)
- Electron Microprobe Analysis (EMPA)
- X-ray Diffraction (XRD)
- Nano Secondary Ion Mass spectrometry (nanoSIMS)
- Induced Coupled Plasma – Mass spectrometry (ICP-MS)

Introduction

- Stable isotope analyses
- Analyses of effluent water
- Measurements of Specific Surface Area (SSA) and density by pycnometry
- Additional analyses by Raman spectroscopy and Tip Enhanced Raman Spectroscopy (TERS) combined with Atomic Force Microscopy (AFM)

By combining all of the above mentioned tools, we have been able to extract considerable amount of information from the studied samples by progressively increasing the resolution of the analyses and comparing results from chemical and elemental analyses with mineralogical and crystallographic techniques such as XRD and Raman spectroscopy (e.g. **Paper I, II and VII**). With this, it is possible to identify, map and quantify the mineralogical alterations, at centimetre, millimetre, micrometre and nanometre-scale. The value of the different methods for EOR-related issues is variable, and some methods have proven to be more suitable than others. However, this process has enabled the selection of which tools should be part of the mentioned toolbox to interpret experiments involving rock-fluid interactions, and which methods are most suitable to answer very specific questions.

The results from this study are therefore important for a wider range of interest groups:

- Mineralogists
- Applied petroleum geologists and engineers
- Technicians to see how far their methods can be stretched on one of the most complicated study material: chalk
- Modellers. The results are basic components for input to models of all scales simulating the effects of EOR fluids and imbibition processes in

Introduction

porous rocks (Appelo et al., 2009; Aursjø et al., 2017; Evje et al., 2011; Helland et al., 2017; Hiorth et al., 2013; Lichtner, 1996; Pedersen et al., 2016; Pedersen et al., 2014; Vinningland et al., 2017; Wei, 2012). Some of the most important input parameters are primary and secondary mineralogy, and the rate of which the mineralogical changes occurs. Investigation of mineralogical alterations after core-flooding experiments may provide validation for or constrain models and simulations. Continuous interaction between the two disciplines provides information to improve both experimental and modelling work.

Hence, geological and mineralogical understanding together with rock mechanical studies and modelling is an ideal fusion to reveal the most important data for processes for every interest group concerned about commodities in rocks. This research therefore represents a mixture of basic research and applied science.

2 Material and methods

2.1 Material

2.1.1 Chalk

Chalk is by definition a fine-grained, sedimentary rock, belonging to the class of carbonates and mostly a pelagic sediment composed mainly of biogenic and authigenic grains. It is a rather simple rock in terms of its mineralogy, with the major constituent being calcite (CaCO_3), and only minor occurrences, varying from a few and up to 15 wt% (weight percent), of other minerals such as dolomite, quartz, opal, apatite, feldspar, pyrite, oxides and different clay minerals, depending on location, age and degree of diagenesis (Hjuler et al., 2009). The colour of chalk is in most cases white to grey or beige, depending on the non-carbonate content. Chalk has commonly a layered structure at centimetre- to metre-scale, due to its low-energy depositional environment and differences in depositional rates. Periods of non-deposition are commonly represented by hardgrounds or thin layers of clay (Brasher et al., 1996). However, in various geographical areas, tectonic movements can destabilize the chalk and allow for movement of large faulted blocks, often towards the deeper basin (Kennedy, 1987), as extensional tectonics were, in a variety of locations, typical for the Cretaceous times. Together with erosion, block faulting also enabled reworking of chalk either as syn- and post-depositional gravitational flows, often producing a more heterogeneous brecciated structure. The rock is composed mainly of skeletal debris of calcareous micro-fossils such as coccolithophores, calcispheres and foraminifera along with fragments of macro-fossils (Scholle et al., 1973; Tucker et al., 1990). Coccolithophores are unicellular algae, belonging to the group of haptophytes, which control intercellular precipitation of calcite into skeletal plates, referred to as coccoliths

(Scholle, 1978; Thiel, 2011). These coccolith plates are transferred to the surface of the algae, forming an exoskeleton of protection. Coccolithophores often dismantle into their individual skeletal plates, coccoliths, as they die and settle to the seafloor. Coccolithophores commonly have a size less than 20 μm (Thiel, 2011), while individual coccolith rings range between 0.3 and 5 μm (Scholle et al., 1973), or even larger (Kennedy, 1987). Each coccolith ring is built up of platelets or grains with sizes of one μm and below (Bjørlykke, 2015), and these platelets are often found in their individual forms in chalk (Figure 1). Coccolithophores have existed from the Mesozoic era, and were extremely abundant during the Cretaceous period. They still exist in oceans today, and play an important part in the global carbon budget (Thiel, 2011).

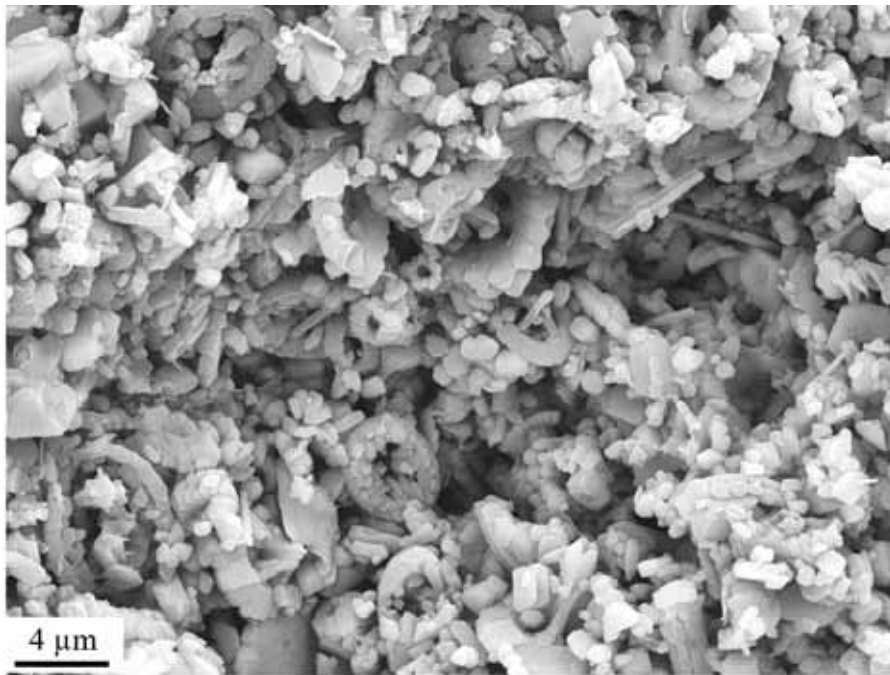


Figure 1: SEM micrograph of Liège chalk showing typical components of chalk; skeletal debris of coccolithophores and other micro-fossils along with minor occurrences of clay minerals.

Foraminifera shells are larger, ranging in size between 20 and 100s of μm , and when preserved, often contribute to larger pore-spaces in chalk (Flügel, 2004;

Scholle, 1978). In addition, shells and fragments from larger fossils like bivalves and gastropods can be observed. As shells and skeletal debris from these organisms fall to the seafloor, they form calcareous ooze. Even though calcareous organisms thrive under warm climatic conditions, oozes accumulate slowly, 1 to 25 cm per thousand year (Garrison, 2010; Tucker et al., 1990), and as such, the over hundreds of metres thick layers of chalk, as found in the North Sea, take millions of years to deposit. The deposition rate is not only related to the accumulation of sediments, but is also affected by dissolution of calcareous material in seawater. Oozes rarely form below the carbon compensation depth (CCD), which is the depth where the dissolution rate is equal to or is higher than the sedimentation rate. This depth usually lies around 4500 meters, depending on e.g. pH, temperature, and CO₂-concentration of the seawater (Garrison, 2010; Hancock, 1975).

Because of the pelagic nature of chalk, the non-carbonate content is generally low. However, clay minerals are often observed, along with other silicates, such as chert and quartz. The origin of these minerals may come from terrigenous inputs in shallow areas or due to depositional lowstands (Brasher et al., 1996), but mainly from volcanic input and diagenesis of siliceous fossils such as sponge spicules, and to a less degree diatoms and radiolarians (Scholle, 1977). After deposition, burial and de-fluidization lead to compaction and lithification of the ooze. During burial the ooze mechanically compacts, leading to a porosity reduction from 60 – 80% to values commonly between 10 – 50% (Hjuler et al., 2009; Scholle et al., 1973), depending on conditions during burial. Chalk has grainsizes mostly between 1 and 20 µm, with the exception of larger fossils, and permeability is low, often in the range between 1 to 5 mD (Scholle et al., 1973; Sulak et al., 1989). The porosity of reservoir chalk is, however, often surprisingly high for rocks found at such deep burial depth with a fine-grained character, and may be caused by overpressure in the reservoir during

burial or by early oil emplacement (Alam et al., 2012; Brasher et al., 1996; Moore, 2001; Risnes, 2001; Scholle, 1977; Tucker et al., 1990).

During the Late Cretaceous, large areas of Northern Europe were covered by shallow seas, where the Central North Sea Graben formed a deeper marine environment (Molenaar et al., 1997). The sea-floor had structural highs and lows where chalk was commonly deposited in deeper areas.

2.1.2 Fractures in chalk reservoirs

Due to the exceptionally low permeability in high porosity chalk, fractures play an important role during fluid-flow. Matrix permeability in the Ekofisk field, where chalk is the reservoir rock, lies in the range of 1 to 5 mD (Sulak et al., 1989), and can as well be reduced by pore collapse due to increase in effective stress during hydrocarbon depletion of the reservoir during production. Production of oil therefore depends on fractures to increase the effective permeability of the reservoir (Snow et al., 1989) and the effective permeability in the Ekofisk field ranges between 1 to 100 mD (Sulak et al., 1989; Torsaeter, 1984).

Fractures also play an important role during fluid-injection into a reservoir. The fluid-flow mainly follows the fracture system, as well caused by the limited permeability of the matrix. Most of the oil in chalk reservoirs is trapped in the matrix and displacement of oil is mostly related to spontaneous imbibition of water into the matrix (Chen et al., 2001; Cuiec et al., 1994; Milter and Austad, 1996; Morrow and Mason, 2001; Standnes and Austad, 2000; Torsaeter, 1984; Zhang et al., 2007). In a fractured reservoir, where the fluid-flow may be limited to fractures, the contact between injected water and the rock may be limited, thus modifying the effect of EOR fluids (Graue et al., 1999; Gutierrez et al., 2000; Hirasaki and Zhang, 2004; Nielsen et al., 2000). Hence, it is important to understand how injected brines use fractures in conjunction with mobilization

of oil from the matrix and create a more efficient sweep. Scenarios, from a mineralogical aspect, would be clogging of fractures forcing brines to enter the matrix and affecting the production of hydrocarbons.

2.2 Outcrop chalks in this study

Reservoir chalk from the North Sea is difficult to sample due to the expense of extracting it and shortage of core material. Laboratory tests are therefore rarely carried out on reservoir rocks from deposits in the North Sea, but more commonly on onshore chalk analogues. There are several outcrops around the world where analogues to North Sea reservoir chalk may be collected. The various onshore chalks have different composition and mechanical properties (Hjuler et al., 2009), and different chalks are therefore used to test different research questions and to understand different reservoirs. For fundamental studies, the application of outcrop samples gives sufficient information for further research and is paramount for all modelling exercises in this field of research and has been applied with success for decades.

Five types of outcrop chalks have been sampled for this study. They are collected from quarries of Lixhe near Liège and Harmignies in Mons, Belgium, along with two Danish chalks: Stevns Klint sampled near Copenhagen and Rørdal near Aalborg, and chalk from the Niobrara Formation in Kansas (USA).

2.2.1.1 Liège: Gulpen Formation

One of the outcrop chalks used in this study is from the Gulpen Formation, sampled from an outcrop near Liège in Belgium, and is found to match the mechanical behaviour of chalk from the Ekofisk field (Collin et al., 2002). The Gulpen Formation is of Late Campanian to early Maastrichtian age (Molenaar et al., 1997).

The chalk from the Liège outcrop has a high carbonate content. The non-carbonate content is approximately 5 wt% and consists of quartz, smectite/mixed smectite-illite layer, mica and clinoptilolite as well as apatite, feldspar, pyroxene and titanium oxide (Hjuler et al., 2009). The preservation of coccoliths and pore-space is medium and good, respectively. Calcite cementation is commonly not found in studies on this type of chalk (Hjuler et al., 2009), pointing to a low degree of diagenesis. The porosity of chalk from Liège lies in the range of 40 to 43%, with a permeability between 1 and 2 mD (Delage et al., 1996; Korsnes et al., 2006; Madland et al., 2011; Risnes et al., 1994; Schroeder et al., 1998).

2.2.1.2 Mons; Trivières Formation

One of two chalk types with extremely high carbonate content used in this study is collected from Mons, Belgium. The chalk from Mons is taken from the Trivières Formation of Campanian age. The chalk was deposited in the Mons basin, the eastern part of the Paris basin, and the sampled outcrop is found in Harmignies. The Trivières Formation is correlated to the Gulpen Formation sampled in Liège (Dusar et al., 2007). Porosity is in the range of 36 to 44% (Gaviglio et al., 1999) and the non-carbonate content only reach less than 1% (**Paper V**). The chalk from the Trivières Formation has a high degree of intact coccoliths (Richard et al., 2005). Chalk samples from this outcrop have together with chalk from Stevns Klint in Denmark been used as an analogue to both the Valhall, Dan and Ekofisk chalk reservoirs in the North Sea.

2.2.1.3 Stevns Klint: Tor Formation, Sigerslev Member

The chalk from Stevns Klint belongs to the Tor Formation, in particular the Sigerslev Member and is of middle Upper Maastrichtian age (Surlyk et al., 2006). It consists of nearly 99% carbonate minerals, with only scars

occurrences of quartz, clay, feldspar and apatite (Hjuler et al., 2009; Håkansson et al., 1975). The chalk has porosity values between 42 and 50% and permeability of 1-2 mD (Hedegaard et al., 2011; Madland et al., 2011).

2.2.1.4 Aalborg: Tor Formation, Rørdal Member

Aalborg chalk has been studied to understand which effects the abundant opal-CT have on mineralogical and mechanical properties of the rock during rock-fluid interaction (**Paper IV**). The chalk is taken from the Rørdal quarry near Aalborg, Denmark and is of Lower Upper Maastrichtian age, and contains 90 – 95% carbonate minerals (Håkansson et al., 1975). The remaining impurities consist mainly of clay and quartz, most commonly in the form of opal-CT along with smectite, mica, kaolinite, clinoptilolite, apatite and feldspar. The exposed chalk at the Rørdal quarry belongs to the Tor Formation of the North Sea and the cyclic Rørdal Member, which is approximately 10 m thick. The rather high non-carbonate content, mainly in the form of diagenetic opal-CT, is linked to the early late Maastrichtian cooling event (Surlyk et al., 2010).

2.2.1.5 Kansas: Niobrara Formation

Furthermore, chalk from a different basin has been used, the so-called ‘Kansas chalk’ sampled from the Niobrara Formation. The samples are taken from the lowermost Fort Hayes Member which is of Early Coniacian age, (Da Gama et al., 2014), deposited as part of the Western Interior Seaway in the Rocky Mountains and Great Plains region, USA. The non-carbonate content is usually less than 5%, and mainly consists of quartz, clay and pyrite and is described as a bioturbated chalk (Hattin et al., 1977; Longman et al., 1998; Runnels et al., 1949). The content of recrystallized, inorganic calcite and calcite cement is higher in the Kansas chalk compared to other outcrop chalks studied in this thesis (Megawati et al., 2015; Scholle, 1977), pointing to deeper burial depth

and a higher degree of diagenesis. Porosity of chalk from the Niobrara Formation is in the range between 37 and 40% and permeability of 2-4 mD (Andersen et al., 2017; Korsnes et al., 2006; Megawati et al., 2013) and has been considered a good analogue to North Sea reservoir chalk with regards to these properties (Tang et al., 2001).

2.2.2 Calcite powder

As an attempt to simplify the experiments further and to be able to study the basic mineral replacement reactions involving Ca^{2+} and Mg^{2+} separately, the mineralogy of the rock itself was simplified by chalk being substituted by cylinders of calcite powder, mimicking the geometry of outcrop chalk core-samples. They consist of 99.95% pure calcite (CaCO_3) powder manufactured by Merck®. Minor impurities of other elements such as Fe and Mg occur. However, the total only adds up to ~0.05%. The particle size has an average of ~14 μm , ranging from 3 to 44 μm . The powder was compressed to cylinders (D~37 mm, L~70 mm) and are hereafter referred to as “artificial chalk cores”.

2.3 Methods

The main goal for the use of the methods in this thesis is to image and positively identify new-grown crystals and minerals in fine-grained sedimentary rock samples. Some of the methods can image and identify the elemental composition of a sample, while others provide both elemental and mineralogical qualitative analyses. However, the crystallographic mineralogical analyses are only in cases accompanied by a high-resolution images, with the possibility to identify the exact crystal of analysis. Therefore, the amount of methods taken into use is large, providing the possibility to combine methods to gain then useful complementary data from the analyses.

One of the aims of this work is to create a “toolbox” for mineral replacement studies related to EOR experiments. However, not all of the described methods are suitable for an effective and quick analysis to interpret experiments and samples from EOR tests, but may be used as additional tools to study questions of special interest. Research shall attempt a variety of possibilities and this study shows that the approach of challenging methods leads to further knowledge. Last, but not least, we are able to combine analytical data of different scales to describe the properties of grains and the pore-network from nano- to centimetre-scales.

2.3.1 Triaxial tests

Cylindrical cores were drilled from the different outcrop chalks. The cores were shaped to one of two diameters ~ 37.0 or ~ 38.1 mm, with a length of ~ 70.0 mm and used for mechanical flow-through experiments in triaxial cells.

After preparation, the cores were dried for 12 hours in a heating chamber at 100 °C to remove water before the dry mass was determined. The carbonate mineralogy is not affected by the drying conditions (MacDonald, 1956). Thereafter all cores were saturated with distilled water (DW) in a vacuum chamber. Dry and saturated core mass were used for porosity determination. When installing the core inside the triaxial cell, a heat shrinkage sleeve was used to separate the core from the confining oil. After mounting the triaxial cell, the confining pressure was increased to 0.5 MPa. Thereafter all experiments were conducted according to the following stages:

1. The cores were flooded with at least three pore volumes (PVs) of DW overnight at ambient temperature to clean the sample before the flooding test. This flooding procedure does not significantly alter the geochemical properties of the core.

2. Subsequently, a change from flooding with DW to the reactive flooding brine by attaching the piston cell into the flow loop was performed.
3. The confining pressure and pore pressure were increased simultaneously to 1.2 and 0.7 MPa, respectively, before the temperature was raised to the chosen values. The pore pressure and temperature were then kept constant throughout the test.
4. The confining pressure was increased from 1.2 MPa until the rock began to deform plastically, i.e. when the stress - strain behaviour became non-linear. The confining pressure was, if applicable to the test, further increased to the chosen creep stress before the cores were left to compact in the following creep phase (deformation at constant stress).
5. The axial deformation at constant temperature and pressure conditions (termed creep) was monitored during continuous flooding. The pore pressure and confining pressure varied within 0.1 MPa such that the effective stresses were stable throughout the test period.
6. The temperature was kept constant throughout the experiment by a heating jacket, ensuring an accuracy of ± 0.1 °C.
7. Before dismantling the core, the samples were cleaned by injection of minimum three PVs of DW to avoid precipitation of any salts.

After testing the cores were divided into six or seven slices for mechanical, chemical and textural analyses and compared to untested material from the same core (Figure 2).

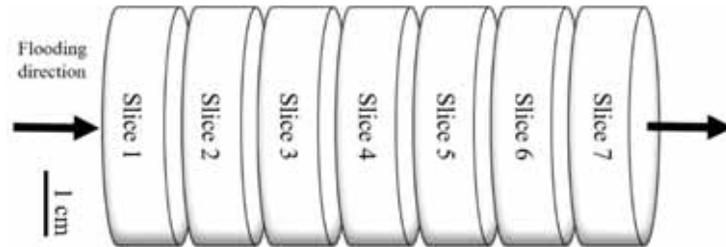


Figure 2: Sketch of a typical core for testing and how it is cut for analyses after ended experiment.

Further details on experimental lay-out and rock mechanical processes can be taken from Madland et al. (2011), Wang et al. (2016) and **Paper IV** and **V** and references therein.

2.3.1.1 Overview over the flooding tests presented in this study

Three long-term tests of injecting MgCl_2 into outcrop chalk from Liège were analysed. The cores were flooded for one and a half, two and three years, and named the Long-Term Test (LTT), the Medium-Long-Term Test (MLTT) and the Ultra-Long-Term Test (ULLT), respectively. All cores were flooded at 130 °C, at high effective stresses, with 0.219 M MgCl_2 and for the MLTT a period of flooding with 0.219 M MgCl_2 + 0,130 M CaCl_2 and with changes in pH. For detailed setups and flooding procedures, the reader is referred to **Paper I** and (Minde et al., 2017; Nermoen et al., 2014; Zimmermann et al., 2015).

Chalk from the five described outcrops were flooded for periods of 45-118 days, either with NaCl or MgCl_2 at different temperatures. For details, the reader is referred to **Paper IV** and **V**. A chalk core from the Liège outcrop was fractured before flooded with synthetic seawater for 34 days at 130 °C (**Paper III**). Two artificial chalk cores were produced from pure calcite powder and flooded at 130 °C with MgCl_2 at close to ambient pressures. The tests lasted for 27 and 289 days. Further description is given in **Paper II**.

2.3.2 *Electron microscopy*

Electron microscopy offers higher resolution than optical microscopy, in extreme cases up to atomic-scale resolution. Unlike with Optical Light Microscopy (OLM), imaging is performed by using an electron beam, with a much smaller wavelength than optical light, thus offering higher resolution than in OLM. Commonly, Scanning Electron Microscopy (SEM) offers also a better depth of field. The interaction of the electron beam with the samples produces different signals, enabling analyses yielding information on topography, texture and composition down to nanometre- and Ångström-scales.

2.3.2.1 *Sample preparation*

Electron microscopy demands high quality samples. When preparing samples for electron microscopy, it is important that the samples have an electronically conductive surface, to ensure a steady flux of electrons across the sample and avoid charging or build-up of electrons. Sedimentary rocks are, in nearly all cases, non-conductive and have therefore to be coated by a conductive layer, such as carbon, palladium or gold. SEM chambers may take rather large samples, up to tens of cm in diameter, but to ensure good results, the samples should be as small as possible. For chalk, small freshly broken pieces of rock in the size-range of 0.5 x 0.5 x 0.5 cm are often used for analyses. In addition, uncovered, polished thin sections and epoxy impregnated mounts have been used.

For Transmission Electron Microscopy (TEM), sample preparation of the brittle and porous chalk is very challenging. Traditional methods such as mechanical and electrolyte polishing are either difficult or not possible, and the methods found to be most fitted in this study was either deposition of powdered rock on copper grids coated with carbon films, or sample-preparation by

Focused Ion Beam (FIB)-SEM, discussed in section “2.3.2.4 Focused Ion Beam Scanning Electron Microscopy (FIB-SEM)”.

2.3.2.2 *Field Emission Gun Scanning Electron Microscope (FEG-SEM)*

In Field Emission Gun Scanning Electron Microscopy (FEG-SEM) electrons are accelerated by an electron gun to create a focused electron beam to scan the sample in an evacuated chamber. The FEG-SEM has a field-emission gun, inducing electrons by an electrostatic field. This allows for a much smaller beam-diameter with higher stability and intensity of electrons; hence, the resolution of this type of SEM is higher than when using a filament as source. Through electromagnetic lenses and apertures, the beam is focused and adjusted to produce an as small as possible spot of primary electrons on the sample surface.

When the beam hits the surface of the sample, various energy signals are reflected or produced from the surface which are collected by different detectors. These are, amongst others, Secondary Electrons (SE), Back-Scattered Electrons (BSE), and characteristic X-rays as well as, in cases, visible and fluorescent light. The beam interacts with the sample in three dimension with a spherical emission volume of which diameter will vary with settings of the microscope and the sample-material, but often lie in the range of 1 μm . The emission of secondary electrons will vary as a function of the topography and only partly of the composition of the sample and enables imaging of the surface (Figure 3). As an atom is bombarded with primary electrons, electrons placed in the shells of the atom may be excited and emitted from the sample as secondary electrons. These are in-elastically scattered, and have therefore a lower energy than the primary electrons. The primary electrons penetrate a certain distance into the sample, depending on which type of material is studied

and the settings of the microscope. However, because of the lower energy of secondary electrons, only signals from the upper 5λ (λ = mean free path of the secondary electrons) will escape the sample (Hjelen et al., 1989). The secondary electrons are gathered by an Everhart-Thornley-detector as the beam scans the surface in a sequence.

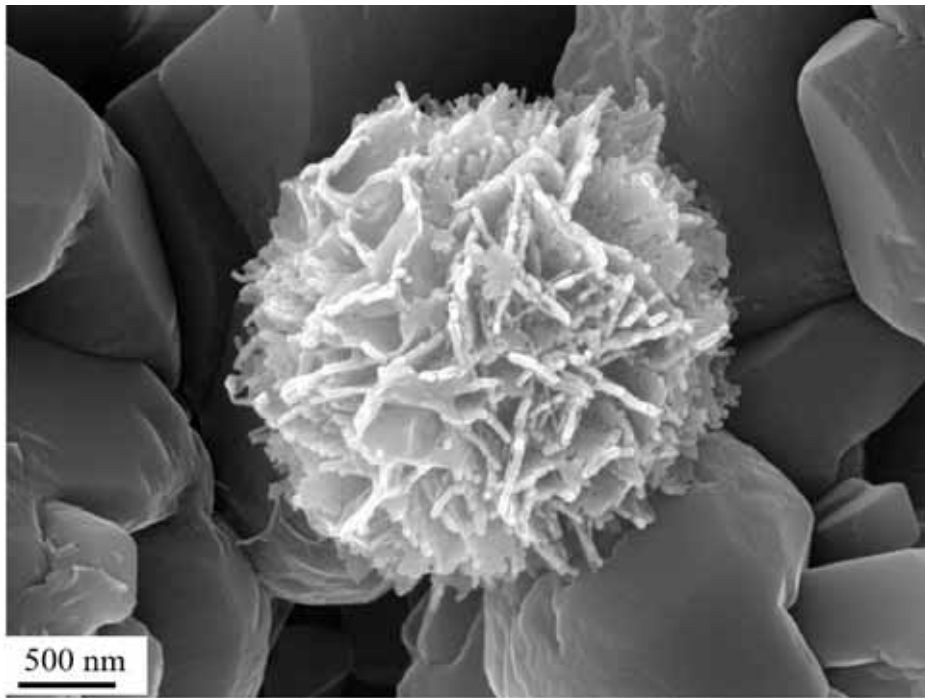


Figure 3: SEM micrograph taken by the use of a SE-detector. The imaged object is an opal-CT lepisphere found in Aalborg chalk.

A BSE detector collects the reflected, or backscattered, primary electrons, which are a result of elastic scattering. The backscattered electrons change direction, while the energy is conserved. The fraction of backscattered electrons produced from the surface is related to the atomic number of the elements in the sample. As such, imaging of different phases in a sample based on composition is possible, returning grey-scale images linked to the Average

Atom Number (AAN) of each phase. A mineral with higher AAN will yield a brighter shade of grey in the image (Figure 4).

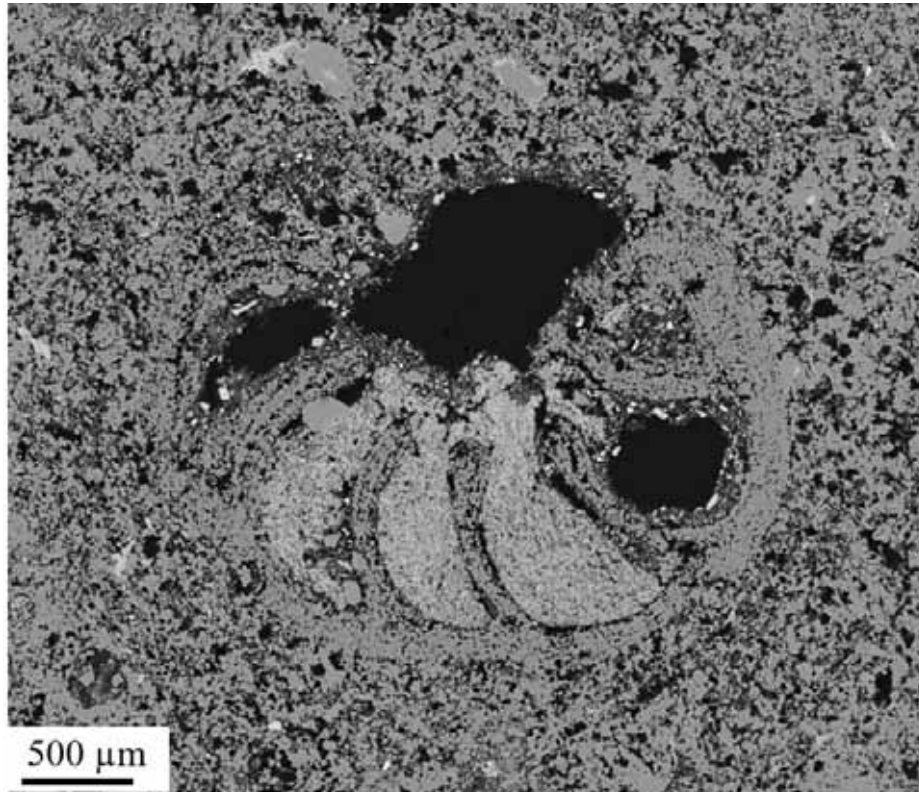


Figure 4: SEM micrograph of a foraminifera fossil found in MgCl_2 -flooded outcrop chalk from Liège using backscattered electrons (BSE). The difference in grey-scale reflects the average atomic number (AAN) of each phase, thereby separating different mineralogies from each other. Here, clay minerals accumulated inside the fossil walls have a brighter shade of grey than the surrounding magnesite, because of a higher AAN. The black areas are pore-spaces filled with epoxy with a low AAN.

As the backscattered electrons keep their high energy level, the emission-volume of these electrons is larger than for secondary electrons. This means that electrons from deeper into the sample may be emitted and detected.

Energy Dispersive X-ray Spectroscopy (EDS) detects characteristic X-rays which are produced as electrons from the inner shells of atoms are excited by incoming primary electrons and electrons from outer shells jump inward to

replace the excited electrons, thus releasing energy in form of characteristic X-rays. Because of the difference in atomic structure, the energy and the wavelength of the released X-rays from each element will differ. The X-rays are detected by a silicon crystal doped with lithium. Based on the detected X-rays and the energy spectrum, quantification of each element is possible. The accuracy varies based on many factors, and lighter elements such as carbon and oxygen are especially difficult to measure precisely, due to lower energy of the X-rays. However, use of standards allow for quantification, mostly at a semi-quantitative level. X-rays may be detected from single grains, spots or areas. It is also possible to perform EDS analyses in an automated sequence which provides repeated scanning of a line or areas to map the presences of one or several elements in the defined area.

In addition to the signals discussed above, samples bombarded with accelerated electrons also emit light, Auger electrons and continuous X-rays.

For these studies a Zeiss Supra 35VP located at the University of Stavanger (UiS) has been used where the settings were varied as follows: 2 – 25 kV acceleration voltage, apertures between 30 and 60 μm , and a working distance from 3 to 15 mm. The FEG-SEM at UiS is equipped with an EDAX EDS-system and to optimize the results of quantification either an Iceland spar calcite crystal or carbonate standards from Astimex have been used to calibrate the system.

2.3.2.3 Mineral Liberation Analyzer (MLA)

Mineral Liberation Analyzer (MLA) combines imaging by SEM-BSE and X-ray mineral identification by EDS to perform a spatial spectral mapping of polished samples, creating color-coded maps of the mineralogy or chemical composition of the samples. The minerals in the samples are identified and

characterised through comparison of their EDS spectra to a list of reference spectra by a "best match" algorithm.

Before the mapping is started X-ray spectra from the different phases in the samples are classified based on elemental composition as a certain mineral or mix of minerals, assigned a colour, and added to the project database together with a pre-defined basis of common minerals. Each EDS-spectrum is coupled to an average grey-scale value in the BSE images and as the average atomic number of each mineral phase corresponds to the number of backscattered electrons from a sample, the average grey-scale-value will therefore be unique to this mineral (Fandrich et al., 2007). To ensure good measurements of the chalk samples with predominant calcite, the grey-scale is calibrated with a copper standard.

After the BSE-images are scanned, processing of the data is required. The first step is particulation: Removal of background data based on a minimum BSE grey-scale value. Anything below this threshold, in this case, epoxy resin or air bubbles, is removed from the image. Subsequently, segmentation takes place, where grain boundaries and internal structures are defined based on BSE characteristics. After segmentation, classification of minerals or phases is performed in the selected area. The measurement mode used for these projects were GXMAP mode, based on a primary identification of particles through BSE imaging, then mapping of each particle in a pre-defined grid, collecting spectra of characteristic X-rays at each point within this grid. This allows for high spatial resolution and avoids limitation by poorly defined grain boundaries in BSE images caused by similar average atomic number of minerals (Fandrich et al., 2007). The scanned areas are coupled to the database of EDS-spectra for classification of minerals in the sample, and color-coded maps of the mineralogical distribution of the surface are produced, enabling objective evaluation of spatial textural and chemical composition in one process.

To produce a clearer image of the mineral distribution in the sample the different spectra may be grouped into one mineral or mineral-group. The resolution of the MLA scanning depends on the size of the area scanned and the time used, but will, however, always be constrained by the spot-size of the electron beam (one to two μm) and the corresponding excitation volume. In this study, samples were scanned by different settings, with a step-sizes between 1.2 and 12 μm . As the grains in the flooded chalk often have a grainsize below the beam-diameter of the MLA, signals from adjacent grains may in cases affect each other.

MLA analyses used in this thesis were carried out at Technische Universität (TU) Bergakademie Freiberg, Germany. The system was set up with SEM type FEI Quanta 650 FEG-SEM together with two Bruker X-Flash EDS detectors. The software controlling the EDS analyses is “Quantax Esprite 1.8”. The mineral liberation analysis software version MLA 2.9 by FEI was used for the automated SEM analyses. Imaging and analyses were performed using 15 kV acceleration voltage and 12 mm working distance. The prepared samples analysed were un-covered thin sections or samples mounted in epoxy, coated with carbon.

2.3.2.4 Focused Ion Beam Scanning Electron Microscopy (FIB-SEM)

Sample preparation of brittle chalk for TEM is a challenging task, because of the demands for extreme thin samples and possible undesired smearing effects if polishing of such small samples is used. The samples were therefore produced by Focused Ion Beam (FIB) milling mounted in a SEM (FIB-SEM) at Saarland University, Germany or at the Institute of Planetary Materials (IPM) at the Okayama University in Misasa, Japan, by the project scientists.

In FIB-SEM sample preparation, predefined samples are placed inside the vacuum chamber of the SEM and tilted at an angle to the ion beam. Lamellas of approximately 20 x 10 μm are cut from the sample by a gallium ion-source gun and transferred by a manipulator to a three mm large copper grid (Figure 5). The FIB-lamellas are then thinned to approximately 100 - 150 nm thickness by the same ion source.

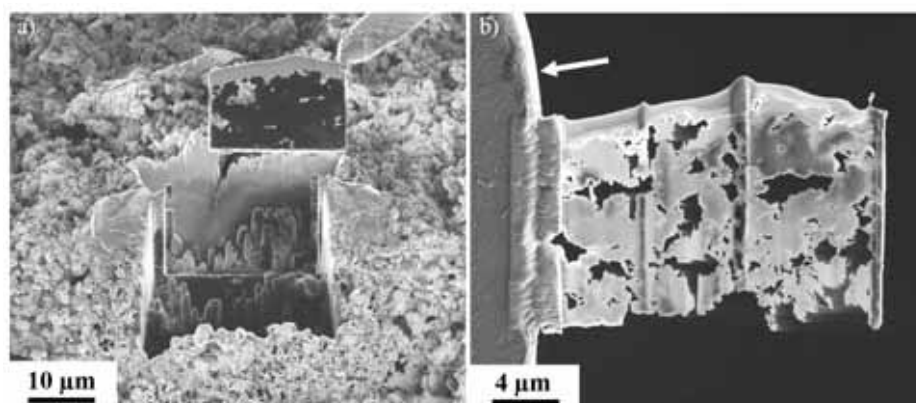


Figure 5: Production of FIB-lamella of MgCl_2 -flooded chalk. a) cut-out of lamella from the sample surface. b) Thinned lamella welded to the copper grid (white arrow).

As it can be observed in Figure 5, the chalk samples produced by FIB-SEM may be fragile due to their high porosity and low degree of cementation and compaction.

2.3.2.5 Transmission Electron Microscopy (TEM)

In Transmission Electron Microscopy (TEM) the electron beam is transmitted through the sample as opposed to reflected off the surface in SEM analyses. This requires higher acceleration voltage, often in the range between 100 and 200 kV, and extremely thin samples. For this study, the samples were prepared by FIB-SEM. The samples are brittle, and may be affected by the electron beam, i.e. burning holes in the samples or creating mineralogical changes due

to beam damage (Hjuler, 2007). Hence, microscope set-up and bombardment times need to be calculated well.

The advantage of studying samples in TEM compared to SEM, is the possibility to obtain higher resolution. The higher acceleration voltage used in TEM produces an electron beam with shorter wavelengths. Therefore, the resolution may reach below 1 nm. In Scanning Transmission Electron Microscopy (STEM) mode, a convergent beam is used and mapping of the elemental distribution at nano-scale is possible. A TEM combined with an EDS detector provides imaging and elemental analyses at high resolution and offers also analyses by electron diffraction, enabling identification of mineral phases based on the lattice parameters in addition to the elemental identification by EDS. In electron diffraction, electrons from the incoming beam are scattered elastically (Bragg scattering) and the direction of the scattering is a result of the periodic positioning of atoms in the crystal structure (Solberg et al., 2007).

A JEOL JEM-2100 TEM at UiS was used with acceleration voltage of 200 kV for bright field imaging (use of the direct beam), together with STEM mode mapping. For X-ray elemental identification, an EDS detector (EDAX) was applied to create color-coded maps of the elemental composition of the samples. Additional analyses were performed at the Institute of Planetary Materials (IPM) at the Okayama University, Misasa, Japan. A field emission JEOL JEM-2100F TEM was used with an accelerating voltage of 200 kV, beam current of 2.6 nA, dwell time of 0.2 ms. The high magnification and small beam-size of TEM enables imaging and EDS-mapping below grain-size-resolution of chalk, in this study at a resolution between 5 and 20 nm.

2.3.2.6 *Electron Microprobe Analyses (EMPA)*

An electron microprobe is a SEM equipped with Wavelength Dispersive X-ray Spectroscopy (WDS) instead of EDS. This method has the advantage of better

quantitative measurements compared to EDS analyses as it analyses the individual wavelength of the X-rays and does not have to identify each element from a partly overlapping energy spectrum, as in EDS. In this study, a JEOL JXA-8900RL was used with 15 kV acceleration voltage, 20 nA current and 2 μm beam at Technische Universität (TU) Bergakademie Freiberg, Germany. The measurements were set up with five separate detectors tuned to detect the wavelengths of specific elements. To test more than five elements, repetitive analyses were performed on the same area on polished thin sections, using standards for the investigated minerals.

2.3.3 Nano Secondary Ion Mass spectrometry (NanoSIMS)

Secondary Ion Mass Spectrometry (SIMS) is based on a primary ion beam striking the sample surface, releasing secondary ions which may provide information about chemical composition and structures of the surface (Hirata et al., 2011). Chalk is very fine-grained and the particle size is often too small to be sufficiently recognized by MLA or EMPA. Therefore, the need for further sub-micron studies is present and one possibility, besides TEM, is nanoSIMS. Using nanoSIMS, the surface is scanned with a focused Cs^+ ion beam. The beam is expected to be less than 100 nm in diameter (lateral resolution) (Zimmermann et al., 2015). For this project, the area that was scanned varied between 55 and 10 μm and as the images have 256 x 256 pixels, this results in a resolution between approximately 200 and 40 nm per pixel.

The impact of the primary beam produces a secondary ion beam, known as “sputtering”. The particles produced from the surface may be positively, negatively, or neutrally charged, depending on the primary ions identity (Griffiths, 2008). The ion-yield varies with respect to the type of beam used, e.g. caesium or oxygen, and the ionization energy of the elements and sample matrix (Handley, 2002) To be able to detect neutral particles, a laser ionizes the

secondary beam and the ions are accelerated and directed into a mass spectrometer by an electric field. Using a Time-Of-Flight (TOF) detector, the amount of ejected ion may be measured for several ions or groups, referred to as masses, at one time. As such, multiple scanning of a fragile surface is avoided (Griffiths, 2008). In this way, identification of which elements are present in one certain grain or crystal down to a resolution of 40 nm is possible.

NanoSIMS scanning provides an intensity-map for each ion, oxide or mass, depicting the relative intensity of ions produced from an area. The intensity-values between two images of e.g. calcium and magnesium is not directly comparable, meaning that the method is not quantitative as such, it is rather a tool to identify whether a certain element is present or not in a grain and evaluate the relative concentrations within one scanned area.

Another application of nanoSIMS is the possibility to make depth profiles and to create 3D-images, scanning an e.g. 10 x 10 μm area repeatedly to measure the composition of a specific area, grain, or crystal, to a depth of approximately 1 μm .

To navigate to the areas of interest in a sample, the nanoSIMS is coupled to an optical camera. Navigation on polished surfaces of chalk is challenging because of the lack of topography and colours and can therefore be very time consuming. Another important issue is that the nanoSIMS needs an extreme high vacuum during measurements and this can be very time-consuming to reach when studying high-porosity chinks.

The samples in this study were analysed with a Cameca NanoSIMS50 application at the “Centre de Recherche Public Gabriel Lippmann” in Luxembourg (now Luxembourg Institute of Science and Technology, LIST).

2.3.4 Carbon and Oxygen Isotopes

Stable isotope analyses of carbon and oxygen isotopes are used as a tool to understand paleo-climate and post-depositional alterations of rocks. The relative abundance of the stable isotopes of an element in a mineral depends upon fractionation by mass, temperature and/or biological processes that underlie mineralization. Formation temperatures, i.e. the temperature when minerals form, can be used as a chemo-stratigraphic tool and to constrain the degree of rock-fluid interactions during e.g. diagenesis or flooding experiments. Based on $\delta^{18}\text{O}$, the formation temperature (T) can be estimated according to the empirical relation described in (Anderson et al., 1983) and (Gómez et al., 2008):

$$T = 16.0 - 4.14(\delta_c - \delta_w) + 0.13(\delta_c - \delta_w)^2 \quad (1)$$

where δ_c attains the values of the oxygen isotope ($\delta^{18}\text{O}$), $\delta_w = -1\%$ according to the assumption Standard Mean Ocean Water (SMOW) of the ambient Cretaceous seawater (Wright, 1987) ('normal' salinity). The estimated temperature is given in centigrade ($^{\circ}\text{C}$). $\delta^{18}\text{O}$ isotopes fractionate due to kinetic processes reflecting the paleo-climate.

Temperature estimates of untested material and expected values of Upper Cretaceous chalk (Hjuler et al., 2009; Jørgensen, 1987; Surlyk et al., 2010; Tucker et al., 1990) are compared to tested core material.

For each sample, a fresh surface was drilled to produce samples of fine powder. Oxygen and carbon stable isotope analyses were performed on crushed 1.0 - 3.0 mg sub-samples. The carbonate powder was dissolved in 100% orthophosphoric acid at 90 $^{\circ}\text{C}$ in an ISOCARB automatic carbonate preparation system. The resulting CO_2 was then analysed on a VG Isogas PRISM III stable isotope ratio mass spectrometer at the University of Edinburgh. The standard

deviation was measured on a powdered coral laboratory standard (COR1D, $\delta^{13}\text{C} = -0.648$, $\delta^{18}\text{O} = -4.920$), run as a sample on the same days as the studied samples. All carbonate isotopic values are quoted relative to the Vienna Pee Dee Belemnite (VPDB).

2.3.5 Whole-rock geochemistry (Inductive Coupled Plasma Mass Spectrometry, ICP-MS)

Using Inductive Coupled Plasma Mass Spectrometry (ICP-MS) the concentrations of oxides and elements in a sample can be studied. For each analysed sample, ideally, material of at least 5 grams is needed. The material is milled and the results will therefore yield an overview of the relative distribution of each element or oxide in the bulk sample material. Representative material was retrieved from all samples. The material was analysed at Bureau Veritas Minerals' laboratories in Canada using a porcelain beaker to avoid any contamination. The process is shortly described here, but detailed information of the analytical method and processing can be found currently at <http://acmelab.com>. The samples are ground in an agate mill and mixed with $\text{LiBO}_2/\text{Li}_2\text{B}_4\text{O}_7$ flux in crucibles and fused in a furnace. After cooling, the bead is dissolved in American Chemical Society (ACS) grade nitric acid and analysed by ICP-MS. Loss on ignition (LOI) is determined by igniting a sample split and then measuring the weight loss. A 1g sample is weighed into a tarred crucible and ignited at 1000°C for one hour, and then cooled to be weighed again. The loss in weight represents the LOI of the sample. Total carbon and sulphur are determined by the LECO® method. Here, induction flux is added to the prepared sample then ignited in an induction furnace. During the process a carrier gas sweeps up released carbon or sulphur to be measured by adsorption in an infrared spectrometric cell. The results are total concentrations and attributed to the presence of carbon or sulphur in all components. The

prepared sample is digested with a modified Aqua Regia solution of equal parts concentrated HCl, HNO₃, and Di-H₂O for one hour in a heating block or hot water bath. The sample volume is increased with dilute HCl-solutions and splits of 0.5 g are analysed. None of the measured concentrations were too far above the possible detection limit, but in standard range, and accuracy and precision are between 1-2%.

2.3.6 Analyses of effluent water

Effluents, or waste-water, from the triaxial flow experiments were collected at regular intervals during the test period to compare effluent composition over time, both with the injected brine and similar experiments, which assist in the understanding of any changes in mineralogical composition of the cores during flooding. The ionic concentrations were analysed with a Dionex Ion Chromatography System (ICS)-3000 or 5000+ ion-exchange chromatograph at UiS. The analyses were performed with IonPac AS16 and IonPac CS12A or IonPac AS20 and IonPac CS19 used as anion and cation exchange columns, respectively. The sampled effluents were diluted by a dilution-pump (Gilson, GX-271) to stay in the linear region of the calibration curve and ionic concentrations were calculated based on an external standard method. The following ion concentrations were quantified: Mg²⁺, Na⁺, Cl⁻ and Ca²⁺.

Si⁴⁺-concentrations were quantified at UiS by using an Optima 4300 DV Inductively Coupled Plasma Optical Emission Spectrometry (ICP-OES) detector from Perkin Elmer. The samples were prepared by separating approximately 1 mL of the fluid before dilution. The method detection limit (MDL) for the analysis of Si⁴⁺ is 0.3 mg/L.

2.3.7 X-ray Diffraction (XRD)

X-ray Diffraction (XRD) is based on elastic scattering of the incoming X-rays on the sample. The angle of the incoming X-rays, θ , yields a reflections pattern after Bragg's law:

$$2d\sin\theta = n\lambda \quad (2)$$

The pattern is related to the lattice parameters of the crystals, where d is the distance between lattice planes, n is a positive integer and λ is the wavelength of the incoming X-rays. Constructive interference of the X-rays diffracted in the crystal lattice produces peaks as the angle of the incoming X-rays is stepwise increased. Based on the yielded pattern, the minerals present in the sample may be identified. The better the orientation of the minerals, the more precise are the peak positions to interpret the minerals. XRD has limitations in detecting low quantities of minerals, often if the occurrence is below 5 wt%. The intensities of the peaks also vary with the crystal structure, thus some minerals are easier to interpret than others. Carbonates are mostly easy to identify, while others, such as clay minerals often need additional analyses by e.g. SEM to be positively identified.

In this study, XRD patterns were obtained from grinded bulk samples and performed by using a Bruker D5005 diffractometer (Cu-K α radiation, 40 kV, 40 mA, 0.02 ° step, at 1 s per step), at the Institute of Earth Sciences Jaume Almera (Barcelona, Spain), together with a Philips X'Pert PRO PW 3040/60 diffractometer (Cu-K α x-ray radiation, Si monochromator, 40kV and 30mA, step scan at ~1.5°/minute, step size of 0.02° 2 θ) at the Facultad de Ciencias Químicas (Universidad Nacional de Córdoba, Argentina). Additional analyses were performed with a Bruker D8 ADVANCE ECO diffractometer with a Lynxeye detector (Cu-K α radiation 1.5406 K α 1, 40 kV 25 mA, 0.6 mm

receiving slit, 0.01 ° step, at 0.2 s per step) at UiS. The measurements were repeated in certain samples to evaluate the reproducibility of the results; particularly for cases involving newly formed trace minerals. The amount of material used for measurements was approximately 1 g.

2.3.8 Specific Surface Area (SSA), Brunauer–Emmett–Teller (BET) theory

The Specific Surface Area (SSA) is a measure of how extended the surface of grains or crystals is per gram sample, commonly given in m²/g. This is measured by the amount of gas which can adsorb as a monolayer on the sample. When injecting e.g. N₂ gas, the change in relative pressure is monitored, producing a measure of how much gas is adsorbed on the surface. Given the sample weight as input, one may calculate the SSA of the sample by the Brunauer–Emmett–Teller (BET) theory (Brunauer et al., 1938). The surface area of a sample will vary as a function of several factors such as grain size and shape, as well as porosity and permeability of a sample and can therefore be used as a tool to interpret the amount of dissolution and precipitation of a sample through changes in grain-size distribution.

SSA on grinded bulk samples was measured by Micromeritics' TriStar II surface area and porosity analyser and the data was calculated by TriStar II 3020 Software. Before inserted into the sample tube, each sample was weighed. The sample tube was connected to a vacuum pump and when the pressure reached 20–30 mTorr, nitrogen gas was introduced into the tube and the change in pressure was logged. The sample tube was submerged in liquid nitrogen (N₂) to cool the sample during the measurement. At increased partial pressures, nitrogen gas fills a greater area of the micro-pores adsorbing as a monolayer on the surface of the grains. The change in pressure is a measure of the amount of

gas adsorbed, thus the surface area of the sample. The SSA was measured on both powdered rock and on small ~0.5 x 0.5 x 0.5 cm sized cubes.

2.3.9 Pycnometry

The solid volume of selected samples was measured with an AccuPyc II 1340 gas pycnometer that measures the amount of displaced helium gas by a porous rock sample in an enclosed chamber. This enables calculation of the average density of a sample, based on the sample-weight, and calculation of the porosity, if also the bulk volume is given.

During measurement, a dry sample is placed into a chamber where helium gas molecules rapidly fills the chamber. A chamber of 35 cm³ was selected to provide the best fit with the samples. The pressure in the chamber is measured and the change in volume is calculated by Boyle's law:

$$P_1V_1 = P_2V_2 \quad (3)$$

where P is the pressure and V is the volume of the chamber.

2.3.10 Raman spectroscopy

To broaden grounds for analyses, Raman spectroscopy was tested for this research. Raman is an analytical technique which uses a monochromatic laser beam focused on the sample. In the scattered light, or secondary radiation, most photons scatter with no energy change, however a number of photons exchange a small amount of energy which causes the molecules in the sample to vibrate, called Raman scattering, discovered in 1928 (Raman, 1928). The vibrational frequency causes a shift in the frequency of the scattered light, hence a shift in wavelength. This shift is referred to as the Raman shift and is linked to lattice parameters of the crystal phase, the atomic weight and strength of the atomic bonds. Identification of mineralogy is therefore possible through analyses of

the Raman spectra. The advantage is that the method is quick and rather cheap, and uses the crystallography instead of the chemical composition and can therefore differentiate polymorphs.

However, when using micro-Raman, the beam-size is approximately 1 μm . The positioning of the laser beam is done through an optical microscope, and it is challenging to identify and analyse one specific chalk grain by the use of this method.

Recently, Tip Enhanced Raman Spectroscopy coupled with Atomic Force Microscopy (TERS-AFM) has been tested as a method to perform Raman analyses at higher resolution with spot-sizes of 20 nm, and to produce topography maps of the analysed areas. However, this method sets extreme demands on sample-preparation, especially the surface-roughness of the sample. This is to avoid the tip of the AFM to crash into topographic features of the surface. Samples for TERS-AFM were prepared by using an ultrasonic drill to cut out small circular disks (3 mm in diameter) from polished thin sections. In regard of chalk, sample preparation is still a major challenge. Principally this method is, together with TEM-EDS and electron diffraction, the only method in this study which can image and identify minerals on nano-scale.

Material and methods

3 Main results and discussion

The research carried out in this project has yielded results on scales from centimetres to Ångström. The different techniques offer results based on imaging and chemical analyses of specific crystals, grains or areas as well as on powdered bulk samples. Some methods provide elemental and textural results, while others reveal the mineralogy based on crystallographic analyses. Combining the results from several methods may therefore provide additional understanding that each method may not provide on its own.

When chalk is flooded with reactive brines in mechanical flow-through experiments, the composition of the flooding brine affects the strength and the stiffness of the chalk plug. Systematic tests have shown that injection of SO_4^{2-} has an effect on yield and bulk modulus during hydrostatic loading (Megawati, 2015), while Mg^{2+} significantly increases the strain rate during the following creep phase (e.g. (Andersen et al., 2017; Korsnes et al., 2008a; Madland et al., 2011)). To be able to understand rock-fluid interactions along with being able to predict and simulate mechanical behaviour during flooding, the exact changes in mineralogy must be understood. Analyses show that changes in creep strain are, in addition to the applied stress, also dependent on time. A series of long-term tests on chalk cores flooded with simplified brines have therefore been performed (LTT, MLTT and ULTT) to observe chemical effects over time. The main results of the textural, chemical and mineralogical analyses of these long-term experiments are presented and discussed here, together with results from tests flooded for shorter time, tests on fractured chalk and on simplified artificial chalk cores made from calcite powder. In general, very few alterations are observed when flooding with NaCl. Only minor alterations in the silicate distribution are observed along with slight dissolution of calcite. In cores flooded with MgCl_2 changes are pronounced.

3.1 Core-scale alterations

3.1.1 Two fronts of alterations

Core-scale mapping of the three long-term test, LTT, MLTT and ULTT (see chapter “2.3.1.1 Overview over the flooding tests presented in this study”), using MLA shows that there are seemingly two fronts of alteration progressing through the cores during long-term flooding of chalk with MgCl_2 . In **Paper I**, chemical mapping of thin sections covering the radius of each core along the flooding axis was performed.

The two fronts of alteration seem to progress at different velocities through the cores during flooding. The first front is observed towards the outlet of the long-term tests. This induces only minor mineralogical alterations, where most of the original calcite is preserved, and individual idiomorphic crystals of magnesite, commonly 1 to 10 μm in size, are precipitated together with polycrystalline clusters of smaller sized magnesite crystals and clay minerals, mainly in open pore-spaces (**Paper I**). Magnesite is visible as small blue pixels inside the red calcite in the MLA-scans of the LTT and the MLTT (the two centre samples, Figure 6). Such occurrences of magnesite is not observed in unflooded chalk (Figure 6, left), but are commonly found in short-term chalk experiments (**Paper IV and V**).

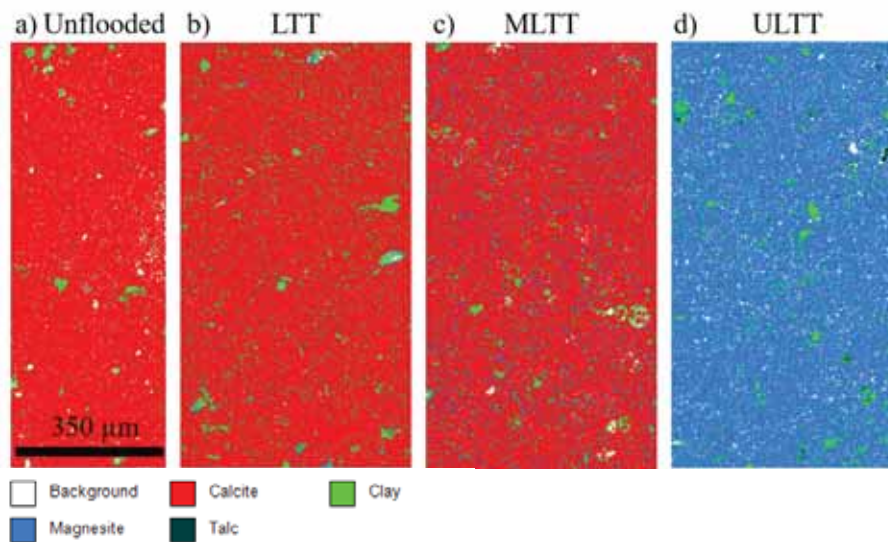


Figure 6: MLA scans of a) unfloded material b), the LTT, slice 4, c) MLTT, Slice 4 and d) the ULTT (slice 5). Legend below. The LTT and MLTT show small abundances of precipitated magnesite (blue) inside the original calcite (red), not observed in unfloded material (a). The ULTT consist only of magnesite (blue) and clay minerals (green).

The abundance of precipitated magnesite is higher in the MLTT, slice 4, compared to the LTT, slice 4, which seems reasonable with the increased flooding time.

The observations in MLA scans are also confirmed by FEG-SEM. No magnesite crystals are observed in unfloded chalk (Figure 7).

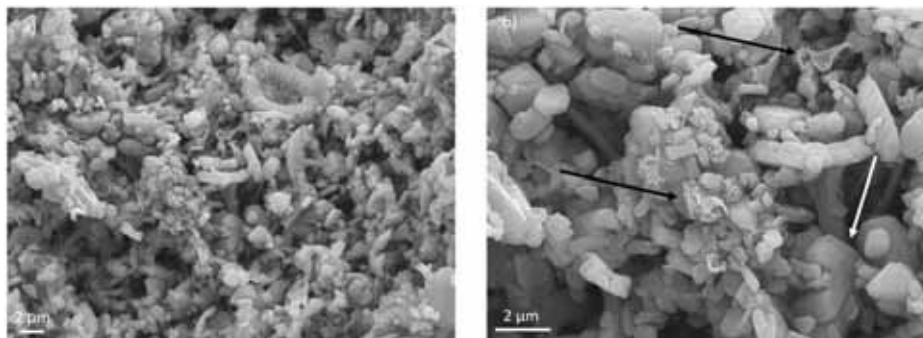


Figure 7: FEG-SEM micrographs of unfloded Liège chalk. a) Recognizable rings (coccoliths) from coccolithophores along with fragments and decoupled grains from micro- and nano-fossils. b) Occurrences of clay minerals (black arrows) and authigenic calcite crystals (white arrow).

Main results and discussion

Inside the first front of alteration, the occurrence of single magnesite crystals is common (up to $\sim 10\ \mu\text{m}$), preferentially in larger pore-spaces where the crystals have space to grow and the rock-fluid equilibrium may be altered due to differences in original composition of grains or fossils and in tortuosity of the flow (**Paper I, III, IV and V**). Magnesite is observed as smaller crystals or polycrystalline aggregates further towards the outlet (Figure 8). These observations of scattered magnesite precipitation, which is linked to dissolution of calcite; the provider of CO_3^{2-} in these experiments, are also found in short-term experiments, typically after 30 to 90 days of flooding (**Paper IV and V**). Together with the occurrences of magnesite, observations of original and newly formed silicates are made.

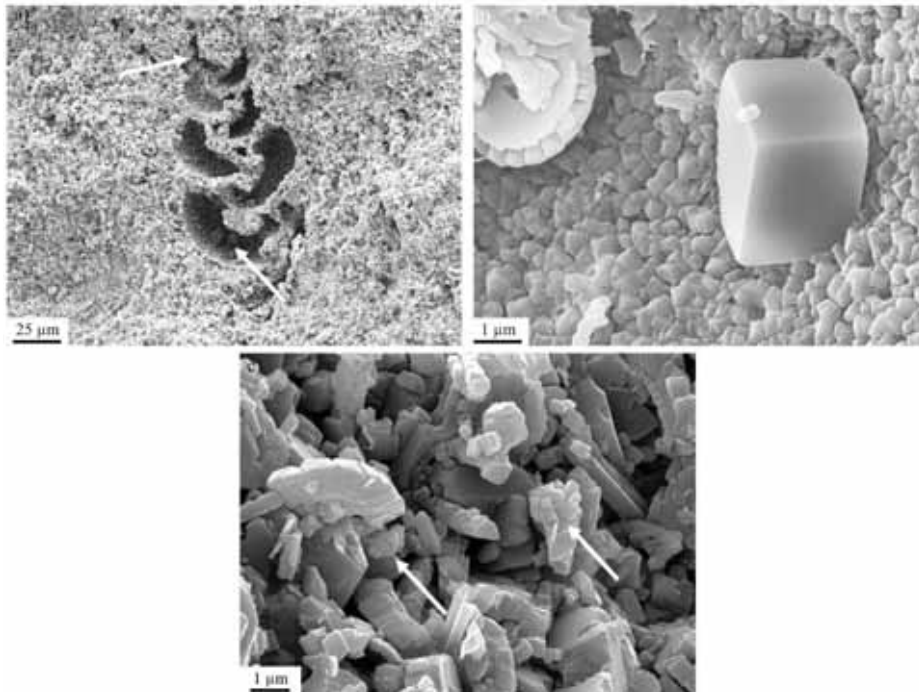


Figure 8: Examples of precipitation of magnesite in a) inside a foraminifera in the LTT (white arrows), b) Close-up of magnesite crystal found at the inlet of outcrop chalk from Stevns Klint flooded with MgCl_2 for 61 days. c) Polycrystalline aggregates of magnesite (white arrows) found in chalk from Kansas flooded for 75 days with MgCl_2 .

The primary mineralogy and diagenetic history of outcrop chalks also affect the mineralogical alterations during flooding. In e.g. outcrop chalk from Kansas, many of the larger pore-spaces of foraminifera are filled with authigenic inorganic calcite, presumably formed during diagenesis (Figure 9). Observations of newly precipitated magnesite crystals of large size in this type of chalk are not so common, compared to other outcrop chalks. There is simply not enough space to grow.

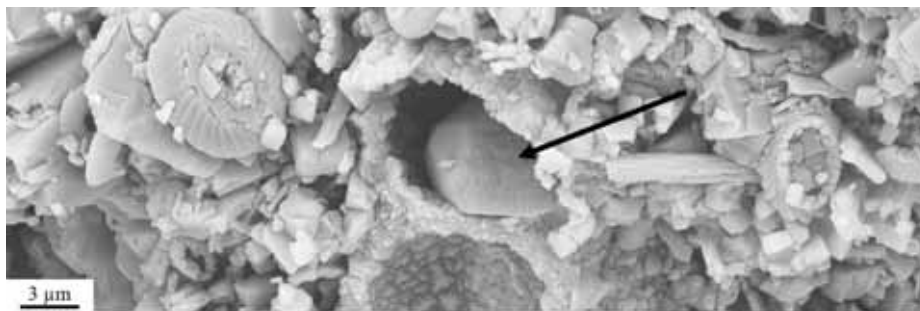


Figure 9: Example of authigenic inorganic calcite (black arrow) found inside a foraminifera shell in unflooded outcrop chalk from Kansas.

The second front progressing through the cores is only observed in the long-term experiments, after more than 500 days of flooding. The alterations are characterized by a complete transformation from calcite and original non-carbonate minerals to magnesite and clay minerals. Minor occurrences of unaltered non-carbonate minerals are also found after flooding. The clay minerals present after flooding seem to be both unaltered original clay minerals together with newly formed phases. The front has a piston shape, and the transition between the two areas of the cores is sharp, and covers only less than 2 mm (**Paper I**).

When imaged by FEG-SEM (Figure 10), both the composition and texture of this completely altered areas are different from unflooded chalk (Figure 7).

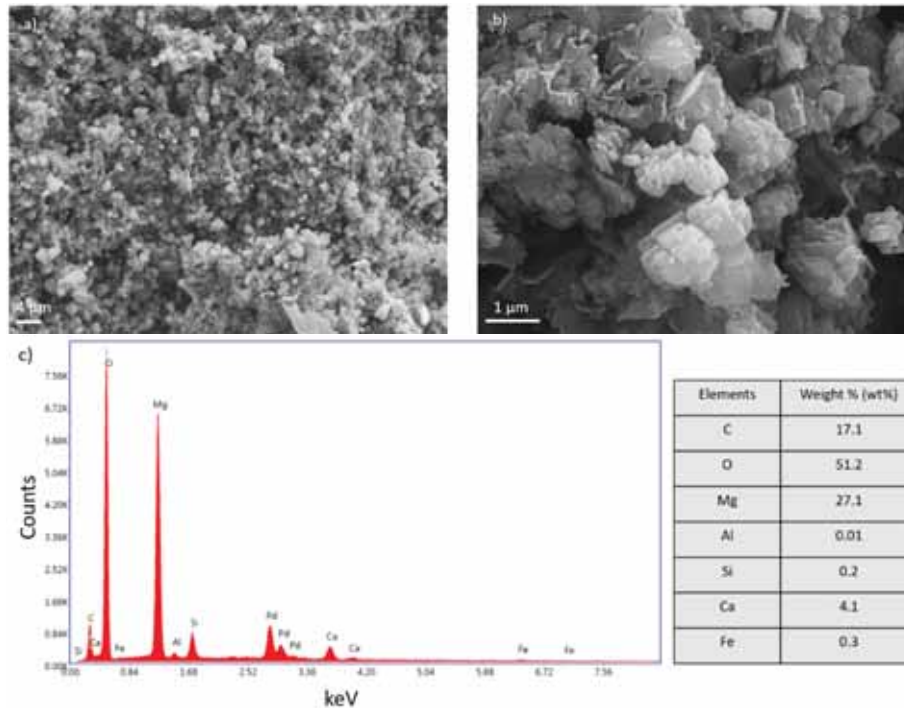


Figure 10: Material from completely altered area in the ULTT. a) Typical texture of the newly formed crystals with rhombic shape and sizes mostly between 100 nm and 2 μm . b) Close-up of crystals in a). c) Spectrum and semi-quantitative analyses of the elemental composition of the area in a). The sample is coated with palladium (Pd), hence the Pd-peak in the spectrum.

The composition after flooding is dominated by magnesite, composed of Mg, C and O, with minor impurities of Ca. The crystals commonly have a grainsize up to 2 μm , and are more angular than in unflooded chalk.

The same type of precipitates is observed in flooded calcite powder (artificial chalk cores, **Paper II**). Unflooded material has grainsizes in the range of the calcite observed in outcrop chalk, between 4 and 33 μm (Figure 11).

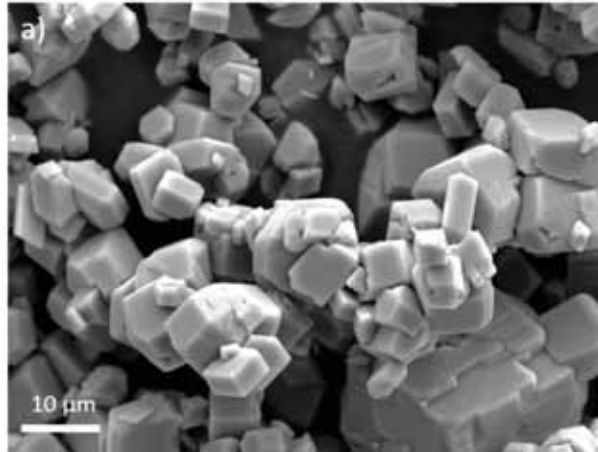


Figure 11: FEG-SEM micrograph of unflooded calcite powder. Grainsize varies between ~ 4 and $33 \mu\text{m}$, with partially interlocking grains.

After short periods of flooding, 27 days, angular grains with trigonal crystal shape varying in size from only tens of nm to $\sim 2 \mu\text{m}$ are observed, growing on top of existing calcite grains (Figure 12). EDS analyses show a significant content of magnesium (not shown here). These are similar to single crystals of magnesite found in flooded outcrop chalk (Figure 8).

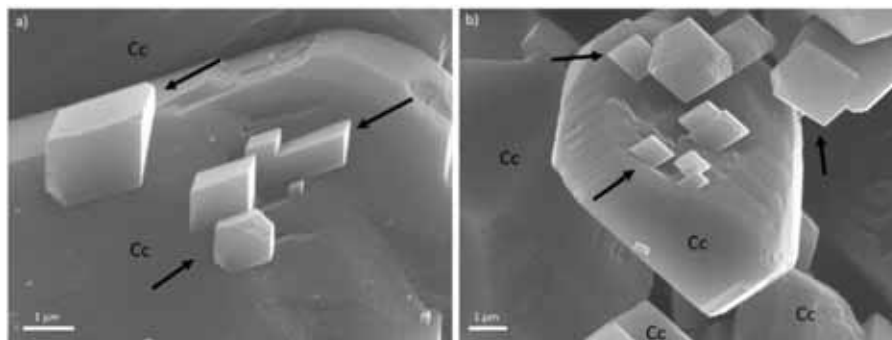


Figure 12: FEG-SEM micrographs of crystals with high magnesium content growing on existing calcite grains at the inlet of an artificial chalk core after 27 days of flooding, marked with black arrows. Original calcite grains are marked with Cc.

In the artificial chalk core flooded for 289 days, polycrystalline aggregates with high magnesium content are found between larger calcite crystals (Figure 13). The clusters comprise of idiomorphic crystals with a trigonal crystal shape and

sizes varying between 100 and 200 nm. The clusters themselves vary in size, most often between 1 and 5 μm , and display a framboidal shape, similar to what can be found for pyrite (Ohfuji et al., 2005). These clusters match the form and composition found in samples of flooded outcrop chalk. In both cases, the aggregates are found from approximately halfway along the flooding axis of the cores and until the outlet.

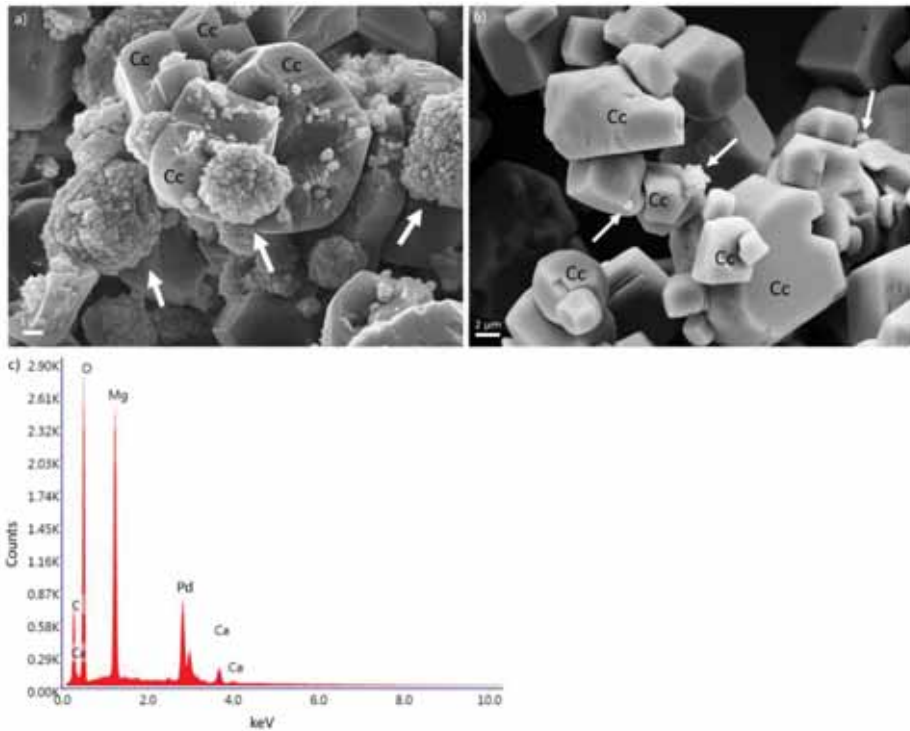


Figure 13: FEG-SEM micrographs of polycrystalline aggregates of new-grown crystals with high magnesium content found after 289 days of flooding with MgCl_2 . Original calcite grains are marked with Cc. a) Observations are made halfway along the flooding-axis and at the outlet (b) Similar observations made at the outlet of the same core, but with smaller aggregates of magnesite. c) EDS spectrum of new-grown minerals with main contents of C, O and Mg and only minor content of Ca, corresponding to clusters in a).

Severe signs of dissolution are observed on calcite grains (Figure 14). The dissolution can be observed as defects on the crystal faces, where layers in the crystals are partly absent (white boxes in Figure 14).

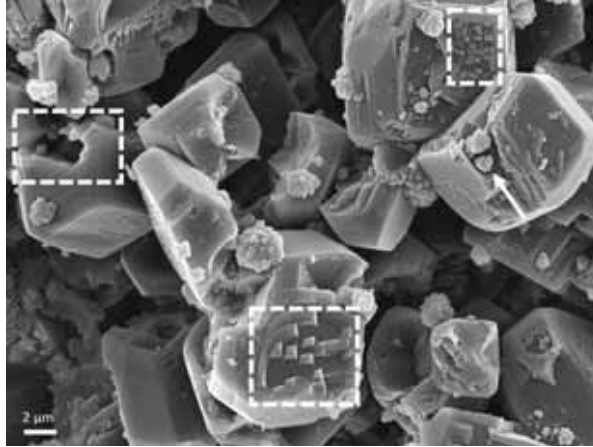


Figure 14: Severe defects on crystal faces found in long-term flooded calcite powder, halfway between the inlet and the outlet of the cylinder. White boxes show partly dissolved surfaces, while the white arrow points to polycrystalline magnesium aggregates inside one of the defects.

At the inlet of the long-term flooded artificial chalk core, most of crystals contain a high amount of magnesium (Figure 15). The crystals are in different sizes and shapes, mainly with a bimodal distribution:

- Smaller angular crystals with a size below 2 μm
- Larger crystals in the size-range between 10 and 15 μm with irregular shapes, partly rounded.

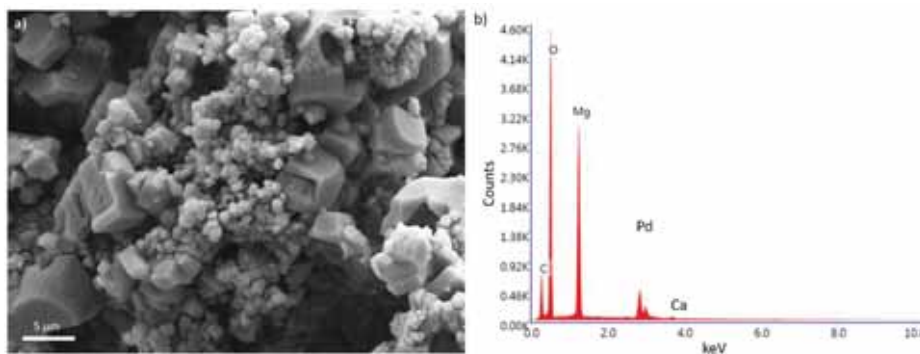


Figure 15: FEG-SEM micrograph of the strongest mineralogical alteration in flooded calcite powder. a) A distribution of crystals of different sizes and shapes is observed. All grains show minimal content of Ca, b) typical EDS spectrum for the crystals. Samples coated with palladium (Pd).

In FEG-SEM analyses no calcite nor dolomite were observed, similar to outcrop chalk. It seems that this area at the inlet of the core flooded for the longest period, mostly consists of magnesite, as also observed in the LTT and the MLTT; two of the long-term flooded outcrop chalk cores. As such, it is reasonable to assume that the artificial chalk cores behave over time much like outcrop chalk, with two fronts of alterations progressing through the cores over time, and that the here observed alterations are part of the secondary front of complete alteration.

Core-scale alterations are also observed by other measurements of the three long-term tests on outcrop chalk (LTT, MLTT and the ULTT) matching the observations made by MLA and FEG-SEM (**Paper I**). As seen in Figure 16, bulk analyses by ICP-MS, show values of CaO (red graph), MgO (black graph), and $\delta^{18}\text{O}$ isotopes (green graph) that follow the same trends as the MLA maps. In the inlet of the two shorter tests, LTT and MLTT, the MgO concentrations are high, while CaO values are low. This adhere to the area which is mapped as blue in the MLA maps, corresponding to magnesite. (For slice 2 in the LTT, there was not enough material to be analysed by ICP-MS, and is in the graph indicated by dashed lines). The crossover between MgO and CaO is shifted towards the outlet in the MLTT, compared to the LTT, which is to be expected with longer flooding time and matches the progression of the secondary magnesite front. At the outlet of the LTT and MLTT, where the mineralogy still is calcite-dominated, CaO values are high, MgO values are low, and they are close to the concentrations of unflooded rock. In the ULTT, the whole core is completely altered after three years of flooding with MgCl_2 and the same high MgO- and low CaO-values are found throughout the core.

Main results and discussion

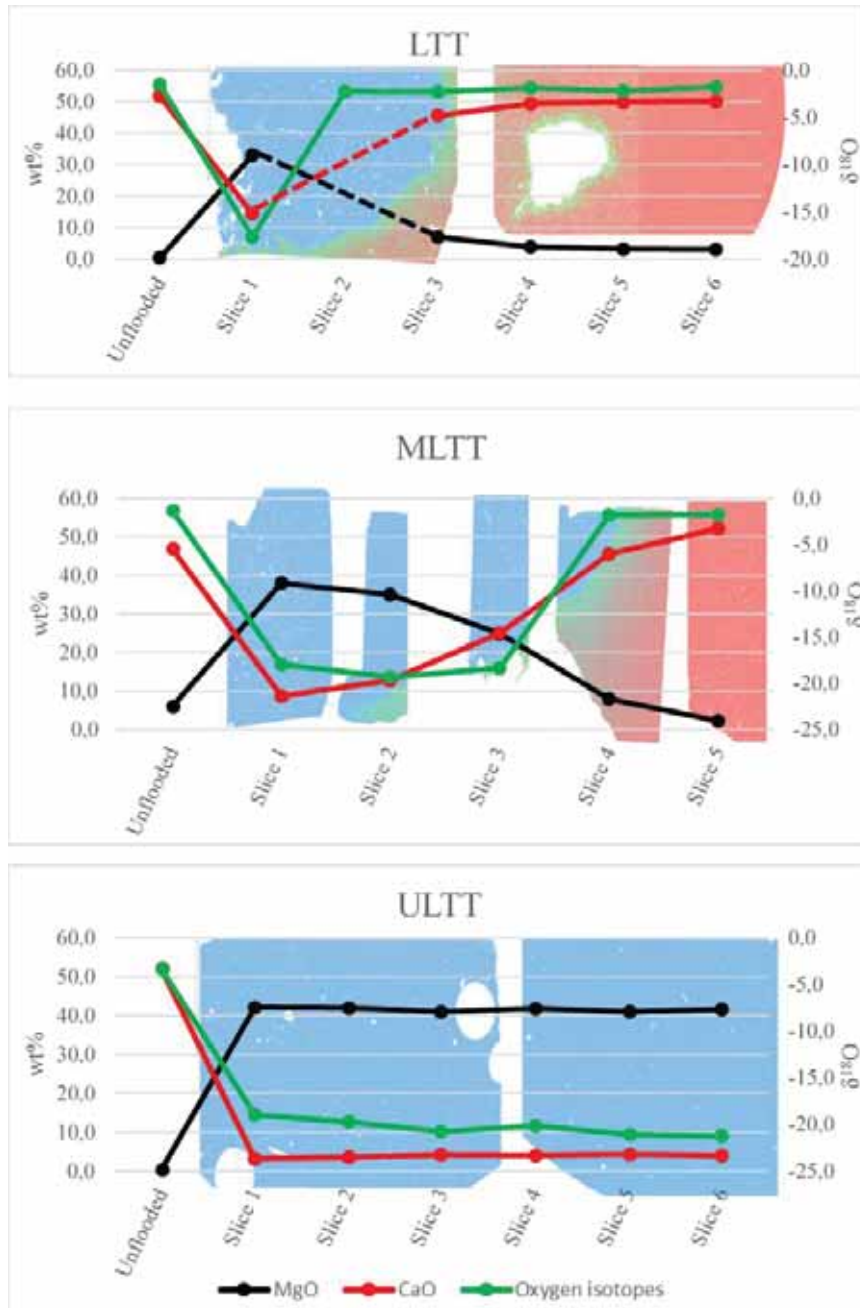


Figure 16: Combination of MLA mapping, ICP-MS analyses and oxygen isotopes measured along the centre of the flooding axis of the three long-term tests. CaO, MgO and $\delta^{18}O$ isotopes vary along the flooding axis, and match the MLA maps. MLA legend in Figure 6.

$\delta^{18}\text{O}$ isotopes fractionate due to temperature, yielding a more negative value, corresponding to an enrichment of lighter isotopes, in warmer formation conditions. In the completely altered areas of the three cores, $\delta^{18}\text{O}$ isotopes are severely disturbed compared to unflooded material.

Although calculations for paleo-temperature from oxygen isotopes are based on fractionation in open ocean seawater and may not necessarily be directly applicable to laboratory experiments such as the ones presented here, it is interesting to estimate the formation temperature of the newly formed minerals in the flooded cores. Based on the equation given in section “2.3.4 Carbon and Oxygen Isotopes”, the calculated precipitation temperature of the magnesite lies in the range of the experiment temperatures (130 °C). The values decrease towards temperatures of unflooded material and the expected values of Cretaceous chalk in the region (Surlyk et al., 2010) towards the outlet of the LTT and MLTT. For chalk cores flooded for shorter periods of time, between 2 and 4 months, an increase in $\delta^{18}\text{O}$ and calculated higher fluid temperatures can be observed at the inlet of the flooded cores, interpreted as a result of newly formed magnesite.

Given information on how oxygen isotopes fractionate due to changes in the global climate with differences in evaporation and precipitation (Appelo et al., 2009), it is clear that this is not the mechanism at play in these laboratory tests. However, the results indicate a considerable enrichment of the lighter ^{16}O isotope on the expense of ^{18}O . This exchange has to be related either to fractionation processes during re-precipitation of minerals, a signature of the isotope composition of the injected brine or even both. The isotope exchange may take place in the fluid when the dissolved species are in solution or through solid-state diffusion. The extent of alteration of isotope ratios is much higher when the process takes place through dissolution and precipitation (Hoefs, 2015). As such, the deviation from normal values of unflooded Cretaceous

outcrop chalk, points to precipitation of carbonate minerals under elevated temperatures and the extent of this deviation can be used as a measure of the amount of newly formed carbonates, in this case magnesite. Carbon isotope ratios, $\delta^{13}\text{C}$, (see **Papers I, IV and V**) are, as expected under the given laboratory conditions, not disturbed and reflect expected values for Late Cretaceous chalk (Jørgensen, 1987; Tucker et al., 1990), hence containing their primary signature.

The same geochemical trends are observed in the artificial chalk cores, made of calcite powder, flooded with 0.219 M MgCl_2 (Figure 17) (**Paper II**). ICP-MS analyses were performed on bulk samples of each slice, and the distribution of MgO compared to the distribution CaO, match observations made in outcrop-chalk, both for short-term (**Paper V**) and long-term tests (Figure 16) (**Paper I**). MgO concentrations are high at the inlet, and are reduced towards the outlet. Longer flooding periods, correspond to higher levels of MgO.

Main results and discussion

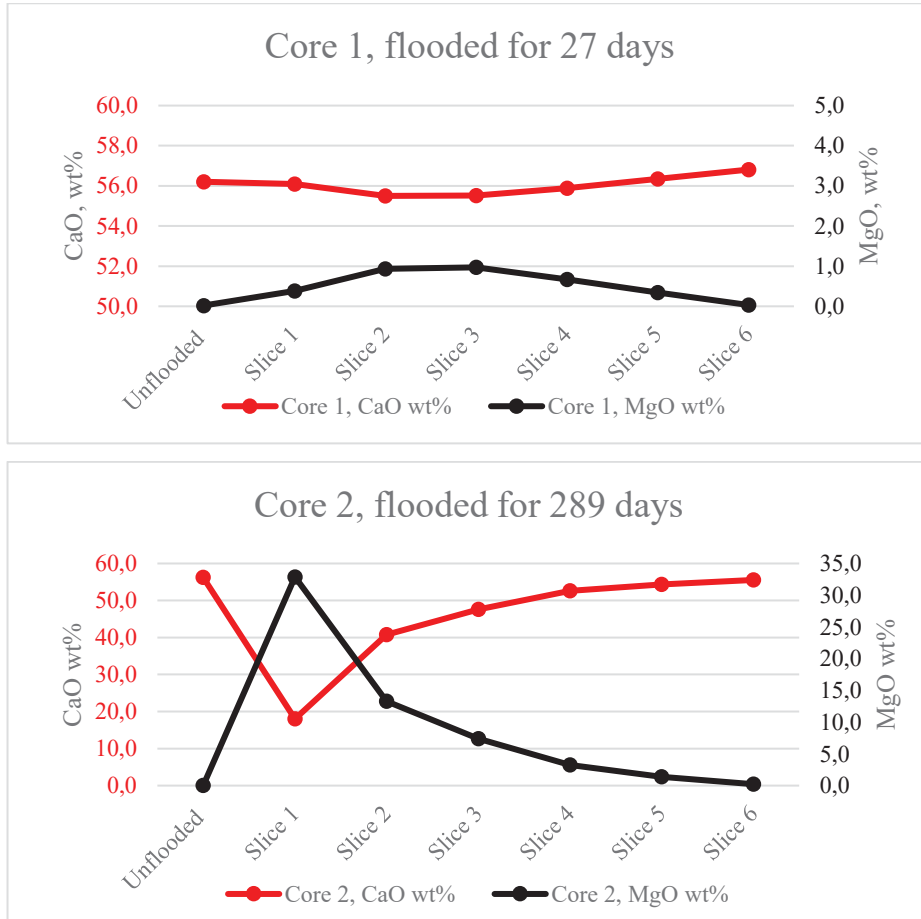


Figure 17: Results of ICP-MS analyses of the two flooded artificial chalk cores, along with the values for unflooded powder. Only the wt% for MgO and CaO are presented. MgO is higher in the inlet of the two cores, and generally higher after longer flooding period (Core 2). Please observe differences in scale of CaO and MgO wt% for the two graphs, Core 1 has been adjusted to show the minor changes in composition.

ICP-MS analyses of both the here presented calcite powder and outcrop chalk yield higher concentration of MgO in all flooded slices compared to unflooded material. It is difficult to observe any newly precipitated mineral phases in all areas of the flooded cores. However, certain replacements between Mg and Ca has to have taken place. This could be through precipitation of minute grains or

crystals of magnesite or other magnesium bearing minerals, or through ion-exchange processes on the surface of the grains inside the cores.

In general, density values change accordingly to variations in MgO and CaO concentrations along the flooding axis of the chalk cores, as discussed in e.g. **Paper IV** and **V** and (Nermoen et al., 2015; Zimmermann et al., 2015). Magnesite has a higher density than calcite and a shift of calcite to magnesite, via the complex processes described above, matches the increases in density observed in flooded chalk along with changes in other mineral phases such as silicates. Correspondingly, SSA measurements on flooded material are significantly altered, reflecting dissolution, precipitation or transportation of mineral phases within the cores (**Paper IV** and **V**). When flooding with NaCl, SSA values are in general lowered at the inlet, and slightly increased towards the outlet of the cores. This indicates small amount of dissolution and re-precipitation of fine-grained minerals, such as clay minerals, or transport of those from the inlet towards the outlet. In silica-rich chalk, as from Aalborg, partly dissolved opal-CT is observed at the inlet, together with newly formed clay minerals when flooding MgCl₂ at temperatures from 25-130 °C, also corresponding to the measured SSA values (**Paper IV**). This, however, complicates the interpretation as opal-CT lepispheres have a high SSA-values, as have clay minerals. For the other chalk types studied in this project, the SSA corresponds to the increase in magnesium content implying the precipitation of new phases, e.g. magnesite and clay, characterized by smaller crystal sizes.

3.1.2 A porous transition zone with sharp boundaries

Possibly, the most compelling observation made when studying the long-term tests is not only the presence of the mm-sized sharp transition between the two mineral regimes in the two shorter tests (LTT and MLTT), but also that this transition zone seems to have higher porosity than the rest of the rock material

in the cores. In MLA-scans of prepared thin-sections (Figure 16 and **Paper I**), this was firstly interpreted as a zone with higher density of clay minerals because of its high values of silicon (Si) and oxygen (O). However, after complementary analyses by FEG-SEM, the areas in question look rather like a high-porosity zones (Figure 18). The detection of Si and O may be affected by the glass slides the thin-sections were prepared on, more visible where the porosity is increased (discussed in **Paper I**).



Figure 18: FEG-SEM micrograph of the transition-zone in the LTT with increased porosity, below the white dashed line, compared to the area still dominated by the original calcite mineralogy to the top of the image.

Additionally, high-magnification FEG-SEM images of the high-porous zones show that clay minerals found distributed in the flooded cores are more visible inside the transition zone (Figure 19), than in other areas inside the secondary front. ICP-MS analyses of two cores (details in **Paper I**), do not show any

increase in Si and Al, elements often associated with clay minerals, in the slices corresponding to the transition zones. It is therefore likely that the reason for the increased visibility of clay minerals in this area is the higher porosity, not a net increase in silicates or clay minerals.

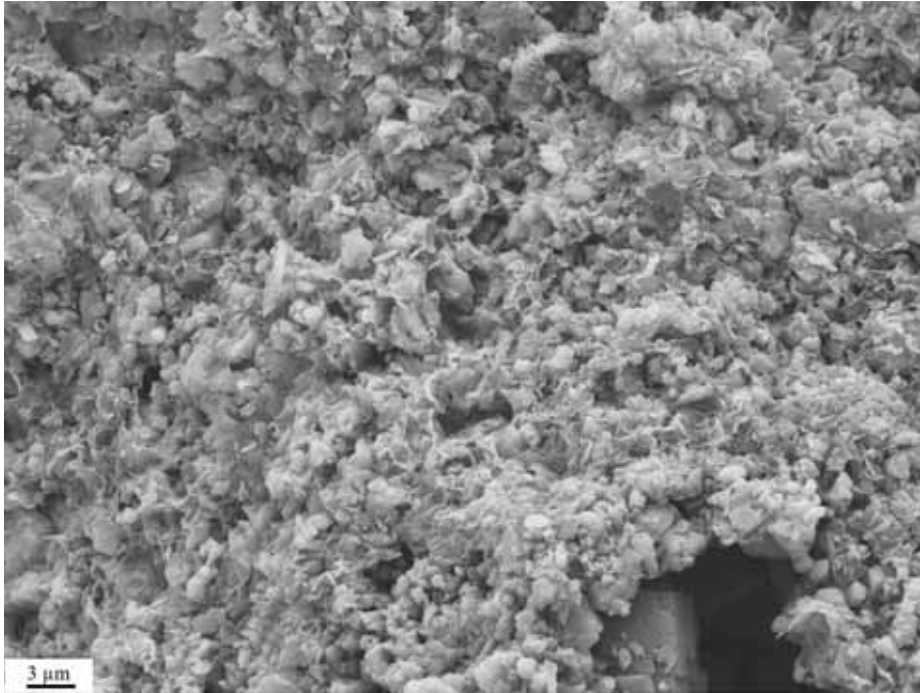


Figure 19: High magnification FEG-SEM micrograph of clay minerals found inside the transition zone of the LTT.

The formation of a high-porosity zone is in agreement of what is observed by e.g. Putnis et al. (2009) when studying mineral replacement reactions in single crystals. The formation of such a zone is the driving mechanism enabling mineral replacement to take place and progress through the crystals. In addition, observations made on outcrop chalk from Mons, St. Vaast Formation, also suggest the presence of such a porous transition zone. Cores drilled with longitudinal holes along the flooding axis were flooded with different brines (Abubeker, 2013; Geitle, 2013). One of the cores were flooded with $MgCl_2$,

prepared as a thin-section and then mapped by FEG-SEM-EDS. Magnesite (red pixels) seems to be precipitated inside the hole, and mimics cementation, reducing porosity and permeability in the hole (Figure 20). A gap, or porous reaction front, towards the calcite (blue pixels) can be observed in slice 5, near the outlet of the core. The interpretation of precipitated magnesite was confirmed by XRD analyses (Bredal, 2018).

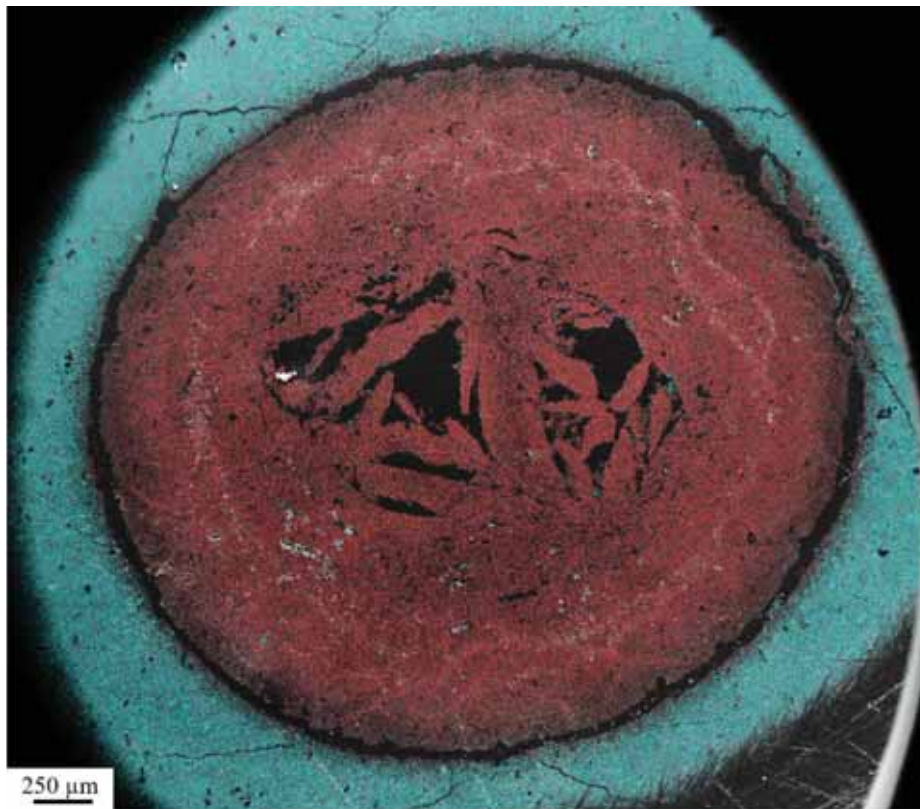


Figure 20: FEG-SEM-EDS mapping of newly grown magnesite in a hollow cylinder chalk core flooded with $MgCl_2$. Red pixels = magnesium, blue pixels = calcium. Cortesey of Tine Vigdel Bredal.

Detailed MLA-scans of the transition zones in the long-term tests show that there is an increasing amount of calcite (red) from the inlet side (left) of the zone towards the outlet (right) here visualized in the LTT (Figure 21).

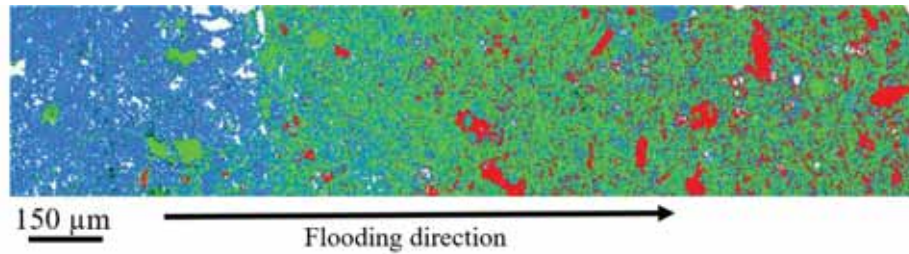


Figure 21: MLA scan of the transition zone in LTT. Legend in Figure 6. Blue pixels = magnesite, red = calcite and green = clay minerals.

The occurrence of calcite, a heavier mineral phase compared to magnesite, yields more backscattered electrons in FEG-SEM-BSE and appears as brighter shade of grey in the SEM-BSE micrograph. The occurrence of calcite inside the front seems to be linked to larger fossils in the chalk, such as foraminifera shells (Figure 22). This is in accordance with what was observed in **Paper III**.

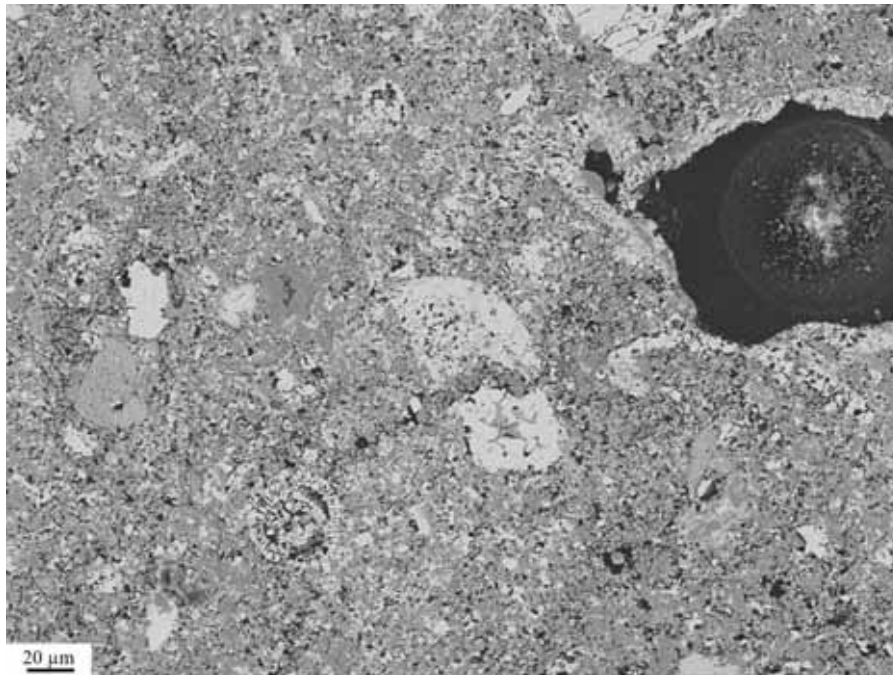


Figure 22: FEG-SEM-BSE micrograph from inside the transition zone of LTT. Lighter mineral phases with lower AAN yield less electrons and are therefore darker in the image.

When preliminary EDS analyses of the transition zones were performed, the results implied that the area had a dolomitic composition, with comparable amounts of Ca and Mg (Minde et al., 2016) (Figure 23).

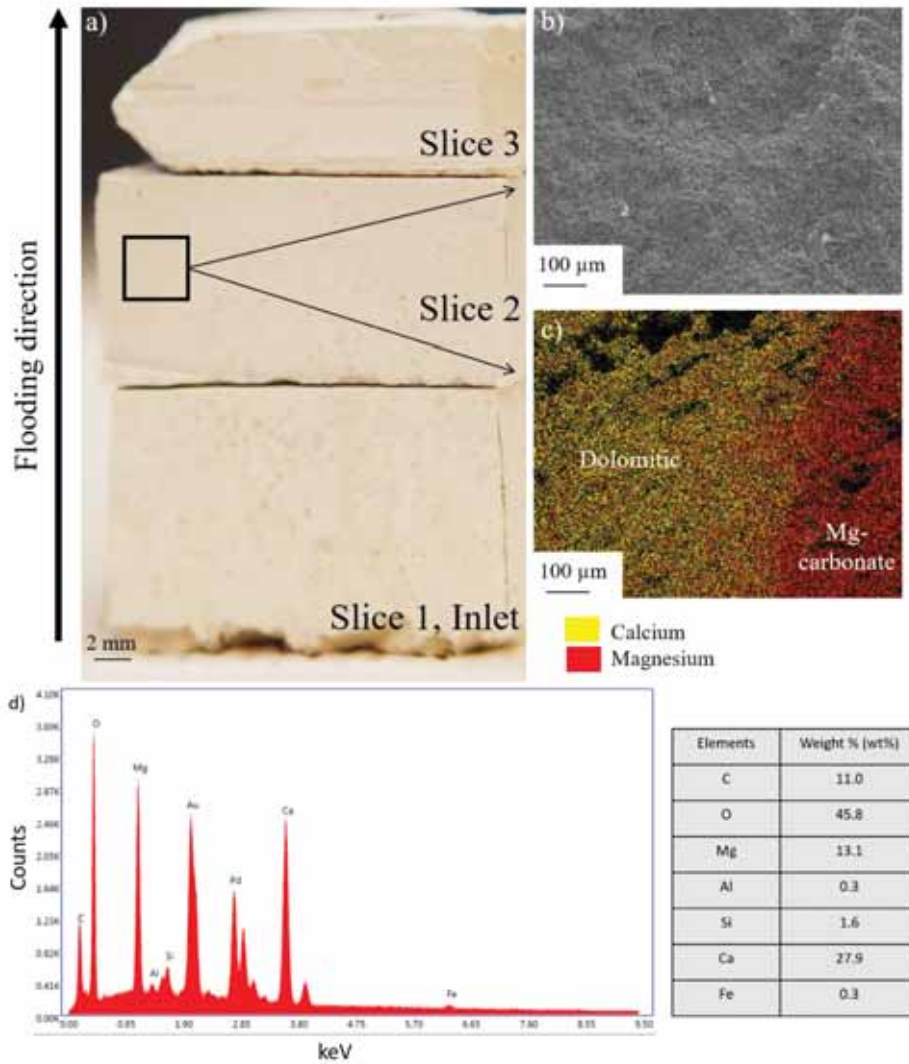


Figure 23: SEM-EDS mapping and analysis of the transition zone in MLTT. a) The three slices closest to the inlet of the core. Black box indicates mapped area b) FEG-SEM micrograph of the mapped area. c) EDS map showing the distribution of calcium (yellow) and magnesium (red) in the area of interest. d) EDS spectrum and quantification from the “dolomitic” part of the sample. The sample was coated with Au and Pd, hence the peaks.

Main results and discussion

Because of the fine-grained character of chalk and the even smaller sized new-formed minerals which precipitated due to flooding with non-equilibrium brines, limitations of methods such as FEG-SEM in terms of resolution may require the results to be controlled by complementary methods.

Material from the transition zone in slice 2 in the MLTT was analysed by XRD, and show the absence of dolomite or any Mg-carbonate at core-scale, but magnesite (Figure 24).

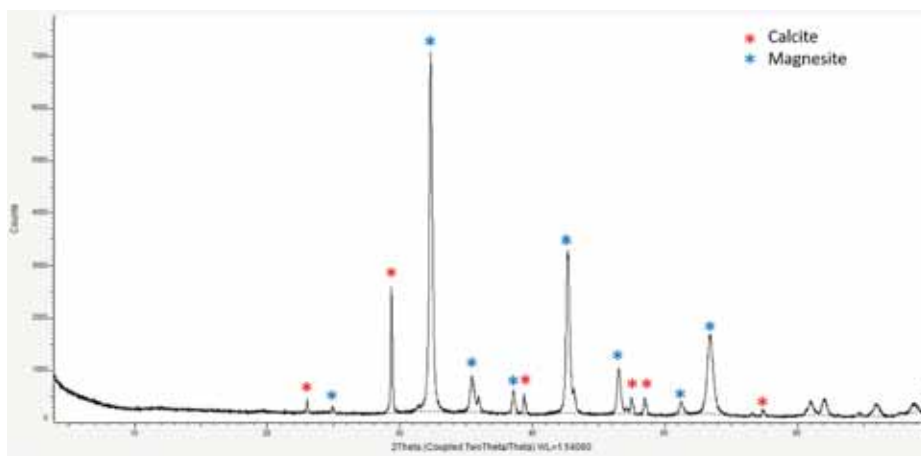


Figure 24: XRD analyses of the transition zone in slice 2 of MLTT, marked with major peaks. Only calcite (red asterisks) and magnesite (blue asterisk) were observed together with possible observations of clay minerals. No dolomite could be observed.

Complementary XRD analyses were also conducted on the artificial chalk cores, confirming the existence of only calcite and magnesite in the cores after flooding (Figure 25). Dolomite was not found.

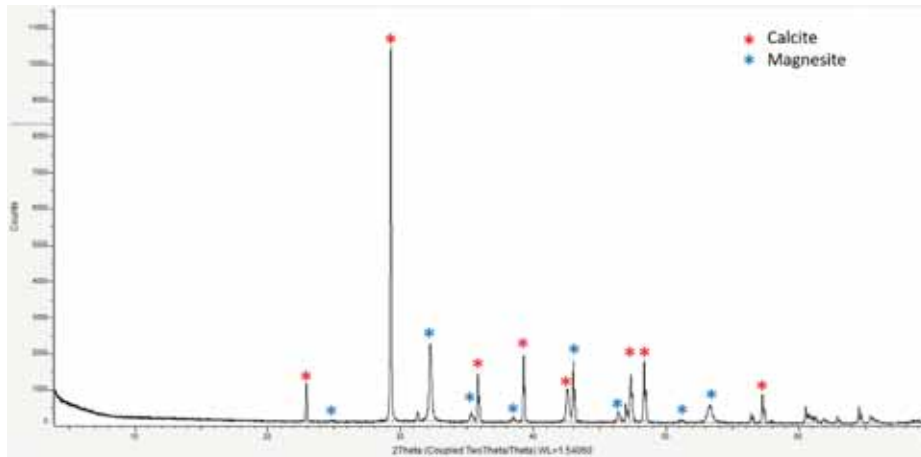


Figure 25: XRD analysis of slice 2 in the artificial chalk core flooded for 289 days with $MgCl_2$, marked with major peaks. Only calcite (red asterisks) and magnesite (blue asterisk) were observed together with possible observations of clay minerals. No dolomite could be observed.

As such, the similar results in XRD-analyses for outcrop chalk and the flooded calcite powder, support observations by FEG-SEM and ICP-MS analyses. Results from all methods suggest a similarity in mineralogical alterations between outcrop and artificial chalk.

Analyses of the three long-term tests by micro-Raman spectroscopy confirmed the results from the XRD, with positive identification of the abundant minerals as magnesite and calcite (**Paper VII**). Again, dolomite could not be detected (Figure 26).

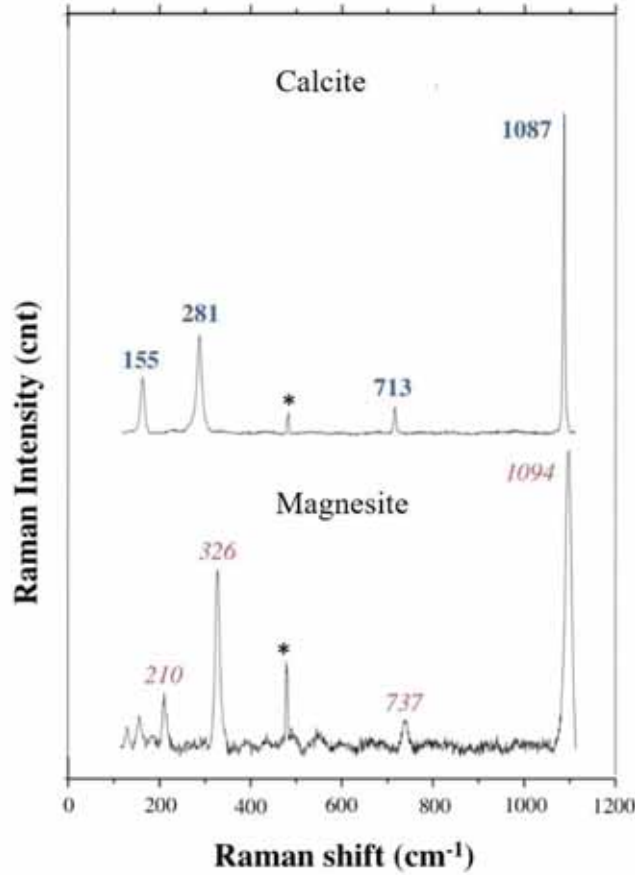


Figure 26: Raman spectra collected on the first slice of the LTT showing the presence of calcite and the presence of recrystallized magnesite. Calcite peaks are reported in blue/bold, magnesite peaks in red/italic. * represent the neon lamp emission line at 476.8 cm⁻¹ used for calibration with the Horiba XploRA spectrometer. Peak positions are reported without decimals.

Limitation in detection limits for XRD in these type of experiments (Zimmermann et al., 2015) and lack of resolution for micron to sub-micron minerals in micro-Raman analyses (**Paper VII**) may be the reason for the absence of observed dolomite, however, the contradictory results from the three methods demonstrated a need to investigate the mineralogy further with even higher resolution at pore-scale.

3.2 Pore-scale alterations

Chalk is a very fine-grained rock with grainsizes often below one μm . This causes single-grain analyses to be challenging. Additionally, the rock is very soft and brittle, a factor which makes sample preparation more difficult. Despite of this, several interesting observations on pore-scale have been made, especially by using TEM.

As discussed in section “3.1.2 A porous transition zone with sharp boundaries”, the composition of flooded chalk can in cases seem to be dolomitic when analysed by EDS at scales of tens of micrometres and above. Samples from the transition zone in the MLTT (Figure 23), were cut from the sample surface and prepared by FIB-SEM, and then analysed by STEM-EDS at UiS. In total, seven samples were taken from the three long-term tests. This is undoubtedly not enough to describe the mineralogy of the entire cores, but can aid in identifying the true changes in mineralogy in these fine-grained rocks.

STEM-EDS analyses from all studied samples show similar results. Inside the transition zone, two types of elemental compositions of the carbonate crystals or grains can be found. Here, newly precipitated magnesite grains containing 1-4 wt% Ca are present (red, Figure 27), together with calcite grains (blue, Figure 27). The calcite grains are more rounded (white arrows, Figure 27), compared to the angular magnesite crystals. The size of these rounded calcite grains is commonly between one and two μm and the grains appear in cases to be partly dissolved, with etch marks at the edges of crystal planes (black arrow, Figure 27). They are often arranged in circular structures, resembling the original coccolithophore ring-type textures of chalk.

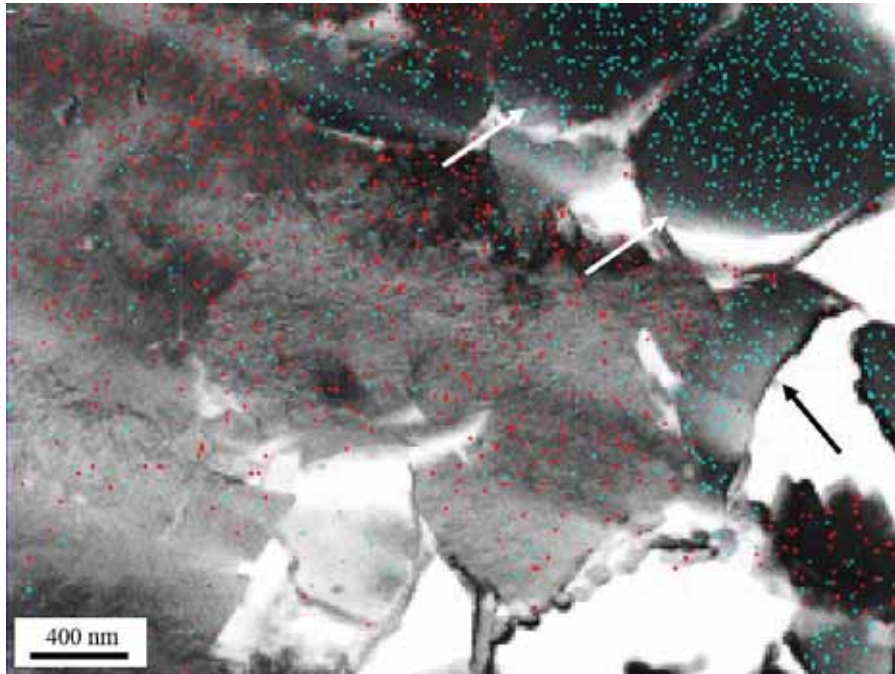


Figure 27: Bright field-STEM image of the primary front in the MLTT, slice 2. Original calcite grains (blue) are rounded (white arrows) and the structure resembles the form of coccolithophore rings. To the right of the image, partly dissolved grains are observed (black arrow). Newly precipitated magnesite grains (red) have a more angular shape and contain small impurities of calcium.

No dolomite was observed in these grain-scale studies and the TEM results support the findings using XRD and micro-Raman.

The areas which were strongest affected by chemical changes, inside the secondary front, are in the three tests characterised by a complete alteration from calcite to magnesite (Figure 28) and all analysed grains (images from the MLTT are shown here) display comparatively the same composition, similar to the magnesite grains found inside the transition zone (Figure 27). The calcium is homogeneously distributed within the imaged crystals, and does not appear as separate grains or crystals. The crystals were precipitated out of a fluid with high Ca-concentration after dissolution of calcite, and the mentioned impurities

Main results and discussion

are therefore not unlikely. The newly formed Mg-rich crystals have an angular shape, and appear in varying sizes, from approximately 100 nm to one μm .

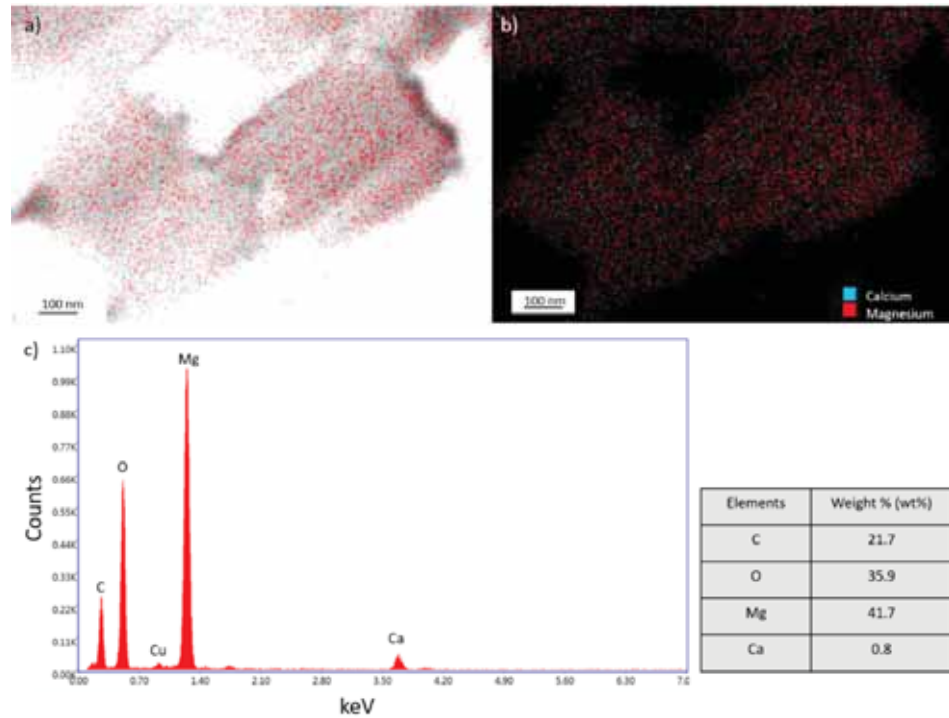


Figure 28: a) Bright field-STEM-EDS image inside the secondary front in the MLTT, slice 2. Newly precipitated magnesite grains (red) with an angular shape, containing small impurities of calcium (blue). b) The distribution of magnesium (red) and calcium (blue) in the crystals c) Typical spectrum and non-standard quantification of the magnesite found in the three long-term flooded cores. The FIB-lamellas are welded to a copper grid (Cu), hence the peak.

To verify the results of TEM-EDS and test out a new analytical method, TERS-AFM was applied to small 3 mm diameter disks drilled from the thin-sections of the three long-term tests (Borromeo, 2018). Even though there were difficulties both in finding suitable sample preparation methods and achieving good high resolution maps by this method, the mineralogy combination of calcite and magnesite was confirmed on pore-scale (Figure 29), as it was with Micro-Raman on core-scale.

Main results and discussion

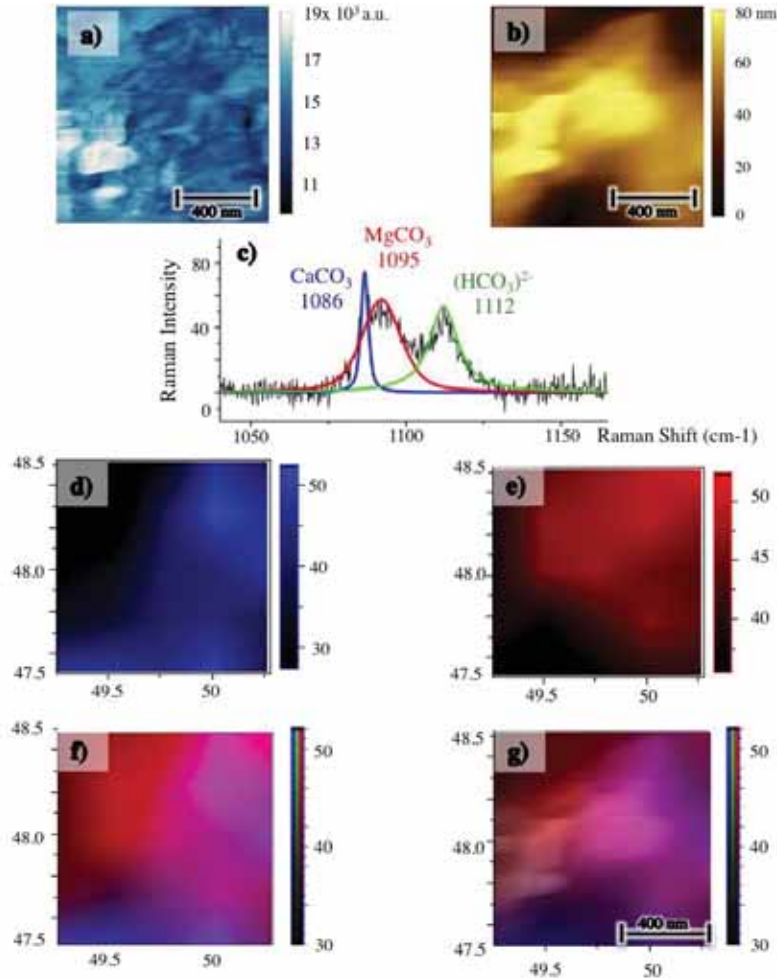


Figure 29: TERS mapping acquired on the MLTT. a) $1 \mu\text{m} \times 1 \mu\text{m}$ topography acquired with tuning-fork based AFM. b) Magnitude signal acquired in the same $1 \mu\text{m} \times 1 \mu\text{m}$ area. c) typical TERS spectrum obtained on a single point, showing peaks at 1086 cm^{-1} (calcite), 1094 cm^{-1} (magnesite) and 1112 cm^{-1} (bicarbonate ion). d) TERS mapping showing the distribution of the 1086 cm^{-1} calcite ν_1 peak. e) TERS mapping showing the distribution of the 1094 cm^{-1} magnesite ν_1 peak. f) Superimposition of the TERS mappings of calcite and magnesite, following the colour code used in the previous panels; g) superimposition of the TERS mappings of calcite and magnesite and of the topography image in a).

As described on core-scale, observations in flooded outcrop chalk are matched by observations in the artificial chalk also on pore-scale. FIB-slices of the flooded calcite powder were analysed by STEM-EDS (**Paper II**). Figure 30a and b show a bright field image of a magnesite crystal precipitated on top of a

calcite crystal along with STEM-mapping of calcium- and magnesium-distribution in the two crystals. The transition between the two adjacent crystals is sharp. The Ca- and Mg-concentrations in both crystals were scanned over a cross-section in Figure 30c and d. The distribution of Mg and Ca is uniform within the two crystals in the line-scan, and the transition between the two phases is nearly instantaneous, only minor impurities of calcium can be found homogeneously distributed within the magnesite crystal.

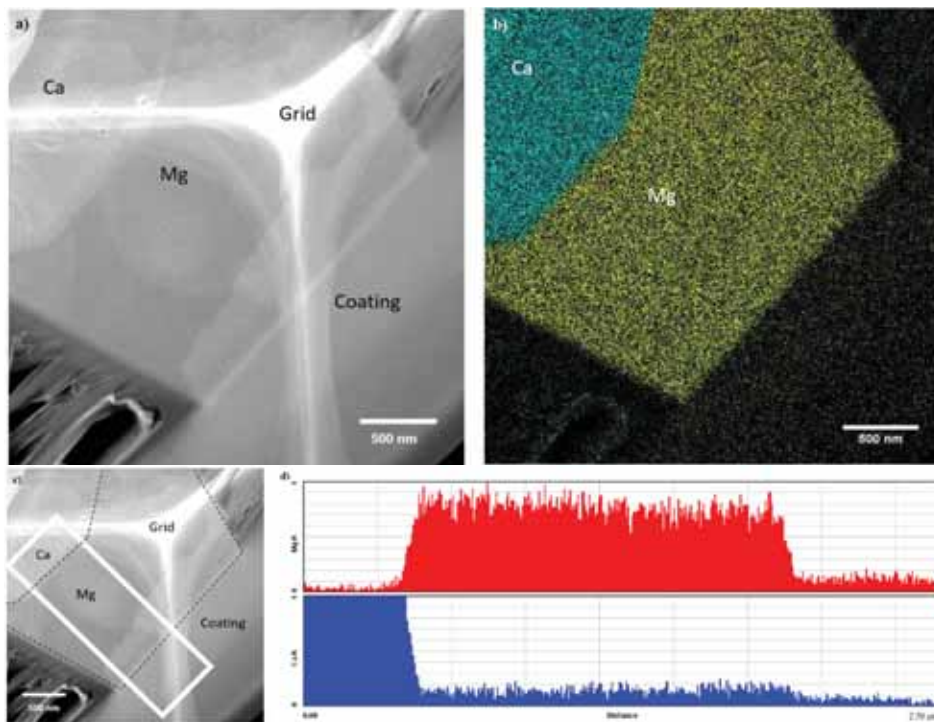


Figure 30: a) Bright field image of adjacent crystals. b) STEM mapping of crystal growing on top of original calcite crystal. Ca = calcium = blue, Mg = magnesium = yellow. c) The position of the line-scan profiles for the crystals in a). d) Chemical analysis along the line scan in c) with X-ray intensities for Mg and Ca. Ca = calcium = blue, Mg = magnesium = red. The white pattern behind the crystals is the copper grid the slice is attached to.

TEM studies (Figure 30) suggests that the processes of alteration are linked to dissolution and precipitation, and not to solid-state molecular diffusion, as the transitions between the Ca- and Mg-phases are rather abrupt. This is also

supported by severe signs of dissolution observed at core-scale in the flooded artificial chalk cores (Figure 14) and indications of minerals precipitated under elevated experiment temperatures measured by $\delta^{18}\text{O}$ isotopes (Figure 16) in flooded onshore chalk. Dolomite was not observed. As such, it is most probable that in MgCl_2 -flooding of outcrop chalk and of calcite powder, the only carbonate mineral phases involved are calcite and magnesite, and that the process of alteration is through dissolution and precipitation.

3.3 Scales of pseudomorphism

By studying the mineralogy at several scales, including nano-scale, the scale of pseudomorphism may also be determined. Pseudomorphism is not uncommon in geological aspect, and involves a change in mineralogy while the original shape is preserved. This is described by several authors based on inorganic-crystal experiments in still-standing fluids, e.g. Jonas et al. (2015), Putnis et al. (2007) and Putnis et al. (2009). The experiments in this study were carried out under continuous fluid-flow and can therefore not directly be compared to the results from these authors.

In the long-term tests, inside the first front, observed at the outlet of the LTT and MLTT, it seems that the diffusion and transport rates are sufficiently high to limit a local process of coupled dissolution and precipitation. In this part of the two cores the accumulation of larger magnesite crystal and polycrystalline aggregates in sizable pore-spaces seem to be the primary alterations, as also observed in flooding-experiments of shorter periods of time (**Paper IV** and **V**). Much of the original calcite is still present in these areas.

In the secondary front, observed at the inlet of the LTT and MLTT along with the entire ULTT, the processes of alteration seem to be different from the primary front. Micro- and macro-fossils have, together with the rest of the rock material, an altered mineralogy while the fossil-structures are preserved, much

like the results described by (Putnis et al., 2007) as pseudomorphism. In Figure 31, a foraminifera shell is easily recognized in a), while in b) a circular structure of magnesite crystals may resemble the shape and size of a coccolith ring. Both these observations indicate pseudomorphism at μm -scale and above. It may therefore be possible that this second alteration front behaves more like the alteration processes in beaker experiments, without fluid-flow.

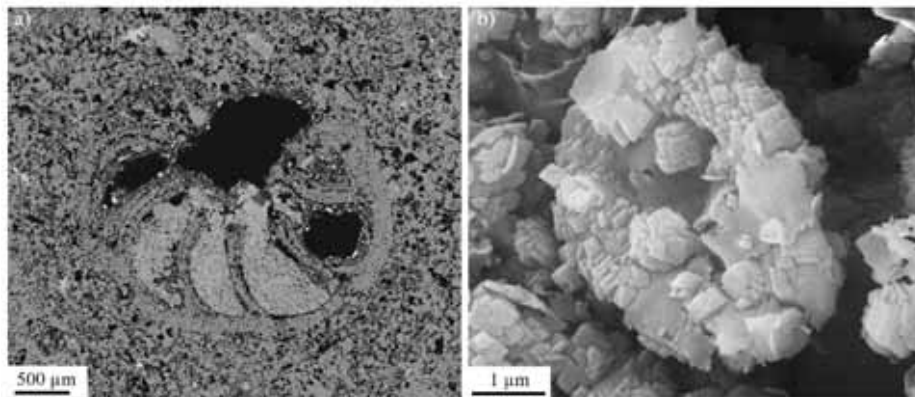


Figure 31: SEM-BSE micrograph of a shell of a foraminifera preserved in the ULTT, ~ 0.5 cm from the outlet (see Figure 2). The shape of the fossil is preserved, but the mineralogy consists of magnesite with calcium impurities. b) Newly formed crystals of magnesite observed in slice 2 of the ULTT, resembling the shape and size of a coccolithophore ring.

Xia et al. (2009) have given an accurate explanation of this phenomenon: As long as the dissolution rate of the primary mineral is the limiting factor, nanometre-scale pseudomorphism is possible, enabling precipitation of the secondary mineral as soon as there is dissolution. If the precipitation rate of the secondary mineral is the limiting factor, pseudomorphism is only visible at a larger scale, typically around $10 \mu\text{m}$, which is also the case in the three long-term flooded cores. A complete understanding of these alteration-mechanisms by analysing the cores after flooding is difficult, and further experiments where in-situ observations are possible would greatly contribute to a complete understanding. This could e.g. be performed by high resolution 3D X-ray

microscopy, micro-Computer Tomography (CT), Magnetic Resonance Imaging (MRI) or Positron Emission Tomography (PET).

In flooded calcite powder, there is after 289 days of flooding an area at the inlet of the core where the distribution of crystal-sizes is bi-modal, with the larger crystals being in the size-range of the original calcite grains. Because of the lack of easily recognizable shapes and features as seen in fossils, it is hard to confirm, however, it could be speculated that this is also a result of micrometre-scale pseudomorphism formed during the progression of the second alteration front.

3.4 Fractures and texture

In chalk reservoirs with low matrix permeability, fluid-flow is significantly affected by fractures and the texture of the rock. Understanding how such features in the chalk affect the mineralogical alteration during flooding of non-equilibrium brines is important to anticipate how the fluid-flow could be altered during injection.

A chalk core from the Liège outcrop was fractured along the flooding direction in a Brazilian test (For more details see **Paper III**). Figure 32 shows part of the fracture after flooding with synthetic seawater (SSW) for 34 days. It was imaged by FEG-SEM-BSE after set in epoxy and polished. The fracture seems to have healed during flooding and only traces of the original fracture are visible as denser areas and as an increase in lighter mineral phases, observed as brighter shades of grey in the BSE micrograph.

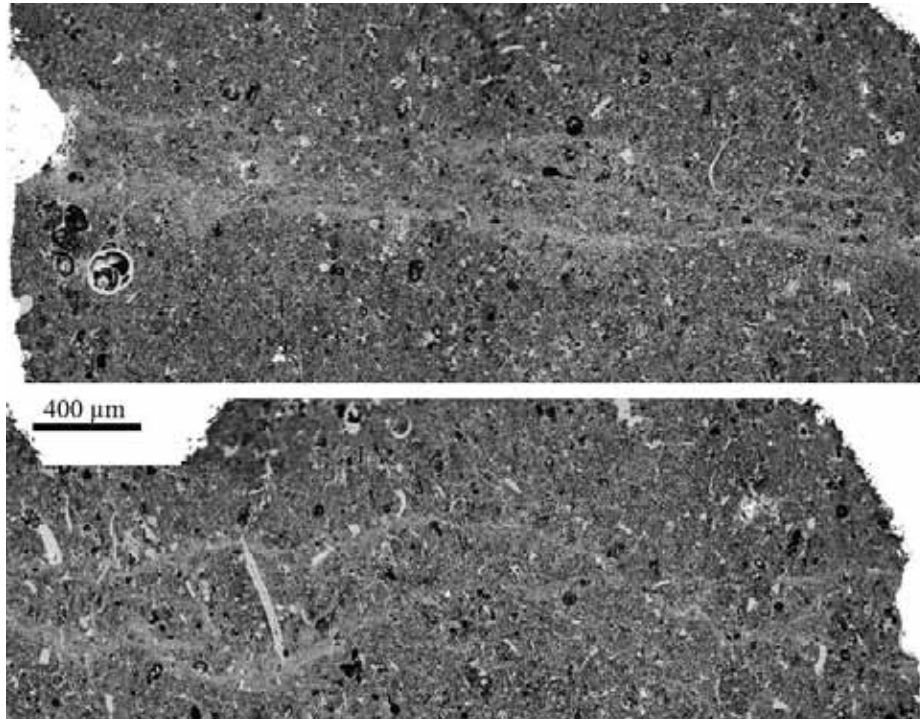


Figure 32. FEG-SEM-BSE micrograph of the fracture after flooding with SSW for 34 days. The flooding direction was horizontally in the images that show approximately one cm of the fracture, split into two images. The lighter phases in the SEM-BSE image are remnants of the fracture, seem denser and have an increase in lighter mineral phases.

Possible healing of fractures during fluid injection in reservoirs is of high importance when studying the effects of EOR-fluids. However, this effect should be further studied at larger scales to investigate how significant this effect is on reservoir-scale.

MLA-images of the same fractured chalk core flooded with SSW, show that inside fractures there is in general a higher concentration of magnesium (Mg), silicon (Si) and aluminium (Al). Shells of micro- and macrofossils stand out to have very low Mg content compared to the matrix. A shell from a macrofossil is embedded perpendicular to the fracture (Figure 33). This texture provokes a significant difference in Mg content between the concave side of the shell, with

Main results and discussion

higher Mg concentrations, and the area of the convex side of the obstruction, with lower concentrations. This trend is confirmed by EMPA data along the profile A-A' in Figure 33, showing higher values for MgO, SiO₂ and Al₂O₃ on the concave side of the shell (Figure 34).

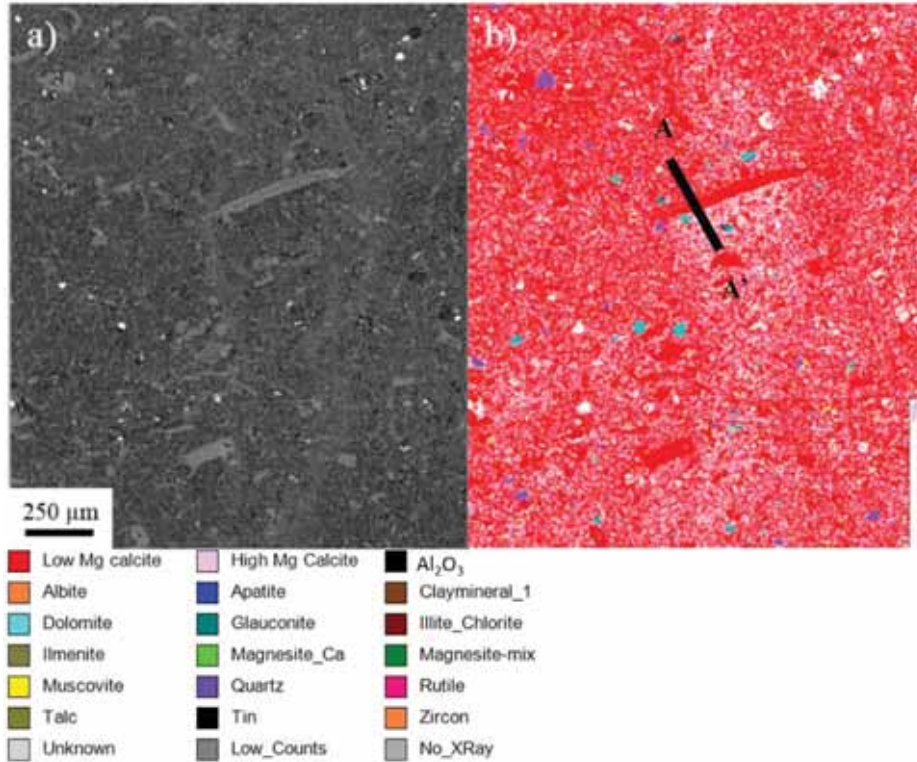


Figure 33: SEM-BSE micrograph (a) and MLA scan (b) of the same area of the fracture. The Mg-content is higher on the concave side (below) of the shell than on the convex side (above). Legend below. White areas relate to pore space. Flooding direction is vertical in the images.

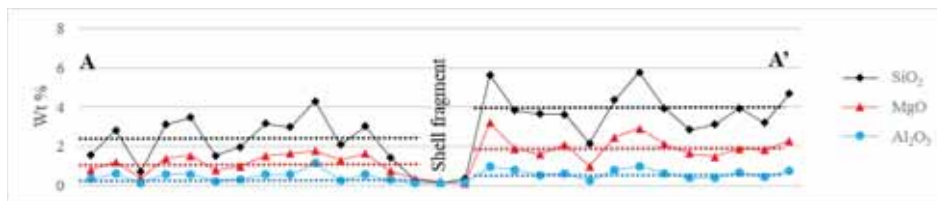


Figure 34: Oxide values measured by EMPA along the profile A - A' in Figure 33. Dotted lines are average values.

Analyses of the fractured core by nanoSIMS show another fragment of a shell embedded in the matrix. The fragment exhibits different alteration behaviour than the surrounding particles (Figure 35), as also observed by FEG-SEM-EDS (Figure 22) and MLA (Figure 21 and Figure 33). The shell fragment does not seem altered by flooding of SSW and shows a clear depletion of Si, Mg, Fe, S, Al and P and, compared to the matrix, it seems to have kept its original calcitic composition.

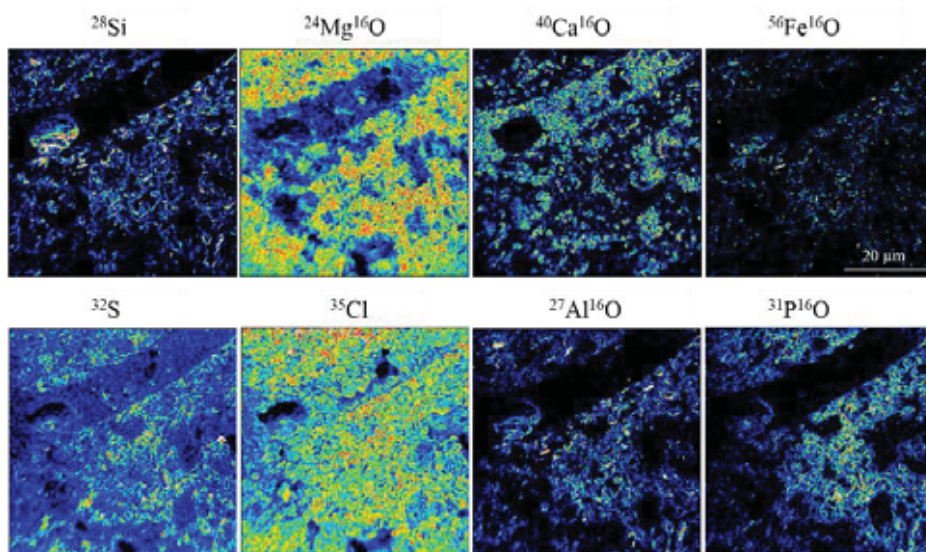


Figure 35: NanoSIMS images showing relative concentrations of elements between a shell-fragment and the surrounding matrix in fractured Liège chalk flooded with synthetic seawater (SSW). Notice the enrichment of Mg in the surrounding matrix compared to the concentration of Mg in the shell-fragment and the opposite pattern for Ca.

The flow is clearly obstructed by the shell-fragments, and the ions in the SSW have not infiltrated the shell during the flooding period. Although most of the surrounding matrix seems affected by the flooding of SSW, the shells and microfossils seem inert to the flooding agent and show to much less degree, if any, mineralogical changes as partly observed in the transition zones in the long-term tests flooded with MgCl_2 (Figure 21). There may be several reasons for this differentiation: 1) The size of the carbonaceous particle matters for the

chemical stability of the grain. Smaller particles may be more prone to alteration and mineralogical changes than larger ones (Oswald ripening). 2) The initial composition of the fossils differs from the finer-grained matrix, such as Mg/Ca ratio depending on e.g. age, seawater composition and temperature at formation. 3) Curvature and surface properties affect the dissolution rates of the initial grains and fossils (Levenson et al., 2013). 4) The increase in other elements in the matrix may be due to precipitation of smaller crystals/grains in the pore-spaces or in the fractures where there is more free space and the stress state is different. All these points could be deciding factors, and the mineralogical composition and texture of the rock itself is therefore paramount for the fluid flow in chalks. From these images and elemental analyses, it seems clear that the larger fossils have a higher resistance to mineralogical alterations than the smaller coccolithophores and fragments in the matrix.

Without the knowledge of the micro-facies, fluid-flow is barely predictable even on core-scale for the length of the experiment here. It is possible that these criteria are of less significance when massive fluid flow affects entire rocks over a longer time. However, they definitely should be acknowledged in simulation and modelling at pore- and core-scale.

3.5 Effects of primary mineralogy

Most of the results presented in this study involve minerals replacement reactions involving Ca^{2+} and Mg^{2+} only. However, in the flooding of outcrop chalk, there is always a presence of clay minerals and other non-carbonate minerals which affect the equilibrium state and the dissolution – precipitation processes in the cores. In **Paper V**, five different outcrop chalks have been studied and compared, and the strength and stiffness of the cores, correspond to the amount and type of non-carbonate minerals which is present. This also affects changes in porosity, and to large extent permeability, especially studied

in **Paper IV**. When flooding e.g. chalk from Aalborg, which has a high content of silica in the form of opal-CT, at different temperatures (25-130 °C), large amounts of clay minerals containing Mg and Si are precipitated in pores, severely reducing permeability (Figure 36) with up to 98% (including compaction effects).

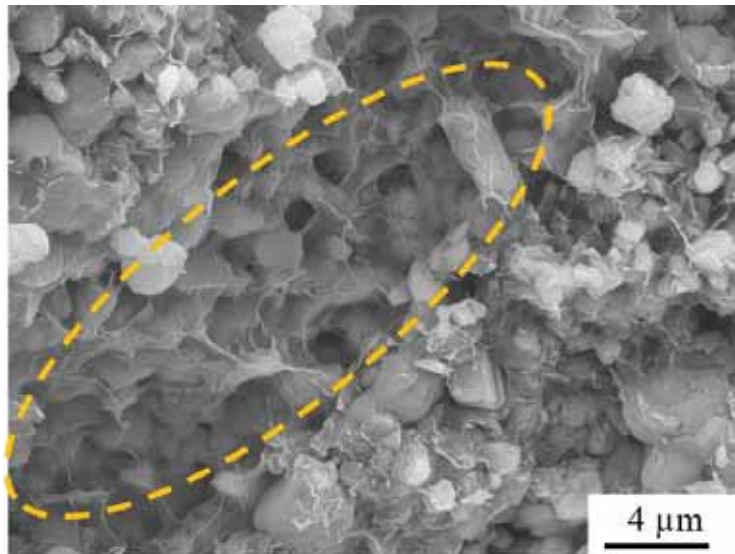


Figure 36: FEG-SEM image of outcrop chalk from Aalborg flooded at 130 °C for 115 days with MgCl_2 (slice 6, near the outlet), showing pore surfaces and throats covered by newly formed Si-Mg-bearing minerals (orange dashed circle). Courtesy of Tania Hildebrand-Habel.

The amount of permeability-reducing clay minerals which precipitate during flooding with MgCl_2 vary in correlation with the temperature of the flooding fluid for the chinks: The higher the temperature, the larger the amount of precipitated minerals. The presence of clay minerals along the flooding axis of the cores can also be correlated with the changes in SSA as described in “3.1.1 Two fronts of alterations”.

In chinks with low non-carbonate content, e.g. from Stevns Klint, no clay minerals are observed precipitating during flooding, and the mineral exchange from calcite to magnesite may rather increase porosity and permeability, if one

does not consider compaction effects. This is also observed in two of the three long-term experiments, where all three cores underwent severe compaction (10 to 18%). However, for the cores flooded for approximately two and three years, the permeability, and the calculated porosity, started to increase after a primary phase of compaction-reduced permeability and porosity. As magnesite precipitates at the expense of calcite, the density is increased, thus filling less space in the core. This enhances porosity and permeability if bulk volume is kept constant.

As discussed in “3.4 Fractures and texture”, the non-carbonate content may also significantly disturb fluid-flow in fractures. The diagenetic history of the rock and the amount of available pore-space may affect fluid-flow, and in turn the distribution of newly formed mineral phases. The knowledge of primary mineralogy and texture of the rock is therefore important parameters to acknowledge if one wants to predict and possibly control the effects an EOR-fluid would have in a chalk core or even in a reservoir.

3.6 Mechanisms controlling crystal shape and distribution of new-grown minerals

In this thesis, analyses of experiments performed on different outcrop chalk and pure calcite powder have been presented. In chalk, the non-carbonate minerals dictate some of the mineral replacement reactions taking place during flooding with non-equilibrium brines, especially when the content of silicate minerals is high. This is e.g. observed in experiments on Aalborg chalk flooded with MgCl_2 , where massive amounts of Si-Mg bearing clay phases fill up pore-spaces and significantly reduce the permeability (Figure 36). However, alongside the precipitation of non-carbonate minerals, there is also observed a process of dissolution of calcite and precipitation of magnesite, with calcium impurities, in all experiments where MgCl_2 is the flooding brine. The

distribution of newly formed magnesite along the flooding axis of the cores, is as expected, with most pronounced alterations at the inlet of the cores. Similar single crystals and polycrystalline aggregates of magnesite can be found in all experiments. Polycrystalline aggregates are observed downstream of larger single crystals found at the inlet of the cores. As discussed in **Paper II**, the saturation indices in MgCl_2 flooded chalk cores (Andersen et al., 2012) do not match the distribution of the shape and size of crystals and aggregates found in the cores after the experiments. Aggregates of smaller crystals are more likely to precipitate at the inlet of the cores, where the saturation index, i.e. the degree of super-saturation, is the highest. Such a state of equilibrium produces high nucleation rates and low growth rates, which favour the formation of abundant small crystals. At states closer to equilibrium, growth rates are higher, favouring the formation of larger single crystals (Myerson et al., 2002). For the calcite powder experiment, the saturation index along the core was modelled by IORCoreSim and show changes over time (Figure 37). The highest values, i.e. where the degree of super-saturation is highest, is found near the inlet of the core, both after 10, 50 and 289 days, where there is a constant supply of Mg^{2+} . Over time, the amount of calcite present at the inlet is reduced meanwhile the amount of magnesite increase. This also affects the saturation index, thus the formation of new crystals. After 289 days, magnesite does not precipitate at the first mm of the core, most likely because all of the calcite is dissolved in this area.

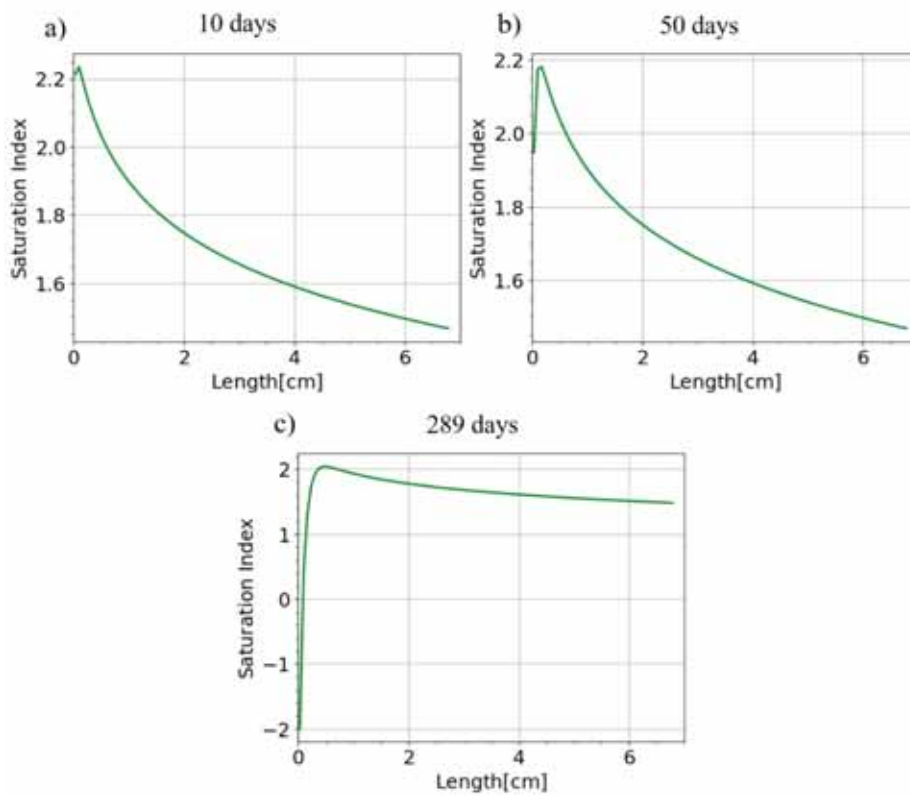


Figure 37: Saturation index of magnesite in the flooded calcite powder after a) 10 days b) 50 days and c) 289 days. After 289 days, magnesite no longer precipitates at the inlet, and may possibly even dissolve, due to changes in e.g. pH. Courtesy of Aksel Hiorth.

The most probable explanation for this miss-match is that small crystals of magnesite precipitate in the fluid phase at the inlet of the cores, where saturation indices are high, aggregate and settle further along the flooding axis of the core. This trend is observed already after months of flooding, but as seen in Figure 37, saturation indices are different towards the end of the flooding periods, and the processes of precipitation may also change. Even though this phenomenon was most easily observed in the artificial chalk cores, the same type of crystals and aggregates are found in experiments on outcrop chalk. It is therefore likely, as observed with other methodologies, that the same mechanisms are at play in outcrop and in reservoir chalk.

The abundance of magnesite and calcite at any given time and point in the core will influence the dissolution or precipitation rate accordingly, along with the surface properties of grains and crystals. As such, a combination of nucleation rate, growth rate and advection controls the distribution and population of magnesite precipitated during flooding. As there seem to be two fronts of alterations in both flooded chalk and possibly in flooded calcite powder (artificial chalk cores), one may presume that the different rates vary relative to each other and therefore impact the alteration processes in different ways with time of flooding and most likely the amount of material already altered. This could be linked to a threshold value of magnesite being precipitated in an area, as observed in the artificial chalk cores, where the level of measured MgO by ICP-MS had to be at least above 0.97 wt% for the core to consolidate (**Paper II**). All “slices” that had an MgO concentration below this value, was still in powdered form after flooding.

As discussed in chapter “3.1.2 A porous transition zone with sharp boundaries” the transition between the two alteration fronts has two features that were not expected before analyses. It is sharp, on mm-scale, and seems to be more porous than the remaining parts of the cores. This opens for discussion if the transformation from one mineralogy in a porous chalk core follows the same laws as the single crystal experiments observed by e.g. (Putnis et al., 2009), where the transformation is described to progress due to the formation of a porous zone. Such a zone is even more visible in the hollow cylinder experiment (Figure 20) described in section “3.1.2 A porous transition zone with sharp boundaries”. Based on this, one may say that the mineral replacement reactions in a porous multi-grain system, behave much like in a single crystal experiments. However, because of the porous nature of the system, occurrences of newly precipitated crystals, clusters or grains, appear downstream of the transition zone, with distribution dependent on saturation

index, the amount of other minerals present and advection of the injected fluid through the system. These factors affect nucleation and growth rates, and therefore the appearance of the precipitated mineral. Additionally, differences in texture, structure and composition affect the rate of dissolution of existing minerals, but also the fluid-flow, or tortuosity, in the core. These factors will also influence the equilibrium-states such that they may differ throughout the system, hence again nucleation and growth rates are affected. It is therefore important to acknowledge the change over time in these factors when interpreting and modelling such experiments.

Special focus has been given to the reactive Mg^{2+} -ion in this work, as in several other research projects in EOR research e.g. (Korsnes et al., 2008a; Korsnes et al., 2008b; Madland et al., 2011; Megawati et al., 2011; Megawati et al., 2015; Nermoen et al., 2015; Wang et al., 2016; Zimmermann et al., 2015). This is because it is found that interactions between calcite and magnesium weaken the chalk. This may be due to differences in density (volume) of newly precipitated minerals. In addition, other processes or phenomena resulting from injection of Mg^{2+} , such as changes in surface charge and electrostatic forces between grains (Nermoen et al., 2018) or changes in non-carbonate content (Megawati et al., 2011) may affect the strength of the chalk. Even though many processes may be at play at one time during flooding, it is important to understand where and when these alterations take place and which minerals do precipitate. These observations are one of the tools used to constrain and validate models at both pore- and core-scale.

3.7 The effect of wettability

All of the presented experiments in this project have been performed on water wet cores, i.e. without oil present in the cores. It is also paramount to understand if the described mineralogical alterations also take place when oil is present in

chalk cores. FEG-SEM-EDS analyses have therefore been carried out on both water wet and mixed wet cores of Kansas chalk, flooded with MgCl_2 , to compare the results. Micrographs show similar alterations in both cores, with smaller grains of precipitated magnesite along with scarce occurrences of larger crystals at the inlet of the cores (Figure 38a and b). Further away from the inlet, approximately at the middle of the cores along the flooding direction, polycrystalline aggregates of magnesite (Figure 38c and d), matching the aggregates found in both calcite powder and other outcrop chalks, are observed.

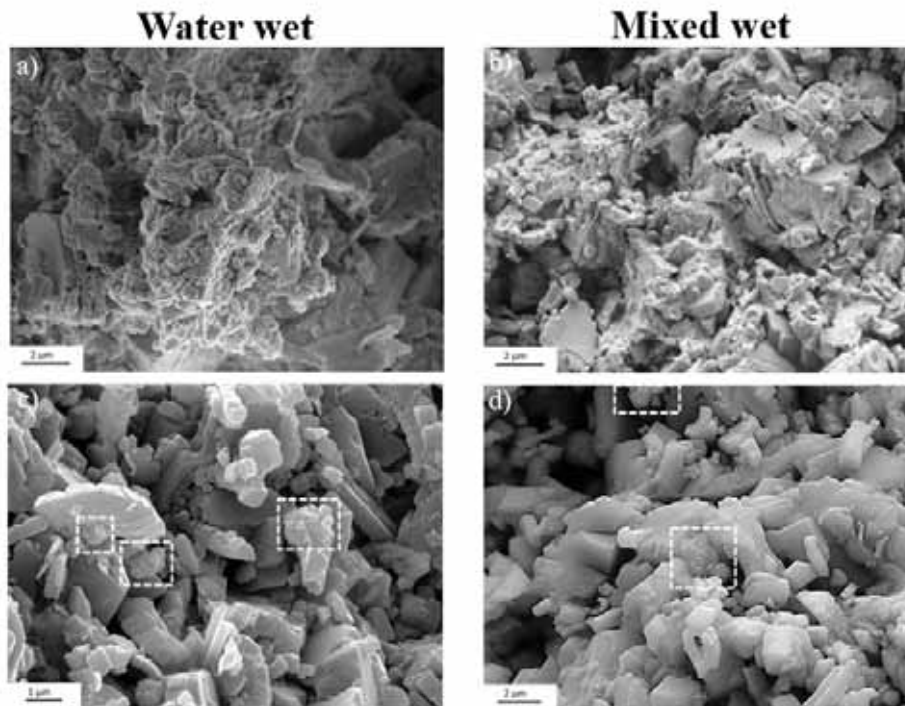


Figure 38: FEG-SEM micrographs of water wet and mixed wet Kansas chalk. At the inlet (a and b), small grains or crystals of magnesite precipitate on top of original calcite grains, while further into the core (c and d), polycrystalline magnesite aggregates precipitate.

Towards the outlet of the cores, no newly formed minerals could be observed by FEG-SEM. Given that also the geomechanical behaviour seems to be similar during creep in water wet and mixed wet chalk during flooding with MgCl_2

(Sachdeva, 2018), the preliminary conclusions of these studies indicate that the results on mineralogical alterations from test performed on water wet chalk, seem also be valid for mixed wet chalk.

3.8 A toolbox to analyse EOR experiments

Part of the objective for this project has been to design a toolbox that hold the capability to sufficiently resolve mineralogical questions related to EOR experiments (**Paper VI**). Not all of the described methods in this project are suitable to use as routine tools for studying the effect on mineralogical alterations due to different EOR-fluids. Several of the methods are challenging both with regards to time, expenses and sample preparation and should therefore only be used in cases when it is necessary to perform high-resolution analyses of e.g. nm-sized single grains, grain-contacts or pore-walls. TEM analyses are in themselves not especially time-consuming or expensive, but sample-preparation of brittle fine-grained rocks is challenging and should be performed with care. One of the methods taken into use is ion milling by FIB-SEM, which could be expensive. In addition, samples prepared by FIB-SEM are only ~100 nm thick, and are therefore easy to damage during measurements. Sample-preparation is also an issue with TERS-AFM, where good results are dependent on a very smooth surface to avoid too large differences in topography, which hampers the analyses. TERS-AFM is also a new technique to EOR research, and needs further tests to be optimized if to be used in this setting. Methods such as TERS-AFM, FIB-SEM and nanoSIMS can therefore not be part of a routine analyses toolbox.

Methods such as FEG-SEM, stable isotope and whole-rock geochemistry along with XRD can provide the user with enough information at a high enough resolution to identify and quantify mineralogical alterations in fine-grained rocks due to flooding with EOR fluids. These are methods, which are not too

expensive and do not take too much time. Complementary methods such as density and SSA measurements are also useful tools to measure the degree of alterations in flooded chalk, along with preliminary identification of mineralogy by Raman spectroscopy, depending on grain-size (**Paper VII**). For mapping of mineralogy on core-scale and down to micrometre-scale, MLA or equivalent methods may be used. The focus of in this thesis has been on fine-grained sedimentary rocks, which demands high-resolution analyses. The methods discussed here can therefore easily be taken into use for other types of rock, where grainsizes are larger and the rock samples are harder.

Last, but not least, it is important to see the huge advantages of using several methods that complement each other. Techniques such as FEG-SEM provides imaging and semi-quantitative results on the “which” and “where” of chemical alterations. This may be complemented by whole-rock and stable isotope geochemistry for more exact quantification in bulk samples and XRD to identify the exact mineralogy before and after flooding. Also, FEG-SEM can identify areas of special interest where one may want to take other methods into use, such as TEM, to gain more detailed information.

3.9 Implications for the industry

Large parts of the research process presented in this thesis can be considered basic research and cannot be directly applied for the oil industry. Directly applicable is the demonstration of which methods are ideally useful to gain quick data for an evaluation of laboratory experiments, and the mentioned ‘toolbox’ provides access to a set of tools ready to aid in interpretation of e.g. pilot tests or field-testing to understand the effects EOR-fluids and induced mineralogical alterations may have on mechanical parameters of the rock.

A deeper understanding of processes within the texture and the relation between primary and secondary mineralogy of the rock during flooding plays an

important part for all EOR efforts. This understanding is valuable as input to models and simulators, especially at pore- and core-scale, but also in the aspect of choosing the correct test material when performing experiments on EOR-effects in the laboratory. And, this study provides an understanding of that more detailed datasets on a nanoscale are necessary, in chalk for instance. Methods to gain those data are tested, although some are work intensive.

The importance of the role of non-carbonate minerals in the rock-fluid interaction cannot be underestimated. In chalk, this component is complex as the abundance is often minute, but can be of high significance during flooding of non-equilibrium brines. Silicates may also be affected by inert fluid-injection, and, when flooded with reactive brines, have significant impact on permeability of the matrix and fractures in the rock due to precipitation of clay minerals or other silicates. However, flooding with the same type of reactive brine in chalks with very low non-carbonate content may instead increase the permeability during the time of flooding. The effects of an EOR-fluid may therefore vary both with the composition of the brine as well as temperature and the primary mineralogy. This is e.g. observed in one of the long-term tests. For the core flooded for approximately two years, the compaction during creep was stopped and the production of calcium in the effluent were insignificant for a period of 63 days, when 0.130 M CaCl₂ was added to the MgCl₂ injection brine (**Paper I** and (Megawati et al., 2011)). This provides evidence that changing the composition of the injected brine, may directly impact the strain evolution of the rock.

Another interesting finding is how inhomogeneous alterations within a core are, with respect to changes in mineralogy, porosity and permeability (Figure 16 and Figure 18, and **Paper I**). This may also be important at larger scales. The geomechanical and mineralogical alterations are also dependent on temperature (**Paper IV**), along with formation fluids, which need to be considered when

Main results and discussion

injecting fluids with different temperatures into a reservoir formation. The study clarifies that the depositional environment of the rocks, and in turn the paleoecology (including grain size, shape, organism-type, etc.) affect the fluid flow and the dissolution and precipitation. How much this is of importance when up-scaling, needs to be tested at larger scales.

The preliminary tests done in this project comparing water wet and mixed wet rock indicate that many of the results from the vast amount of experiments performed studying the effect of EOR-fluids in water wet rock, seem also to be valid for rocks containing oil, and may be used to understand reservoir behaviour. However, the studies performed here needs to be continued to validate this hypothesis.

4 Conclusion and future work

4.1 Conclusions

When searching for an optimized brine for EOR purposes, it is important to study the interactions between the brine and the rock, and the consequences for geomechanical parameters of the rock. In chalk, many of these interactions involve mineral replacement reactions. Therefore, the overall aim of this project has been to identify the minerals replacement reactions at play during mechanical flow-through experiments using various outcrop chalks and artificial chalk cores made of pure calcite powder. A thorough investigation has been conducted at core- pore- and nano-scale, and the results from all scales match, and, in cases, the combination of scales supplement each other to an improved understanding of the data. Most of the experiments presented in this thesis used reactive MgCl_2 -brine as flooding agent, and some valuable conclusions can be drawn from the combination of their results.

The **which**: Besides silicate mineral phases such as talc, chlorite or possibly saponite, the main replacement of minerals involve dissolution of calcite and precipitation of magnesite with $\sim 1\text{--}4$ wt% calcium impurities, even after years of flooding (Figure 10). The clay minerals and magnesite vary in their distribution, shape and size, depending on flooding time and the type of chalk which is flooded. Differences in primary mineralogy, texture and diagenetic history affect precipitation of new mineral phases with respect to types of minerals, size, shape and abundance at any point in the core. However, certain similarities are observed. Within the original calcite mineralogy, magnesite is found as single crystals in the size-range from a few nm up to $10\ \mu\text{m}$, depending on available space and flooding time (Figure 8). Polycrystalline aggregates of the same type of magnesite also precipitate. The aggregates mostly comprise of

idiomorphic crystals of 100-200 nm, and the clusters themselves typically vary in size from 1 to 5 μm . These alterations are interpreted to take place as a primary mineralization front. After longer flooding periods, more than 500 days, a complete alteration of the mineralogy from calcite to magnesite is observed in parts of the chalk cores, the secondary front. Similar observations are found in flooded calcite powder (Figure 12, Figure 13 and Figure 15).

The **how**: The mineralogical transformations in long-term flooded chalk can be described to take place in two stages, identified by the primary and secondary mineralization fronts progressing through the cores, separated by a more porous transition zone with a sharp boundary (Figure 18). This process may also take place for tests flooded for shorter periods of time, but be difficult to observe.

Three interesting observations have been made on how these processes of alterations take place. 1) SEM and TEM-studies confirm that the contact-planes between adjacent calcite and magnesite crystals are sharp (Figure 30). The alterations are therefore considered to take place through dissolution and precipitation, and not molecular solid state diffusion through the crystal lattice. Severe dissolution defects observed on original calcite crystals support this result. 2) Crystal shapes and sizes vary with where in the core magnesite precipitate. During precipitation, shape and size of a crystal vary depending on the degree of super-saturation at any given point in the core, and the resulting nucleation and growth rates. In the studied experiments, the shapes and sizes of magnesite crystals, are not necessarily matched to the calculated saturation indices, where clusters of smaller crystals are found further along the flooding axis than expected. This may be explained by nanometre-sized crystals precipitating in the fluid-phase at the inlet of cores, where the saturation index are highest, for so to be transported further into the core by advection. The distribution of saturation indices can also be more complex and do, as seen when modelled by IORCoreSim, change over the time of the flooding

experiment (Figure 37). 3) The transition between the two alteration-regimes seems to be a sharp, highly porous zone. This observation matches what is observed by others on single crystal experiments, where the transformation process is driven by the formation of a porous zone between the old and the new mineralogy and is controlled by the equilibrium state within this zone, not of the saturation index of the bulk fluid (Putnis et al., 2009).

The **where**: The amount of newly formed magnesium-bearing minerals is highest at the inlet. The distribution of silicates after flooding vary with primary mineralogy and temperature. The crystal shapes and sizes are dictated by a combination of nucleation, growth and advection rates. Nucleation and growth rates are linked to the degree of super-saturation in the fluid with regards to magnesite. A miss-match in calculated saturation indices and the observed crystal shapes and sized in the core suggest that magnesite can be formed in one part of the core and transported to other places by the fluid-flow.

Another factor which affect crystal growth is the available space to grow in and available ions in the pore-fluid. Larger crystals are observed in larger pore-spaces and the concentration of precipitated clay minerals are enriched in pores and fractures.

A couple of other conclusions can also be drawn from this work. When flooding fine-grained chalk, commonly with low permeability, the texture of the rock, hence, the depositional environment and diagenetic history, seem to affect the fluid-flow and subsequently the degree of alteration due to rock-fluid interactions. Certain fossils are less prone to dissolution (Figure 22 and Figure 35) and may also block fluid-flow or locally alter the tortuosity of the flow, creating differences in the equilibrium state. Similar observations have been made with regards to fractures in chalk flooded with synthetic seawater (Figure 33). Accumulation of new-grown minerals are observed in the fractures, causing alterations of the fluid-flow and healing of fractures on centimetre-

scale (Figure 32). Thus, flooding with reactive brines may lead to altered permeability, blocking of existing fractures and re-direction of fluid-flow pathways, both at core-scale and possibly at reservoir-scale. Healing of fractures seems to, in these experiments, mainly involve precipitation of clay minerals, which are also observed to greatly reduce permeability during flooding of silicate rich chalk (Figure 36). The primary mineralogy affects the strength of the rock and which minerals precipitate during flooding as observed when comparing the results of flooding different outcrop chalks (**Paper V**) and the amount of non-carbonate content in chalk contribute to dictate which mineral replacement reactions take place.

A much discussed topic in the studies of mineral replacement reactions is the process of pseudomorphism. In the here presented experiments, pseudomorphism may be observed at several scales. In the ULTT, the whole core is transformed from calcite to magnesite, while keeping its cylindrical form. This may be considered pseudomorphism at centimetre-scale. However, more interesting is the pseudomorphism observed at micrometre-scale, where the shapes of macro-and micro-fossils are preserved, while the mineralogy is altered (Figure 31). As pseudomorphism is not observed on nanometre-scale, it may be concluded that the overall limiting factor is the precipitation rate of magnesite, not the dissolution rate of calcite (Xia et al., 2009).

Even though not directly applicable to a hydrocarbon reservoir, the results from this study show that mineralogical alterations in chalk due to flooding with reactive brines can be linked to certain observed changes in geomechanical parameters. As magnesite precipitates on the expense of calcite, measurements show that both the density and specific surface area increase after flooding with MgCl_2 . This fits well with an increase in porosity and permeability and changes in mineralogy over the time of flooding, as observed in the MLTT and the ULTT after longer periods. Additionally, the process of dissolution and

precipitation may directly impact the strength of the chalk together with changes in surface-charge and electrostatic forces (Nermoen et al., 2018). Manipulating the composition of the injection-fluid may directly affect the changes that occur in geomechanical parameters of chalk (**Paper I** and (Megawati et al., 2011)). Insights into the “which, how and where” of these mechanisms are paramount input information to simulators used to model and predict the effects of EOR fluids at all scales. The true mineralogical data and their distribution are important to constrain and validate models.

FEG-SEM analyses conducted in this study can lead to preliminary conclusion that the mineralogical alterations observed in flooded chalk are the same whether the rock is water wet or mixed wet (Figure 38).

A toolbox which may be used to study mineralogical alterations from pore- to core-scale on effects of EOR-fluids has been put together. Analyses by FEG-SEM, XRD and whole-rock and stable isotope analyses can, along with analyses by SEM-based mapping techniques, provide enough data to assess the mineralogical alterations in most EOR-related experiments, or in pilot test and field-scale testing. When higher resolution is needed, tools like TEM and nanoSIMS may complement the results further.

4.2 Future work

In the future, core- and pore-scale research on EOR-fluids needs to be continued together with experiments to understand the effects such brines have on the rock. Several different EOR strategies are suggested, e.g. polymer and low salinity injection. Even though a lot of knowledge in this field already is in place, the impacts these fluids have on mineralogy should to be fully understood, down to nano-scale.

As mentioned, the amount and character of non-carbonate material are affecting several rock parameters during flooding. Clay minerals are, however, difficult

Conclusion and future work

to positively identify based on elemental compositions alone and not possible to identify with Raman spectroscopy. The combination of textural analyses by SEM-EDS often aids in identification, along with crystallographic analyses such as XRD. Most clay minerals have similar dimensions in two directions, and only differ in the Z-dimension. Producing XRD signals that yield detailed enough patterns to separate clay minerals from each other is therefore challenging. TERS or sub-micron Raman studies are not favourable for chalk because of the softness of the material (Borromeo, 2018), but AFM and measurements of surface charges would be a method to identify distribution of clay minerals (Skovbjerg et al., 2012), but not feasible for a larger (> 5 micron) area of study. The best way would be to separate clay minerals from the chalk to be able to gain more accurate results in identifying these in the future.

With regards to the two stages of alterations observed during long-term testing of chalk, further experiments should be performed to investigate the timing and propagation of the front of complete transformation from calcite to magnesite. The onset of this alteration process may explain phenomena observed during flooding such as delayed creep for certain chalk types and the in-homogenous alteration processes in chalk may also be essential also at reservoir-scale. In-situ studies during flooding may be performed by using e.g. high resolution 3D X-ray microscopy, micro-Computer Tomography (CT), Magnetic Resonance Imaging (MRI) or Positron Emission Tomography (PET), and could contribute to the full understanding of this phenomena. Similarly, the possible healing effect of fractures and the distribution of silicate in chalk during flooding should be further studied, both in-situ on smaller scales, but also on larger scales to understand the effect of possible healing of fractures by flooding with reactive brines of different ionic compositions, inducing precipitation of e.g. clay minerals, anhydrite or gypsum.

Conclusion and future work

An important point is to intensify the mineralogical analyses of mechanical flow-through experiments on mixed wet or oil wet systems. Our preliminary studies suggests that the results from water systems may be used to understand rock-fluid interactions in mixed wet systems and in a hydrocarbon reservoir. However, these analyses should be continued to understand the exact similarities and differences with regards to the wetting state of the rock when injecting EOR fluids at all scales.

One of the major challenges in EOR research is up-scaling of EOR-effects to reservoir-scale. This thesis describes processes that are important at pore- and core-scale, but the effect at field-scale (kilometre-scale) is not sufficiently studied. Injection of brines should therefore also be tested at scales of meter, or tens of meters to bridge the gap between centimetre- and kilometre-scale. Tests on larger blocks and cores have been performed (e.g. (Graue, 1994; Graue et al., 2000)), however, even larger facilities are needed to be able to understand which parameters and effects are important at reservoir-scale. Reservoir-scale testing has shown to be useful in studies of e.g. CO₂-foam e.g. (Sharma, 2019). This study, however, gave several inputs to possible consequences and factors which need to be acknowledged when studying the effect of EOR-fluids. These factors may be combined at shortest with the expression ‘depositional environment’. To determine this parameter in chalk is difficult and a meticulous effort, but the impact this has in up-scaling may be observed when tests are monitored on larger scales. On a pore- and core-scale this certainly plays an important role.

References

- Abubeker, E. (2013) Water weakening of chalks - comparison of intact and fractured cores. University of Stavanger, Norway.
- Alam, M.M., Fabricius, I.L. and Christensen, H.F. (2012) Static and dynamic effective stress coefficient of chalk. *Geophysics* 77, L1-L11.
- Andersen, P.Ø., Evje, S., Madland, M.V. and Hiorth, A. (2012) A geochemical model for interpretation of chalk core flooding experiments. *Chemical Engineering Science* 84, 218-241.
- Andersen, P.Ø., Wang, W., Madland, M.V., Zimmermann, U., Korsnes, R.I., Bertolino, S.R.A., Minde, M., Schulz, B. and Gilbricht, S. (2017) Comparative Study of Five Outcrop Chalks Flooded at Reservoir Conditions: Chemo-mechanical Behaviour and Profiles of Compositional Alteration. *Transport in Porous Media* 121, 135–181.
- Anderson, T. and Arthur, M. (1983) Stable isotopes of oxygen and carbon and their application to sedimentologic and paleoenvironmental problems. *Stable Isotopes in Sedimentary Geology, SEPM Short Course* 10, 1-151.
- Andersson, M.P., Dideriksen, K., Sakuma, H. and Stipp, S.L.S. (2016) Modelling how incorporation of divalent cations affects calcite wettability—implications for biomineralisation and oil recovery. *Scientific Reports* 6.
- Appelo, C.A.J. and Postma, D. (2009) *Geochemistry, groundwater and pollution*, 2 ed. CRC Press, New York.
- Aursjø, O., Jettestuen, E., Vinningland, J.L. and Hiorth, A. (2017) An improved lattice Boltzmann method for simulating advective–diffusive processes in fluids. *J. Comput. Phys.* 332, 363-375.
- Austad, T., Strand, S., Madland, M.V., Puntervold, T. and Korsnes, R.I. (2008) Seawater in chalk: An EOR and compaction fluid. *SPE Reservoir Evaluation and Engineering* 11, 648-654.
- Bjørlykke, K. (2015) *Introduction to sedimentology: Sediment transport and sedimentary environments*. Springer International Publishing Berlin
- Borchardt, J.K., Yen, T.F. and Chemical Congress of North, A. (1989) *Oil-field chemistry : enhanced recovery and production stimulation*. American Chemical Society, Washington, DC.
- Borromeo, L. (2018) Raman spectroscopy applied to the mineralogical analysis of flooded chalk. University of Stavanger, Faculty of Science and Technology, Department of Energy Resources, Stavanger.
- Brasher, J.E. and Vagle, K.R. (1996) Influence of lithofacies and diagenesis on Norwegian North Sea chalk reservoirs. *AAPG Bulletin* 80, 746-769.
- Bredal, T.V. (2018) Micro- and nano-analyses of fracture-filling after flooding on-shore chalk with different IOR fluids. University of Stavanger.

References

- Brunauer, S., Emmett, P.H. and Teller, E. (1938) Adsorption of Gases in Multimolecular Layers. *Journal of the American Chemical Society* 60, 309-319.
- Carles, P. and Lapointe, P. (2005) Water-Weakening of Carbonates under Stress: New Insights into Pore-Volume Compressibility Measurements. *PETROPHYSICS* 46.
- Collin, F., Cui, Y.J., Schroeder, C. and Charlier, R. (2002) Mechanical behaviour of Lixhe chalk partly saturated by oil and water: experiment and modelling. *International Journal for Numerical and Analytical Methods in Geomechanics* 26, 897-924.
- Da Gama, R.O.B.P., Lutz, B., Desjardins, P., Thompson, M., Prince, I. and Espejo, I. (2014) Integrated paleoenvironmental analysis of the Niobrara Formation: Cretaceous Western Interior Seaway, northern Colorado. *Palaeogeography, Palaeoclimatology, Palaeoecology* 413, 66-80.
- Delage, P., Cui, Y.J. and Schroeder, C. (1996) Subsidence And Capillary Effects In Chalks, *ISRM International Symposium - EUROCK 96. International Society for Rock Mechanics and Rock Engineering, Turin - Italy*.
- Dusar, M. and Lagrou, D. (2007) Cretaceous flooding of the Brabant Massif and the lithostratigraphic characteristics of its chalk cover in northern Belgium. *Geologica Belgica*.
- Evje, S. and Hiorth, A. (2011) A model for interpretation of brine-dependent spontaneous imbibition experiments. *Advances in Water Resources* 34, 1627-1642.
- Fandrich, R., Gu, Y., Burrows, D. and Moeller, K. (2007) Modern SEM-based mineral liberation analysis. *International Journal of Mineral Processing* 84, 310-320.
- Fathi, S.J., Austad, T. and Strand, S. (2011) Water-based enhanced oil recovery (EOR) by "Smart Water": optimal ionic composition for EOR in carbonates. *Energy and Fuels* 25.
- Fernø, M.A., Grønsdal, R., Åsheim, J., Nyheim, A., Berge, M. and Graue, A. (2011) Use of sulfate for water based enhanced oil recovery during spontaneous imbibition in chalk. *Energy and Fuels* 25, 1697-1706.
- Flügel, E. (2004) *Microfacies of carbonate rocks : analysis, interpretation and application*. Springer, Berlin.
- Garrison, T. (2010) *Oceanography : an invitation to marine science*, 7th ed. ed. Brooks/Cole Cengage Learning, Belmont, Calif.
- Gaviglio, P., Vandycke, S., Schroeder, C., Coulon, M., Bergerat, F., Dubois, C. and Pointeau, I. (1999) Matrix strains along normal fault planes in the Campanian White Chalk of Belgium: structural consequences. *Tectonophysics* 309, 41-56.
- Geitle, K. (2013) Chemically induced compaction in fractured and intact chalk cores. University of Stavanger, Norway.
- Generosi, J., Ceccato, M., Andersson, M.P., Hassenkam, T., Dobberschütz, S., Bovet, N. and Stipp, S.L.S. (2017) Calcite wettability in the presence of dissolved Mg²⁺ and SO₄²⁻. *Energy and Fuels* 31, 1005-1014.

References

- Gómez, J., Goy, A. and Canales, M. (2008) Seawater temperature and carbon isotope variations in belemnites linked to mass extinction during the Toarcian (Early Jurassic) in Central and Northern Spain. *Palaeogeography, Palaeoclimatology, and Palaeoecology* 258, 28-58.
- Graue, A. (1994) Imaging the Effect of Capillary Heterogeneities on Local Saturation Development in Long-Core Floods. *SPEDC* 9.
- Graue, A., Moe, R.W. and Bognø, T. (2000) Oil Recovery in Fractured Reservoirs, 6th Nordic Symposium on Petrophysics, Trondheim.
- Griffiths, J. (2008) Secondary Ion Mass Spectrometry. *Analytical Chemistry* 80, 7194-7197.
- Gutierrez, M., Øino, L.E. and Høeg, K. (2000) The Effect of Fluid Content on the Mechanical Behaviour of Fractures in Chalk. *Rock Mechanics and Rock Engineering* 33, 93-117.
- Hancock, J.M. (1975) The petrology of the Chalk. *Proceedings of the Geologists Association* 86, 499-535.
- Handley, J. (2002) Product Review: Secondary Ion Mass Spectrometry. *Analytical Chemistry* 74, 335 A-341 A.
- Hattin, D.E. and Cobban, W.A. (1977) Fourth and Fifth Days Upper Cretaceous Stratigraphy, Paleontology and Paleecology of Western Kansas. *The Mountain Geologist*.
- Hedegaard, K. and Graue, A. (2011) Does Wettability Affect the Strength of Chalk?, *45th U.S. Rock Mechanics / Geomechanics Symposium*. American Rock Mechanics Association, San Francisco, California.
- Heggheim, T., Madland, M.V., Risnes, R. and Austad, T. (2005) A chemical induced enhanced weakening of chalk by seawater. *Journal of Petroleum Science and Engineering* 46, 171 - 184.
- Helland, J.O., Friis, H.A., Jettestuen, E. and Skjæveland, S.M. (2017) Footprints of spontaneous fluid redistribution on capillary pressure in porous rock. *Geophysical Research Letters* 44.
- Hellmann, R., J N Renders, P., Gratier, J.-P. and Robert Guiguet, A. (2002) *Experimental pressure solution compaction of chalk in aqueous solutions Part 1. Deformation behavior and chemistry*.
- Hermansen, H., Landa, G.H., Sylte, J.E. and Thomas, L.K. (2000) Experiences after 10 years of waterflooding the Ekofisk Field, Norway. *Journal of Petroleum Science and Engineering* 26, 11-18.
- Hermansen, H., Thomas, L.K., Sylte, J.E. and Aasboe, B.T. (1997) Twenty Five Years of Ekofisk Reservoir Management. *Society of Petroleum Engineers*.
- Hiorth, A., Cathles, L.M. and Madland, M.V. (2010) The Impact of Pore Water Chemistry on Carbonate Surface Charge and Oil Wettability. *Transport in Porous Media* 85, 1-21.

References

- Hiorth, A., Jettestuen, E., Cathles, L.M. and Madland, M.V. (2013) Precipitation, dissolution, and ion exchange processes coupled with a lattice Boltzmann advection diffusion solver. *Geochim. Cosmochim. Acta* 104, 99-110.
- Hirata, K., Saitoh, Y., Chiba, A., Yamada, K., Takahashi, Y. and Narumi, K. (2011) Secondary ion counting for surface-sensitive chemical analysis of organic compounds using time-of-flight secondary ion mass spectroscopy with cluster ion impact ionization. *Review of Scientific Instruments* 82.
- Hjelen, J. and Sintef (1989) *Scanning elektron-mikroskopi*. SINTEF, Trondheim.
- Hjuler, M.L. (2007) Diagenesis of Upper Cretaceous onshore and offshore chalk from the North Sea area, Institute of Environment & Resources. Technical University of Denmark.
- Hjuler, M.L. and Fabricius, I.L. (2009) Engineering properties of chalk related to diagenetic variations of Upper Cretaceous onshore and offshore chalk in the North Sea area. *Journal of Petroleum Science and Engineering* 68, 151-170.
- Hoefs, J. (2015) *Stable Isotope Geochemistry*, 7th ed. 2015. ed. Springer International Publishing, Berlin.
- Håkansson, E., Bromley, R. and Perch-Nielsen, K. (1975) Maastrichtian chalk of north-west Europe—a pelagic shelf sediment. *Pelagic Sediments: on Land and under the Sea*, 211-233.
- Jackson, M., Al-Mahrouqi, D. and Vinogradov, J. (2016) Zeta potential in oil-water-carbonate systems and its impact on oil recovery during controlled salinity water-flooding. *Scientific Reports (Nature Publisher Group)* 6, 37363.
- Jonas, L., Mueller, T., Dohmen, R., Baumgartner, L. and Putlitz, B. (2015) Transport-controlled hydrothermal replacement of calcite by Mg-carbonates. *Geology (Boulder)* 43, 779-782.
- Jørgensen, N.O. (1987) Oxygen and carbon isotope compositions of Upper Cretaceous chalk from the Danish sub-basin and the North Sea Central Graben. *Sedimentology* 34, 559-570.
- Kennedy, W.J. (1987) *Late Cretaceous and early Palaeocene Chalk Group sedimentation in the Greater Ekofisk area, North Sea central graben*.
- Korsnes, R.I., Hiorth, A. and Madland, M.V. (2008a) Detection of chemical processes affecting chalk mechanical strength with the use of different flooding brines at elevated temperatures, *33rd International Geological Congress*, Oslo.
- Korsnes, R.I., Madland, M.V., Austad, T., Haver, S. and Røsland, G. (2008b) The effects of temperature on the water weakening of chalk by seawater. *Journal of Petroleum Science and Engineering* 60, 183-193.
- Korsnes, R.I., Risnes, R., Faldaas, I. and Norland, T. (2006) End effects on stress dependent permeability measurements. *Tectonophysics* 426, 239-251.
- Lawrence, J.A., Mortimore, R.N., Stone, K.J. and Busby, J.P. (2013) Sea saltwater weakening of chalk and the impact on cliff instability. *Geomorphology* 191, 14-22.

References

- Levenson, Y. and Emmanuel, S. (2013) Pore-scale heterogeneous reaction rates on a dissolving. *Geochimica et Cosmochimica Acta* 119, 188 - 197.
- Lichtner, P.C., Steefel, C. I., Oelkers, E. H. (1996) *Reactive Transport in Porous Media*. Mineralogical Society of America, Washington D.C., USA.
- Longman, M., Luneau, B.A. and Landon, S.M. (1998) *Nature and distribution of Niobrara lithologies in the Cretaceous Western Interior Seaway of the Rocky Mountain region*.
- MacDonald, G.J.F. (1956) Experimental determination of calcite-aragonite equilibrium relations at elevated temperatures and pressures. *American Mineralogist* 41, 744-756.
- Madland, M., Hiorth, A., Omdal, E., Megawati, M., Hildebrand-Habel, T., Korsnes, R., Evje, S. and Cathles, L. (2011) Chemical Alterations Induced by Rock–Fluid Interactions When Injecting Brines in High Porosity Chalks. *Transport in Porous Media* 87, 679-702.
- Maury, V., Piau, J.M. and Halle, G. (1996) Subsidence induced by water injection in water sensitive reservoir rocks: The example of Ekofisk, *SPE European Petroleum Conference*, Milan, Italy, pp. 153-170.
- Megawati, M. (2015) Geochemical aspects of water-induced compaction in high-porosity chalks, Institutt for petroleumsteknologi. University of Stavanger, Faculty of Science and Technology, Department of Petroleum Engineering, Stavanger.
- Megawati, M., Andersen, P.Ø., Korsnes, R.I., Evje, S., Hiorth, A. and Madland, M.V. (2011) The effect of aqueous chemistry pH on the time dependent deformation behaviour of chalk - experimental and modeling studies, *Flows and and mechanics in natural porous media from pore to field scale. Pore2Field*, Paris.
- Megawati, M., Hiorth, A. and Madland, M.V. (2013) The Impact of Surface Charge on the Mechanical Behavior of High-Porosity Chalk. *Rock Mechanics and Rock Engineering* 46, 1073-1090.
- Megawati, M., Madland, M.V. and Hiorth, A. (2015) Mechanical and physical behavior of high-porosity chalks exposed to chemical perturbation. *Journal of Petroleum Science and Engineering* 133, 313-327.
- Milner, J. and Øxnevad, I.E.I. (1996) Spontaneous imbibition in two different chalk facies. *Petroleum Geoscience* 2, 231-240.
- Minde, M.W., Haser, S., Korsnes, R.I., Zimmermann, U. and Madland, M.V. (2017) Comparative Studies of Mineralogical Alterations of Three Ultra-long-term Tests of Onshore Chalk at Reservoir Conditions, *EAGE - 19th European Symposium on Improved Oil Recovery/IOR NORWAY 2017*, Stavanger.
- Minde, M.W., Zimmermann, U., Madland, M.V. and Korsnes, R.I. (2016) Micron and submicron investigation - what can we learn?, *IOR NORWAY 2016*, Stavanger.
- Molenaar, N. and Zijlstra, J.J.P. (1997) Differential early diagenetic low-Mg calcite cementation and rhythmic hardground development in Campanian-Maastrichtian chalk. *Sedimentary Geology* 109, 261-281.

References

- Moore, C.H. (2001) *Carbonate reservoirs : porosity evolution and diagenesis in a sequence stratigraphic framework*. Elsevier, Amsterdam.
- Morse, J.W. and Arvidson, R.S. (2002) The dissolution kinetics of major sedimentary carbonate minerals. *Earth Science Reviews* 58, 51-84.
- Mortimore, R.N., Stone, K.J., Lawrence, J. and Duperret, A. (2004) Chalk physical properties and cliff instability. *Geological Society, London, Engineering Geology Special Publications* 20, 75-88.
- Myerson, A. and Myerson, A.S. (2002) *Handbook of industrial crystallization*, 2nd ed. Butterworth-Heinemann, Boston.
- Nagel, N.B. (1998) Ekofisk Field Overburden Modelling. *Society of Petroleum Engineers*.
- Nermoen, A., Korsnes, R.I., Hiorth, A. and Madland, M.V. (2014) Insights from long term experiments of compaction and non-equilibrium water flooding of chalks, *Geological Society of London*, 2014, London.
- Nermoen, A., Korsnes, R.I., Hiorth, A. and Madland, M.V. (2015) Porosity and permeability development in compacting chalks during flooding of nonequilibrium brines: Insights from long-term experiment. *Journal of Geophysical Research: Solid Earth* 120, 2935-2960.
- Nermoen, A., Korsnes, R.I., Storm, E.V., Stødle, T., Madland, M.V. and Fabricius, I.L. (2018) Incorporating electrostatic effects into the effective stress relation — Insights from chalk experiments. *Geophysics* 33 (3).
- Newman, G.H. (1983) The Effect of Water Chemistry on the Laboratory Compression and Permeability Characteristics of Some North Sea Chalks. *Journal of Petroleum Technology* 35(05). 976-980.
- Oelkers, E.H. and Schott, J. (2009) *Thermodynamics and Kinetics of Water-Rock Interaction*. Mineralogical Society of America, Cantilly, Virginia, USA.
- Ohfuji, H. and Rickard, D. (2005) Experimental syntheses of framboids—a review. *Earth Science Reviews* 71, 147-170.
- Pedersen, J., Jettestuen, E., Madland, M.V., Hildebrand-Habel, T., Korsnes, R.I., Vinningland, J.L. and Hiorth, A. (2016) A dissolution model that accounts for coverage of mineral surfaces by precipitation in core floods. *Advances in Water Resources* 87, 68-79.
- Pedersen, J., Jettestuen, E., Vinningland, J.L. and Hiorth, A. (2014) Improved Lattice Boltzmann Models for Precipitation and Dissolution. *Transport in Porous Media* 104, 593-605.
- Piau, J.M. and Maury, V. (1994) Mechanical effects of water injection on chalk reservoirs, *Rock Mechanics in Petroleum Engineering*. Society of Petroleum Engineers, Delft, Netherlands.
- Punternvold, T. and Austad, T. (2008) Injection of seawater and mixtures with produced water into North Sea chalk formation: Impact of fluid-rock interactions on wettability and scale formation. *J. Pet. Sci. Eng.* 63, 23-33.

References

- Putnis, A., Oelkers, E.H. and Schott, J. (2009) Mineral replacement reactions. *Reviews in Mineralogy and Geochemistry* 70, 87-124.
- Putnis, A. and Putnis, C.V. (2007) The mechanism of reequilibration of solids in the presence of a fluid phase. *Journal of Solid State Chemistry* 180, 1783-1786.
- Raman, C.V. (1928) A new radiation*. *Indian Journal of Physics* 2, 387-398.
- Rhett, D.W. and Lord, C.J. (2001) Water weakening in sedimentary rocks, DC Rocks 2001, *The 38th U.S. Symposium on Rock Mechanics (USRMS)*. American Rock Mechanics Association, Washington, D.C.
- Richard, J., Sizun, J.P. and Machhour, L. (2005) Environmental and diagenetic records from a new reference section for the Boreal realm: The Campanian chalk of the Mons basin (Belgium). *Sedimentary Geology* 178, 99-111.
- Risnes, M.V., Madland, M.V., Hole, M.V. and Kwabiah, M.V. (2005) Water weakening of chalk - Mechanical effects of water-glycol mixtures. *Journal of Petroleum Science and Engineering* 48, 21-36.
- Risnes, R. (2001) Deformation and yield in high porosity outcrop chalk. *Phys. Chem. Earth Pt. A-Solid Earth Geod.* 26, 53-57.
- Risnes, R., Gjesdal, S.A., Landaas, T.L. and Madland, I. (1994) Changes in mechanical properties of chalk caused by deformation and by pore pressure, *Rock Mechanics in Petroleum Engineering*. Society of Petroleum Engineers, Delft, Netherlands.
- Roehl, P.O. and Choquette, P.W. (1985) *Carbonate petroleum reservoirs*. Springer, New York.
- Runnels, R.T. and Dubins, I.M. (1949) Chemical and petrographic studies of the Fort Hays Chalk in Kansas. *Kansas Geological Survey Bulletin* 82, 1-36.
- Sachdeva, J.S., Neramoen, Anders, Korsnes, Reidar I., Madland, Merete V., (2018) Effect of presence of oil and water on chalk mechanics, *IOR NORWAY 2018*. Stavanger, Norway.
- Sakuma, H., Andersson, M.P., Bechgaard, K., Stipp, S.L.S. and Sakuma, S.L.S. (2014) Surface tension alteration on calcite, induced by ion substitution. *Journal of Physical Chemistry C* 118, 3078-3087.
- Scholle, P.A. (1977) Chalk diagenesis and its relation to petroleum exploration; oil from chinks, a modern miracle? *AAPG Bulletin* 61, 982-1009.
- Scholle, P.A. (1978) *A color illustrated guide to carbonate rock constituents, textures, cements, and porosities*. American Ass. of Petroleum geologists, Tulsa.
- Scholle, P.A. and Kinsman, D.J.J. (1973) Diagenesis of upper Cretaceous chinks from North Sea, England and Northern Ireland. *The American Association of Petroleum Geologists Bulletin* 57, 803-804.
- Schroeder, C., Bois, A.P., Maury, V. and Halle, G. (1998) Water/Chalk (or Collapsible Soil) Interaction: Part II. Results of Tests Performed In Laboratory On Lixhe Chalk to Calibrate Water/Chalk Models, *SPE/ISRM Rock Mechanics in Petroleum Engineering*. Society of Petroleum Engineers, Trondheim, Norway.

References

- Sharma, M.A., Z. P., Fredriksen, S. B., Fernø, M. A., Graue, A. (2019) Foam for CO₂ EOR in a Carbonate Reservoir: Scale-up from Lab to Field, in: Singh, K.H., Joshi, R.M. (Ed.), *Petro-physics and Rock Physics of Carbonate Reservoirs*. Springer Singapore, Singapore.
- Skovbjerg, L.L., Hassenkam, T., Makovicky, E., Hem, C.P., Yang, M., Bovet, N. and Stipp, S.L.S. (2012) Nano sized clay detected on chalk particle surfaces.(Report). *Geochim. Cosmochim. Acta* 99, 57.
- Snow, S.E. and Brownlee, M.H. (1989) Practical and Theoretical Aspects of Well Testing in the Ekofisk Area Chalk Fields, *SPE Annual Technical Conference and Exhibition. Society of Petroleum Engineers*, San Antonio, Texas.
- Solberg, J.K. and Hansen, V. (2007) *Innføring i transmisjon elektronmikroskopi*. s.n., S.I.
- Strand, S., Hognesen, E.J. and Austad, T. (2006) Wettability alteration of carbonates - Effects of potential determining ions (Ca²⁺ and SO₄²⁻) and temperature. *Colloid Surf. A-Physicochem. Eng. Asp.* 275, 1-10.
- Sulak, R.M. and Danielsen, J. (1989) Reservoir Aspects of Ekofisk Subsidence. *Journal of Petroleum Technology* 41, 709-716.
- Surlyk, F., Damholt, T. and Bjerager, M. (2006) *Stevns Klint, Denmark: Uppermost Maastrichtian chalk, Cretaceous-Tertiary boundary, and lower Danian bryozoan mound complex*.
- Surlyk, F., Stemmerik, L., Ahlborn, M., Harlou, R., Lauridsen, B., Rasmussen, S., Schovsbo, N., Sheldon, E. and Thibault, N. (2010) *The cyclic Rordal Member - a new lithostratigraphic unit of chronostratigraphic and palaeoclimatic importance in the upper Maastrichtian of Denmark*.
- Tang, G.-Q. and Firoozabadi, A. (2001) Effect of Pressure Gradient and Initial Water Saturation on Water Injection in Water-Wet and Mixed-Wet Fractured Porous Media. *SPE Reservoir Evaluation & Engineering* 4, 516-524.
- Teufel, L.W., Rhett, D.W. and Farrell, H.E. (1991) Effect of Reservoir Depletion And Pore Pressure Drawdown On In Situ Stress And Deformation In the Ekofisk Field, North Sea. *American Rock Mechanics Association*.
- Thiel, V. (2011) Coccolithophores, in: Reitner, J. (Ed.), *Encyclopedia of Geobiology*. Springer, Dordrecht pp. 277-278.
- Torsaeter, O. (1984) An Experimental Study of Water Imbibition in Chalk From the Ekofisk Field, *SPE Enhanced Oil Recovery Symposium. Society of Petroleum Engineers*, Tulsa, Oklahoma.
- Tucker, M.E., Wright, V.P. and Dickson, J.A.D. (1990) *Carbonate sedimentology*. Blackwell, Oxford.
- Vinningland, J.L., Jettestuen, E., Aursjø, O., Madland, M.V. and Hiorth, A. (2017) *Mineral Dissolution and Precipitation Rate Laws Predicted from Reactive Pore Scale Simulations*.

References

Wang, W., Madland, M.V., Zimmermann, U., Neramoen, A., Korsnes, R.I., Bertolino, S.R.A. and Hildebrand-Habel, T. (2016) Evaluation of porosity change during chemo-mechanical compaction in flooding experiments on Liège outcrop chalk. *Geological Society, London, Special Publications* 435.

Wei, L. (2012) Sequential Coupling of Geochemical Reactions With Reservoir Simulations for Waterflood and EOR Studies. *Society of Petroleum Engineers*.

Wright, E. (1987) Stratification and paleocirculation of the Late Cretaceous Western interior seaway of North America. *Geological Society of America Bulletin* 99, pp. 480-490.

Xia, F., Brugger, J., Chen, G., Ngothai, Y., O'Neill, B., Putnis, A. and Pring, A. (2009) Mechanism and kinetics of pseudomorphic mineral replacement reactions: A case study of the replacement of pentlandite by violarite. *Geochim. Cosmochim. Acta* 73, 1945-1969.

Zhang, P., Tweheyo, M.T. and Austad, T. (2007) Wettability alteration and improved oil recovery by spontaneous imbibition of seawater into chalk: Impact of the potential determining ions Ca^{2+} , Mg^{2+} , and SO_4^{2-} . *Colloids and Surfaces A: Physicochemical and Engineering Aspects* 301, 199-208.

Zimmermann, U., Madland, M.V., Neramoen, A., Hildebrand-Habel, T., Bertolino, S.A.R., Hiorth, A., Korsnes, R.I., Audinot, J.-N. and Grysan, P. (2015) Evaluation of the compositional changes during flooding of reactive fluids using scanning electron microscopy, nano-secondary ion mass spectrometry, X-ray diffraction, and whole-rock geochemistry. *AAPG Bulletin* 99, 791-805.

Part 2

Paper I: Mineral Replacement in Long-Term Flooded Porous Carbonate Rocks

Minde, M.W., Zimmermann, U., Madland, M.V., Korsnes, R.I., Schulz, B., Gilbricht, S. (In review).
Geochimica et Cosmochimica Acta

NOT AVAILABLE IN THE BRAGE REPOSITORY

Paper II: Mineralogical alterations in calcite powder flooded with MgCl₂ to study Enhanced Oil Recovery (EOR) mechanisms at pore scale

Minde, M.W., Madland, M.V., Zimmermann, U., Egeland, N., Korsnes, R.L., Nakamura, E., Kobayashi, K., Ota, T. (In review).

Microporous and mesoporous materials

NOT AVAILBLE IN THE BRAGE REPOSITORY

Paper III: Fluid-flow during EOR experiments in chalk: insights using SEM-MLA, EMPA and nanoSIMS applications

Minde, M.W., Zimmermann, U., Madland, M.V., Korsnes, R.I., Schulz, B. and Audinot, J.-N. (2016). *SCA annual symposium, Snowmass Colorado*

NOT AVAILBLE IN THE BRAGE REPOSITORY

Paper III

Paper IV: Temperature effects on rock engineering properties and rock-fluid chemistry in opal-CT-bearing chalk

Minde, M.W., Wang, W., Madland, M.V., Zimmermann, U., Korsnes, R.I., Bertolino, S.R.A. and Andersen, P.Ø. (2018).

Journal of Petroleum Science and Engineering 169, 454-470



Contents lists available at ScienceDirect

Journal of Petroleum Science and Engineering

journal homepage: www.elsevier.com/locate/petrol

Temperature effects on rock engineering properties and rock-fluid chemistry in opal-CT-bearing chalk



Mona W. Minde^{a,b,*}, Wenxia Wang^{a,b}, Merete V. Madland^{a,b}, Udo Zimmermann^{a,b},
Reidar I. Korsnes^{a,b}, Silvana R.A. Bertolino^c, Pål Ø. Andersen^{a,b}

^a Department of Energy Resources, University of Stavanger, Norway

^b The National IOR Centre of Norway, University of Stavanger, Ullandhaug, 4036 Stavanger, Norway

^c Consejo Nacional de Investigaciones Científicas y Técnicas, Instituto de Física Enrique Gaviola, Univ. Nac. de Córdoba, Medina Allende s/n, Ciudad Universitaria, Córdoba, Argentina

ARTICLE INFO

Keywords:

Chalk
Compaction
Dissolution/precipitation
Permeability
Opal-CT
Mineralogical changes

ABSTRACT

In this study, eight tri-axial tests on Cretaceous age outcrop chalk from Aalborg have been performed systematically by injecting $MgCl_2$ for the first time at different temperatures (25, 60, 92, 110 and 130 °C) and for comparison, NaCl at 130 °C. Whole-rock geochemistry, stable isotope measurements, pycnometry, Field Emission Gun Scanning Electron Microscopy with Energy-Dispersive X-ray Spectroscopy, X-Ray Diffraction (XRD) and measurements of Specific Surface Area (Brunauer-Emmett-Teller theory (N_2)) were applied to analyse unflooded and flooded cores. Based on analyses of changes in brine composition, mineralogy, specific surface area, solid density, porosity and permeability some conclusions can be drawn on temperature effects on rock engineering properties and rock-fluid chemistry.

The $MgCl_2$ flooded cores show systematically higher creep rates at higher temperature and the cores tested at 25 and 60 °C show similar creep rates as the two NaCl flooded cores at 130 °C. All fluid-rock interactions were more pronounced at higher temperature. After flooding with $MgCl_2$ at 110 and 130 °C newly formed magnesite is observed. In the cores tested at 25, 60 and 92 °C magnesite crystals have not been positively identified, but minute increases in MgO in whole-rock geochemistry analyses are seen. Si^{4+} originating from the dissolution of silica bearing phases (mainly diagenetic opal-CT), has taken part in the re-precipitation of Si-Mg-bearing minerals during $MgCl_2$ injection from 25 to 130 °C, leading to an increase of the specific surface area. This is partly balanced by opal-CT dissolution, which should lower the specific surface area. The flaky Si-Mg-bearing minerals, covering significant portions of the pore surfaces and throats are the main drivers to reduce permeability in cores flooded at high temperatures. Additionally, in NaCl flooded cores where mineralogical changes are minute, the dissolution of parts of the existing opal-CT has lowered the SSA. At high temperatures, the following chemical changes must be carefully acknowledged when porosity reduction is calculated: calcite and opal-CT dissolution and precipitation of new minerals, particularly Mg-bearing minerals. The presence of opal-CT strongly influences the mineralogical alterations in flooded cores, hence the geo-mechanical evolution.

1. Introduction

Fluid injection into hydrocarbon reservoirs is one of the most often used methods for Enhanced Oil Recovery (EOR). The chemical fluid-rock interplay and induced changes in mechanical and petrological properties have led to research towards finding more optimal injection fluids and possibilities of applying optimized water on field scale (André et al., 2007; Hermansen et al., 2000). The relationships between mechanical properties of reservoir chalk and pore fluids have been of

significant interest in scientific research and in industry since the Ekofisk field encountered severe subsidence effects, recognized in the 1980s (Hermansen et al., 1997, 2000; Korsnes et al., 2006a; b; 2008; Kristiansen et al., 2005; Madland et al., 2008, 2011; Nagel, 2001; Newman, 1983; Risnes and Flaageng, 1999; Risnes et al., 2005).

Chalk compaction can be affected by effective stresses, pore fluid compositions and testing temperatures (Korsnes et al., 2008; Madland et al., 2011; Megawati et al., 2013; Neramoen et al., 2016). Chemical reactions involving Mg^{2+} causes calcite dissolution and magnesite

* Corresponding author. Department of Energy Resources, University of Stavanger, Norway.

E-mail addresses: mona.w.minde@uis.no (M.W. Minde), wenxia.wang@uis.no (W. Wang), merete.v.madland@uis.no (M.V. Madland), udo.zimmermann@uis.no (U. Zimmermann), reidar.i.korsnes@uis.no (R.I. Korsnes), silvanarbertolino@gmail.com (S.R.A. Bertolino), pal.andersen@uis.no (P.Ø. Andersen).

<https://doi.org/10.1016/j.petrol.2018.05.072>

Received 22 January 2018; Received in revised form 17 April 2018; Accepted 28 May 2018

Available online 02 June 2018

0920-4105/ © 2018 Elsevier B.V. All rights reserved.

List of parameters	
<i>D</i>	Core diameter, mm
<i>K_i</i>	Initial permeability, mD
<i>L</i>	Core length, mm
<i>M</i>	Mass, g
<i>V</i>	Volume, cm ³
$\delta^{13}\text{C}$	A measure of the ratio of stable isotopes ¹³ C and ¹² C, ‰
$\delta^{18}\text{O}$	A measure of the ratio of stable isotopes ¹⁸ O and ¹⁶ O, ‰
ϵ	Axial creep strain, %
<i>P</i>	Solid density, cm ³ /L
ρ_w	Brine density, cm ³ /L
Φ	Porosity, %
Subscripts	
<i>Core</i>	Based on the core piece
<i>Dry</i>	Dry sample
<i>End</i>	State after compaction-flooding tests
<i>i</i>	Initial/unflooded state
<i>Sat</i>	Saturated sample
<i>Vol</i>	volume
<i>P</i>	Pore
<i>S</i>	solid
Abbreviations	
<i>Na130</i>	NaCl-flooded core at 130 °C for 60 days (corresponding to the unflooded core <i>Na130-U</i>)
<i>Mg25</i>	MgCl ₂ -flooded core at 25 °C for 61 days (corresponding to the unflooded core <i>Mg25-U</i>)
<i>Mg60</i>	MgCl ₂ -flooded core at 60 °C for 62 days (corresponding to the unflooded core <i>Mg60-U</i>)
<i>Mg92</i>	MgCl ₂ -flooded core at 92 °C for 60 days (corresponding to the unflooded core <i>Mg92-U</i>)
<i>Mg110</i>	MgCl ₂ -flooded core at 110 °C for 66 days (corresponding to the unflooded core <i>Mg110-U</i>)
<i>Mg130</i>	MgCl ₂ -flooded core at 130 °C for 61 days (corresponding to the unflooded core <i>Mg130-U</i>)
b.d.l.	Below detection limit
BET	Brunauer-Emmett-Teller theory
DI-H ₂ O	Deionized water
DW	Distilled water
EDS	Energy-dispersive X-ray spectroscopy
FEG-SEM	Field emission gun – scanning electron microscopy
FEP	Fluorinated ethylene propylene
HPLC	High performance liquid chromatography
ICP-MS	Inductively coupled plasma – mass spectrometry
ICS	Ion chromatography system
LOI	Loss on ignition
<i>LNa130</i>	NaCl-flooded Aalborg core at 130 °C for 118 days (corresponding to the unflooded core <i>LNa130-U</i>)
<i>LMg130</i>	MgCl ₂ -flooded Aalborg core at 130 °C for 115 days (corresponding to the unflooded core <i>LMg130-U</i>)
LVDT	Linear variable displacement transducer
PID	Proportional integral derivative
PPM	Part per million
PV	Pore volume
SSA	Specific surface area, m ² /g
sup. mat	Supplementary material
TDS	Total dissolved solids, g/L
TEM	Transmission electron microscopy
TOT/C	Total carbon, %
wt%	Weight percent
XRD	X-Ray diffraction

precipitation during MgCl₂ injection at 130 °C (Andersen et al., 2017; Madland et al., 2011; Megawati et al., 2015; Wang et al., 2016; Zimmermann et al., 2013, 2015). As temperatures increase, dissolution and precipitation effects increase when injecting seawater (Korsnes et al., 2008; Zhang et al., 2007) or MgCl₂ (Nermoen et al., 2016) into chalk. Nermoen et al. (2016) observed that with MgCl₂ injection in outcrop chalk from Obourg St. Vaast (Mons, Belgium) chalk, higher compaction was obtained at 130 °C than at 92 °C. Moreover, authors propose that the rate of deformation changes with temperature and is linked to chemical alteration (Hellmann et al., 2002). We also refer to Andersen et al. (2012, 2017), Andersen and Evje (2016) and Evje et al. (2009) for modelling works that couple geochemical reactions with transport to interpret core flooding tests in both pure and impure chalks.

Several authors (Andersen et al., 2017; Fabricius, 2001; Fabricius et al., 2007; Hjuler, 2007; Hjuler and Fabricius, 2009; Madland et al., 2011; Megawati et al., 2011) have highlighted the importance of investigating the role of non-carbonate minerals in brine-chalk systems. Madland et al. (2011) tested outcrop chalk from Liège (Belgium), flooded with 0.1095 mol/L MgCl₂ for ~ 17 days. Silicate minerals dissolved and re-precipitated forming a new silicate mineral phase, containing magnesium, with a clay-like appearance observed in SEM images. Nermoen et al. (2016) emphasized that geochemical analyses were required to investigate more alteration details, particularly the role of silicates. High temperature as a primary factor can also increase silica dissolution (Fournier, 1973) and an increase in brine salinity can substantially increase silica dissolution rate during chemical EOR processes (Elraies and Basbar, 2015).

Outcrop chalk collected close to Aalborg (Denmark), which is typically characterised by a relatively high non-carbonate content

compared to other onshore chalks (Hjuler and Fabricius, 2009), indicated by a higher SiO₂ content, shows a complex behaviour in chemo-mechanical experiments (Andersen et al., 2017; Megawati et al., 2015). This is, in particular, related to the abundance of opal-CT (SiO₂·nH₂O), instead of the stable mineral quartz (SiO₂), which dominates the non-carbonate content in other outcrop chalks, such as chalks exposed close to Liège, and in the Midwest of the USA (Kansas and Colorado) (Andersen et al., 2017; Hjuler and Fabricius, 2009; Madland et al., 2011; Megawati et al., 2015; Wang et al., 2016). Even though the North Sea reservoir chalk does not typically contain much opal-CT, it is argued that opal-CT is the source for abundant quartz, mainly occurring as chert (as nodules or bands), created through diagenetic processes (Bromley, 1968; Fabricius and Borre, 2007; Hjuler, 2007). Therefore, one of the objectives of this study is to investigate how opal-CT behaves in porous media, under different temperatures.

Due to shortage of core material, laboratory tests are rarely carried out on reservoir rocks from hydrocarbon deposits in the North Sea, but are commonly performed on on-shore chalk. Chalk from exposures is used to gain information during specific engineering tests with injection of fluids with different compositions. Systematic investigations on reservoir cores are generally expensive and difficult due to issues with core-to-core heterogeneity, cleaning, preservation and sample sizes. For fundamental studies, therefore, the application of outcrop samples, preferably drilled from the same block, gives sufficient information for further research and is paramount for all modelling exercises in this field of research. Reservoir conditions can then be mimicked by selecting samples of comparable mineralogy as reservoir chalk, applying similar fluid compositions, pressure and temperature as found in the reservoir. Such studies contribute in the understanding of EOR processes related to injection of fluids not only for the North Sea reservoirs,

but also for comparable geological settings worldwide.

In this study, we present data from cores drilled out of Cretaceous successions at Aalborg (Denmark), a possible geo-mechanical analogue to North Sea reservoir chalk (Hjuler and Fabricius, 2009), using $MgCl_2$ and NaCl as injection brines with focus on the role of temperature when performing identical flooding - compaction tests at different temperatures. Subsequently, we present the resulting rock mechanical parameters, porosity and permeability and elucidate geochemical and mineralogical changes. The aim of this study is to observe and interpret the chemo-mechanical effects during systematic tri-axial tests with $MgCl_2$ injection at 25, 60, 92 (Valhall reservoir temperature), 110 and 130 °C (Ekofisk reservoir temperature) and NaCl injection at 130 °C for the sake of comparison. As NaCl has been considered to be an inert fluid when flooding chalk, the NaCl-tests at 130 °C were performed as benchmark tests, and variations when flooding NaCl with different temperatures is therefore outside the scope of this paper.

2. Experimental procedures and methods

2.1. Core properties and injection brines

Large chalk blocks were sampled from the Rørdal quarry in Aalborg (Denmark) and eight cores were drilled from these blocks for use in this study. The Aalborg chalk was studied earlier in detail regarding petrology, mineralogical and rheological characteristics (Hjuler, 2007; Hjuler and Fabricius, 2009; Lauridsen et al., 2011; Stenestad, 2006; Surlyk et al., 2010). For identification purposes, the cores have been named with the following notations: Na: Flooded with NaCl, Mg: Flooded with $MgCl_2$, numbers indicating which temperature the experiment was conducted under and L: noting the cores flooded a prolonged time, i. e. for close to 120 days, while all other cores were flooded for ~60 days. Cores-samples denoted -U, points to the unflooded end-pieces of the original cores (Fig. 1a). The flooding rate for all experiments were chosen to approximately one initial pore-volume per day. This is slightly lower than, but comparable to, water-injections rates at field-scale with typical values of 1 ft/day = 0.3048 m/day (Green and Willhite, 1998).

Core properties, prior to flooding (denoted by i), such as length (L_i), diameter (D_i), dry mass ($M_{dry,i}$), saturated mass ($M_{sat,i}$), permeability (k_i), porosity (ϕ_i), solid density (ρ_i) and specific surface area (SSA_i) together with flooding time, and flooding rate are summarized in Table 1. The initial porosity (ϕ_i) was calculated by the difference in saturated and dry mass ($M_{sat,i}$ and $M_{dry,i}$, respectively) divided by the density of distilled water (ρ_{dw}) and initial bulk volume ($V_{b,i}$):

$$\phi_i = \frac{(M_{sat,i} - M_{dry,i})}{\rho_{dw} V_{b,i}} \quad (1)$$

The range was 46.8%–47.9%. The initial permeability (k_i) was measured when the hydrostatic loading started, with values in the range of 0.9–2.5 mD. The initial specific surface area (SSA_i), measured on unflooded end pieces (see Fig. 1a), varies between 3.7 m²/g and 4.9 m²/g, correlating positively with the abundance of SiO₂. The solid volumes of unflooded material (end pieces, Fig. 1a) were measured by pycnometry and used to calculate solid densities (ρ_i) of the pieces ranging from 2.62 to 2.68 g/cm³, slightly lower than the density of calcite (2.71 g/cm³), implying the presence of a lighter phase, opal-CT ($\rho = 1.9 - 2.3$ g/cm³). The solid density ($\rho_{core,i}$) of the whole cores which are to be used for flooding (Fig. 1a) was also calculated by Eq. (2):

$$\rho_{core,i} = \frac{M_{dry,i}}{V_{b,i} - (M_{sat,i} - M_{dry,i})/\rho_w} \quad (2)$$

The densities ($\rho_{core,i}$), calculated based on bulk volume $V_{b,i}$ along with dry and saturated masses ($M_{dry,i}$ and $M_{sat,i}$, respectively) and the density of water (ρ_w), are similar to the pycnometry measurements (ρ_i) in cores Mg25-U, Mg60-U, LMg130-U and LNa130-U, but slightly lower in cores Mg92-U ($\rho = 0.01$ g/cm³), Mg110-U ($\rho = 0.05$ g/cm³), Mg130-

U ($\rho = 0.02$ g/cm³) and Na130-U ($\rho = 0.03$ g/cm³). These deviations can be attributed to the higher amount of uncertainties for whole core calculations, introduced by the large amount of parameters.

2.2. Flooding experiments in standard tri-axial cells

Cylindrical samples were drilled from collected outcrop material. Each sample was divided axially into three parts (Fig. 1a). The central parts were shaped to cylindrical cores with one of two diameters ~37.0 or ~38.1 mm with a length of ~70.0 mm and used for flooding-compaction tests. The two adjacent parts were used for analysis of unflooded material (Fig. 1a).

The cores have a length to diameter ratio close to two as such that their strength can be expected to be insensitive to differences in diameter (see e.g. Fig. 7.2 in Fjær et al., 2008). After preparation, the cores were dried for 12 h in a heating chamber at 100 °C to remove the water before the dry mass was determined. The mineralogy is not affected by the drying conditions (MacDonald, 1956). The cores were then evacuated by vacuum prior to being saturated with distilled water and weighed to obtain the saturated mass. The same experimental procedure was used on all cores. The saturated cores were mounted into identical tri-axial cells. For detailed set-up of the cells, the reader is referred to Andersen et al., 2017. To isolate the cores from the confining oil, a heat shrinkage sleeve (1- 1/2" FEP with diameter of 33 – 43 mm and 0.5 mm wall thickness) was installed between the core and the confining oil. After mounting the core, the confining pressure was increased to 0.5 MPa. Thereafter the experiments were conducted according to the following stages:

1. The samples were flooded with three pore volumes (PVs) of distilled water (DW) overnight at ambient temperature to clean the sample before the flooding test. This flooding procedure does not significantly alter the geochemical measurements of the core.
2. Change from flooding with DW to $MgCl_2$ or NaCl by attaching the piston cell into the flow loop. The ion compositions of the injected brines are shown in Table 2. Throughout the rest of the test, the flow rate was set to 1 initial PV per day.

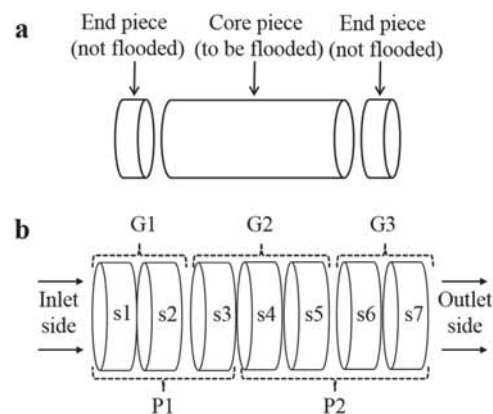


Fig. 1. (A): Material selection procedure: A cylindrical sample is cut into 3 pieces: the central core to be used in flooding-compaction tests and two adjacent end pieces used to measure properties of unflooded material, assumedly also representative of the core. (b): Scheme of the sectioning of the core after the flooding-compaction tests. The cores were cut to two parts (P1, P2) before cut to seven slices (s1, s2 ... s7). The inlet is at s1 and the outlet is at s7 (arrows indicate flow direction). The two parts (P1, P2) and slices, grouped into G1 (s1 + s2), G2 (s3 + s4 + s5), and G3 (s6 + s7), were measured by pycnometry. The specific surface area was measured using material from slices s1, s3 and s7.

Table 1

Geo-mechanical properties of the cores applied in the tests before flooding. ' L_i ', initial length (mm); ' D_i ', initial diameter (mm); $M_{sat,i}$ and $M_{dry,i}$ are saturated and dry mass (g) before flooding, respectively; ' SSA_i ', initial specific surface area before flooding (m^2/g); ' k_i ', the initial permeability (mD); ' ϕ_i ', initial porosity (%), ' ρ_i ', initial solid density (g/cm^3) of unflooded material measured by pycnometry and $\rho_{core,i}$ initial solid density (g/cm^3) of whole cores; This difference between ρ_i and $\rho_{core,i}$ might be caused by differences in the vacuum pressure when saturating the cores with distilled water. Flooding rate was 1 pore volume (PV)/day.

Core	L_i	D_i	$M_{sat,i}$	$M_{dry,i}$	Flooding time	Flooding rate	k_i	ϕ_i	ρ_i	$\rho_{core,i}$	SSA_i
	(mm)	(mm)	(g)	(g)	(days)	(ml/min)	(mD)	(%)	(g/cm^3)	(g/cm^3)	(m^2/g)
Mg25-U	71.8	37	143.52	106.62	61	0.026	5.24	47.9	2.65	2.65	4.3
Mg60-U	72.6	37	146.79	110.28	62	0.025	3.46	46.8	2.66	2.66	3.7
Mg92-U	69.2	38.1	147.79	110.74	60	0.026	2.58	47.1	2.66	2.65	4.8
Mg110-U	69.4	37.1	138.44	102.93	66	0.025	2.93	47.4	2.66	2.61	4.8
Mg130-U	70.4	38.1	150.18	112.33	61	0.026	1.52	47.2	2.67	2.65	3.8
LMg130-U	75	38.1	160.43	119.84	115	0.028	1.34	47.5	2.67	2.67	4.9
Na130-U	70.4	38.2	150.64	112.96	60	0.026	2.35	46.9	2.67	2.63	4.5
LNNa130-U	70.4	37	142.14	106.17	118	0.025	1.79	47.5	2.68	2.68	4.5

Two brines were used for core flooding: 0.219 mol/L $MgCl_2$ and 0.657 mol/L NaCl, (see Table 2). The ionic strength (0.657) was kept the same as in North Sea seawater.

Table 2

Injected brine composition for tests. TDS = total dissolved solids.

Brine	Cl^-	Mg^{2+}	Na^+	Ion strength	TDS
	(mol/L)	(mol/L)	(mol/L)		
$MgCl_2$	0.438	0.219	0	0.657	20.84
NaCl	0.657	0	0.657	0.657	38.4

- The confining pressure and pore pressure were increased simultaneously to 1.2 and 0.7 MPa, respectively before the temperature was raised to the chosen values. The pore pressure and temperature were subsequently kept constant throughout the test.
- The confining pressure was increased from 1.2 MPa by injecting hydraulic oil at a constant flow rate into the confining chamber using pump 2. During pressurization the piston pressure was set to 0.5 MPa to overcome friction of the piston (0.3 – 0.4 MPa). This increased the axial stress to a value of 0.1 – 0.2 MPa above the radial stress. Because the additional axial stress is small compared to the radial stress, the stress condition can be considered near hydrostatic. The axial strain was measured by an external axial linear variable displacement transducer (LVDT) placed on top of the piston to monitor the sample length with time. The stress-strain behaviour was monitored during the increase in confining pressure. When the rock began to deform plastically, i.e. when the stress strain behaviour became non-linear, the stress at onset of yield was noted until the confining pressure was increased over yield point. The confining pressure was further increased to the chosen creep stress (between 8 and 12 MPa) before the cores were left to compact in the following creep phase (deformation at constant stress).
- The axial deformation at constant temperature and pressure conditions (termed creep) was monitored during continuous flooding of $MgCl_2$ -or NaCl-brine. The pore pressure and confining pressure varied within 0.1 MPa such that the effective stresses were stable throughout the test period.

The pore pressure, hydraulic pressure difference, confining pressure, piston pressure, sample length (axial strain) and flooding time were logged continuously via a LabView program. Before dismantling the core, the sample was cleaned by injection of minimum three PVs of distilled water to avoid precipitation of salts from $MgCl_2$ -or NaCl-brines during drying. The saturated weight ($M_{sat,end}$) was measured immediately after the dismantling of the cell. Then the core was placed in the drying cabinet at 100 °C and weighed several times until the dry mass ($M_{dry,end}$) stayed constant. All experiments have been performed in the same way such that the temperature dependent behaviour can be identified. The basic core details before and after flooding are collected

in Tables 1, 3–5. Each core was cut to two parts (P1: Part one, to be cut into slice 1, 2 and 3; P2: Part two, to be cut into slice 4, 5, 6, 7, Fig. 1b) to measure the average core solid density ($\rho_{core,avg}$) before cut into the mentioned seven slices (s1, s2, s3, s4, s5, s6 and s7) using a Struers Discotom-5 cutting machine (see Fig. 1b for the sectioning scheme). The slices were used for geological analyses to identify chemical and mechanical changes along the core.

2.3. Field emission gun-scanning electron microscopy (FEG-SEM)

Fresh surfaces from each slice were analysed using a Zeiss Supra 35 VP field emission gun scanning electron microscope (FEG-SEM) in high vacuum mode with an accelerating voltage of 15 kV (occasionally lowered for high resolution images), aperture size of 30 μm , and working distance of 10 – 12 mm. To ensure a steady flux of electrons, the samples were coated with palladium with an Emitec K550 sputtering device. EDAX (Company name) Genesis energy-dispersive X-ray spectroscopy (EDS) was used for determining the mineralogical and elemental composition of the chalk samples. Because the chalk dominantly consists of calcite, the EDS system was calibrated using an Iceland spar calcite crystal. EDS measurements are not presented as independent results, but used as a complementary analysis for changes in elemental composition in the cores and identification of minerals imaged by FEG-SEM.

2.4. X-ray diffraction (XRD)

X-Ray Diffraction patterns were obtained from grinded bulk samples of unflooded material and the different slices of flooded cores (Sup. Mat. Fig. 9). The analyses were performed by using a Bruker D5005 diffractometer (Cu-K α radiation, 40 kV, 40 mA, 0.02° step, at 1 s per step), at the Institute of Earth Sciences Jaume Almera (ICTJA, Barcelona, Spain), together a Philips X'Pert PRO PW 3040/60 diffractometer (Cu-K α x-ray radiation, Si monochromator, 40 kV and 30 mA, step scan at $\sim 1.5^\circ$ /minute, step size of 0.02° 2 θ) at the Facultad de Ciencias Químicas (Universidad Nacional de Córdoba, Argentina), and a with a Bruker D8 ADVANCE ECO diffractometer with a Lynxeye detector (Cu-K α radiation 1.5406 K α 1, 40 kV 25 mA, 0.6 mm receiving slit, 0.01° step, at 0.2 s per step) at the University of Stavanger. The measurements were repeated in certain samples to evaluate the reproducibility of the results; particularly for cases involving newly formed trace minerals. The used amount for measurements was approximately 1 g.

2.5. Whole-rock geochemistry

Representative sample material from each slice was carefully separated from the core and milled to a very fine mesh in a clean agate

mill. Geochemical data were obtained by Inductively Coupled Plasma-Mass Spectrometry (ICP-MS) analysis at Acme laboratory (Vancouver, Canada). Details for the analytical method and processing is compiled here: The milled sample was mixed with $\text{LiBO}_2/\text{Li}_2\text{B}_4\text{O}_7$ flux in crucibles and fused in a furnace. The cooled bead was dissolved in the American Chemical Society (ACS) grade nitric acid and analysed by ICP-MS. Loss on ignition (LOI) was determined by igniting a sample split then measuring the weight loss: A 1 g sample was weighed into a tarred crucible and ignited to 1000 °C for 1 h, then cooled and weighed again. The loss in weight is the LOI of the sample. Total Carbon and Sulphur were determined by the Leco method. Here, induction flux was added to the prepared sample then ignited in an induction furnace. A carrier gas sweeps up released carbon to be measured by adsorption in an infrared spectrometric cell. Results are total concentrations and attributed to the presence of carbon and sulphur in all components. An additional 14 elements were measured after dilution in Aqua Regia. The prepared sample was digested with a modified Aqua Regia solution of equal parts concentrated HCl, HNO_3 , and $\text{DI-H}_2\text{O}$ for 1 h in a heating block or hot water bath. The sample volume was increased with dilute HCl-solutions and splits of 0.5 g were analysed. None of the measured concentrations was too far above the possible detection limit, but in standard range, and accuracy and precision are between 2–3%.

2.6. Stable isotope geochemistry (C-O isotope)

Isotope analyses were performed at the University of Edinburgh geological lab and reported by $\delta^{13}\text{C}_{\text{SMOW}}$ and $\delta^{18}\text{O}_{\text{SMOW}}$ (isotope ratios with reference to standard mean ocean water (SMOW) composition in Vienna Pee Dee Belemnite). Oxygen and carbon stable isotope analyses were performed on crushed 0.5 – 1.0 mg sub-samples. The carbonate powder was reacted with 100% orthophosphoric acid at 90 °C in an ISOCARB automatic carbonate preparation system. The resulting CO_2 was then analysed on a VG Isogas PRISM III stable isotope ratio mass spectrometer. The standard deviation ($n = 24$) of a powdered coral laboratory standard (CORID, $\delta^{13}\text{C} = -0.647$, $\delta^{18}\text{O} = -4.920$) run as a sample on the same days as the study samples, was $\pm 0.07\text{‰}$ for $\delta^{13}\text{C}$ and $\pm 0.08\text{‰}$ for $\delta^{18}\text{O}$.

2.7. Ion chromatography

During the flooding experiment, the effluent samples were collected for chemical comparison between the produced and injected water. The ionic concentrations were analysed with a Dionex Ion Chromatography System (ICS)-3000 ion-exchange chromatograph. The analyses were performed with ICS 3000 CD Conductivity Detector. IonPac AS16 and IonPac CS12A were used as anion and cation exchange columns, respectively. The sampled effluents were diluted (Gilson, GX-271) to stay in the linear region of the calibration curve and ionic concentrations were calculated based on an external standard method. The following ion concentrations were quantified: Mg^{2+} , Na^+ , Cl^- and Ca^{2+} .

2.8. Inductively coupled plasma-atomic emission spectroscopy (ICP-AES)

The Inductively coupled plasma (ICP) analyses of effluents for measuring Si^{4+} concentrations were performed using the Optima 4300 DV inductively coupled plasma optical emission spectrometry (ICP-OES) detector instrument from Perkin Elmer. The samples were prepared by separating approximately 1 mL of the fluid before dilution. The method detection limit (MDL) for the analysis of Si^{4+} on the machine (University of Stavanger) is 0.3 mg/L.

2.9. Pycnometry

The solid volume was measured with an AccuPyc II 1340 gas pycnometer that measures the amount of displaced helium gas within a porous rock sample. The dry sample was placed into the volume

chamber where helium gas molecules rapidly fills the pores enabling measurement of the solid volume filled by the sample. A chamber of 35 cm^3 was selected to provide the best fit with the samples. Based on the measured solid volume and dry mass, estimates of the average mineral densities were obtained. The pycnometry measurements represent a complimentary way of estimating the porosity, in addition to the porosity estimate from the difference between the dry and DW-saturated cores.

2.10. Specific surface area (SSA)

Specific surface area on grinded bulk chalk samples was measured by Micromeritics' TriStar II surface area and porosity analyser and the data was calculated by TriStar II 3020 Software. Each sample was weighed and inserted into a sample tube before the dry sample tube was then carefully connected to vacuum until the vacuum had stabilized (20–30 mTorr). The sample tube was submerged in liquid nitrogen (N_2) to cool the sample during the measurement. At increased partial pressures, nitrogen gas fills a greater area of the micro-pores adsorbing as a monolayer on the surface of the grains. The change in pressure is a measure of the amount of gas adsorbed, thus the surface area of the sample. Given the sample weight as input, the program can calculate the specific surface area of the sample by the Brunauer–Emmett–Teller (BET) theory (Brunauer et al., 1938).

2.11. Porosity estimation

Porosity development within the brine-chalk system can be described by considering mass exchange and mechanical compaction (Nermoen et al., 2015; Wang et al., 2016). In this study, we focus on the porosity estimation after flooding; therefore, we apply the methods proposed by Wang et al. (2016), which will be summarized below.

After the experiment was finished and the core dismantled, the diameter (D_j) was measured at intervals (L_j) along the core to estimate the total bulk volume ($V_{b, \text{end}}$) from the sum of contributions from each slice $j = 1, 2 \dots 7$:

$$V_{b, \text{end}} = \sum_j \frac{L_j \pi}{12} ((D_j)^2 + (D_j D_{j+1}) + (D_{j+1})^2) \quad (3)$$

The above formula assumes diameters D_j and D_{j+1} are measured at the end faces of slice j (see Fig. 1b) and that the diameter varies linearly in between. The overall change in bulk volume between initial volume ($V_{b, i}$) and the volume after testing ($V_{b, \text{end}}$, from Eq. (3)) was used to estimate the total volumetric strain ϵ_{vol} :

$$\epsilon_{\text{vol}} = \frac{V_{b, i} - V_{b, \text{end}}}{V_{b, i}} \quad (4)$$

End porosity is, by definition, the ratio of pore (p) and bulk (b) volume, where each end volume equals the original volume plus the volume change after testing:

$$\phi_{\text{end}} = \frac{V_{p, i} + \Delta V_p}{V_{b, i} + \Delta V_b} = \frac{V_{p, i} + \Delta V_b - \Delta V_s}{V_{b, i} + \Delta V_b} = \frac{\phi_i - \epsilon_{\text{vol}} - \frac{\Delta V_s}{V_{b, i}}}{1 - \epsilon_{\text{vol}}} \quad (5)$$

The change in solid volume is not directly measured, thus porosity will be estimated as discussed in the following.

If all deformation is accommodated by pore volume reduction and the solid volume (s) remains constant ($\Delta V_s = 0$, i.e. $\Delta V_b = \Delta V_p$) (assuming incompressible mineral grains, and either no rock-fluid interactions or that the alteration of mineral density and transport processes preserve the mineralogical mass) then the porosity estimate after flooding is described by:

$$\phi_{\text{end}, 1} = \frac{V_{p, i} + \Delta V_b}{V_{b, i} + \Delta V_b} = \frac{\phi_i - \epsilon_{\text{vol}}}{1 - \epsilon_{\text{vol}}} \quad (6)$$

As stated, this is theoretically the porosity of the rock, if the solid

Table 3

Geochemical analyses, solid density (in two parts and three groups, g/cm³, Fig. 1), difference between the current density and average density (2.66 g/cm³, in bold, italic), specific surface area measurement (m²/g) and difference between current SSA and initial average SSA, (a) NaCl flooded cores, (b) MgCl₂ flooded cores. The abbreviations are 'PPM' for part per million 'wt%' for weight percent, 'T', temperature estimation, °C, and 'TOT/C' total carbon, 'I.S.': not analysed because of insufficient sample for analyses after cutting, *: not analysed by the given method or not applicable. For each unflooded sample, δ¹³C_{SMOW} and δ¹⁸O_{SMOW} respectively are average of two measurements. SMOW (standard mean ocean water) is given in per mil (‰). Temperatures have been calculated after Anderson and Arthur (1983) with salinity values by Wright (1987).

(a) NaCl flooded	SiO ₂	MgO	CaO	δ ¹³ C SMOW	δ ¹⁸ O SMOW	T	SSA	ΔSSA	sample	ρ _{end}	sample	ρ _{end}
	(wt%)	(wt%)	(wt%)	(‰)	(‰)	(°)	m ² /g	m ² /g		g/cm ³		g/cm ³
Na130-U	5.0	0.4	52.1	2.1	-1.3	17.3	4.5	*	Na130-U	2.67	Na130-U	2.67
Na130-1	2.4	0.5	53.9	2.2	-1.4	17.7	2.1	-2.3	Na130-P1	2.68	Na130-G1	2.67
Na130-2	2.4	0.5	53.6	2.1	-1.5	18.1	*	*		(+ 0.02)		(+ 0.01)
Na130-3	4.5	0.5	52.4	2.2	-1.4	17.7	4.0	-0.4			Na130-G2	2.67
Na130-4	6.0	0.4	51.2	2.1	-1.5	18.1	*	*	Na130-P2	2.67		(+ 0.01)
Na130-5	4.4	0.5	52.2	2.2	-1.4	17.7	*	*		(+ 0.01)		
Na130-6	6.1	0.4	51.0	2.1	-1.5	18.1	*	*			Na130-G3	2.65
Na130-7	5.9	0.4	51.5	2.1	-1.5	18.1	4.6	+0.2				(-0.01)
LNa130-U	4.8	0.4	52.4	2.1	-1.0	16.0	4.5	*	LNa130-U	2.68	LNa130-U	2.68
LNa130-1	2.0	0.4	52.3	2.1	-1.2	16.8	1.8	-2.6	LNa130-P1	2.69	LNa130-G1	2.69
LNa130-2	3.0	0.4	51.5	2.1	-1.4	17.7	*	*		(+ 0.03)		(+ 0.03)
LNa130-3	1.9	0.5	55.4	2.1	-1.4	17.7	2.1	-2.3			LNa130-G2	2.68
LNa130-4	2.9	0.4	53.8	2.1	-1.4	17.7	*	*	LNa130-P2	2.68		(+ 0.02)
LNa130-5	7.9	0.4	50.5	2.2	-1.3	17.3	*	*		(+ 0.02)		2.68
LNa130-6	5.1	0.4	52.1	2.2	-1.3	17.3	*	*			LNa130-G3	2.68
LNa130-7	4.1	0.4	52.6	2.1	-1.3	17.3	3.8	-0.6				(+ 0.02)
(b) MgCl ₂ flooded	SiO ₂	MgO	CaO	δ ¹³ C SMOW	δ ¹⁸ O SMOW	T	SSA	ΔSSA	sample	ρ _{end}	sample	ρ _{end}
	(wt%)	(wt%)	(wt%)	(‰)	(‰)	(°)	m ² /g	m ² /g		g/cm ³		g/cm ³
Mg25-U	4.5	0.4	53.6	2.2	-0.9	15.6	4.3	*	Mg25-U	2.65	Mg25-U	2.65
Mg25-1	3.5	0.7	53.1	2.3	-1.1	16.3	6.1	+1.7	Mg25-P1	2.66	Mg25-G1	*
Mg25-2	3.5	0.5	53.2	2.1	-1.2	16.7	*	*		(0.00)		
Mg25-3	3.7	0.5	53.5	2.2	-0.9	15.7	4.5	+0.1			Mg25-G2	*
Mg25-4	3.8	0.5	53.1	2.3	-0.9	15.8	*	*	Mg25-P2	2.65		
Mg25-5	4.4	0.5	52.3	2.3	-1.0	16.1	*	*		(-0.01)		
Mg25-6	3.5	0.5	53.2	2.3	-1.0	16.0	*	*			Mg25-G3	*
Mg25-7	5.0	0.5	52.3	2.3	-1.0	16.1	3.9	-0.5				
Mg60-U	3.5	0.4	53.1	1.9	-1.3	17.3	3.7	*	Mg60-U	2.66	Mg60-U	2.66
Mg60-1	3.5	1.4	51.9	2.2	-0.8	15.2	6.7	+2.3	Mg60-P1	2.69	Mg60-G1	2.69
Mg60-2	3.7	0.7	52.7	2.2	-1.0	16.2	*	*		(+0.03)		(+0.03)
Mg60-3	4.6	0.6	52.5	2.3	-0.9	15.7	6.4	+2.0			Mg60-G2	2.68
Mg60-4	5.5	0.5	52.0	2.2	-1.0	16.1	*	*	Mg60-P2	2.69		(+0.02)
Mg60-5	3.6	0.5	53	2.1	-1.2	17.0	*	*		(+0.03)		
Mg60-6	3.4	0.5	53.1	2.1	-1.0	16.1	*	*			MgMg60-G3	2.69
Mg60-7	3.2	0.5	53.1	2.3	-1.0	16.2	3.6	-0.8				(+0.03)
Mg92-U	4.1	0.4	52.6	2.1	-1.3	17.3	4.8	*	Mg92-U	2.66	Mg92-U	2.66
Mg92-1	I.S.	I.S.	I.S.	2.2	-1.4	17.7	6.8	+2.4	Mg92-P1	2.69	Mg92-G1	2.7
Mg92-2	3.3	1.9	51.8	2.2	-1.2	16.8	*	*		(+0.03)		(+0.04)
Mg92-3	3.8	1.1	52.0	2.2	-1.3	17.3	4.5	+0.1			Mg92-G2	2.69
Mg92-4	3.6	1.0	52.0	2.2	-1.3	17.3	*	*	Mg92-P2	2.68		(+0.03)
Mg92-5	3.8	0.9	52.3	2.2	-1.3	17.3	*	*		(+0.02)		
Mg92-6	3.8	0.8	52.5	2.2	-1.2	16.8	*	*			Mg92-G3	2.68
Mg92-7	3.9	0.7	52.4	2.2	-1.2	16.8	3.9	-0.5				(+0.02)
Mg110-U	4.2	0.4	53.1	2.2	-0.9	15.6	4.8	*	Mg110-U	2.66	Mg110-U	2.66
Mg110-1	2.9	2.6	52.0	2.3	-1.4	17.5	6.8	+2.4	Mg110-P1	2.69	Mg110-G1	*
Mg110-2	3.7	2.4	51.7	2.3	-1.1	16.2	*	*		(+0.03)		
Mg110-3	3.5	2.2	52.2	2.2	-1.0	16.2	7.9	+3.5			Mg110-G2	*
Mg110-4	3.6	2.0	52.1	2.3	-1.1	16.3	*	*	Mg110-P2	2.69		
Mg110-5	3.0	1.6	52.8	2.3	-0.9	15.6	*	*		(+0.03)		
Mg110-6	3.8	1.0	52.8	2.3	-1.0	16.0	4.8	+0.4			Mg110-G3	*
Mg130-U	4.0	0.4	53.0	2.1	-1.1	16.4	3.8	*	Mg130-U	2.67	Mg130-U	2.67
Mg130-1	3.8	3.2	50.2	2.2	-1.3	17.3	6.7	+2.3	Mg130-P1	2.70	Mg130-G1	2.69
Mg130-2	4.1	3.6	49.4	2.2	-1.2	16.8	*	*		(+0.04)		(+0.03)
Mg130-3	3.7	3.3	50.0	2.2	-1.3	17.3	7.8	+3.4			Mg130-G2	2.69
Mg130-4	4.3	2.8	50.3	2.2	-1.2	16.8	*	*	Mg130-P2	2.70		(+0.03)
Mg130-5	5.3	2.9	49.5	2.2	-1.2	16.8	*	*		(+0.04)		
Mg130-6	5.2	2.6	49.7	2.2	-1.1	16.4	*	*			Mg130-G3	2.68
Mg130-7	6.2	2.6	49.3	2.3	-0.9	15.6	9.0	+4.6				(+0.02)
LMg130-U	6.0	0.4	51.5	2.2	-1.6	18.5	4.9	*	LMg130-U	2.67	LMg130-U	2.67

(continued on next page)

Table 3 (continued)

(b) MgCl ₂ flooded	SiO ₂	MgO	CaO	δ ¹³ C SMOW	δ ¹⁸ O SMOW	T	SSA	ΔSSA	sample	ρ _{end}	sample	ρ _{end}
	(wt%)	(wt%)	(wt%)	(‰)	(‰)	(°)	m ² /g	m ² /g		g/cm ³		g/cm ³
LMg130-1	4.0	5.7	46.8	1.5	−3.0	24.8	6.8	+2.4	LMg130-P1	2.71	LMg130-G1	2.72
LMg130-2	4.4	7.5	44.5	1.9	−2.9	24.3	*	*		(+0.05)		(+0.06)
LMg130-3	7.3	5.2	46.0	2.0	−2.2	21.2	7.7	+3.3			LMg130-G2	2.69
LMg130-4	3.9	3.2	50.0	2.0	−2.0	20.3	*	*	LMg130-P2	2.69		(+0.03)
LMg130-5	3.8	2.4	51.1	2.0	−1.7	19.0	*	*		(+0.03)		
LMg130-6	I.S.	I.S.	I.S.	2.0	−1.7	19.0	*	*			LMg130-G3	2.69
LMg130-7	4.1	2.4	51.1	1.7	−1.9	19.8	5.7	+1.3				(+0.03)

volume has remained constant during the compaction process.

Estimates of the true porosity, i.e. the ratio of pore volume and bulk volume after flooding-compaction tests must necessarily account for all volume changes. This is found by direct measurement using end state properties only.

One such estimate is made using the difference between the saturated and dry weights ($M_{sat,end}$ and $M_{dry,end}$) divided by the density of distilled water (ρ_{dw}) and the bulk volume ($V_{b,end}$, which is given by Eq. (3)):

$$\phi_{end,2} = \frac{(M_{sat,end} - M_{dry,end})}{\rho_{dw} V_{b,end}} \quad (7)$$

just as for the evaluation of the initial porosity, see Eq. (1).

The true porosity can also be estimated by combining the solid density ($\rho_{s,end}$), the dry mass ($M_{dry,end}$) and bulk volume ($V_{b,end}$) after the experiment as:

$$\phi_{end,3} = \frac{V_p}{V_b} = 1 - \frac{V_s}{V_b} = 1 - \frac{M_{dry,end}}{V_{b,end} \rho_{s,end}} \quad (8)$$

Here, the solid density ($\rho_{s,end}$) is the weighted average ($\rho_{core,avg}$) from parts P1 and P2, listed in Table 3 (see 2.9. Solid density estimation).

2.12. Permeability estimation

From the differential pressure (ΔP) across the core plug and with known flooding volumetric rate (Q), the permeability during testing (k) was calculated according to Darcy's equation:

$$k = \frac{Q \cdot \mu \cdot L}{\Delta P \cdot A} \quad (9)$$

where L is the length of the core, A is the cross-sectional area, and μ is the brine viscosity, varying with temperature (Crittenden et al., 2012).

3. Results

3.1. Field emission gun-scanning electron microscopy (FEG-SEM)

3.1.1. Unflooded samples

Aalborg chalk can be classified as a coccolithophore-containing mudstone or wackestone with high abundance of foraminifer shells and fragments of a variety of shells. Well-preserved coccolithophore plates (coccoliths) are present (Fig. 2a, c, pink arrows), but commonly show some overgrowth. However, the matrix is dominated by small calcite grains, originating most likely from broken coccolithophore species and foraminifera shells. Intra-fossil porosity is partly preserved. This chalk contains large amounts of authigenic opal-CT lepispheres (Fig. 2a, c, yellow squares). In cases, opal-CT fills entire foraminifer shells. Flake shaped clay minerals are observed (Fig. 2a, c, green circles), some of which might be mica as also documented by Hjuler (2007). In addition, large elongated pores are found, interpreted to be sponge spicule moulds (Fig. 2b, light orange dotted circle).

3.1.2. NaCl flooded samples

In both cores (*Na130* and *LNa130*) flooded with NaCl at 130 °C, inorganic calcite together with preserved coccolithophores (Fig. 3a, b, c pink arrows) and clay minerals (Fig. 3a, green circles) can still be found, similar to observations in unflooded Aalborg chalk (Fig. 2). FEG-SEM images of each slice from *Na130* and *LNa130* are documented in supplementary material (sup. mat. Figs. 1 and 2). There is no indication of newly-formed minerals, in agreement with former studies (Andersen et al., 2017; Madland et al., 2011; Megawati et al., 2015; Wang et al., 2016). The calcite grains appear, however, somewhat more rounded (Fig. 3a and b) compared to unflooded material (Fig. 2). This might be linked to the slight dissolution of calcite also indicated in effluent measurements (see below). Unbroken microfossils besides coccolithophores can still be observed in the cores.

In *Na130*, opal-CT cannot be found in slice 1 in areas imaged by FEG-SEM (sup. mat. Fig. 1a), but partly preserved opal-CT in slice 2 (sup. mat. Fig. 1b) can be observed. In slice 3 (sup. mat. Figs. 1c) and 4 (sup. mat. Fig. 1d) of the core, partly dissolved and/or dismantled opal-CT can still be found, and in slice 4 large pores filled with opal-CT are present, as in unflooded material. From approximately slice 5 (sup. mat. Fig. 1e) along the flooding axis until the outlet (Fig. 1), opal-CT seems preserved. Near the outlet part of the core, small flakes of clay-like minerals can be observed (Fig. 3a green circle in slice 7).

In *LNa130*, within slice 1 (sup. mat. Fig. 2a), partly preserved opal-CT is infrequently observed (Fig. 3b and c, yellow squares), which is different from slice 1 in *Na130*, however, in most areas of this sample, opal-CT cannot be found. In all slices towards the outlet of the core (sup. mat. Fig. 2g), a trend from partly preserved opal-CT towards well-preserved opal-CT is observed. In slice 6 large pore spaces can be observed filled with opal-CT (Fig. 3c, yellow squares), similar as in unflooded material. Unbroken microfossil shells are still observed in all slices.

3.1.3. MgCl₂ flooded samples

FEG-SEM images from MgCl₂ flooded cores under different temperatures are shown in Fig. 4 and sup. mat. Figs. 3–8. In the cores flooded with MgCl₂ organic and inorganic calcite is still present along with occurrences of flake shaped clay minerals and quartz. The calcite grains in all samples appear more rounded (Fig. 4a and b), indicative of dissolution, but unbroken microfossil shells and coccolithophores can still be observed.

The two cores, *LMg130* and *Mg130*, tested at 130 °C, definitely show the strongest mineralogical changes. Magnesite crystals are observed from the inlet along the flooding direction (Fig. 1) until slice 4 (Fig. 4d). Large magnesite crystals, typically between 1 and 6 μm, are found in open pore spaces, mostly inside foraminifera shells (Fig. 4c). In addition, smaller crystals (~50–100 nm) in clusters with high content of magnesium are observed at the inlet of the cores flooded with MgCl₂ at 130 °C (Fig. 4d), which also are interpreted to be newly grown magnesite. Such observations of smaller magnesite crystals grown in aggregates inside pore spaces are found throughout both cores flooded at 130 °C (Fig. 4e). In the cores tested at 25, 60, 92 and 110 °C, magnesite crystals are not observed (sup. mat. Figs. 3–6), however in core

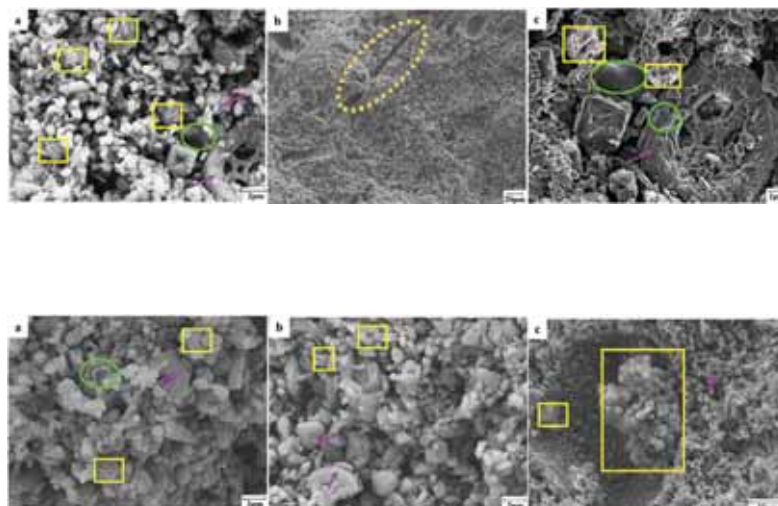


Fig. 2. FEG-SEM images of unflooded Aalborg cores. (a) Opal-CT and coccolithophores are widespread in unflooded material; (b) Sponge spicule moulds are observed in unflooded Aalborg chalk; (c) SEM-micrograph of unflooded Aalborg chalk. Along with microfossils such as coccoliths, intact and dismantled, clay minerals and phyllosilicates can be observed. Yellow square: opal-CT; pink arrow: coccoliths; green circle: clay minerals; orange dotted line: sponge spicule mould. (For interpretation of the references to colour in this figure legend, the reader is referred to the Web version of this article.)



Fig. 3. (A) Clay-minerals, preserved opal-CT and coccolithophores in the Na130 (slice 7); (b) SEM-micrograph of NaCl-flooded LNa130 (slice 2). Partly preserved opal-CT (yellow square) are widespread. (c) Large cluster of opal-CT found inside foraminifera shells in LNa130 (slice 6). Yellow square: opal-CT; pink arrow: coccoliths; green circle: clay minerals. (For interpretation of the references to colour in this figure legend, the reader is referred to the Web version of this article.)

Mg92 (flooded with $MgCl_2$ at 92 °C) small crystals less than 100 nm in size are observed on surface of larger calcite grains (Fig. 4b, blue circle).

Opal-CT can still be found in all cores flooded with $MgCl_2$. However, the lepispheres have different morphology depending on which temperature the cores were flooded at. Samples Mg25 and Mg60 (Fig. 4h) contain minute amount of Si-Mg-bearing precipitates near the inlet according to FEG-SEM-EDS, while well preserved opal-CT is widespread from slice 2 (sup. mat. Figs. 3b and 4b) up to the outlet of the cores (Fig. 4a, yellow square). For the core flooded at 92 °C clay-minerals are found from the inlet until slice 5 (sup. mat. Fig. 5e) in the core, while in slice 6 (sup. mat. Figs. 5f) and 7 (sup. mat. Fig. 5g) the flooded material again appears quite similar to the unflooded rock. In core Mg110 newly formed Si-Mg-bearing minerals are observed from slice 1 (sup. mat. Fig. 6a) towards the outlet (sup. mat. Fig. 6g). In the high-temperature tested cores (Mg130 and LMg130), minute opal-CTs can still be found at the inlet of the cores, but their texture and composition are changed (Fig. 4f, blue dotted arrow) as follows: the blades in the lepispheres are partly dissolved and smaller, and connected in a film-like manner. From slice 2 (sup. mat. Figs. 7b and 8b) up to the outlet (sup. mat. Figs. 7g and 8g), opal-CT can no longer be observed, but instead Si-Mg-bearing minerals are abundant throughout the two cores flooded at 130 °C (Fig. 4g, pink dotted square), as also seen in Mg110. An increase of Si-Mg-bearing minerals content towards the outlet of the cores is observed.

As described (above 2. **Experimental procedures and methods**), the effluent was collected during all tests. White particles have been suspended in the effluent produced by core LMg130, which was not observed in other tests. These effluent samples were filtered and dried at 100 °C in a heating chamber before analysed by FEG-SEM-EDS. Fig. 4i and l shows the FEG-SEM-EDS analysis of the white particles. The particles are SiO_2 -bearing minerals, precipitated from the fluid saturated with Si^{4+} through dissolution in core LMg130.

3.2. X-Ray Diffraction (XRD)

3.2.1. Unflooded samples

The mineralogy of Aalborg chalk, the clastic and the < 2 μm fractions of the chalk were determined by XRD on representative samples (sup. mat. Fig. 9a) (Bertolino et al., 2013). The unflooded Aalborg chalk contains calcite and non-carbonate phases, which are composed of

scarce quartz, scarce phyllosilicates (broad peak at 4.44 – 4.50 Å) and traces of opal-CT (two broad reflections at 4.32 Å and 4.09 Å) (Wilson, 2014), minor clinoptilolite and scarce illite and illite/smectite.

3.2.2. NaCl flooded samples

The NaCl flooded cores do not show any new minerals, in agreement with previous studies (Madland et al., 2011; Megawati et al., 2015). Both NaCl flooded cores (Na130 and LNa130, sup. mat. Fig. 9b and c) contain calcite as the dominant mineral, along with scarce quartz, scarce phyllosilicates and traces of opal-CT, also found in unflooded material. In Na130 quartz and opal-CT are observed in all slices. Clay minerals are recognized only in slice 7. LNa130 differs slightly from Na130. As in Na130, scarce quartz is distributed in all slices of LNa130, however, traces of opal-CT can only be found from slice 5 on and increases from slice 5 to 7 along with scarce clay minerals.

3.2.3. $MgCl_2$ flooded samples

XRD analyses of $MgCl_2$ flooded cores are shown in sup. mat. Fig. 9d–i. All $MgCl_2$ flooded cores still contain calcite as the dominant mineral, along with minor quartz, and scarce phyllosilicates, which were also found in unflooded material. In Mg25 opal-CT was detected from inlet to the outlet while in Mg60 opal-CT was absent in slice 1 (sup. mat. Fig. 9d and e), but present from slice 2 to 7. Opal-CT is concentrated mainly in slice 4 to 6 in core Mg92 and opal-CT is not found in cores Mg110, Mg130 and LMg130 (sup. mat. Fig. 9f, g, h, i). Traces of magnesite were detected in slice 4 of Mg110 (110 °C), and the cores tested at 130 °C (Mg130 and LMg130) show well-developed peaks of magnesite at 2.74 – 2.76 Å in slices 1–4.

3.3. Whole-rock geochemistry

Geochemical analyses of the unflooded chalk are summarized in Table 3 (complete data set is in sup. mat. Table 1) together with the exact sample position of the unflooded samples.

3.3.1. Unflooded samples

Calcite is the dominant mineral and CaO ranges from 51.4 to 53.6 wt% (weight percentage). Al_2O_3 and MgO contents are low, 0.34 and 0.40 wt%, respectively, with total carbon (TOC) around 12%. SiO_2 appears in concentrations between 3.5 wt% and 6.0 wt% and is mainly present as opal-CT, according to FEG-SEM and XRD studies. Opal-CT

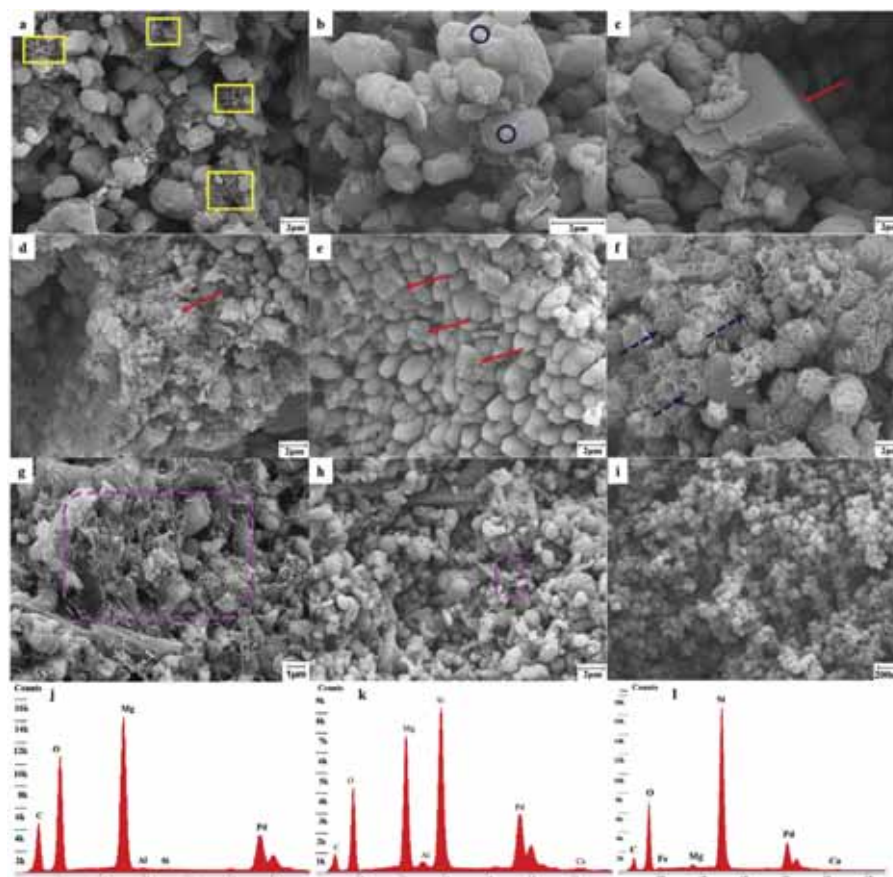


Fig. 4. (A) The calcite grains seem more rounded after flooding (*Mg60*, slice 5). Opal-CT is widespread; (b) Small crystals on top of calcite grains found in *Mg92* (slice 1). These are similar to high Mg-content grains observed in chalk flooded with $MgCl_2$ at 130 °C; (c) Magnesite in *LMg130* (slice 1); (d) Smaller grains with high magnesium content, interpreted to be new-grown magnesite from *LMg130* (slice 1); (e) Aggregates of magnesite crystals in core *Mg130* (slice 5); (f) Remnants of opal-CT lepispheres with changed texture and composition from *LMg130*, slice 1; (g) Si-Mg-bearing minerals are widespread in *Mg130*, slice 7; (h) Minute Si-Mg-bearing minerals are observed in *Mg60*, slice 1; (i) SEM image of white particles found in the effluent of *LMg130* flooding test; (j) EDS analysis of the large crystal in the centre of c (k) EDS analysis of the altered opal-CT in f (l) EDS analysis (identified as SiO_2) of the white particles found in the effluent of *LMg130* flooding test (sample coated with palladium, Pd, for sufficient electron flux). Red arrow: magnesite; yellow square: opal-CT; pink dotted square: Si-Mg-bearing minerals; blue dotted arrow: changed opal-CT; blue circle: high magnesium content particles. (For interpretation of the references to colour in this figure legend, the reader is referred to the Web version of this article.)

constitutes the main non-carbonate mineral. Sr abundance varies between 692 and 881 ppm but does not correlate positively with CaO. Trace element geochemistry does not point to any significant clastic input. Rb and Y, with values far below 5 and 6 ppm respectively, are even below 10% of the typical upper continental crust composition (McLennan et al., 2006).

3.3.2. NaCl flooded samples

Compared to unflooded material; in the NaCl flooded cores the whole-rock geochemical analyses show significant changes only for SiO_2 (Table 3a and sup. mat. Table 1). In *Na130*, SiO_2 increases from low values at the inlet (2.4 wt%) towards higher at the outlet (5.9 wt%). The values at the inlet are 50% lower than in the unflooded sample and at the outlet approximately 20% higher than in unflooded chalk in this study (Table 3a and sup. mat. Table 1). The same trend can be observed

in *LN130*. Highly fluid-sensitive Sr and TOC are constant. The content of major elements (Mg, Al, Na and K) varies slightly along the cores, however this is not possible to interpret as other than natural variation and the initial low abundance being the dominant factors, rather than effects of flooding.

3.3.3. $MgCl_2$ flooded samples

The whole-rock geochemistry analysis of $MgCl_2$ flooded cores is summarized in Table 3b. The flooded cores display in general an increase in MgO and a decrease in CaO and SiO_2 , although trends are by far more complex dependent on temperature. The MgO enrichment increases with increasing temperatures. All the unflooded cores had similar very low concentrations of MgO (0.4 wt%), but obtained different enrichments of MgO after flooding. The cores flooded at lower temperatures (25, 60, 92 and 110 °C) show decreasing trends of MgO

content from the inlet to the outlet, with the most significant increase of MgO near the inlet (Table 3b). In Mg130 and LMg130 the MgO-concentrations showed similar decreasing trends, however with the highest content in slice 2 (Mg130: 3.6 wt%; Mg130: 7.5 wt%), and then decreasing towards the outlet slice (Mg130: 2.6 wt%; Mg130: 2.4 wt%). Mg130 obtained less MgO enrichment (on average: 3.0 wt%, 61 days) than LMg130 (on average: 4.4 wt%, 115 days) as expected with the shorter flooding time.

In core Mg25 the amount of SiO₂ increases from inlet (3.5 wt%) to outlet (5 wt%). Mg92, Mg110 and Mg130 show similar trends as Mg25. The long-time flooded core LMg130 shows a rather uniform SiO₂-distribution besides in slice 3, with enriched abundances (22% higher) compared to the unflooded sample. Mg60 shows constant SiO₂-concentrations with an enrichment in slices 3 and 4. It should be noted that the SiO₂-content in the flooded cores may also be influenced by natural SiO₂-variations (varying between 3.5 and 6.0 wt% in unflooded material, sup. mat. Table 1a), mainly linked to the abundance of opal-CT. Flooding did not measurably affect the concentrations of Al₂O₃, Fe₂O₃, K₂O and TOC (Table 3b).

3.4. Stable isotope geochemistry

3.4.1. Unflooded samples

C-O isotope measurements are summarized in Table 3. For unflooded material, the $\delta^{13}\text{C}_{\text{SMOW}}$ values are homogeneous, varying between 2.0 and 2.3‰, besides one value of 1.9‰ in sample Mg60-U (sup. mat. Table 1a). $\delta^{18}\text{O}_{\text{SMOW}}$ values vary more strongly, between -0.9 and -1.6‰ (sup. mat. Table 1a). However, both isotope proxies still reflect primary signatures in accordance to earlier studies (Surlyk et al., 2010). Facies differences in chalk through time of deposition of the Rørdal Member were observed by Surlyk et al. (2010) and expressed with a trend from lighter to heavier isotopes for $\delta^{18}\text{O}_{\text{SMOW}}$, hence from warmer to colder environment stratigraphically towards younger rocks. If applying this trend as criteria for a stratigraphic position for the samples studied here (and explaining value differences) LMg130-U, AA2-U, Na130-U and Mg92-U are from the bottom of the member and the others rather from the top with Mg110-U, AA7-U and AA4-U being the youngest (sup. mat. Table 1a) of the cores.

3.4.2. NaCl flooded samples

$\delta^{13}\text{C}_{\text{SMOW}}$ values in the NaCl flooded cores (Table 3a) are comparable to those of unflooded cores. In contrast, $\delta^{18}\text{O}_{\text{SMOW}}$ values for LNa130 are over 30% more negative than in the unflooded sample, uniformly throughout the core. The difference before and after flooding within sample Na130 is less, which was flooded only 60 days compared to 118 days for LNa130. Nevertheless, both samples are still in vicinity of the expected isotope range for the Rørdal Member (Surlyk et al., 2010), but the altered values could indicate a reactivity to the flooding process.

Table 4

Core properties (yield point and bulk modulus) during hydrostatic loading and confining pressure during creep.

Core	Yield point	Bulk modulus	Confining pressure during creep
	(MPa)	(GPa)	(MPa)
Mg25	8.23	0.30	10
Mg60	7.23	0.21	10
Mg92	8.86	0.31	11
Mg110	4.39	0.29	8
Mg130	8.41	0.23	11
LMg130	8.48	0.24	11
Na130	8.77	0.28	12
LNa130	8.92	0.23	12

3.4.3. MgCl₂ flooded samples

After MgCl₂ flooding, the average $\delta^{13}\text{C}_{\text{SMOW}}$ values (Table 3b) are mostly similar to those of the unflooded cores with few exceptions. This may reflect natural variation rather than effects of the flooding experiments. $\delta^{18}\text{O}_{\text{SMOW}}$ values vary, but generally reflect Cretaceous values (Surlyk et al., 2010). Sample Mg25, shows more negative values in slice 1 and 2, the other slices are comparable to unflooded values. Mg60 and Mg92 contain values which match the unflooded samples, while Mg110 and Mg130 have slightly more negative values in the first two and three slices, respectively, and then show similar values to those of the unflooded samples. Only LMg130 is different with strongly more negative values throughout the entire sample, with the most negative values in slice 1 and 2.

3.5. Mechanical tests-hydrostatic loading and creep compaction

The measured axial stress versus axial strain during loading phase is plotted in Fig. 5a. Yield points, bulk modulus and confining pressure during the creep phase are reported in Table 4. The cores flooded at the same temperature and same fluid show similar yield point and bulk modulus (see Table 4). Concerning yield point and bulk modulus no direct trend due to temperature, nor injected brines, could be drawn, which is consistent with previous observation (Madland et al., 2011; Megawati et al., 2015; Wang et al., 2016).

During the creep phase, the impacts of both brines and the flooding temperatures are clearly demonstrated in the axial creep strain profiles, see Fig. 5b. Cores, flooded at the same temperature and with the same fluids (Na130 and LNa130; LMg130 and Mg130), showed good repeatability. Longer flooding time led to more creep compaction with the same brine injection at 130 °C (LMg130: 6.51% and Mg130: 5.36%; LNa130: 2.41% and Na130: 1.60%) and MgCl₂-flooded cores compacted more than NaCl-flooded cores at 130 °C, similar to previous studies (Madland et al., 2011; Megawati et al., 2015; Wang et al., 2016). As Fig. 5b shows, after 60 days of creep, all MgCl₂-flooded cores

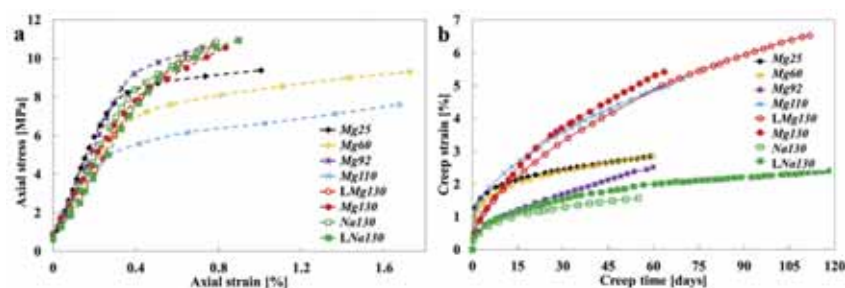


Fig. 5. (A) Axial stress versus axial strain for MgCl₂ or NaCl flooded cores; (b) axial creep strain versus creep time during MgCl₂ or NaCl flooding. Note that LMg130 and LNa130 were flooded for 115 and 118 days respectively.

in the temperature range from 25 to 110 °C compacted more than the NaCl-flooded cores at 130 °C.

We divided the creep behaviour of MgCl₂- and NaCl-flooded cores into two phases. During the primary phase (the first ~ 10 days), cores *Mg25*, *Mg60*, *Mg110* showed higher creep rates than other cores *Mg92*, *Mg130*, *LMg130*, *LNa130* and *Na130* due to higher compaction rates at the end of the hydrostatic loading and thereby entering the creep phase at higher strain rates. The remaining part of the creep phase, where loading phase effects are assumed negligible, is defined as the secondary phase. During this part of the test, systematically higher creep rates (axial creep strain divided by creep time) were observed at higher temperatures for MgCl₂-flooded cores (*Mg25*: 0.015%/day; *Mg60*: 0.015%/day; *Mg92*: 0.029%/day; *Mg110*: 0.039%/day; *LMg130*: 0.045%/day; *Mg130*: 0.052%/day). Cores *Mg25* and *Mg60* had similar low compaction rates as the NaCl flooded cores from 20 until 60 days of creep (Fig. 5b, black and green curves, *LNa130*: 0.013%/day; *Na130*: 0.013%/day).

3.6. Effluent analyses

During NaCl flooding the effluent concentrations of Na⁺ and Cl⁻ are practically the same as the injected (not shown), i.e. 0.657 mol/L, and only minute Ca²⁺ concentrations are observed (Fig. 6a), in line with previous studies (Andersen et al., 2017; Madland et al., 2011; Megawati et al., 2015; Wang et al., 2016). Fig. 6a, b and c show the measured Ca²⁺, Mg²⁺ and Si⁴⁺ concentration profiles with time during flooding, respectively. As temperature increases, more Ca²⁺ is produced and more Mg²⁺ is retained inside the cores (Fig. 6a and b), which is expected based upon findings from a previous studies (Korsnes et al., 2006a; Nermoen et al., 2016). Ca²⁺ production in *Mg25* (~ 0.003 mol/L) is comparable to that of the two NaCl flooded cores (*LNa130*: ~ 0.002 mol/L; *Na130*: ~ 0.003 mol/L), and is slightly lower than *Mg60* (~ 0.007 mol/L). All cores show Ca²⁺ peaks initially (Fig. 6a)

followed by a slightly decreasing trend until the concentrations stabilize (Fig. 6a, Ca²⁺ concentration: *LNa130*: ~ 0.002 mol/L; *Na130*: ~ 0.003 mol/L; *Mg25*: ~ 0.003 mol/L; *Mg60*: ~ 0.007 mol/L; *Mg92*: ~ 0.010 mol/L; *Mg110*: ~ 0.014 mol/L; *LMg130*: ~ 0.016 mol/L; *Mg130*: ~ 0.023 mol/L). In the cores flooded with MgCl₂ at high temperatures (110 and 130 °C), a clear decrease in Ca²⁺ concentrations is observed and negatively correlated with Mg²⁺ concentrations from the same cores. In all other cores, the production of Ca²⁺ is rather stable over time.

Fig. 6b shows the Mg²⁺ concentration in the effluent of the MgCl₂ flooded cores. The trends are similar but opposite to the Ca²⁺ profiles, i.e. the sum of produced Ca²⁺ and Mg²⁺ was stable and close to equal to the injected concentration of 0.219 mol/L (not shown), consistent with earlier studies (Andersen et al., 2017; Madland et al., 2011; Megawati et al., 2015; Wang et al., 2016). The Mg²⁺ concentration in the effluent of tests from *Mg25* (~ 0.22 mol/L) and *Mg60* (~ 0.22 mol/L) were almost stable over the entire test period. For *Mg92*, *Mg110*, *LMg130* and *Mg130* the magnesium concentration increased from low values in the first sample points (*Mg92*: 0.198 mol/L; *Mg110*: 0.196 mol/L; *LMg130*: 0.167 mol/L; *Mg130*: 0.175 mol/L), until they stabilized (Fig. 6b, Mg²⁺ concentration: *Mg92*: ~ 0.21 mol/L; *Mg110*: ~ 0.21 mol/L; *LMg130*: ~ 0.20 mol/L; *Mg130*: ~ 0.20 mol/L).

Concentrations of Si⁴⁺ were detected in the effluent (Fig. 6c), indicating dissolution of Si-bearing minerals. For a given core the Si⁴⁺ concentration was stable over time. *Na130* (~ 0.0012 mol/L) and *Mg60* (~ 0.0012 mol/L) produced similar amounts, which is a factor 2 higher than *Mg25*. Highest Si⁴⁺ concentration has been observed in the effluent from the core *Mg92* (~ 0.0019 mol/L) and *Mg110* (~ 0.0019 mol/L), while the two cores tested at 130 °C (*Mg130*: ~ 0.0014 mol/L; *LMg130*: ~ 0.0013 mol/L) produced less Si⁴⁺ than the two mentioned cores (*Mg92* and *Mg110*). For all effluent analyses, fluctuations may occur due to possible evaporation during storage and dilution uncertainties.

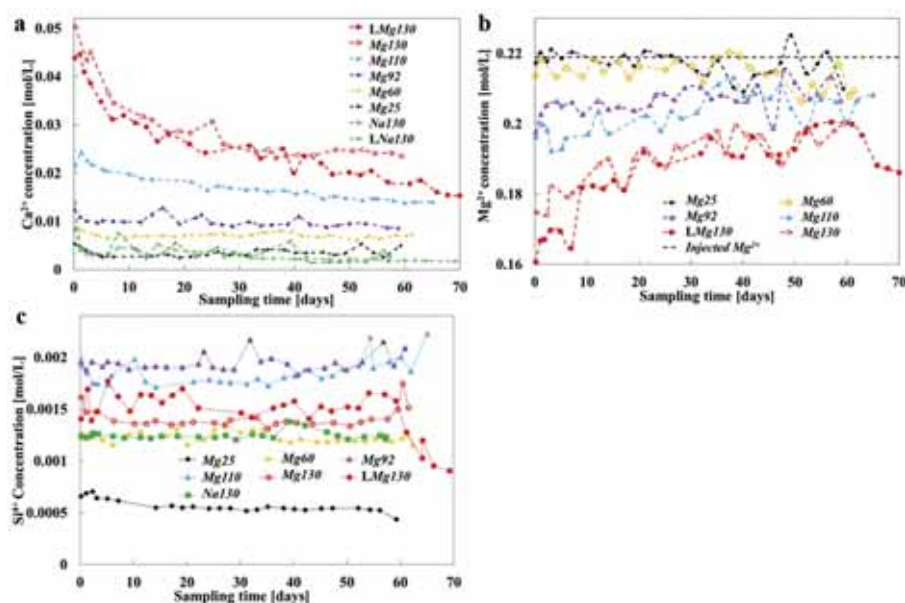


Fig. 6. Ion concentrations in the effluent samples measured by ion chromatography (a) Ca²⁺ concentration over time; (b) Mg²⁺ concentration over time; (c) Si⁴⁺ concentration measured by inductively coupled plasma. Note: Sample (*LNa130*) was not measured due to machine malfunction. Sampling times for ions (Ca²⁺, Mg²⁺, and Si⁴⁺) were initiated at the start of the creep phases.

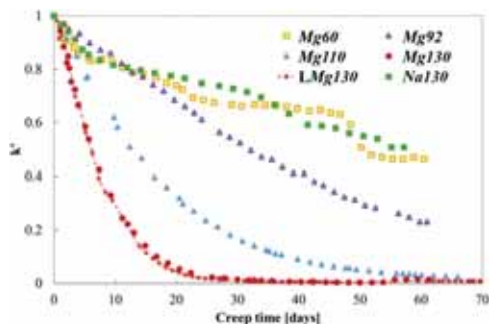


Fig. 7. Normalized permeability values ($k' = k/k_{ref}$) with creep time. In this figure, two cores (LNa130 and Mg25) are not included due to fluctuations of the permeability values related to issues with the backpressure-regulator.

3.7. Solid density estimation

Table 3A, b shows the density values (ρ_{end}) from parts P1 and P2 and groups G1, G2 and G3 (see Fig. 1b) together with the calculated difference ($\Delta\rho$) between the end measurement (ρ_{end}) and the average pycnometry measurements (ρ_0) (2.66 g/cm³) of unflooded material.

For the two NaCl flooded cores, $\Delta\rho$ (by group) was in the range between -0.01 and $+0.03$ g/cm³, where the increase is seen in the first group (Na130: G1: $+0.01$ g/cm³ and LNa130: G1: $+0.03$ g/cm³) with a decreasing trend towards the outlet of each core (Na130: G3: -0.01 g/cm³ and LNa130: G3: $+0.02$ g/cm³). This may be explained by a higher dissolution of opal-CT near the inlet and possible transported or precipitated lighter phases at the outlet.

For the MgCl₂ flooded cores, the density increase of P1 and P2 varied from zero to $+0.05$ g/cm³ except for Mg25, which saw a small decrease in P2 (-0.01 g/cm³) (Table 3b). Compared to the NaCl flooded cores the solid density increased more in the cores flooded with MgCl₂ at 130 °C, as observed in Wang et al. (2016). Mg110 shows an increase in solid density in both P1 and P2 of 0.03 g/cm³. Also by group measurements (G1, G2, G3), not performed on Mg25 and Mg110, the MgCl₂ flooded cores showed the highest increase in solid density near the inlet (G1). LMg130 shows the highest increase near the inlet (G1: $+0.06$ g/cm³), while a lower increase towards the outlet is observed (G2: $+0.03$ g/cm³; G3: $+0.03$ g/cm³). Mg60, Mg92 and Mg130 revealed similar trends as LMg130, but in these cores the increase of the values is less (Mg60, G1: $+0.03$ g/cm³; G3: $+0.03$ g/cm³; Mg92, G1: $+0.04$ g/cm³; G3: $+0.02$ g/cm³; Mg130, G1: $+0.03$ g/cm³; G3: $+0.02$ g/cm³) than in LMg130.

3.8. Specific surface area (SSA)

Measurements of the specific surface area (SSA) in slices 1, 3 and 7 of all flooded cores are listed in Table 3a and b together with the difference (Δ SSA) between measurements of material from the flooded cores and unflooded material (Table 1, average value unflooded: 4.4 m²/g).

The SSA in the two NaCl flooded cores is decreased compared to the unflooded material measurement. The strongest decrease is observed near the inlet (Na130: -2.3 m²/g; LNa130: -2.6 m²/g) (Table 3a) while at the outlet, the measured values are (Na130: 4.6 m²/g; LNa130: 3.8 m²/g) close to the average value for unflooded material (4.4 m²/g). The SSA values in the long-time (118 days) flooded core LNa130 are lower than those of the short-time test (60 days) core Na130.

In Mg25, the SSA is increased in the first slice ($+1.8$ m²/g) compared to the unflooded material (4.4 m²/g). In the centre of the core (slice 3) there is only a slight increase ($+0.1$ m²/g) while at the outlet (slice 7) the SSA has decreased to 3.9 m²/g (-0.5 m²/g compared to the average unflooded value). Only the significant increase in slice 1 can be considered an impact of the flooding process, while the other deviations are low enough to be within the natural variation of the rock (between 3.7 and 4.9 m²/g, see Table 1).

Mg60 follows the same trend as Mg25, with a significant increase in the inlet slice ($+2.3$ m²/g to 6.7 m²/g) compared to the average value for unflooded material. However, in this core a considerable increase in SSA can also be found in slice 3 ($+2.0$ m²/g), followed by a value of 3.6 m²/g (-0.8 m²/g) in slice 7. It should, however, be noted that the SSA for unflooded material from this particular core has been measured to 3.7 m²/g and that local variation may impact the difference in measured SSA.

In the core flooded at 92 °C, Mg92, the initial SSA was higher, 4.8 m²/g, and the SSA measured after flooding is increased at the inlet (slice 1: $+2.4$ m²/g to 6.8 m²/g compared to the average of unflooded material), while remained at approximately the initial value in slice 3 (-0.2 m²/g). At the outlet, the value decreased to 3.9 m²/g, much lower than both the average of unflooded material and the unflooded value for this specific core. However, the value is still within the range of natural variation in the core-samples of this study (Table 1).

Mg110 shows similar increase in SSA ($+2.4$ m²/g from 4.4 m²/g) in the inlet slice as the tests at lower temperature, which increase with values between $+1.7$ and $+2.4$ m²/g, but display an even higher value in slice 3 ($+3.5$ m²/g to 7.9 m²/g). At the outlet (Fig. 1b) the value is the same as unflooded material for this core (4.8 m²/g).

The SSA values for the two cores flooded at 130 °C behaves somewhat different from the other MgCl₂-flooded cores. In the core flooded the shortest time, 60 days, the SSA increased in all measured slices, with a peak in slice 7 ($+4.6$ m²/g to 9.0 m²/g), while the other two slices show increases of $+2.9$ m²/g (slice 1) and $+4.0$ m²/g (slice 3), compared to unflooded material from the same core (3.8 m²/g). In the long-term test, LMg130, the SSA peak appears in slice 3 ($+2.8$ m²/g

Table 5

Core properties, saturated weight ($M_{sat,end}$), dry weight ($M_{dry,end}$), bulk volume ($V_{b,end}$), volumetric strain (ϵ_{vol}), and porosity estimation $\phi_{1,end}$, $\phi_{2,end}$ and $\phi_{3,end}$ after flooding, permeability at starting point (k_{ref}) and end state (k), mass loss ($\Delta m = M_{dry,end} - M_{dry,0}$).

Core	Fluid	T (°C)	$M_{dry,end}$ (g)	$M_{sat,end}$ (g)	$V_{b,end}$ (cm ³)	ϕ_i (%)	ϵ_{vol} (%)	$\phi_{1,end}$ (%)	$\phi_{2,end}$ (%)	$\phi_{3,end}$ (%)	k_{ref} (mD)	k (mD)	Δm (g)
Mg25	MgCl ₂	25	106.0	139.5	73.9	47.9	4.2	45.6	45.3	45.9	1.916	0.753	-0.59
Mg60		60	108.8	141.4	72.9	46.8	6.5	43.1	44.7	44.5	1.201	0.557	-1.48
Mg92		92	108.5	139.9	71.8	47.1	8.9	41.9	43.7	43.8	0.977	0.223	-2.24
Mg110		110	99.9	128.1	65.3	47.4	12.8	39.7	43.2	43.1	1.643	0.04	-3.03
Mg130		130	108.2	135.2	67.2	47.2	16.3	36.9	40.2	40.4	0.755	0.011	-4.13
LMg130		130	114.7	142.7	70.6	47.5	17.5	36.4	39.7	39.8	0.77	0.009	-5.14
Na130	NaCl	130	111.5	144.6	76.3	46.9	5.1	44.0	43.4	45.5	1.118	0.568	-1.51
LNa130		130	104	135	70.6	47.5	6.9	43.6	43.9	45.0	1.173	0.13	-2.19

compared the initial value of 4.9 m²/g). Slices 1 and 7 have increased values of +1.9 m²/g and +0.8 m²/g, respectively, compared to 4.9 m²/g.

3.9. Permeability estimation

Fig. 7 shows the evolution of normalized permeability ($k' = k/k_{ref}$) through time during the creep phase. The starting points in the plots are based on the permeability measurements k_{ref} at the end of hydrostatic loading, i.e. start of creep. Table 5 includes the permeability of each core at starting point (k_{ref}) and end state (k). The permeability of LNa130 (decreased by 88%) reduced more than that of Na130 (decreased by 49%). At the end of the creep phases, Mg60 and Na130 showed similar permeability reduction (Mg60: 58%, Na130: 49%) and Mg92 and LNa130 had similar decrease (Mg92: 77%, LNa130: 88%), while Mg25 decreased by 61%. LMg130 and Mg130 showed good repeatability, with closely overlapping graphs in Fig. 7 and also, the most significant permeability reductions. In LMg130 and Mg130 (130 °C) the permeability reduced from 0.77 to 0.76 mD to ~0.009 and ~0.0119 mD, respectively, after ~32 days of creep compaction. Mg110 also displayed permeability reduction, but not as severe as Mg130 and LMg130. In Mg110 it took ~42 days to observe a strong reduction (97.6%), from 1.6 to ~0.04 mD. The experimental set-ups were dismantled and cleaned after the tests and no restrictions in the form of precipitation or transported material were found in the tubing or other experimental equipment. Thus, the strong increase in differential pressure was induced by flow restrictions inside the cores from the compaction and flooding processes.

3.10. Porosity estimation

The porosities at the end of the tests were calculated (see 3.10. Porosity estimation in 2. Experimental procedure) and summarized in Table 5. For the NaCl flooded cores (130 °C). They each show variations by ~1–2 porosity units: Na130: $\phi_{end,1}$: 44.0%; $\phi_{end,2}$: 43.4%; $\phi_{end,3}$: 45.5% and LNa130: $\phi_{end,1}$: 43.6%; $\phi_{end,2}$: 43.9%; $\phi_{end,3}$: 45.0%. For the two NaCl-tests, Na130 and LNa130, the estimate $\phi_{end,1}$ ignoring chemistry is within the range of the other two estimates and the uncertainties of the measurements.

For the MgCl₂ flooded cores the estimates taking both chemical reactions and volumetric strain into account ($\phi_{end,2}$ and $\phi_{end,3}$) are generally similar, varying only by 0.2 units except for Mg25 (0.6 units difference). The porosity reduction (difference between end porosity (average of $\phi_{end,2}$ and $\phi_{end,3}$) and initial porosity) increases with temperature: Mg25: -2.3%; Mg60: -2.2%; Mg92: -3.4%; Mg110: -4.2% Mg130: -6.9%; LMg130: -7.8%. The porosity estimate $\phi_{end,1}$ (not accounting for chemistry) deviates gradually more from $\phi_{end,2}$ and $\phi_{end,3}$ with increasing temperature, underestimating the porosity by several units. This indicates that there has been a net solid volume reduction for these cores.

4. Discussion

4.1. Chemistry, mineralogy and temperatures

In Aalborg chalk samples flooded with NaCl at 130 °C, no newly precipitated minerals were observed using FEG-SEM (Fig. 3, sup. mat. Figs. 1 and 2) or XRD (sup. mat. Fig. 9b and c), in agreement with previous studies (Andersen et al., 2017; Madland et al., 2011; Megawati et al., 2015; Wang et al., 2016). This also shows that we can use the NaCl test series as comparison for those with MgCl₂. The limited changes in the samples are reflected by only small amounts of Ca²⁺ and Si⁴⁺ in the effluents (Fig. 6a, c) with more or less unchanged whole rock geochemistry measurements (Table 3a). The two mentioned NaCl flooded cores had slightly higher solid density (LNa130: 2.69 g/cm³, Na130: 2.68 g/cm³) near the inlet and same density (LNa130: 2.68 g/cm³,

Na130: 2.67 g/cm³) near the outlet compared to the initial solid density (LNa130-U: 2.68 g/cm³, Na130-U: 2.67 g/cm³). Furthermore, the SSA values (LNa130: 1.8 m²/g, Na130: 2.1 m²/g) near the inlet are close to values reported from pure chalk (Stevens Klint: 1.7 m²/g after Hjuler and Fabricius, 2009), while near the outlet they (LNa130: 3.8 m²/g; Na130: 4.6 m²/g) are closer to unflooded Aalborg material (4.4 m²/g, Table 1). These changes along the cores can be explained by dissolution of the lighter phase opal-CT, resulting in increased density and decreased SSA, which is supported by FEG-SEM, SiO₂ geochemical measurements (Table 3) and effluent analysis (Fig. 6c). This indicates that opal-CT is a component prone to changes and contributes to a significant impact on the mineralogical core properties as exposed to NaCl at elevated temperatures, a fluid earlier seen upon as being inert towards chalk.

Kinetic rates of geochemical reactions, such as mineral dissolution and precipitation, are temperature-dependent and typically increase with temperature. Previous studies have shown that chalk is more reactive towards MgCl₂ (Neremoen et al., 2016) and seawater (Korsnes et al., 2008; Zhang et al., 2007) when temperature is increased, by observations of more Ca²⁺ produced and more Mg²⁺ retained during flooding. The present study made the same observations from effluent measurements (Fig. 6) for Aalborg chalk that bears reactive opal-CT, and further consistently documented increased MgO content in the core with increasing temperature as a result of flooding with MgCl₂, revealed in whole-rock geochemical measurements (Table 3b).

FEG-SEM of LMg130 and Mg130 (Fig. 4c, d, e, sup. mat. Figs. 7 and 8) and XRD (sup. mat. Fig. 9h and i) clearly show precipitation of rhomboidal magnesite crystals, comparable to previous studies (Hiorth et al., 2013; Madland et al., 2011; Megawati et al., 2015; Wang et al., 2016; Zimmermann et al., 2015). Stable oxygen isotope values measured in LMg130 are significantly altered towards more negative (Table 3b), particularly in slice 1, thus pointing to new growth of carbonate minerals. Magnesite formation is accelerated by increasing temperature (e.g., Möller, 1989). From 80 to 120 °C, magnesite can be readily precipitated by a spiral growth mechanism (Saldi et al., 2009), but rates of magnesite precipitation are severely limited at temperatures below 60 °C due to the strong hydration of Mg²⁺ ions in solution (Hänchen et al., 2008). Rhomboidal magnesite crystals were not observed with FEG-SEM in the cores flooded at 25, 60, 92 and 110 °C (sup. mat. Figs. 3–6), even though the samples showed MgO enrichment after flooding (Table 3b). Certainly, this might be related to the small grain size of newly formed crystals. Magnesite crystals or other carbonate phases, such as possible Mg-rich calcite, are in many cases too small (< 100 nm) to be imaged and analysed by FEG-SEM-EDS and the amount too low for the applied analytical techniques, such as XRD. TEM-EDS (transmission electron microscopy – EDS) and TERS (tip enhanced Raman spectroscopy) coupled with AFM (atomic force microscopy) studies show that the minerals are of that small size and can be imaged at the same time when they are determined (Borromeo et al., 2017; Egeland et al., 2017; Minde et al., 2017).

Fournier (1973) reported that the solubility of silica minerals such as amorphous silica, opal-CT, quartz and chalcedony increases with temperature in the range 25–250 °C in water. Dissolved silica can react with Mg²⁺ to form minerals of the form (MgO)_x(SiO₂)_x(H₂O)_x (x = variable) and the precipitation mechanism occurs faster, producing larger amounts at high temperatures (Meyers, 1975). The principal solid alteration products include quartz, chrysotile, talc, kerolite, calcite, kaolinite, smectite, and amorphous silicate material with spongy, smectite-like morphology, identified by transmission electron microscopy (TEM), selected-area electron diffraction (SAED), and X-ray analytical electron microscopy (AEM) at ~45 and ~70 °C (Gislason et al., 1993; Gunnarsson et al., 2005). This confirms our observation of Si-Mg-bearing minerals in FEG-SEM, produced by chemical interactions of Si⁴⁺, dissolved from the host rock, with the reactive injected brine MgCl₂. At higher temperature, flaky minerals containing both Si and Mg are widespread throughout the cores, but the amount is low at the

inlet of the cores flooded at 25 and 60 °C. In general, the amounts of the new mineral phase(s) were too low to be identified using XRD. In the other four MgCl₂-flooded cores, the quantity of Si-Mg minerals increases with increasing flooding temperature. However, effluent analyses showed that Si⁴⁺ production during MgCl₂ injection was higher at 92 and 110 °C than at 130 °C (Fig. 6c). In addition, the effluent from LMg130 was oversaturated with Si⁴⁺ as such that SiO₂ even precipitated from the effluent (Fig. 4i, l). This is also reflected in the average SiO₂ concentrations in the flooded slices, which was the lowest for Mg92 and Mg110, 3.70 and 3.42 wt% respectively, significantly lower than the two cores flooded with MgCl₂ at 130 °C with values of 4.66 (Mg130) and 4.58 (LMg130). We interpret this observation, as a result of superimposed dissolution and precipitation processes: the chemical reaction rates are higher at higher temperature; therefore, more calcite and SiO₂ dissolves, while on the other hand more magnesite and Si-Mg-bearing minerals precipitate, as also observed by FEG-SEM. Hence, the cores flooded at 130 °C produced a lower net amount of Si⁴⁺ than at 92 and 110 °C.

Geochemical analyses and FEG-SEM-EDS measurements show the strongest enrichments in MgO in slice 2 in Mg130 and LMg130, while the other cores show the highest amount of MgO in slice 1. However, at 130 °C, there is also observed an increasing trend in SiO₂ and SSA accompanying MgO from slice 1 and further along the flooding axis of the core, both indications of precipitation of Si-Mg clay minerals. As more negative stable oxygen isotope values, in this study linked to newly precipitated carbonates, are observed in slice 1, it is likely to deduce that the magnesite precipitation peaks in slice 1. In both the high-temperature cores, an increase in flaky clay-minerals are observed, by FEG-SEM, increasing from the inlet towards the outlet of the cores, indicating that clay mineral precipitation has a peak further into the cores. As the clay minerals observed are Si-Mg minerals, the strong enrichment of MgO in slice 2 may originate from a combination of magnesite and clay-minerals. In previous studies and for the cores flooded at lower temperatures (where dissolution of opal-CT and precipitation of new Si-Mg clay minerals is less reactive) the peak in MgO is observed in slice 1. The enrichment of MgO in slice 2 is most visible in the longer of the two tests (Table 3b), and together with variations in SiO₂ profiles in the cores, may suggest that the interplay between the non-equilibrium brine, the rock and precipitated minerals together with the distribution of minerals are time-dependent processes (Minde et al., 2017).

Newly formed carbonate minerals, such as magnesite (3.0 g/cm³) and Mg-rich calcite have higher density than calcite (2.71 g/cm³). Precipitation of these minerals as well as of possible talc (2.76 g/cm³) and dissolution of opal-CT (2.09 g/cm³) are possibly the main processes leading to increased solid density at 60, 92, 110 and 130 °C. At 25 °C, limited dissolution of opal-CT and calcite results in only a small increase in solid density (Table 3b).

The changes in mineralogy with temperature are also reflected in the specific surface area (SSA) measurements. The precipitation of flaky Si-Mg-bearing phyllosilicates balances the reduction of the SSA by the dissolution of opal-CT lepispheres, both having significantly higher SSA than calcite. In the inlet slice, SSA increases more when going from 25 to 130 °C; correspondingly, Mg25, which undergoes the least chemical reactions, gained the smallest increase in SSA. The SSA might also increase due to the formation of nano-sized magnesite and possible high-Mg calcite crystals. SSA slightly decreases near the outlet of the cores tested at 25, 60 and 92 °C. This may be explained by dissolution of opal-CT and calcite, accompanied by only limited precipitation as indicated by FEG-SEM (sup. mat. Figs. 3g, 4g and 5g). The data from this study shows that an increase in SSA, combined with an increase in SiO₂ and observed textural alterations by FEG-SEM, can be linked to higher abundances of newly formed clay-minerals, balancing dissolution of opal-CT. Additionally, presence of minute magnesite is believed to increase the SSA even more. LMg130 has a smaller increase of SSA values, compared to unflooded material of the same core, than Mg130. FEG-

SEM micrographs comparing these cores show that in the core flooded for the longer time, larger magnesite crystals are formed, most likely due to the time aspect together with effects of Oswald ripening. This confirms that precipitation of magnesite also impacts SSA values. It should be noted that in Aalborg chalk, the original concentration of opal-CT and precipitation of euhedral magnesite crystals are influenced by the presence of larger pore-spaces, formed by foraminifera microfossils. These fossils are present throughout all tested cores, but vary strongly in abundance, and may therefore affect measurements of composition, SSA and density within each core.

4.2. Creep compaction and chemistry

During the primary creep compaction phase (~10 days, Fig. 5b), Mg25, Mg60 and Mg110 showed higher creep rates than Mg92, Mg130, LMg130, LNa130 due to the higher compaction rates towards the end of the hydrostatic loading (Fig. 5a). Loading phase effects were negligible in the following period (the remaining test time), and the MgCl₂-flooded cores then experienced higher compaction rates (Fig. 5b) with increasing temperatures. MgCl₂-flooded chalk cores compacted more than NaCl-flooded cores at 130 °C, in agreement with previous reports (Madland et al., 2011; Megawati et al., 2015; Wang et al., 2016). Mg25 and Mg60 obtained higher creep rates in the primary creep phase, and therefore show a high overall compaction.

NaCl-flooded cores at 130 °C behave similar to the ones, Mg25 and Mg60, which have been injected by MgCl₂-brine at low compaction rates (LNa130: 0.013%/day; Na130: 0.013%/day; Mg25: 0.015%/day; Mg60: 0.015%/day). The chemical reactivity is low and dominated by weak dissolution. Mechanical deformation under effective stress is therefore the governing process during compaction.

The cores flooded with MgCl₂ at 92, 110 and 130 °C systematically showed higher compaction rates (Mg92: 0.029%/day; Mg110: 0.039%/day; LMg130: 0.045%/day; Mg130: 0.052%/day). A similar trend was observed when flooding Obourg chalk (Mons, Belgium) with MgCl₂ at 92 and 130 °C (Nermoen et al., 2016). The rate of deformation with time is strongly linked to chemical alterations when injecting MgCl₂ at 130 °C (Megawati et al., 2015; Nermoen et al., 2015; Wang et al., 2016) since relatively inert brines such as NaCl result in much less compaction. Solid volume reduction induced by dissolution may affect the bulk volume directly. There are strong chalk-fluid interactions reducing the strength of particle bonds (Risnes, 2001). The dominating mechanism underlying the rate-type creep model is the off-sliding asperities under friction between granular contacts (Andersen et al., 1992; Anderson, 1995). Rounding of calcite grains by dissolution may decrease the intergranular friction and increase the probability for the grains to 'unlock' from their current organization and shift into nearby pores, thus effectively promoting the creep mechanisms.

Newly formed secondary minerals can trigger enhanced dissolution. On the other hand, the Mg-bearing minerals, particularly the flaky Si-Mg-bearing minerals, can act as contact cementation and strengthen the grain contacts, thus increasing the resistance against deformation (Olsen, 2007; Wetzel, 1989). However, this does not seem to be the case in our study, as increased strain is observed along with an increase in clay content after flooding.

4.3. Permeability evaluation

In brine-chalk systems, the permeability evolution is mainly affected by two coupled mechanisms: mechanical compaction and chemical alteration. This study shows that chemical reactions are weak at 25 and 60 °C when injecting MgCl₂ and at 130 °C when flooding with NaCl. Consequently, permeability reduction was lower in these cores than in cores tested at high temperature (Table 5). Permeability was reduced slightly more in the core flooded for a long time (LNa130) than in the core tested for a shorter period (Na130). Therefore, mechanical

compaction seems to be the dominant factor controlling permeability in **Mg25** and **Mg60** and the two NaCl flooded cores at higher temperatures (130 °C).

The cores tested at higher temperatures (110 and 130 °C) flooded with $MgCl_2$ showed significant permeability reductions (**LMg130**: 98.8%; **Mg130**: 98.5%; **Mg110**: 97.6%) and the strong reduction in permeability is most likely related to the chemical reactions in the cores. FEG-SEM analyses show precipitation of Si-Mg-bearing minerals with thin flaky appearance. These minerals can cover significant portions of the pore surfaces and throats (Fig. 8), effectively reducing the permeability. Therefore, the dominating factor in the permeability development at higher temperature is chemical reactions, especially the formation of Si-Mg-bearing minerals. The formation of these minerals are dependent on a source of Si^{4+} , in this case, the abundant opal-CT.

Nermoen et al. (2015) observed that the permeability in a Liège chalk core (flooded with $MgCl_2$ at 130 °C) started to increase during a period between 140 and 160 days of flooding, after decreasing during the first ~112 days. This observation is different from ours, and most likely caused by the difference in flooding rates, primary mineralogy, with quartz representing the main non-carbonate phase in Liège chalk (Hjuler and Fabricius, 2009; Wang et al., 2016) instead of very fragile opal-CT, like in this study, besides the differences of absolute abundance of silica. Hence, the permeability development is strongly dependent on the presence of specific non-carbonate phases and their abundances as well as their stability and other mineralogical characteristics (e.g. form, surface charge, etc.).

4.4. Porosity evaluation

The three porosity estimates (see section 2.12. Porosity estimation) after flooding are calculated (Table 5) and plotted versus test temperature (Fig. 9). For the cores flooded with $MgCl_2$ at 25 °C and the two NaCl flooded cores (**LN130** and **Na130**), there were no significant differences between the porosity estimates ignoring chemical reactions ($\phi_{end,1}$) and the porosity estimates taking the chemistry into account ($\phi_{end,2}$ and $\phi_{end,3}$) (Fig. 9; and according to Wang et al., 2016). Geochemical analyses, FEG-SEM and effluent measurements indicated limited chemical interaction and correspondingly minor changes in solid density and solid volume for these three cores, and the volumetric deformation was also low (Table 5). Therefore, mechanical compaction seems to be the main factor causing porosity reduction (Eq. (6)) in these cores.

From 60 to 130 °C, more volumetric compaction was observed in the $MgCl_2$ flooded cores (Fig. 5). Solid volume changes are related to calcite and opal-CT dissolution and precipitation of secondary minerals. As expected, the estimates $\phi_{end,2}$ and $\phi_{end,3}$ are generally similar, as they both are based on measuring porosity directly. With increasing temperatures, the porosity estimated by $\phi_{end,1}$ is increasingly imprecise, giving too low values, indicating that pore volume reduction alone does not explain the bulk volume changes, but rather that the solid volume also changes significantly. In particular, this estimate being systematically lower than the others, indicates a net reduction of the solid volume.

From 60 to 130 °C, the measured mass loss of the cores ($\Delta m = M_{dry,end} - M_{dry,o}$, **Mg60**: -1.48 g; **Mg92**: -2.24 g; **Mg110**: -3.03 g; **Mg130**: -4.13 g; **LMg130**: -5.14 g, Table 5) becomes larger with increasing temperature due to stronger chemical reaction rates. Referring to Eqs. (6) and (10), a lower value of $\phi_{end,1}$ than $\phi_{end,2}$ and $\phi_{end,3}$ is indicative of $\Delta V_s < 0$. The loss of mass is consistent with an increasing deviation of $\phi_{end,1}$ from the two other estimates and a higher net dissolution of volume with higher temperature. It is known that Mg-Ca substitutions could cause a significant mass removal. However, we have observed a discrepancy between the measured mass loss ($M_{dry,end} - M_{dry,o}$) and the estimated core mass loss (from Mg^{2+} retention in the cores and Ca^{2+} production in the effluent, **Mg60**: -0.25 g; **Mg92**: -0.35 g; **Mg110**: -0.64 g; **Mg130**: -1.01 g; **LMg130**: -1.50 g).

The mismatch in mass loss may rather be strongly linked to calcium carbonate dissolution, as proposed by Nermoen et al. (2015) as well as, in this case, opal-CT ($SiO_2 \cdot H_2O$) dissolution. The exact explanation for the significant mass loss requires more detailed analysis of the newly formed minerals and pH changes in the effluent samples during the testing period and will not be part of this study, but rather a topic for future research.

We discussed earlier that at higher temperatures not only precipitation of higher density minerals, such as Mg-bearing minerals (magnesite: 3.0 g/cm³), but also dissolution of low density minerals (opal-CT: 1.9–2.3 g/cm³) may increase the solid density. The increased density, together with the decreased dry mass is the cause of the strong reduction in solid volume. These observations suggest that the dominating porosity reduction mechanisms at high temperature are chemical reactions; partly related to Mg-bearing minerals.

4.5. Application of the results

In the presented study, Aalborg cores were tested under specific North Sea reservoir temperatures (Valhall Field, 92 °C and Ekofisk Field, 130 °C), and compared with varying temperatures approaching surface conditions, e.g. injection well temperatures (25, 60, 110 °C) in a series of tests. The presence of opal-CT in chalk when flooding with non-equilibrium brines has a major effect on the permeability, as well as on the intensity of mineralogical changes. Even though the North Sea reservoir chalk does not commonly contain much opal-CT, it does contain abundant quartz, and it is believed that opal-CT is the source of this content created through diagenetic processes (Fabricius and Borre, 2007; Hjuler, 2007). Temperature dependent chemical reactions can induce changes in mineralogy, permeability and porosity in chalk. This is of relevance when using fluid injection for improved or enhanced oil recovery (EOR) in silica-rich reservoir chalk. Our serial laboratory experiments investigating chalk-brine interactions are paramount for prediction of effects related to non-carbonate phases, particularly opal-CT. Additionally, dissolution of other silicate phases, may produce similar Si^{4+} concentrations in pore-fluids and initiate similar precipitation-reactions as seen in this study. In field application, there will always be a temperature gradient between the injector and producer and it is thus important to characterize the chemo-mechanical interactions as function of temperature. The presented series of experiments may be helpful in predicting reservoir behaviour in terms of changes in mineralogy, permeability and porosity in chalk reservoirs, hence is important for all modelling exercises.

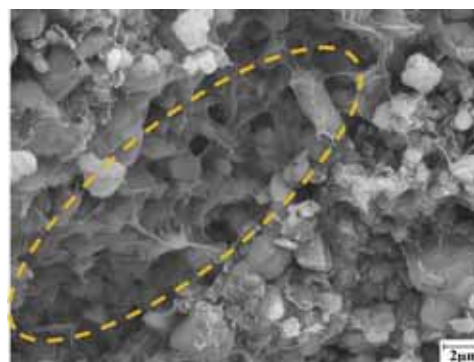


Fig. 8. FEG-SEM image of flooded **LMg130** (slice 6), showing pore surfaces and throats covered by newly formed Si-Mg-bearing minerals (orange dashed circle). (For interpretation of the references to colour in this figure legend, the reader is referred to the Web version of this article.)

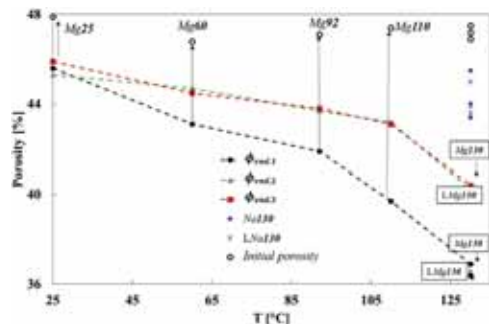


Fig. 9. Porosity values ($\phi_{\text{end},1}$, $\phi_{\text{end},2}$, $\phi_{\text{end},3}$) of each flooded core (Mg25, Mg60, Mg92, Mg110, Mg130, LMg130, LNa130 and Na130) versus applied temperatures.

5. Conclusions

In previous works selected outcrop chalks have been studied in terms of rock mechanical behaviour and chemical interactions when flooding various brines or more general fluids to gain information related to enhanced oil recovery (EOR) in the North Sea. Reservoir chalks and some on-shore chalks contain high amounts of SiO_2 , but the role of silicates in rock-fluid interactions has not yet been fully understood.

For the first time, a systematic study is presented on silica-rich (3.5–6 wt percent) reactive chalk from Aalborg (Denmark) flooded in experiments under a variety of different temperatures comparable to the reservoir and injection well conditions in the North Sea. The cores were flooded with 0.219 mol/L MgCl_2 or 0.657 mol/L NaCl brine at North Sea reservoir temperatures (Valhall field, 92 °C and Ekofisk field, 130 °C) and other temperatures (25, 60 and 110 °C) in a series of tri-axial tests over 2–4 months. The NaCl flooded cores (flooded at 130 °C only) show comparable creep rates as MgCl_2 flooded cores tested at 25 and 60 °C. Cores flooded with MgCl_2 -brine show systematically higher creep rates at increasing temperatures.

Effluent profiles show that calcite and opal-CT dissolution and magnesium retention increase with increasing temperatures, supported by whole-rock geochemical analyses, FEG-SEM-EDS, XRD and solid density measurements. After flooding with MgCl_2 at 110 and 130 °C newly formed magnesite is observed, size and abundance increasing with temperature and time. In the cores tested at temperatures 25, 60 and 92 °C, magnesite crystals have not been positively identified but an increase in MgO in whole-rock analyses is detected. Simultaneously, silica-distribution is altered by flooding, both through dissolution of silica-bearing phases, primary opal-CT, and precipitation of Mg-Si-bearing minerals, identified by whole-rock geochemistry, effluent measurements and FEG-SEM-EDS.

Our findings suggest that the presence of reactive opal-CT in Aalborg chalk plays a crucial role in the temperature range from 25 to 130 °C. The Si^{4+} ions obtained by dissolution of silicate-bearing phases allow for interaction with Mg^{2+} in the brine, resulting in precipitation of Si-Mg-bearing minerals, which in turn affected the SSA, precipitation of other minerals and changes in geo-mechanical parameters.

A novel observation for opal-CT bearing chalk was the identification, by FEG-SEM-EDS, of significant re-precipitation of Si-Mg-bearing minerals during MgCl_2 injection at all temperatures; distributed throughout the cores tested at 92, 110 and 130 °C, but only near the inlet of the cores tested at 25 and 60 °C. Specific surface area (SSA) increases accordingly in the MgCl_2 flooded cores, as expected, caused by the formation of flaky Si-Mg-bearing minerals and minute magnesium bearing carbonate crystals during the tests at mentioned temperatures; however, in NaCl flooded cores dissolution of silica-bearing

phases, mainly opal-CT, can alter the distribution of silica and reduce the SSA. Consequently, the processes of dissolution of silicate and calcite and re-precipitation as magnesite, Mg-Si-bearing minerals and possibly other Mg-rich minerals are the dominant control for the strong reduction (> 90%) in permeability for the MgCl_2 flooded cores at higher temperatures (92, 110 and 130 °C). The temperature effects on chemical alterations are also reflected in the porosity evolution. With increasing temperature, chemical alterations play an increasingly significant role, based on deviations in porosity estimates solely based on pore volume reduction, compared to direct calculations of porosity after flooding. The presence of opal-CT affects the distribution of MgO in the flooded cores, especially at high temperature. This shows the increased complexity of chemical reactions and in equilibrium states when adding relatively small amounts (3.5–6.0 wt%) of reactive silica-phases.

This study confirms that in brine-rock systems, temperature, together with the original composition (mineralogy), are active factors in controlling chemo-mechanical interactions. Specifically, siliceous phases in the form of opal-CT reacts actively towards MgCl_2 and significantly influence permeability. The results from this study should be taken into consideration when predicting the mechanical behaviour and mineralogical changes during brine injection in reservoir under various temperatures.

Acknowledgements

The authors thank the Faculty of Science and Technology at UiS for the PhD grant for Wenxia Wang and the National IOR Centre of Norway for the PhD grant for Mona Wethrus Minde. We are grateful to Tania Hildebrand-Habel for the FEG-SEM work on two of the cores (Mg130, LMg130). The authors thank COREC and also acknowledge the Research Council of Norway (230303) and the industry partners; ConocoPhillips Skandinavia AS, Aker BP ASA, Eni Norge AS, Maersk Oil Norway AS, DONG Energy A/S, Denmark, Statoil Petroleum AS, ENGIE E&P NORGE AS, Lundin Norway AS, Halliburton AS, Schlumberger Norge AS, Wintershall Norge AS, DEA Norge AS of The National IOR Centre of Norway for support.

The research presented is integral part of the PhD theses of Mona Wethrus Minde and Wenxia Wang at UiS.

Appendix A. Supplementary data

Supplementary data related to this article can be found at <http://dx.doi.org/10.1016/j.petrol.2018.05.072>.

References

- Andersen, M.A., Foged, N., Pedersen, H.F., 1992. The rate-type compaction of a weak North Sea chalk. In: Wawersik, T. (Ed.), *Rock Mechanics*. Balkema, Rotterdam.
- Andersen, P.Ø., Evje, S., Madland, M.V., Hiorth, A., 2012. A geochemical model for interpretation of chalk core flooding experiments. *Chem. Eng. Sci.* 84, 218–241. <http://dx.doi.org/10.1016/j.ces.2012.08.038>.
- Andersen, P.Ø., Evje, S., 2016. A model for reactive flow in fractured porous media. *Chem. Eng. Sci.* 145, 196–213. <http://dx.doi.org/10.1016/j.ces.2016.02.008>.
- Andersen, P.Ø., Wang, W., Madland, M.V., Zimmermann, U., Korsnes, R.I., Bertolino, S.R.A., Minde, M.W., Schulz, B., Gilbricht, S., 2017. Comparative study of five outcrop chalks flooded at reservoir conditions: chemo-mechanical behaviour and profiles of compositional alteration. *Transport Porous Media* 1–47. <http://dx.doi.org/10.1007/s11242-017-0953-6>.
- Anderson, T.F., Arthur, M.A., 1983. Stable isotopes of oxygen and carbon and their application to sedimentologic and environmental problems. In: Arthur, M.A., Anderson, T.F., Kaplan, I.R., Veizer, J., Land, L.S. (Eds.), *Stable Isotopes in Sedimentary Geology*. Society of Economic Paleontologists and Mineralogists, Short Course Notes, vol. 10 1–151.
- Anderson, T.L., 1995. *Fracture Mechanics: Fundamentals and Applications*, second ed. CRC Press, Boca Raton.
- André, L., Audigane, P., Azaroual, M., Menjoz, A., 2007. Numerical modeling of fluid-rock chemical interactions at the supercritical CO_2 -liquid interface during CO_2 injection into a carbonate reservoir, the Dogger aquifer (Paris Basin, France). *Energy Conversion and Management* 48, 1782–1797. <http://dx.doi.org/10.1016/j.enconman.2007.01.006>.
- Bertolino, S.R., Zimmermann, U., Madland, M.V., Hildebrand-Habel, T., Hiorth, A., Korsnes, R.I., 2013. Mineralogy, geochemistry and isotope geochemistry to reveal fluid flow processes in flooded chalk under long term test conditions for EOR purposes. In: XV International Clay Conference, Brasil, pp. 676.

- Borromeo, L., Minde, M.W., Zimmermann, U., Andò, S., toccafondi, c., Ossikovski, R., 2017. A new frontier technique for nano-analysis on flooded chalk: TERS (Tip Enhanced Raman Spectroscopy). In: EAGE - 19th European Symposium on Improved Oil Recovery. University of Stavanger.
- Bromley, R.G., 1968. Burrows and borings in hardgrounds. *Medd. Dansk Geol.Foren.* 18, 247–250.
- Brunauer, S., Emmett, P.H., Teller, E., 1938. Adsorption of gases in multimolecular layers. *J. Am. Chem. Soc.* 60, 309–319. <http://dx.doi.org/10.1021/ja01269a023>.
- Crittenden, J.C., Trussell, D.W., Hand, K.J., Howe, G., Tchobanoglous, G., 2012. *MWH's Water Treatment: Principles and Design*, third ed. .
- Egeland, N., Minde, M.W., Kobayashi, K., Ota, T., Nakamura, E., Zimmermann, U., Madland, M.V., Korsnes, R.I., 2017. Quantification of mineralogical changes in flooded carbonate under reservoir conditions. In: 19th European Symposium on Improved Oil Recovery/IOR Norway 2017, Stavanger.
- Elraies, K.A., Basbar, A.E.A., 2015. The effect of water salinity on silica dissolution rate and subsequent formation damage during chemical EOR process. *Petroleum & environmental biotechnology* 6, 1–6. <http://dx.doi.org/10.4172/2157-7463.100020906>.
- Evje, S., Hiorth, A., Madland, M.V., Korsnes, R.I., 2009. A mathematical model relevant for weakening of chalk reservoirs due to chemical reactions. *Netw. Heterogeneous Media* 4 (4), 755–788.
- Fabricius, I.L., 2001. Compaction of microfossil and clay-rich chalk sediments. *Phys. Chem. Earth Part a Solid Earth and Geodesy* 26, 59–62.
- Fabricius, I.L., Høier, C., Japsen, P., Korsboch, U., 2007. Modelling elastic properties of impure chalk from South Arne field, North Sea. *Geophys. Prospect* 55, 487–506.
- Fabricius, I.L., Borre, M.K., 2007. Stylolites, porosity, depositional texture, and silicates in chalk facies sediments, Ontong Java Plateau-Gorm and Tyra fields, North Sea. *Sedimentology* 54, 183–205.
- Fjær, E., Holt, R.M., Horsrud, P., Raaen, A.M., Risnes, R., 2008. *Petroleum Related Rock Mechanics*, second ed. Elsevier, Amsterdam, Netherlands, pp. 491–492.
- Fournier, R.O., 1973. Silica in thermal water: laboratory and field investigations. In: *Proceedings of the International Symposium on Hydrogeochemistry and Biochemistry*. vol. 1, pp. 122–139.
- Gislason, S.R., Veblen, D.R., Livi, K.J.T., 1993. Experimental meteoric water-basalt interaction-Characterization and interpretation of alteration products. *Geochem. Cosmochim. Acta* 57, 1459–1471. [http://dx.doi.org/10.1016/0016-7037\(93\)90006-1](http://dx.doi.org/10.1016/0016-7037(93)90006-1).
- Green, D.W., Willhite, G.P., 1998. Enhanced oil recovery. In: Henry, L. (Ed.), *Doherty Memorial Fund of AIME. Society of Petroleum Engineers*, Richardson, TX.
- Gunnarsson, I., Arnrösson, S., Jakobsdottir, S., 2005. Precipitation of poorly crystalline antigorite under hydrothermal conditions. *Geochem. Cosmochim. Acta* 69, 2813–2828. <http://dx.doi.org/10.1016/j.gca.2005.02.001>.
- Hellmann, R., Rengers, P., Gratier, J., Guiguet, R., 2002. Experimental pressure solution compaction of chalk in aqueous solutions Part 1. Deformation behavior and chemistry. In: Hellmann, R., Wood, S.A. (Eds.), *Water-rock Interactions, Ore Deposits, and Environmental Geochemistry: a Tribute to Davod a. Crerar*. vol. 7, pp. 129–152.
- Hermansen, H., Thomas, L.K., Sylte, J.E., Aasboe, B.T., 1997. Twenty Five Years of Ekofisk Reservoir Management. pp. 873–885. <http://dx.doi.org/10.2118/38927-ms>.
- Hermansen, H., Landa, G.H., Sylte, J.E., Thomas, L.K., 2000. Experiences after 10 years of waterflooding the Ekofisk field, Norway. *J. Petrol. Sci. Eng.* 26, 11–18.
- Hiorth, A., Jøttessuen, E., Cathles, L.M., Madland, M.V., 2013. Precipitation, dissolution, and ion exchange processes coupled with a lattice Boltzmann advection diffusion solver. *Geochem. Cosmochim. Acta* 104, 99–110. <http://dx.doi.org/10.1016/j.gca.2012.11.019>.
- Hjuler, M.L., 2007. *Diagenesis of Upper Cretaceous Onshore and Offshore Chalk from the North Sea Area*. PhD thesis, Technical University of Denmark.
- Hjuler, M.L., Fabricius, I.L., 2009. Engineering properties of chalk related to diagenetic variations of Upper Cretaceous onshore and offshore chalk in the North Sea area. *J. Petrol. Sci. Eng.* 68, 151–170. <http://dx.doi.org/10.1016/j.petrol.2009.06.005>.
- Hänchen, M., Prigiobbe, V., Baciocchi, R., Mazzotti, M., 2008. Precipitation in the Mg-carbonate system-effects of temperature and CO₂ pressure. *Chem. Eng. Sci.* 63 (4), 1012–1028.
- Korsnes, R.I., Strand, S., Hoff, Ø., Pedersen, T., Madland, M.V., Austad, T., 2006a. Does the chemical interaction between seawater and chalk affect the mechanical properties of chalk. In: *The International Symposium of the International Society for Rock Mechanics*. <http://dx.doi.org/10.1201/9781439833469.ch61>.
- Korsnes, R.I., Madland, M.V., Austad, T., 2006b. Impact of brine composition on the mechanical strength of chalk at high temperature. In: *The International Symposium of the International Society for Rock Mechanics*. Liège, Belgium, <http://dx.doi.org/10.1201/9781439833469.ch18>.
- Korsnes, R.I., Madland, M.V., Austad, T., Haver, S., Røslund, G., 2008. The effects of temperature on the water weakening of chalk by seawater. *J. Petrol. Sci. Eng.* 60, 183–193. <http://dx.doi.org/10.1016/j.petrol.2007.06.001>.
- Kristiansen, T.G., Barkved, O.I., Buer, K., Bakke, R., 2005. Production-induced deformations outside the reservoir and their impact on 4D seismic. *International Petroleum Technology Conference* 1–12. <http://dx.doi.org/10.2523/IPTC-10818-MS>.
- Lauridsen, B.W., Surlyk, F., Bromley, R.G., 2011. Trace fossils of a cyclic chalk–marl succession: the upper Maastrichtian Rørdal Member, Denmark. *Cretac. Res.* 32, 194–202. <http://dx.doi.org/10.1016/j.cretres.2010.12.002>.
- MacDonald, Gordon J.F., 1956. Experimental determination of calcite-aragonite equilibrium relations at elevated temperatures and pressures. *Am. Mineral.* 41, 744–756.
- Madland, M.V., Midtgarden, K., Manafov, R., Korsnes, R.I., Kristiansen, T.G., Hiorth, A., 2008. The effect of temperature and brine composition on the mechanical strength of Kansas chalk. In: *International Symposium of the Society of Core Analysts*. Abu Dhabi.
- Madland, M.V., Hiorth, A., Omdal, E., Megawati, M., Hildebrand-Habel, T., Korsnes, R.I., Evje, S., Cathles, L.M., 2011. Chemical alterations induced by rock–fluid interactions when injecting brines in high porosity chalks. *Transport Porous Media* 87, 679–702. <http://dx.doi.org/10.1007/s11242-010-9708-3>.
- McLennan, S.M., Taylor, S.R., Hemming, S.R., 2006. Composition, differentiation, and evolution of continental crust: constraints from sedimentary rocks and heat flow. In: Brown, M., Rushmer, T. (Eds.), *Evolution and Differentiation of the Continental Crust*. Cambridge Univ Press, Cambridge, pp. 92–134.
- Megawati, M., Andersen, P.O., Korsnes, R.I., Evje, S., Hiorth, A., Madland, M.V., 2011. The effect of aqueous chemistry pH on the time-dependent deformation behavior of chalk experimental and modelling study. In: *Pore2Fluid International Conference*. 16–18 Nov, Paris, France.
- Megawati, M., Hiorth, A., Madland, M.V., 2013. The impact of surface charge on the mechanical behaviour of high-porosity chalk. *Rock Mech. Rock Eng.* 46, 1073–1090. <http://dx.doi.org/10.1007/s00603-012-0317-z>.
- Megawati, M., Madland, M.V., Hiorth, A., 2015. Mechanical and physical behavior of high-porosity chalks exposed to chemical perturbation. *J. Petrol. Sci. Eng.* 133, 313–327. <http://dx.doi.org/10.1016/j.petrol.2015.06.026>.
- Meyers, P., 1975. Behaviour of silica in ion exchange and other systems. In: *The International Water Conference*, Pittsburgh, March. 1–10.
- Minde, M.W., Haser, S., Korsnes, R.I., Zimmermann, U., Madland, M.V., 2017. Comparative studies of mineralogical alterations of three ultra-long-term tests of onshore chalk at reservoir conditions. In: 19th European Symposium on Improved Oil Recovery/IOR NORWAY 2017, Stavanger.
- Möller, P., 1989. *Magnesite - geology, mineralogy, geochemistry, formation of Mg-carbonates*. In: Möller, P. (Ed.), *Monograph Series on mineral Deposits*. 28 1–300.
- Nagel, N.B., 2001. Compaction and subsidence issues within the petroleum industry: from Wilmington to Ekofisk and beyond. *Phys. Chem. Earth Solid Earth Geodes.* 26, 3–14. [http://dx.doi.org/10.1016/S1464-1895\(01\)00015-1](http://dx.doi.org/10.1016/S1464-1895(01)00015-1).
- Nermoen, A., Korsnes, R.I., Hiorth, A., Madland, M.V., 2015. Porosity and permeability development in compacting chalks during flooding of nonequilibrium brines: insights from long-term experiment. *Journal of Geophysical Research-Solid Earth* 120, 2935–2960. <http://dx.doi.org/10.1002/2014JB011631>.
- Nermoen, A., Korsnes, R.I., Aursjø, O., Madland, M.V., Kjorslevik, T.A.C., Østensen, G., 2016. How stress and temperature conditions affect rock-fluid chemistry and mechanical deformation. *Frontiers in Physics* 4, 1–19. <http://dx.doi.org/10.3389/fphy.2016.00002>.
- Newman, G.H., 1983. The effect of water chemistry on the laboratory compression and permeability characteristics of some North Sea chalks. *J. Petrol. Technol.* 35, 976–980. <http://dx.doi.org/10.2118/10203-pa>.
- Olsen, C., 2007. *Elastic and Electric Properties of North Sea Chalk*. PhD thesis. .
- Risnes, R., Flaegeng, O., 1999. Mechanical properties of chalk with emphasis on chalk–fluid interactions and micromechanical aspects. *Oil & Gas Science and Technology- Revue D Ipf Energies Nouvelles* 54, 751–758. <http://dx.doi.org/10.2516/Ogst-1999063>.
- Risnes, R., 2001. Deformation and yield in high porosity outcrop chalk. *Phys. Chem. Earth Solid Earth Geodes.* 26, 53–57. [http://dx.doi.org/10.1016/S1464-1895\(01\)00022-9](http://dx.doi.org/10.1016/S1464-1895(01)00022-9).
- Risnes, R., Madland, M.V., Hole, M., Kwabiah, N.K., 2005. Water weakening of chalk-mechanical effects of water-glycol mixtures. *J. Petrol. Sci. Eng.* 48, 21–36. <http://dx.doi.org/10.1016/j.petrol.2005.04.004>.
- Saldi, G.D., Jordan, G., Schott, J., Oelkers, Eric H., 2009. Magnesite growth rates as a function of temperature and saturation state. *Geochem. Cosmochim. Acta* 73, 5646–5657.
- Stenestad, E., 2006. *Fluviokarst in the top of the Maastrichtian chalk at Rørdal, Northern Jutland*. Denmark. *Bull. geo. Soc. Denmark* 53, 93–110.
- Surlyk, F., Stemmerik, L., Ahlborn, M., Harlou, R., Lauridsen, B.W., Rasmussen, S.L., Schovsbo, N., Sheldon, E., Thibault, N., 2010. The cyclic Rørdal Member-a new lithostratigraphic unit of chronostratigraphic and palaeoclimatic importance in the upper Maastrichtian of Denmark. *Bull. Geol. Soc. Den.* 58, 89–98.
- Wang, W., Madland, M.V., Zimmermann, U., Nermoen, A., Korsnes, R.I., Bertolino, S.A.R., Hildebrand-Habel, T., 2016. Evaluation of Porosity Change during Chemo-mechanical Compaction in Flooding Experiments on Liège Outcrop Chalk. *The Geological Society of London*<http://dx.doi.org/10.1144/SP435.10>. Special publication.
- Wetzel, A., 1989. Influence of heat flow on ooze/chalk cementation: quantification from consolidation parameters in DSDP Sites 504 and 505 sediments. *J. Sediment. Petrol.* 59, 539–547.
- Wilson, M.J., 2014. The structure of opal-CT revisited. *Journal of Non-Crystalline Solids* 405, 68–75. <http://dx.doi.org/10.1016/j.jnoncrysol.2014.08.052>.
- Wright, E.K., 1987. Stratification and paleocirculation of the late cretaceous Western interior seaway of North America. *Geol. Soc. Am. Bull.* 99, 480–490. [http://dx.doi.org/10.1130/0016-7606\(1987\)99<480:SAPOTL>2.0.CO;2](http://dx.doi.org/10.1130/0016-7606(1987)99<480:SAPOTL>2.0.CO;2).
- Zhang, P., Tweheyo, M.T., Austad, T., 2007. Wettability alteration and improved oil recovery by spontaneous imbibition of seawater into chalk: impact of the potential determining ions Ca²⁺, Mg²⁺, and SO₄²⁻. *Colloid. Interface. Physicochem. Eng. Aspect.* 301, 199–208. <http://dx.doi.org/10.1016/j.colsurfa.2006.12.058>.
- Zimmermann, U., Madland, M.V., Bertolino, S.A.R., Hildebrand-Habel, T., 2013. Tracing fluid flow in flooded chalk under long term test conditions. In: *75th EAGE Conference & Exhibition Incorporating SPE*. London.
- Zimmermann, U., Madland, M.V., Nermoen, A., Hildebrand-Habel, T., Bertolino, S.A.R., Hiorth, A., Korsnes, R.I., Audinot, J.N., Grysan, P., 2015. Evaluation of the compositional changes during flooding of reactive fluids using scanning electron microscopy, nano-secondary ion mass spectrometry, x-ray diffraction and whole rock geochemistry. *AAPG (Am. Assoc. Pet. Geol.) Bull.* 99, 791–805. <http://dx.doi.org/10.1306/12221412196>.


Paper V: Comparative Study of Five Outcrop Chalks Flooded at Reservoir Conditions: Chemo-mechanical Behaviour and Profiles of Compositional Alteration

Andersen, P.Ø., Wang, W., Madland, M.V., Zimmermann, U., Korsnes, R.I., Bertolino, S.R.A., Minde, M.W., Schulz, B. and Gilbricht, S. (2017).

Transport in Porous Media 121, 135–181

The online version of this article (<https://doi.org/10.1007/s11242-017-0953-6>) contains supplementary material, which is available to authorized users.

Comparative Study of Five Outcrop Chalks Flooded at Reservoir Conditions: Chemo-mechanical Behaviour and Profiles of Compositional Alteration

P. Ø. Andersen,  W. Wang, M. V. Madland, U. Zimmermann, R. I. Korsnes, S. R. A. Bertolino, M. Minde, B. Schulz, S. Gilbricht,

Abstract This study presents experimental results from a flooding test series performed at reservoir conditions for five high-porosity Cretaceous onshore chalks from Denmark, Belgium and the USA, analogous to North Sea reservoir chalk. The chalks are studied in regard to their chemo-mechanical behaviour when performing tri-axial compaction tests while injecting brines (0.219 mol/L MgCl_2 or 0.657 mol/L NaCl) at reservoir conditions for 2–3 months ($T = 130\text{ °C}$; 1 PV/d). Each chalk type was examined in terms of its mineralogical and chemical composition before and after the mechanical flooding tests, using an extensive set of analysis methods, to evaluate the chalk- and brine-dependent chemical alterations.

All MgCl_2 -flooded cores showed precipitation of Mg-bearing minerals (mainly magnesite). The distribution of newly formed Mg-bearing minerals appears to be chalk-dependent with varying peaks of enrichment. The chalk samples from Aalborg originally contained abundant opal-CT, which was dissolved with both NaCl and MgCl_2 and partly re-precipitated as Si-Mg-bearing minerals. The Aalborg core injected with MgCl_2 indicated strongly increased specific surface area (from 4.9 m^2/g to within 7–9 m^2/g). Mineral precipitation effects were negligible in chalk samples flooded with NaCl compared to MgCl_2 . Silicates were the main mineralogical impurity in the studied chalk samples (0.3–6 wt%). The cores with higher SiO_2 content showed less deformation when injecting NaCl brine, but more compaction

when injecting MgCl_2 -brine. The observations were successfully interpreted by mathematical geochemical modelling which suggests that the re-precipitation of Si-bearing minerals leads to enhanced calcite dissolution and mass loss (as seen experimentally) explaining the high compaction seen in MgCl_2 -flooded Aalborg chalk. Our work demonstrates that the original mineralogy, together with the newly formed minerals, can control the chemo-mechanical interactions during flooding and should be taken into account when predicting reservoir behaviour from laboratory studies. This study improves the understanding of complex flow reaction mechanisms also relevant for field-scale dynamics seen during brine injection.

Keywords Chalk compaction · Creep acceleration · Dissolution–precipitation · Core flooding at reservoir conditions · Non-carbonate composition

List of symbols

a_h	Activity of H^+
A	Area (m^2)
C_i	Concentration variable of species i (mol/L pore volume)
D	Core diameter (mm)
$k_{1,i}, k_{2,i}$	Reaction rate parameter for mineral i ($\text{mol}/\text{m}^2/\text{s}$)
k_o	Original permeability (mD)
K_i	Solubility constant of mineral i (–)
L	Core length (mm)
M	Mass (g)
p_i, q_i, r_i, n_i	Reaction order parameters (–)
Q	Injection rate (mL/d)
V	Volume (L or cm^3)
$\delta^{13}\text{C}$	A measure of the ratio of stable isotopes ^{13}C and ^{12}C (‰)
$\delta^{18}\text{O}$	A measure of the ratio of stable isotopes ^{18}O and ^{16}O (‰)
ε	Axial creep strain ($\%$)
P	Solid density (cm^3/L)
ρ_w	Brine density (cm^3/L)
Φ	Porosity ($\%$)
Ω_i	Saturation state of mineral i (–)

Subscripts

bulk	Bulk volume (solids and pores)
core	Based on the core piece
dry	Dry sample
end	State after compaction–flooding tests
o	Original/unflooded state
pyc	Based on pycnometry
sat	Saturated sample

Abbreviations

AA	Aalborg
aq	Aqueous

b.d.l.	Below detection limit
BET	Brunauer–Emmett–Teller theory
DI-H ₂ O	Deionized water
DW	Distilled water
EDS	Energy-dispersive X-ray spectroscopy
EDX	Energy-dispersive X-ray
FEG-SEM	Field emission gun-scanning electron microscopy
FEP	Fluorinated ethylene propylene
Fm	Formation
HPLC	High-performance liquid chromatography
ICP-AES	Inductively coupled plasma atomic emission spectroscopy
ICP-MS	Inductively coupled plasma mass spectrometry
ICS	Ion chromatography system
KA	Kansas
LI	Liège
LOI	Loss on ignition (wt%)
LVDT	Linear variable displacement transducer
MLA	(Automated SEM) mineral liberation analysis
MO	Mons
PID	Proportional integral derivative
PPM	Part per million
PV	Pore volume
s	Solid
SK	Stevens Klint
SMOW	Standard mean ocean water composition in Vienna Pee Dee Belemnite
SSA	Specific surface area (m ² /g)
Sup. Mat.	Supplementary Material
TDS	Total dissolved solids (g/L)
TEM	Transmission electron microscopy
TOT/C	Total carbon (wt%)
wt%	Weight per cent
XRD	X-ray diffraction

1 Introduction

The physicochemical interplay between minerals and fluids is of great importance in many natural and industrial settings (Putnis 2002; Ruiz-Agudo et al. 2014). Water injection into reservoirs is extensively applied to increase oil recovery and the inherent chemical fluid–rock interactions, and subsequent changes in mechanical properties have led to investigations towards more optimal injection fluids. In the chalk field Ekofisk in the North Sea, reservoir compaction (initiated by production) continued even after reservoir re-pressurization by seawater injection. The relationships between mechanical properties of reservoir chalk and pore fluids have been of significant interest in scientific research and industry ever since (Hermansen et al. 1997, 2000; Risnes and Flaageng 1999; Nagel 2001; Risnes et al. 2005; Fabricius and Borre 2007).

Research shows that compaction is affected mechanically by effective stresses, but also depends on porosity, chemistry, diagenetic processes and cementation (Engstrom 1992;

Havmøller and Foged 1996; Bjørlykke and Høeg 1997; Zhang et al. 2010; Bjørlykke 2014). Varying the ionic concentrations of Ca^{2+} , Mg^{2+} and SO_4^{2-} in the injected brines can lead to changes (weakening) in mechanical properties of chalk rock (Newman 1983; Strand et al. 2003; Korsnes et al. 2006a, b, 2008; Madland et al. 2008). This effect has among others been related to chemical reactions involving dissolution of the chalk matrix (Madland et al. 2011; Zimmermann et al. 2013, 2015; Megawati et al. 2015; Wang et al. 2016), which is also coupled to formation of new minerals. Injection of synthetic seawater into Liège chalk resulted in precipitation of anhydrite and Mg-bearing minerals, while abundant Mg-bearing minerals formed when MgCl_2 was injected (Madland et al. 2011). Long-term MgCl_2 -flooding tests (516 and 1072 d) on Liège chalk produced significant mineralogical changes where complete sections of the core were transformed from calcite to Mg-bearing minerals (Nerموen et al. 2015; Zimmermann et al. 2015), which is in line with modelling results (Hiorth et al. 2013). Magnesite was the dominant new phase. Compaction while exposing the rock to inert brines normally results in less deformation compared to using reactive brines that can dissolve more calcite (Hellmann et al. 2002). Switching injection from 0.219 mol/L MgCl_2 to a similar brine that was equilibrated with chalk, and thus inert, significantly reduced the creep rate (Megawati et al. 2011). Several researchers have also emphasized the role of non-carbonate minerals in chalk (Fabricius 2001; Fabricius et al. 2007; Hjuler 2007; Strand et al. 2007; Hjuler and Fabricius 2009; Megawati et al. 2011). Fabricius and Borre (2007) suggest that formation of Ca–Si complexes can lead to increased solubility of calcite with possible impacts on geological processes in the North Sea. Madland et al. (2011) tested Liège cores while flooding 0.1095 mol/L MgCl_2 for ~ 17 d. Parts of the original non-carbonate phase, in form of silicate minerals, were dissolved and re-precipitated forming a new silicate mineral phase with a clay-like appearance as observed in scanning electron microscopy (SEM) images. Megawati et al. (2015) studied a variety of outcrop chalks in terms of their compaction behaviour and noted a strong dependence on non-carbonate content. In particular, clean chalks displayed a very slow creep phase with a sudden acceleration later on, while more impure chalks had a high and steady compaction. Research has also shown that compaction can affect chemistry by pressure solution (Newman 1983): when increasing the applied stress on a core, which is transferred to the grain-to-grain contacts, these contact points effectively obtain increased mineral equilibrium constants compared to open surfaces (Paterson 1973; Rutter 1976) which can result in a progressive local dissolution (Hellmann et al. 2002; Zhang et al. 2011). Neveux et al. (2014) observed increased brine–mineral interaction during flooding experiments when systematically increasing the differential stresses.

Outcrop chalks and synthetic brines are ideally suited for systematic research. Searching for reservoir chalk substitutes, it is desirable to have similarity in mineralogy, sedimentary age and environment, permeability and porosity, hence combining geological with engineering data sets. In this contribution we test samples from five outcrop chalks of Cretaceous age from Kansas, Mons, Liège, Aalborg and Stevns Klint. They have similar age (Cretaceous) and porosity as North Sea reservoir chalk. The Mons and Stevns Klint samples were pure (> 99 wt% calcite), while the others contained more impurities. Previous XRD analyses of the clay fraction ($< 2 \mu\text{m}$) from the five chalk types have shown significant differences in mineralogical assemblage (Bertolino et al. 2013), indicative of different diagenetic conditions. Stevns Klint and Aalborg chalks have been suggested as suitable geomechanical analogues to the Valhall field chalk due to their modest calcite redistribution and poorly connected particles (Hjuler and Fabricius 2009). Liège chalk is comparable to the Ekofisk field in terms of mechanical properties (Collin et al. 2002; Jarvis 2006; Hjuler and Fabricius 2009). The aim in this work is to investigate how different chalks behave under similar experimental conditions. In similarity to the work by Megawati et al. (2015), chalk cores from the men-

tioned five outcrops were flooded with two simplified brines (0.219 mol/L MgCl_2 or 0.657 mol/L NaCl) at Ekofisk reservoir temperature, 130 °C, while compacting in creep state. Strain and effluent measurements were taken continuously. The tests in this work were performed for a longer period of time (2–4 months) to properly document the creep behaviour for the various outcrops. The main new contribution of this paper is, however, the comparative analysis of chemical alterations along the cores after the compaction–flooding tests: each core was divided along its flooding direction into seven slices of comparable size (see Fig. 1b, in Sect. 2.2.1). Further, each slice was examined in terms of composition and mineralogy using geological analysis tools such as pycnometry, field emission gun-scanning electron microscopy (FEG-SEM), mineral liberation analyses (MLA), X-ray diffraction (XRD), C–O stable isotope analyses, whole-rock geochemistry and measurement of specific surface area (Brunauer–Emmett–Teller (BET) method with liquid nitrogen). This allows a qualitative and quantitative description of the alteration profiles along each core. The measurements were compared to representative unflooded material. Cutting a core to examine individual slices has been performed previously in works such as Megawati et al. (2015), Nermoen et al. (2015), Zimmermann et al. (2015), and Wang et al. (2016), but have been limited to the study of one chalk type or one core and using only a few of the methods considered in this paper, making knowledge transfer more restricted. In particular, we compare five different chalk types exposed to similar experimental conditions. This work will focus on the geochemical alterations resulting from the tests. Impacts on engineering properties such as porosity and permeability will be left for future publication. We will highlight possible relations between the chemo-mechanical behaviour and the chalk types, which may originate from differences in non-carbonate mineral content, textural differences or geological histories. This can add more understanding to whether and to which extent non-carbonates in chalks play a role in the water-weakening process and allow us to evaluate the feasibility of these onshore chalks when comparing to reservoir chalks.

2 Experimental Procedures and Methods

2.1 Core Material and Injection Brines

Outcrop chalks were collected from five locations (from old to young): Kansas (KA), Mons (MO), Liège (LI), Aalborg (AA) and Stevns Klint (SK), see Table 1 for more details. All five types were deposited during the Cretaceous. Mons chalk (from the Trivières Formation) and Stevns Klint chalks are very pure (> 99 weight per cent (wt%) calcite), Kansas and Liège chalks are less pure with calcite content around 95–97 wt%, and Aalborg chalk contains 92–94 wt% calcite.

More details on the mentioned chalks in terms of petrography, petrophysics and mineralogy can be found in Molenaar and Zijlstra (1997), Gaviglio et al. (1999), Fabricius (2001), Frykman (2001), Tang and Firoozabadi (2001), Hart et al. (2004, 2005), Schroeder et al. (2006), Strand et al. (2007), Hjuler and Fabricius (2009) and Bertolino et al. (2013). Mechanical properties and compositions will be presented.

Table 2 contains information of the core samples applied in the tests. The original solid density ($\rho_{0\text{-pyc}}$) (between 2.67 and 2.70 g/cm^3), estimated by pycnometry measurements (see Sect. 2.2.9) of unflooded end pieces (Fig. 1a), is similar to that of calcite mineral, 2.71 g/cm^3 , but slightly lower, especially for AA5 (2.67 g/cm^3), AA1 (2.67 g/cm^3) and AA21 (2.67 g/cm^3). A second estimate of solid density was obtained using the whole cores ($\rho_{0\text{-core}}$),

Table 1 Geographical origin, geological age and calcite wt% of the studied chalks

Sample	Abbreviation	Location	Formation/member	Age	wt% calcite
Kansas	KA	USA, Niobrara	Niobrara Formation, Fort Hays Member	Late Cretaceous	95–97
Mons	MO	Belgium, Harmignies	Trivières Formation	Campanian	> 99
Liège	LI	Belgium, Hallembaye	Gulpen Formation	Campanian	95–97
Aalborg	AA	Denmark, Rørdal	Tor Formation, Rørdal Member	Maastrichtian	92–94
Stevns Klint	SK	Denmark, Sigerslev	Tor Formation, Sigerslev Member	Maastrichtian	> 99

from dividing the dry mass by the solid volume:

$$\rho_{\text{o-core}} = \frac{M_{\text{dry,o}}}{V_{\text{bulk,o}} - (M_{\text{sat,o}} - M_{\text{dry,o}}) / \rho_w}, \quad (1)$$

where $M_{\text{dry,o}}$ (g) is dry weight, $M_{\text{sat,o}}$ (g) saturated weight, $V_{\text{bulk,o}}$ (cm^3) bulk volume, and ρ_w (g/cm^3) brine density. These measurements yielded a wider range (between 2.63 and 2.71 g/cm^3) with often lower values (not more than 0.04 g/cm^3 as seen for AA21 and SK1) than the pycnometry estimates, although for KA6 (+ 0 g/cm^3), KA8 (+ 0.01 g/cm^3), AA1 (+ 0 g/cm^3) and SK2 (+ 0.02 g/cm^3) the estimate was the same or higher. The original porosities (ϕ_o) were high, in the range 37–47%. The initial permeabilities (k_o) were in the range 1.2–3.2 mD.

All cores were flooded for a period of 60–95 days (d), besides SK1 (45 d) and AA1 (115 d). For SK1 and AA1 mainly compaction results will be presented in this work, to illustrate repeatability compared to the cores SK6 and AA5. These four tests all applied the same injection brine: MgCl_2 .

Two brines were used for core flooding: 0.219 mol/L MgCl_2 and 0.657 mol/L NaCl, see Table 3. Their ionic strength is the same as of North Sea seawater: 0.657.

2.2 Experimental Preparation and Procedures

2.2.1 Flooding Experiments at 130 °C in a Standard Tri-axial Cell

Cylindrical samples were drilled from blocks collected from the five different outcrops (Table 1). Each sample was divided into three parts along the flooding direction (Fig. 1a). The central part was cut to a cylindrical core of diameter ~ 37 and ~ 38 mm and length ~ 70 mm and used for flooding–compaction tests. The two adjacent end pieces were used for analysis of unflooded material (Fig. 1a).

The cores have a length-to-diameter ratio close to two so that their strength can be expected to be insensitive to differences in diameter [see, for example, Fig. 7.2 in page 257 in Fjær et al. (2008)]. After preparation, the cores were dried for 12 h in a heating chamber at 100 °C to remove more than 99% water in the core before the dry mass $M_{\text{dry,o}}$ was determined. The calcite crystals are assumed to be unaffected by the drying conditions. Then the cores were

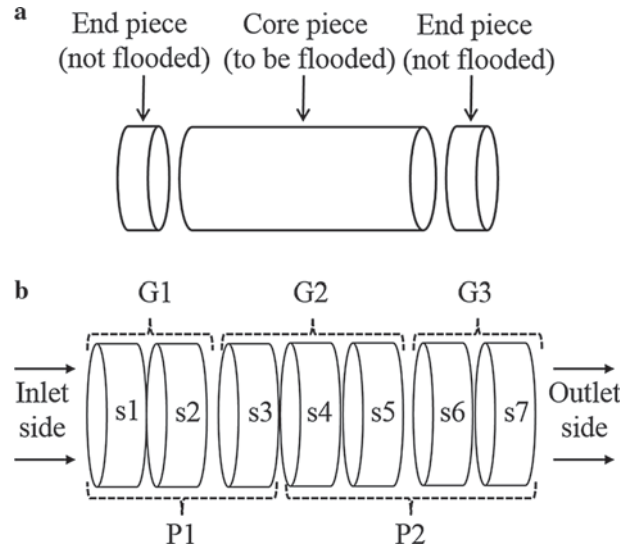


Fig. 1 **a** Material selection procedure: A cylindrical sample is cut into three pieces: the central core to be used in flooding–compaction tests and two adjacent end pieces used to measure properties of unflooded material, assumedly also representative of the core. **b** Scheme of the sectioning of the core after the flooding–compaction tests. Arrows indicate flow direction. The core was first cut into two parts P1 and P2 from which solid density was measured by dry weight and solid volume. The core was further cut into slices s1–s7 (from inlet to outlet) which were grouped into G1 (s1 + s2), G2 (s3 + s4 + s5) and G3 (s6 + s7). Each group was measured with pycnometry. The slices were analysed using the methods described in Sect. 2.2

evacuated by vacuum prior to being saturated with distilled water (DW) and then weighed to obtain the saturated mass $M_{\text{sat,o}}$. Porosity was then calculated from the ratio of volume water that could be saturated in the dried core divided by the bulk volume $V_{\text{bulk,o}}$ of the core:

$$\varphi = \frac{(M_{\text{sat,o}} - M_{\text{dry,o}})}{\rho_w V_{\text{bulk,o}}}. \quad (2)$$

ρ_w is the DW density. Calculated porosity values are listed in Table 2. The same experimental procedure was applied on all the cores studied in this paper such that brine- and chalk-dependent behaviour could be distinguished. The saturated cores were mounted into identical tri-axial cells. (For a description of the set-up, see Fig. 2.) Three Gilson (model 307 high-performance liquid chromatography—HPLC) pressure pumps were connected to each tri-axial cell enabling independent control of the piston pressure, confining pressure (radial stress) and injected flow rate (i.e. pump 1–3 in Fig. 2). The confining pressure balances the piston such that the axial stress has to be calculated from the confining pressure plus the piston pressure, to control the pore pressure and at the same time allow for continuous sampling of the effluent fluids. The cells were equipped with a heating jacket and a regulating system (Omron E5CN) with precise proportional integral derivative (PID) temperature control (± 0.1 °C). The axial strain was measured by an external axial linear variable displacement transducer (LVDT) placed on top of the piston to monitor the sample length with time. To isolate the core from the confining oil, a heat shrinkage sleeve (1–1/2” fluorinated ethylene propylene (FEP) with diameter of 33–43 mm and 0.5 mm wall thickness) was installed between the core and the confining oil. After core mounting, the confining pressure was

Table 2 Core labels, applied brines, dry core weight $M_{\text{dry},o}$ (g), length L_o (mm), diameter D_o (mm), solid density from pycnometry of end pieces $\rho_{o\text{-pyc}}$ (g/cm^3), and of whole core $\rho_{o\text{-core}}$ (g/cm^3), porosity φ_o (%), permeability k_o (mD), flooding rate Q (corresponding to 1 pore volume per day, PV/d), flooding time T (d) and specific surface area SSA (m^2/g)

Core	Brine	$M_{\text{dry},o}$ (g)	L_o (mm)	D_o (mm)	$\rho_{o\text{-pyc}}$ (g/cm^3)	$\rho_{o\text{-core}}$ (g/cm^3)	φ_o (%)	k_o (mD)	Q (mL/min)	T (d)	SSA (m^2/g)
KA6	NaCl	134.90	69.7	38.1	2.70	2.70	37.0	1.47	0.020	61	3.0
KA8	MgCl ₂	136.24	70.1	38.1	2.70	2.71	37.0	1.96	0.020	75	
MO12	NaCl	124.52	69.8	38.1	2.70	2.67	41.4	1.58	0.023	61	2.2
MO10	MgCl ₂	125.58	70.3	38.1	2.70	2.68	41.5	1.19	0.023	60	
LI2	NaCl	126.05	72.7	38.2	2.69	2.67	43.3	1.75	0.025	90	2.7
LI1	MgCl ₂	112.38	68.9	37.1	2.68	2.66	43.3	1.92	0.022	65	
AA21	NaCl	112.96	70.4	38.2	2.67	2.63	46.7	1.22	0.026	61	4.9
AA5	MgCl ₂	112.33	70.4	38.1	2.67	2.65	47.2	1.34	0.026	63	
AA1*	MgCl ₂	119.84	75.0	38.1	2.67	2.67	47.5	1.50	0.028	115	
SK2	NaCl	121.31	73.1	38.0	2.69	2.71	45.9	3.20	0.026	91	2.0
SK6	MgCl ₂	115.08	70.3	38.1	2.69	2.68	46.4	2.69	0.028	61	
SK1*	MgCl ₂	117.41	74.0	38.1	2.69	2.65	47.4	2.34	0.028	45	

Index 'o' refers to 'original state' before flooding and compaction. Results from SK1 and AA1 (marked *) are focused on compaction behaviour in this work

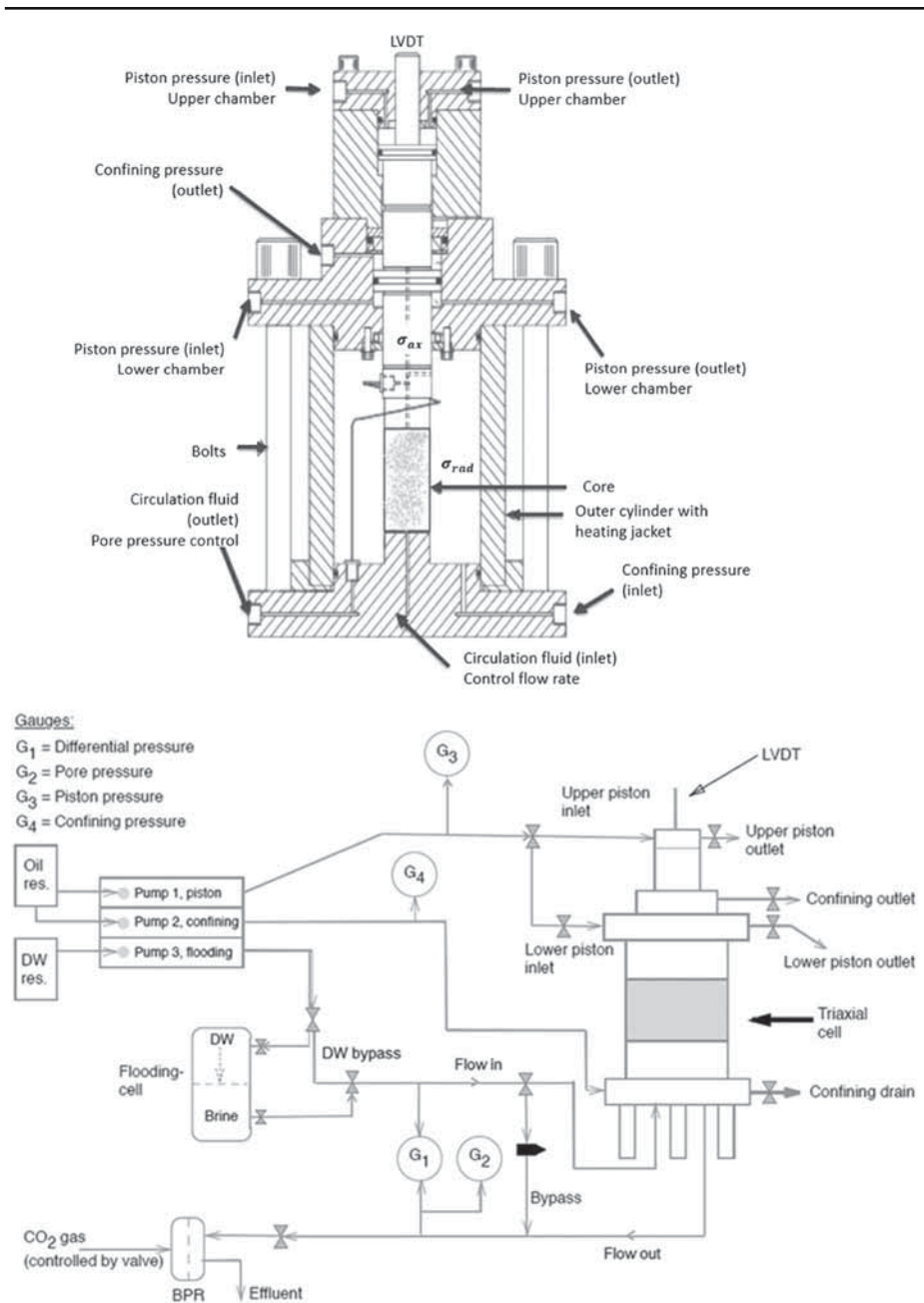


Fig. 2 Experimental set-up used in the flooding–compaction tests (figure originally from Nermoen et al. (2016), where more details are presented). Three pumps (piston, confining and flooding pump) were connected to the tri-axial cell (seen in detail in top figure). The flooding cell contained distilled water (upper chamber) and $MgCl_2/NaCl$ (lower chamber). Injection fluid enters the cell at ‘Circulation fluid (inlet)’ passes through the compacting core and is led out of the cell at ‘Circulation fluid (outlet)’. The whole set-up was connected to a computer and complete data, including confining, pore and piston pressure, flooding rate and time, which were logged automatically

Table 3 Brine compositions in flooding tests

Brine	Cl ⁻ (mol/L)	Mg ²⁺ (mol/L)	Na ⁺ (mol/L)	Ionic strength	TDS (g/L)
MgCl ₂	0.438	0.219	0	0.657	20.84
NaCl	0.657	0	0.657	0.657	38.4

TDS total dissolved solids

increased to 0.5 MPa. Thereafter, the experiments were conducted according to the following stages:

1. The core samples were flooded with three pore volumes (PVs) of distilled water (DW) overnight at ambient temperature to remove any salt precipitates that could affect the flooding tests. This flooding procedure does not significantly alter the geochemical measurements of the non-salt minerals in the core.
2. Change from flooding with DW to MgCl₂ or NaCl by attaching the flooding cell into the flow loop (see Fig. 2). The ion compositions of the injected brines are shown in Table 3. Throughout the rest of the test, the flow rate was set to 1 initial PV per day (Table 2).
3. The confining pressure and pore pressure were increased to 1.2 and 0.7 MPa, respectively, before the temperature was raised to 130 °C. The pore pressure and temperature were subsequently kept constant throughout the test. The core was left to equilibrate overnight.
4. After equilibration overnight, the confining pressure was increased from 1.2 MPa up to its creep stress by injecting hydraulic oil at a constant flow rate into the confining chamber using pump 2. During pressurization the piston pressure was set to 0.5 MPa to slightly overcome friction of the piston (0.3–0.4 MPa). This increased the axial stress to a value of 0.1–0.2 MPa above the radial stress. Because the additional axial stress is small compared to the radial stress the stress condition can be considered near hydrostatic. The stress–strain behaviour was monitored during increase in confining pressure. The bulk modulus parameter was calculated as the ratio of hydrostatic effective stress σ_h divided by volumetric strain ε_V during the linear deformation of the loading phase (see Fig. 6 in Sect. 3.7). The radial strain was not monitored and was for simplicity assumed equal to the axial strain ε_a (which is reasonable during hydrostatic deformation):

$$\text{Bulk modulus} = \frac{\sigma_h}{\varepsilon_V} \approx \frac{\sigma_h}{3\varepsilon_a} \quad (3)$$

When the rock began to deform plastically (Fig. 7 in Sect. 3.7), i.e. when the stress–strain behaviour became nonlinear, the yield point, i.e. the stress at onset of yield, was noted (Table 8). The confining pressure was further increased to the chosen creep stress (up to 8.5–23 MPa, Table 8 in Sect. 3.7) before the cores were left to compact in the following creep phase (deformation at constant stress).

The axial deformation at constant temperature, stress and pressure conditions (termed creep) was monitored during continuous flooding of MgCl₂ or NaCl brine. The creep magnitude through time is shown in Fig. 7. The pore pressure and confining pressure varied within 0.1 MPa such that the effective stresses were stable throughout the test period (assuming the Biot stress coefficient is ~ 1 , see Fjær et al. 2008, p. 33).

The pore pressure, hydraulic pressure difference, confining pressure, piston pressure, sample length (axial strain) and flooding time were logged continuously via a LabView program. Before dismantling the core, the sample was cleaned by injecting 3 PVs of distilled water to avoid precipitation of salts from the MgCl₂ and NaCl brines during drying. The

saturated weight ($M_{\text{sat, end}}$) was measured immediately after the dismantling of the cell. Then the core was placed in a drying cabinet at 100 °C and weighed several times until the dry mass ($M_{\text{dry, end}}$) stabilized. Each core was first cut into two parts P1 and P2 (see Fig. 1b) from which the solid mass and solid volume (from pycnometry) were used to estimate solid density ($\rho_{\text{end-pyc}}$). The core was further cut into seven slices, labelled s1 (inlet) to s7 (outlet), using a Struers Discotom-5 cutting machine (see Fig. 1b for the sectioning scheme). The slices were grouped into G1 (s1 + s2), G2 (s3 + s4 + s5) and G3 (s6 + s7) as seen in Fig. 1b, and a solid density estimate ($\rho_{\text{end-pyc}}$) was made by pycnometry for each group. The slices were then individually subjected to extensive geochemical analysis to identify the mineralogical changes along the core.

In the following, we list the analytical techniques used to study the core material prior and post flooding. Details regarding each technique, equipment and settings used and resulting accuracy are elaborated in Supplementary Material (Sup. Mat.).

2.2.2 Field Emission Gun-Scanning Electron Microscopy (FEG-SEM)

Fresh surfaces of unflooded and flooded material were examined to obtain visual images of the grains and rock structure on μm scale.

2.2.3 X-Ray Diffraction (XRD)

Provides the mineralogical composition of bulk samples (ca 1 g).

2.2.4 Automated SEM Mineral Liberation Analysis (SEM-MLA)

Applied to thin sections to estimate mineralogical distribution.

2.2.5 Stable Isotope Geochemistry (C–O Isotopes)

Oxygen and carbon isotope composition was measured on bulk samples.

2.2.6 Mass Measurements

Each core was measured before and after flooding to detect mass changes.

2.2.7 Ion Chromatography

Effluent samples were collected continuously. The concentrations of ions Mg^{2+} , Na^+ , Cl^- and Ca^{2+} were quantified.

2.2.8 Inductively Coupled Plasma Atomic Emission Spectroscopy (ICP-AES)

Analysis of effluent samples to obtain Si^{4+} concentrations.

2.2.9 Pycnometry (Solid Density Estimation)

Solid volume of bulk samples was measured with pycnometer. In combination with dry weight, solid density was calculated.

2.2.10 Specific Surface Area (SSA)

Specific surface area of bulk samples was measured by the Brunauer–Emmett–Teller (BET) theory.

2.2.11 Whole-Rock Geochemistry (Geochemical Composition)

Sample bulk material (ca 1 g) from unflooded material or each slice was examined for geochemical composition.

3 Results

3.1 Field Emission Gun-Scanning Electron Microscopy (FEG-SEM)

3.1.1 Unflooded Samples

The chalk samples from Kansas are coccolithic mudstone or wackestone, characterized by moderately preserved coccolithophores. Calcite grains often show significant overgrowth, and intra-fossil porosity is partly preserved (Fig. 3a, pink arrow, Sup. Mat. Fig. 1a). The microfossils are often filled with calcite crystals. The Mons chalk cores, collected from the Trivières Formation, are pure coccolithic mudstones. Large amounts of very small coccoliths and broken calcite crystals of organic or unknown origin are observed (Sup. Mat. Fig. 1b). Moderately well-preserved coccoliths are abundant. In the coccolithic mudstone from Liège, the microfossils are well preserved and some overgrowth and re-crystallization can be observed. The rocks contain significant amounts of shell fragments, also from macro-

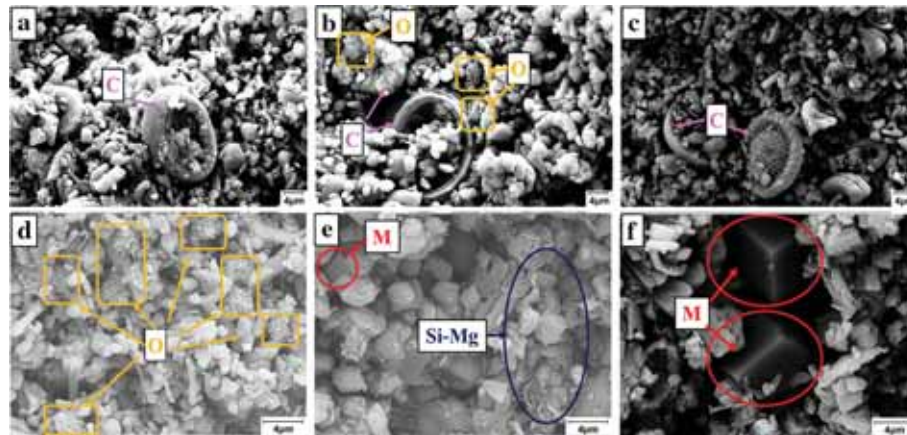


Fig. 3 SEM secondary electron (SE) images of unflooded material (end pieces) and flooded cores, with non-polished sample surfaces. **a** Unflooded Kansas chalk; **b** unflooded Aalborg chalk; **c** unflooded Stevns Klint chalk; **d** Aalborg core AA21 flooded with NaCl (slice 7); **e** Aalborg core AA5 flooded with MgCl₂ (slice 2); **(f)** Kansas core KA8 flooded with MgCl₂ (slice 1). ‘C’: Coccoliths are observed in all unflooded samples (indicated by pink arrows). ‘O’: Opal-CT lepispheres were spotted in Aalborg (marked by yellow square). ‘Si-Mg’: Si-Mg-bearing minerals were observed in AA5 (in dark blue), ‘M’: Magnesite is precipitated in MgCl₂-flooded cores (in red). The scale bar equals 4 micron

fossils (Sup. Mat. Fig. 1c). Aalborg chalk cores can be classified as a coccolithic mudstone or wackestone with large numbers of foraminifer shells and even layers of macrofossil debris (Sup. Mat. Fig. 1d). Coccolithophores are well preserved, but commonly show some overgrowth. Intra-fossil porosity is mostly preserved (Fig. 3b, pink arrow). This chalk contains accumulations of well-developed opal-CT lepispheres that often occur in larger intra-fossil pores (Fig. 3b, yellow square). Chalk cores from Stevns Klint consist of extremely pure coccolithic mudstone. Well-preserved coccolithophores and foraminifer shell fragments exist. Larger pore spaces of shell fragments are filled with minute calcite grains (Fig. 3c, pink arrow). Only a limited degree of overgrowth and re-crystallization can be observed (Sup. Mat. Fig. 1e).

3.1.2 NaCl-Flooded Cores

Applied FEG-SEM (Sup. Mat. Fig. 2a–e) showed no indication of precipitation of any new minerals, in agreement with earlier studies (Madland et al. 2011). The calcite grains observed near the inlet appear somewhat corner-rounded compared to unflooded material (see Fig. 9a (AA21, slice 1) and Sup. Mat. Fig. 1d; unflooded Aalborg material). In AA21, opal-CT was not observed near the inlet but found preserved further inside the flooded core (Fig. 3d, yellow square; Fig. 11b, c). Euhedral microfossils could still be observed in all the tested chalk types.

3.1.3 MgCl₂-Flooded Cores

Supplementary Material Fig. 3 shows FEG-SEM images from the MgCl₂-flooded cores. For all chalk types, the calcite grains appear corner-rounded, indicative for dissolution, although intact microfossils and coccolithophores can still be observed. The images also clearly reveal that crystals in hexagonal or trigonal shape, magnesite MgCO₃, have precipitated (Fig. 3e, f, red circles). In MO10, LI1, AA5 and SK6, euhedral magnesite crystals were not detected from slice 4 and towards the outlet, although geochemistry indicated MgO wt% between 2 and 9 times the average of unflooded material in those slices, (see Table 6a, c in Sect. 3.4). For KA8, euhedral magnesite crystals could only be found in slice 1 (Fig. 3f, inlet of KA8). Si–Mg-rich minerals in flake shape were found spread along the AA5 core (see Figs. 3e, 9e, f, green circle).

3.2 X-Ray Diffraction (XRD)

3.2.1 Unflooded Samples

Chalk material from Kansas contains calcite, traces of quartz and phyllosilicates (peak at 4.44–4.50 Å, Sup. Mat. Fig. 4a) such as the clay minerals illite, illite/smectite and kaolinite (Sup. Mat. Fig. 4b). Mons chalk contains almost pure calcite (Sup. Mat. Fig. 4a); traces of quartz were identified along with poorly ordered illite/smectite (Sup. Mat. Fig. 4b). The chalk from Liège appears homogeneous in XRD studies: besides calcite, only traces of quartz and feldspar can be identified (Sup. Mat. Fig. 4a). The clays are dominated by smectite and minor illite (Sup. Mat. Fig. 4b). Aalborg chalk contains dominant calcite with scarce quartz, very scarce opal-CT and gibbsite and traces of illite/smectite (Fig. 4a, Sup. Mat. Fig. 4b). The chalk sample from Stevns Klint differs from the other chalks because it is composed of almost pure calcium carbonate minerals, both calcite and Mg–calcite (Sup. Mat. Fig. 4a). Only traces of smectite with minor illite and quartz are observed (Sup. Mat. Fig. 4b).

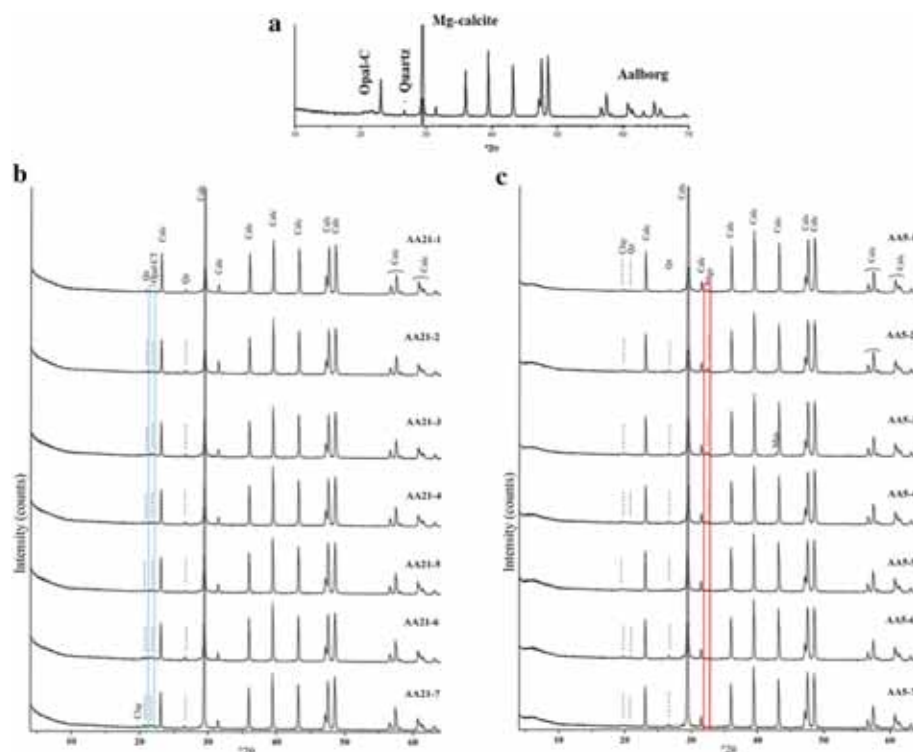


Fig. 4 XRD profiles **a** material from unflushed Aalborg chalk; **b** NaCl-flooded AA21 (slice 1–7); **c** MgCl₂-flooded AA5 (slice 1–7). Opal-CT is marked in blue dotted line. Magnesite is marked in red solid line. Remaining peaks marked ‘Cal’, ‘Clay’ and ‘Qz’ represent calcite, clay and quartz minerals, respectively

3.2.2 NaCl-Flooded Cores

There are no new grown minerals observed in the NaCl-flooded cores (Sup. Mat. Fig. 5, XRD analysis of slice 3 of each core). The description is reported in Table 4.

3.2.3 MgCl₂-Flooded Cores

All chalks flooded with MgCl₂ contain different proportions of magnesite, always exhibiting broad XRD peaks denoting the small crystal size of this mineral. Supplementary Material Fig. 6a, b shows an XRD comparison of slice 1 (inlet) and slice 3 from the MgCl₂-flooded cores. The analysis indicated more magnesite in slice 3 than slice 1 in all cases except KA8, which had the strongest magnesite peak in slice 1. Quartz was identified in all cores (as in unflushed material).

The Kansas core (KA8) was characterized by a higher content of magnesite compared to the other flooded chalks. Another important difference is that magnesite was more abundant in slice 1 than the other slices (Sup. Mat. Fig. 6a, b) and its XRD peak intensities diminishing progressively in the other slices; however, traces could still be found in slice 6. In the Mons core (MO10), magnesite was identified in increasing amounts from slice 1 to slice 3 (Sup. Mat. Fig. 6a, b), diminishing from slice 3 to 6 (only traces in this slice). In the Liège core (LI1), the XRD analysis identified the largest amount of magnesite in slice 3. Magnesite was

Table 4 Mineralogical analysis of XRD profiles for NaCl and MgCl₂-flooded cores

Core	Mineralogical description in NaCl-flooded cores	Core	Mineralogical description in MgCl ₂ -flooded cores
KA6	No new grown minerals	KA8	Magnesite was more abundant than in the other flooded chalks. Magnesite was more abundant in slice 1 than the other slices, diminishing progressively, but still noticeable in traces in slice 6
MO12	No new grown minerals	MO10	Magnesite was identified in increasing amounts from slice 1 to slice 3, diminishing from slice 3 to 6 (only traces in this slice)
LI2	No new grown minerals	LI1	Magnesite was observed in slice 1, 3 and 4, with most in slice 3, but not in the remaining slices. Traces of high-Mg calcite were found in slice 4
AA21	No new grown minerals	AA5	Scarce to minor magnesite was identified in slices 1–5 with a maximum in slices 2 and 3
SK2	No new grown minerals	SK6	Magnesite was identified in increasing amounts from slice 1 to slice 3, diminishing from slice 3 to 6 (only traces in slice 6)

also identified in slices 1 and 4, but not in the remaining slices. Traces of high-Mg calcite (Brindley and Brown 1980) were found in slice 4 (Sup. Mat. Fig. 6a, b). In the AA5 core (Fig. 4c), scarce to minor magnesite was identified in slices 1 to 5 with maximum amount in slices 2 and 3. Opal-CT, which was widespread in unflooded Aalborg chalk, was not identified in AA5 by XRD after flooding (Fig. 4c). The Stevns Klint core (SK6) gave similar observations as MO10. Magnesite was identified in increasing amounts from slice 1 to slice 3, diminishing from slice 3 to 6 (only traces in this slice), but slice 1 of SK6 contained more magnesite than slice 1 of MO10 (Sup. Mat. Fig. 6a, b).

3.3 Automated SEM Mineral Liberation Analysis (SEM-MLA)

SEM-MLA involving EDX spectral mapping (GXMAP mode) was applied on unflooded material and slices 1, 3 and 7 of flooded cores with flooded surfaces to interpret the mineralogical changes. The results are summarized in Table 5.

3.3.1 Unflooded Samples

MLA analyses confirmed the mineralogical properties of unflooded chalk as described above. An MLA image of unflooded Aalborg chalk is given in Fig. 5a. Images of the other samples are found in Sup. Mat. Fig. 7. Calcite was the dominant mineral. Quartz could also be detected (grey grains in Fig. 7a) in qualitatively larger amounts for Liège and Aalborg compared to Kansas, Mons and Stevns Klint. MLA also detected clay minerals: illite and/or chlorite in all samples and kaolinite in Kansas and Mons; glauconite was detected in Kansas, Mons, Liège and Stevns Klint; apatite was observed in Mons, Aalborg and Stevns Klint. In Aalborg chalk, more microfossils could be observed than for other chalk material. The EDX spectral mapping did not discriminate opal-CT from other Si-bearing phases such as quartz. These phases can be distinguished by their crystallographic properties in X-ray diffraction, but not by their equivalent elemental compositions (Si, O). Also, due to small particle sizes of the

Table 5 Mineralogical analysis of MLA images for unflooded end piece material and NaCl- and MgCl₂-flooded cores

Unflooded material	MLA interpretation	NaCl-flooded cores	MLA interpretation	MgCl ₂ -flooded cores	MLA interpretation
KA	Mg-Calcite, calcite-Si mix, magnesite, dolomite, quartz-silica polymorphs, glauconite, illite and/or chlorite, kaolinite and/or clay	KA6	KA6-1: Mg-Calcite, calcite-Si mix, magnesite, dolomite, quartz-silica polymorphs, glauconite, illite and/or chlorite, kaolinite and/or clay	KA8	KA8-1: Mg-Calcite, calcite-Si mix, magnesite, dolomite, quartz-silica polymorphs, illite and/or chlorite KA8-3: Mg-Calcite, calcite-Si mix, magnesite, dolomite, quartz-silica polymorphs, illite and/or chlorite KA8-7: Mg-Calcite, calcite-Si mix, dolomite, quartz-silica polymorphs, apatite, illite and/or chlorite,
MO	Mg-Calcite, calcite-Si mix, apatite, quartz-silica polymorphs, glauconite, illite and/or chlorite, kaolinite and/or clay	MO12	MO12-1: Mg-Calcite, calcite-Si mix, quartz-silica polymorphs, glauconite, apatite, illite and/or chlorite, kaolinite and/or clay	MO10	No data
LI	Calcite-Si mix, dolomite, quartz-silica polymorphs, glauconite, illite and/or chlorite	LI2	LI2-1: Calcite-Si mix, dolomite, quartz-silica polymorphs, glauconite, illite and/or chlorite	LI1	LI1-1: Mg-Calcite, calcite-Si mix, magnesite, dolomite, quartz-silica polymorphs, apatite, illite and/or chlorite LI1-3: Mg-Calcite, calcite-Si mix, magnesite, dolomite, quartz-silica polymorphs, apatite, illite and/or chlorite LI1-7: Mg-Calcite, calcite-Si mix, dolomite, quartz-silica polymorphs, apatite, illite and/or chlorite

Table 5 continued

Unflooded material	MLA interpretation	NaCl-flooded cores	MLA interpretation	MgCl ₂ -flooded cores	MLA interpretation
AA	Mg-Calcite, calcite-Si mix, quartz-silica polymorphs, apatite, illite and/or chlorite	AA21	AA21-1: Mg-Calcite, calcite-Si mix, quartz-silica polymorphs, apatite, illite and/or chlorite	AA5	AA5-1: Mg-Calcite, magnesite, dolomite, quartz-silica polymorphs, talc, illite and/or chlorite AA5-3: Mg-Calcite, calcite-Si mix, magnesite, dolomite, quartz-silica polymorphs, apatite, talc, illite and/or chlorite AA5-7: Mg-Calcite, calcite-Si mix, magnesite, dolomite, quartz-silica polymorphs, apatite, talc, illite and/or chlorite
SK	Mg-Calcite, calcite-Si mix, quartz-silica polymorphs, glauconite, apatite, illite and/or chlorite	SK2	SK2-1: Mg-Calcite, calcite-Si mix, quartz-silica polymorphs, glauconite, apatite, illite and/or chlorite	SK6	SK6-1: Mg-Calcite, calcite-Si mix, magnesite, dolomite, quartz-silica polymorphs, illite and/or chlorite SK6-3: Mg-Calcite, calcite-Si mix, magnesite, dolomite, quartz-silica polymorphs, illite and/or chlorite SK6-7: Mg-Calcite, calcite-Si mix, dolomite, quartz-silica polymorphs, illite and/or chlorite

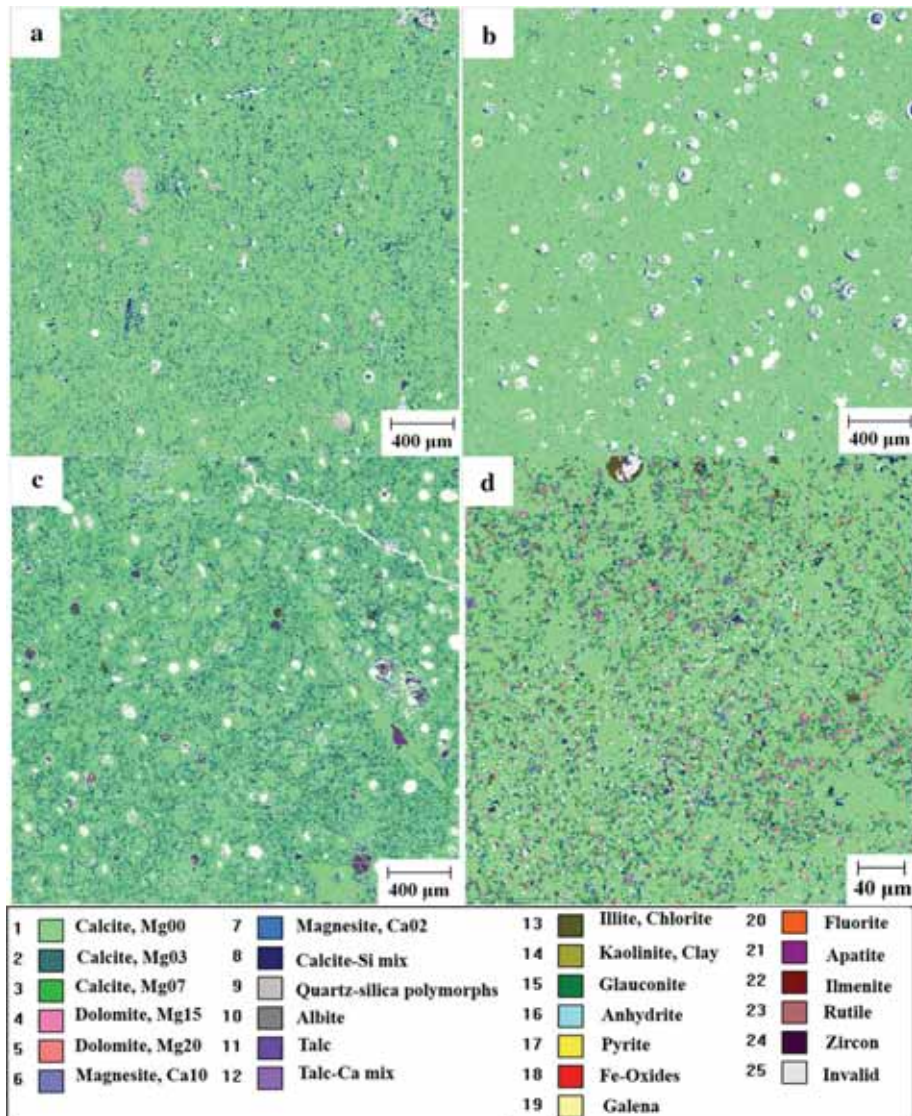


Fig. 5 MLA images **a** unflooded Aalborg chalk; **b** NaCl-flooded AA21 (slice 1); **c** MgCl₂-flooded AA5 (slice 1); **d** MgCl₂-flooded KA8 (slice 1). ‘bright green’—calcite, ‘bright blue’—magnesite, ‘pink’—dolomite, ‘purple’—talc. Element content information in the legend refers to quantified EDX spectra, e.g. Mg–Calcite10 corresponds to calcite with up to 10 wt% Mg

Si–O bearing phases like opal-CT, the electron beam will excite neighbouring grains like calcite, producing so-called mixed spectra, such as ‘Calcite–Si mix’.

3.3.2 NaCl-Flooded Cores

No significant new minerals were observed in NaCl-flooded material, see Table 5 for results from slice 1 of each chalk type. Calcite and non-carbonate phases like quartz, illite/chlorite, apatite, kaolinite and glaucanite could still be found, as in unflooded material (Table 5).

Figure 5a shows an MLA image of unflooded Aalborg chalk. In addition to a dominant green (calcite indication), a dense pattern of dark blue spots ('Calcite-Si mix') is seen, likely representing opal-CT or quartz mineral phases mixed with calcite. Considering Fig. 5b of slice 1 from AA21 (flooded with NaCl), the dark blue spots are much less abundant, implying that these phases have been partly removed, either by transport or by dissolution processes. Microfossils can still be observed in their nearly original shape, but several of them with open pore space. Some have dark blue accumulations of 'Calcite-Si mix' where this phase could have been re-deposited or re-precipitated during flooding. More images of NaCl-flooded samples are found in Sup. Mat. Fig. 8a-c.

3.3.3 $MgCl_2$ -Flooded Cores

SEM-MLA detected significant changes in the $MgCl_2$ -flooded cores. (Data from MO10 were not available.) As for unflooded samples, calcite and quartz were indicated. In addition, all cores indicated magnesite (bright blue colour) and dolomite (pink colour) in slice 1, as seen in Fig. 5c-d (AA5 and KA8) and Sup. Mat. Fig. 9a, b (LI1 and SK6). AA5, KA8 and SK6 indicated more precipitation of dolomite (pink colour) and magnesite (bright blue colour) than LI1. In AA5, talc was indicated in slice 1 (Fig. 5c, purple colour), 3 (to lesser extent) and 7, as a new mineral phase not observed in unflooded material or the other chalks. The microfossils in AA5, slice 1, appear to be filled with newly formed minerals, i. e. talc, or partly dissolved with pore space left. Illite and/or chlorite could still be found in the five cores after flooding. Kaolinite (observed in unflooded Kansas material) could not be observed in KA8 after flooding.

3.4 Geochemistry

3.4.1 Unflooded Samples

The geochemical analysis of untested chalk is summarized in Table 6a. (The complete data set is in Sup. Mat. Table 1 together with details of detection limits.) These statistics are based on 5-9 cores of each chalk type to indicate natural compositional variations.

The chalks are all as expected dominated by CaO, and they have low MgO concentrations (0.23-0.42 wt%) with total carbon around 12%. Sr correlates in general positively with CaO. Trace element geochemistry does not point to any significant clastic input measured by Rb and Zr with values often below 5 ppm, which is 10-15 times below the typical upper continental crust composition (McLennan et al. 2006).

Chalk samples from Kansas (KA) contain CaO between 54.2 and 55.1 wt% and relatively small amounts of non-carbonate phases with content of SiO₂ between 1.1 and 1.5 wt% and minute K₂O (0.1 wt%) and Al₂O₃ between 0.3 and 0.5 wt%. Clastic input is as well minute with concentrations for Rb, Zr and Y, trace elements, which solely occur in clastic material, below 5 ppm. Chalk from Mons (MO) contains slightly lower SiO₂ (0.98 wt%) than chalk cores from Kansas with CaO straddling 55 wt%. With Al₂O₃ as low as 0.2 wt% and even lower trace element concentrations, this chalk type seems to be 'cleaner' than the cores from Kansas. Samples from Liège (LI) contain more SiO₂ comparable to Kansas chalk (KA). Concentrations of CaO are around 54 wt%, Al₂O₃ is around 0.3 wt%, and values of Rb, Zr and Y are higher than in the above presented chalks point to slightly more clastic material. The Aalborg chalk samples (AA) show the highest amount of non-carbonate material compared

Table 6 Geochemical analysis of (a) unflooded end piece material from several different cores of same chalk type summarized by average and standard deviation (data from each core are given in Sup. Mat. Table 1), (b) unflooded end piece material and flooded slices from NaCl-flooded cores and (c) unflooded end piece material and flooded slices from MgCl₂-flooded cores

	SiO ₂ (wt%)	Al ₂ O ₃ (wt%)	MgO (wt%)	CaO (wt%)	K ₂ O (wt%)	Rb (PPM)	Sr (PPM)	Zr (PPM)	TOT/C (PPM)
<i>a) Unflooded chalk</i>									
Kansas average	1.23	0.36	0.23	54.66	0.09	2.3	895.6	6.6	12.1
SD	0.17	0.08	0.02	0.34	0.01	0.6	37.3	0.8	0.2
Mons average	0.98	0.24	0.27	55.02	0.07	2.2	828.7	3.8	12.2
SD	0.06	0.03	0.02	0.08	0.02	0.4	30.7	1.4	0.1
Liège average	1.98	0.34	0.27	54.17	0.08	3.2	947.6	7.3	12.0
SD	0.13	0.03	0.02	0.17	0.01	0.5	32.8	1.1	0.1
Aalborg average	5.06	0.35	0.42	52.10	0.09	3.1	736.8	5.2	11.7
SD	0.84	0.05	0.02	0.65	0.01	0.4	42.5	0.8	0.2
Stevens Klint average	0.37	0.08	0.29	55.59	0.02	0.8	1165.3	2.4	12.3
SD	0.04	0.02	0.01	0.15	< 0.01	0.2	40.8	1.1	0.2
<i>b) NaCl-flooded chalk cores</i>									
KA6 (unflooded)	1.50	0.50	0.20	54.20	0.10	3.3	842.2	7.0	11.9
KA6-1	1.20	0.40	0.20	54.00	0.10	1.5	918.0	8.9	12.1
KA6-2	1.50	0.50	0.20	53.50	0.10	2.4	910.2	7.8	11.9
KA6-3	1.60	0.50	0.20	54.20	0.10	2.9	988.3	8.2	12.2
KA6-4	1.60	0.50	0.20	54.00	0.10	2.9	1015.3	8.1	12.4
KA6-5	1.80	0.60	0.20	53.70	0.10	3.2	984.9	8.8	12.1
KA6-6	1.70	0.60	0.20	53.60	0.10	3.2	1025.1	8.6	12.1
KA6-7	1.70	0.60	0.20	53.70	0.10	3.4	1061.5	8.4	12.1

Table 6 continued

	SiO ₂ (wt%)	Al ₂ O ₃ (wt%)	MgO (wt%)	CaO (wt%)	K ₂ O (wt%)	Rb (PPM)	Sr (PPM)	Zr (PPM)	TOT/C (PPM)
MO12 (unflooded)	1.00	0.20	0.30	55.10	0.10	2.3	874.3	5.2	12.0
MO12-1	0.70	0.20	0.27	56.20	0.00	1.6	935.5	3.1	12.3
MO12-2	0.90	0.20	0.26	55.20	0.10	1.8	874.0	3.0	12.4
MO12-3	0.90	0.30	0.26	55.30	0.10	2.0	903.1	3.3	12.2
MO12-4	0.90	0.30	0.25	54.70	0.10	2.0	970.0	2.9	12.5
MO12-5	1.00	0.30	0.25	54.70	0.10	2.2	944.5	2.9	12.4
MO12-6	0.90	0.30	0.26	56.50	0.10	1.9	938.5	2.9	12.4
MO12-7	1.00	0.30	0.24	57.40	0.10	2.1	944.0	3.4	12.4
LI2 (unflooded)	1.90	0.30	0.30	54.10	0.10	3.6	910.4	8.2	11.8
LI2-1	1.40	0.30	0.30	54.40	0.00	1.8	1042.7	8.1	12.5
LI2-2	1.80	0.40	0.30	55.50	0.10	2.1	1039.2	5.7	12.7
LI2-3	1.80	0.30	0.30	55.70	0.10	1.9	1033.9	5.6	12.7
LI2-4	2.00	0.40	0.30	54.70	0.10	2.3	1019.8	7.8	12.8
LI2-5	2.00	0.40	0.30	54.10	0.10	2.7	947.0	9.3	12.5
LI2-6	2.00	0.40	0.30	54.20	0.10	2.5	968.0	8.6	12.6
LI2-7	2.10	0.40	0.30	53.80	0.10	2.8	997.3	9.0	12.8
AA21 (unflooded)	5.00	0.30	0.40	52.10	0.10	2.9	817.6	6.1	11.6
AA21-1	2.40	0.30	0.50	53.90	0.00	1.6	783.1	4.3	12.1
AA21-2	2.40	0.40	0.50	53.60	0.00	1.5	774.0	7.0	12.1
AA21-3	4.50	0.40	0.50	52.40	0.10	2.3	776.3	5.5	11.9
AA21-4	6.00	0.50	0.40	51.20	0.10	3.1	820.6	7.9	11.5
AA21-5	4.40	0.40	0.50	52.20	0.10	2.6	769.6	7.1	11.6
AA21-6	6.10	0.50	0.40	51.00	0.10	3.1	834.0	7.4	11.6
AA21-7	5.90	0.40	0.40	51.50	0.10	3.0	793.0	6.5	11.5

Table 6 continued

	SiO ₂ (wt%)	Al ₂ O ₃ (wt%)	MgO (wt%)	CaO (wt%)	K ₂ O (wt%)	Rb (PPM)	Sr (PPM)	Zr (PPM)	TOT/C (PPM)
SK2 (unflooded)	0.40	0.10	0.30	55.60	b.d.l.	1.0	1090.1	3.3	12.3
SK2-1	0.20	0.10	0.40	56.00	b.d.l.	b.d.l.	1133.5	2.6	12.7
SK2-2	0.20	0.00	0.30	56.10	b.d.l.	b.d.l.	1137.6	3.2	13.1
SK2-3	0.20	0.10	0.30	55.70	b.d.l.	b.d.l.	1160.0	2.3	12.9
SK2-4	0.20	0.10	0.30	55.80	b.d.l.	b.d.l.	1197.7	2.7	12.8
SK2-5	0.20	0.10	0.30	55.70	b.d.l.	0.1	1197.3	3.0	12.8
SK2-6	0.20	0.00	0.30	55.90	b.d.l.	0.2	1197.4	1.3	12.9
SK2-7	0.20	0.00	0.30	55.90	b.d.l.	b.d.l.	1168.9	0.8	12.9
<i>c) MgCl₂-flooded chalk cores</i>									
KA8 (unflooded)	1.30	0.30	0.20	54.50	0.10	2.0	932.9	7.7	12.0
KA8-1	1.20	0.40	6.50	46.40	0.00	1.5	763.2	6.0	12.3
KA8-2	1.10	0.30	3.70	50.50	0.00	1.4	830.0	10.7	12.1
KA8-3	1.10	0.30	1.80	52.70	0.00	1.4	880.9	6.5	11.9
KA8-4	1.10	0.30	1.30	53.50	0.00	1.5	928.3	6.2	12.1
KA8-5	1.10	0.30	1.00	53.70	0.00	1.3	911.2	5.7	12.1
KA8-6	1.10	0.30	0.90	54.10	0.00	1.4	927.2	6.1	11.7
KA8-7	1.00	0.30	0.80	54.00	0.00	1.2	886.8	5.4	12.2
MO10 (unflooded)	0.90	0.20	0.30	55.10	0.10	2.2	871.1	2.6	12.3
MO10-1	1.00	0.30	1.31	53.60	0.10	2.3	980.9	3.2	11.9
MO10-2	1.00	0.30	2.26	52.90	0.10	2.4	964.8	3.1	12.1
MO10-3	1.00	0.30	2.51	54.00	0.00	2.1	933.7	3.0	12.6
MO10-4	0.80	0.20	1.64	53.40	0.00	2.0	939.9	3.4	12.3
MO10-5	0.90	0.20	1.08	54.60	0.00	2.0	914.2	3.3	12.3
MO10-6	0.80	0.20	0.84	54.40	0.00	1.9	890.4	3.4	12.2
MO10-7	0.90	0.20	0.79	57.90	0.00	1.8	914.6	2.9	12.0

Table 6 continued

	SiO ₂ (wt%)	Al ₂ O ₃ (wt%)	MgO (wt%)	CaO (wt%)	K ₂ O (wt%)	Rb (PPM)	Sr (PPM)	Zr (PPM)	TOT/C (PPM)
L11 (unflooded)	2.20	0.40	0.30	54.00	0.10	2.2	994.9	5.2	11.9
L1-1	1.70	0.30	1.70	52.80	0.00	2.5	1007.2	7.2	11.9
L1-2	2.00	0.40	2.30	51.50	0.10	2.6	957.6	7.5	12.1
L1-3	2.10	0.40	3.20	50.80	0.10	2.7	891.4	8.9	12.5
L1-4	2.10	0.40	2.10	51.90	0.10	3.1	921.6	10.0	12.4
L1-5	2.10	0.40	1.40	52.60	0.10	2.9	963.3	11.5	12.7
L1-6	2.10	0.40	1.20	53.20	0.10	2.7	1008.0	11.0	12.6
L1-7	2.00	0.40	1.00	53.40	0.10	2.6	978.4	10.4	12.4
AA5 (unflooded)	4.00	0.30	0.40	53.00	0.10	2.8	691.6	5.2	11.9
AA5-1	3.80	0.40	3.20	50.20	0.00	1.8	680.3	5.5	11.8
AA5-2	4.10	0.40	3.60	49.40	0.10	2.0	714.3	4.9	11.6
AA5-3	3.70	0.30	3.30	50.00	0.00	1.9	663.4	4.1	11.8
AA5-4	4.30	0.30	2.80	50.30	0.00	1.8	720.2	5.1	11.6
AA5-5	5.30	0.50	2.90	49.50	0.10	3.1	790.9	6.0	11.3
AA5-6	5.20	0.40	2.60	49.70	0.10	3.0	782.6	8.6	11.4
AA5-7	6.20	0.50	2.60	49.30	0.10	3.4	839.0	7.5	11.2
SK6 (unflooded)	0.30	0.10	0.30	55.30	b.d.l.	0.8	1166.6	2.0	12.1
SK6-1	I.S.	I.S.	I.S.	I.S.	I.S.	0.3	1162.4	2.2	12.2
SK6-2	I.S.	I.S.	I.S.	I.S.	I.S.	0.2	1124.9	1.6	12.4
SK6-3	0.40	0.10	2.90	51.80	b.d.l.	b.d.l.	1105.8	1.6	12.3
SK6-4	0.40	0.10	2.20	52.50	b.d.l.	0.2	1150.0	1.6	12.3
SK6-5	0.40	0.10	1.20	53.80	b.d.l.	0.3	1031.0	2.1	12.2
SK6-6	0.40	0.10	0.80	54.50	b.d.l.	0.3	1016.4	1.8	12.2
SK6-7	0.30	0.10	0.60	54.60	b.d.l.	0.3	1019.5	1.7	12.4

PPM part per million, wt% weight per cent, TOT/C total carbon, SD standard deviation, b.d.l. below detection limit, I.S. no valid measurement. The exact sampling position of the unflooded material relative to the core samples is shown in Fig. 1a

to the other chalks. Therefore, CaO concentrations are lower between 51.4 and 53.0 wt% compared to all other chalks. SiO₂ is between 4 and 6 wt% and Al₂O₃ is only around 0.4 wt%, pointing to quartz or opal rather than more complex silicates. Chalk exposed at Stevns Klint (SK) is the cleanest one, with the lowest values of MgO and SiO₂. These samples contain CaO around 56 wt%.

3.4.2 NaCl-Flooded Cores

For the NaCl-flooded cores, the whole-rock geochemical analysis revealed minor, but detectable changes compared to unflooded material (Table 6b). The major elements (Mg, Al, Na and K) vary only slightly along the core. The SiO₂ fraction generally decreased compared to unflooded material, except for KA6 where an increase was measured. The lowest content of SiO₂ was found in the inlet slice for all five cores (KA6, MO12, LI2, AA21 and SK2). In SK2 all slices show the same content of SiO₂ (0.2 wt%), which is roughly a factor 2 lower than unflooded material (0.4 wt%). In MO12 and LI2, when disregarding slice 1 (MO12: 0.7 wt%; LI2: 1.4 wt%), the SiO₂ measurements (average MO12: 0.9 wt%; LI2: 1.95 wt%) are close to the values from unflooded material (MO12: 1 wt%; LI2: 1.9 wt%). For KA6, all values (average 1.65 wt%) except the first slice (1.2 wt%) are higher than unflooded material content (1.5 wt%). The most pronounced changes were seen in AA21, where SiO₂ content showed a strong increasing trend from the inlet slice (2.4 wt%) to the outlet slice (5.9 wt%). From slices 1 to 3 and in slice 5, the values were lower than for unflooded material (5.0 wt%), while near the outlet (for slices 4, 6 and 7) the values were higher than that of unflooded material.

3.4.3 MgCl₂-Flooded Cores

The geochemical data of the MgCl₂-flooded cores are reported in Table 6c. The average SiO₂ content in KA8 and LI1 (respectively, 1.1 and 2.0 wt%) is moderately lower than unflooded material (KA: 1.3 wt%; LI: 2.2 wt%), while for MO10 and SK6 the change was negligible (from 0.90 and 0.3 wt% in unflooded material to 0.91 and 0.38 wt%). The variations in silica for these samples seem to be related to natural variation rather than significant changes resulting from the tests. The SiO₂ content in AA5 after flooding (4.6 wt% on average) is lower than the average of unflooded Aalborg samples (5.1 wt%), with an increasing trend from the inlet (3.8 wt%) towards the outlet (6.2 wt%). Variations in wt% of Al₂O₃ and K₂O correlated positively with SiO₂ for Stevns Klint, Mons and Kansas chalks, which could indicate phyllosilicates and/or feldspar. The correlation was not significant for Liège and Aalborg, pointing to a more mixed composition. The different cores had very similar trace content of MgO before flooding (Table 6c), which in the different chalk samples increased significantly after flooding. KA8 has most of its MgO (6.5 wt%) in the inlet slice, with rapidly decreasing amounts towards the outlet (0.8 wt%). MO10 (from Mons) and LI1 (from Liège) are similar and show a peak (2.5 and 3.2 wt%, respectively) of MgO increase in slice 3. AA5 has again a different characteristic with a rather uniform MgO distribution (between 2.6 and 3.6 wt%) with the highest value (3.6 wt%) in slice 2 and then decreasing. SK6 unfortunately lacks data from slices 1 and 2, but shows decreasing MgO amounts from slice 3 (2.9 wt%) towards the outlet (0.6 wt%).

3.5 Stable Isotope Geochemistry

3.5.1 Unflooded Samples

C and O isotope measurements of unflooded material and flooded core material are given in Sup. Mat. Table 2. The unflooded samples were very homogeneous. The isotope parameters $\delta^{13}\text{C}_{\text{SMOW}}$ and $\delta^{18}\text{O}_{\text{SMOW}}$ were mostly in the range 1.5 to 2.1 ‰ and -1.9 to -1 ‰, respectively, for all chalks except for samples from Kansas ($\delta^{13}\text{C}_{\text{SMOW}}$ and $\delta^{18}\text{O}_{\text{SMOW}}$ on average 0.2 and -5 ‰, respectively). All measured values for $\delta^{13}\text{C}_{\text{SMOW}}$ and $\delta^{18}\text{O}_{\text{SMOW}}$ from Mons (on average: 2 and -1.7 ‰, respectively), Liège (on average: 1.5 and -1.9 ‰, respectively), Aalborg (on average: 2.1 and -1.2 ‰, respectively) and Stevns Klint (on average: 1.6 and -1.6 ‰, respectively) seem to be primarily reflecting global isotope excursions. Exceptions are the samples from Kansas, and their oxygen isotope ratios are strongly altered and do not reflect primary compositions.

3.5.2 NaCl-Flooded Cores

In NaCl-flooded cores, $\delta^{13}\text{C}_{\text{SMOW}}$ values are almost the same as for untested material and observed variations are natural ones. $\delta^{18}\text{O}_{\text{SMOW}}$ is also comparable to unflooded material, but the values are slightly more negative in the flooded cores MO12 (-2.2 ‰), SK2 (-1.9 ‰) and KA6 (-5.1 ‰).

3.5.3 MgCl₂-Flooded Cores

In the MgCl₂-flooded cores, $\delta^{13}\text{C}_{\text{SMOW}}$ was also almost the same as for untested material, while $\delta^{18}\text{O}_{\text{SMOW}}$ values tended to be slightly more negative (MO10: -2.0 ‰; LI1: -2.0 ‰; AA5: -1.2 ‰; SK6: -1.8 ‰; KA8: -5.3 ‰).

3.6 Mass Measurements

As described (see Sect. 2.2.1), the dry weight of the applied cores was measured before ($M_{\text{dry},o}$) and after ($M_{\text{dry},end}$) flooding and the difference $\Delta M = M_{\text{dry},end} - M_{\text{dry},o}$ was calculated along with the average rate of mass changes $\Delta M/\Delta t$, see results in Table 7. In all tests the cores experienced a net mass loss. The NaCl-flooded cores KA6, MO12 and LI2 lost 0.5–0.6 g, SK2 had a smaller loss of 0.16 g, while AA21 had a comparatively large mass reduction of 1.51 g. With MgCl₂ flooding, the purest chalk cores (SK1: 1.71 g; SK6: 1.11 g; MO10: 1.57 g) obtained a lower mass loss than the more impure chalk cores (LI1: 2.1 g; KA8: 1.86 g), with especially high mass reduction in the Aalborg cores (AA1: 5.14 g; AA5: 4.15 g). The mentioned trends were similar when normalizing for flooding time (i.e. mass rate) although the distinction between the MgCl₂-flooded cores became less apparent (between -0.02 and -0.04 g/d), except for the Aalborg cores AA5 and AA1 standing out with a high mass rate (-0.045 to -0.067 g/d). Note that the mass change in the cores was on the order of $\sim 0.1\%$ of the original mass for some of the NaCl-flooded cores and thus very sensitive to unaccounted losses, e.g. during unloading or to remaining fluid after drying.

3.7 Mechanical Tests: Hydrostatic Loading and Creep Compaction

The axial stress plotted versus strain from the loading phase is given in Fig. 6, with corresponding yield points (stress at which nonlinear deformation initiates) and bulk moduli in

Table 7 Dry mass $M_{\text{dry, end}}$ (g) after flooding, mass change $\Delta M = M_{\text{dry, end}} - M_{\text{dry, o}}$ (g) compared to original state and corresponding average mass rate of the core $\Delta M / \Delta t$ (g/d)

NaCl-flooded cores				MgCl ₂ -flooded cores			
Core	$M_{\text{dry, end}}$ (g)	ΔM (g)	$\Delta M / \Delta t$ (g/d)	Core	$M_{\text{dry, end}}$ (g)	ΔM (g)	$\Delta M / \Delta t$ (g/d)
KA6	134.40	-0.50	-0.008	KA8	134.38	-1.86	-0.025
MO12	123.92	-0.60	-0.010	MO10	124.01	-1.57	-0.026
LJ2	125.51	-0.54	-0.006	LJ1	110.28	-2.10	-0.032
AA21	111.45	-1.51	-0.025	AA5	108.18	-4.15	-0.067
SK2	121.15	-0.16	-0.002	AA1*	114.7	-5.14	-0.045
				SK6	113.97	-1.11	-0.018
				SK1*	115.70	-1.71	-0.038

*Cores included mainly for testing repeatability of compaction results

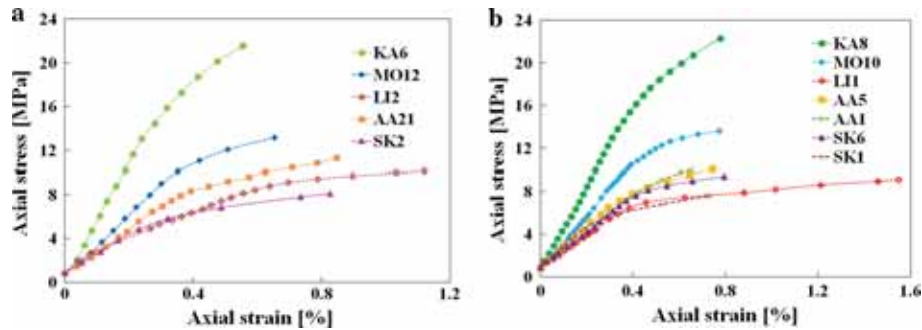


Fig. 6 Axial stress versus axial strain obtained during hydrostatic loading for the NaCl (a)- and MgCl₂ (b)-flooded cores

Table 8 Yield point (MPa) and bulk modulus (GPa) of the different cores as determined during the loading phase

Core	Brine	Yield point (MPa)	Bulk modulus (GPa)	Confining pressure during creep (MPa)
KA6	NaCl	13.0	0.69	23.0
KA8	MgCl ₂	15.4	0.51	23.0
MO12	NaCl	9.0	0.38	14.0
MO10	MgCl ₂	10.5	0.34	14.0
LI2	NaCl	7.4	0.18	10.5
LI1	MgCl ₂	6.5	0.23	9.5
AA21	NaCl	7.9	0.27	12.0
AA5	MgCl ₂	7.2	0.26	11.0
AA1*	MgCl ₂	7.9	0.24	11.0
SK2	NaCl	5.8	0.22	8.5
SK6	MgCl ₂	7.6	0.23	10.0
SK1*	MgCl ₂	4.8	0.27	8.5

*Cores included mainly for testing repeatability of compaction results

Table 8. Cores of same chalk type obtained similar bulk modulus regardless of the brines and there were no direct trends between the given brines and yield points. This is in agreement with (Madland et al. 2011; Megawati et al. 2015). A general trend was that higher (initial) porosity cores displayed lower yield point and bulk modulus (see Sup. Mat. Fig. 10), consistent with Engstrom (1992) and Havmøller and Foged (1996). Kansas was the strongest chalk, followed by Mons. The rest behaves similarly, and the yield points are mainly between 5 and 8 MPa. SK1 is the weakest core, with yield point at 4.8 MPa.

The creep strain development (compaction under constant stress) for the five NaCl-flooded cores is shown in Fig. 7a. The strain rate is gradually decreasing throughout the tests. In the case of SK2, the piston did not move smoothly during the first 25 days, resulting in somewhat erroneous measurements. Interestingly, AA21 with highest porosity (46.7%) compacted the least.

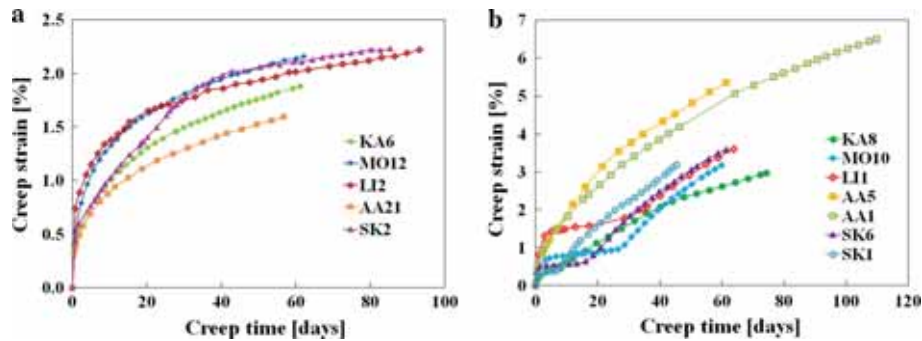


Fig. 7 Axial creep strain versus time profiles of the NaCl (a)- and MgCl₂ (b)-flooded cores. The NaCl-flooded cores (a) display continuous compaction. The impure cores deformed less with NaCl flooding. The MgCl₂-flooded cores (b) display accelerated creep for pure cores (SK1, SK6 and MO10) and LI1. Note that the figures have different scales

Creep compaction profiles for MgCl₂ injected cores are shown in Fig. 7b. Note that two Stevns Klint cores (SK1 and SK6) and two Aalborg cores (AA1 and AA5) were used in order to check the reproducibility of the compaction behaviour. These chalk types, respectively, contained least and most non-carbonate content, see Table 6a, c. The Aalborg cores (AA1 and AA5) compacted the most, with a continuously decreasing compaction rate. The cores MO10, LI1, SK6 and SK1 shared another type of behaviour: in the initial few days the strain rate was high, followed by a period of slow compaction (lasting up to ~ 24 d for MO10, ~ 28 d for LI1, ~ 14 d for SK6 and ~ 6 d for SK1). The compaction then accelerated, initiating a new period of continuous compaction with similar creep rate as the Aalborg cores (AA5 and AA1). KA8 also displayed a behaviour initial rapid compaction, followed by a low strain rate, and increased compaction rate after ~ 8 d. Compared to the four aforementioned cores, this core compacted the least in axial creep in the long run, likely due to its lower original porosity compared to the other cores (37%, see Table 2), i.e. it had less volume for the grains to reorganize in. These observations agreed to a wide extent with previous results (Madland et al. 2011; Megawati et al. 2015), in which accelerated creep for the pure chalks Mons and Stevns Klint was observed after a certain period of time while Kansas, Liège and Aalborg cores compacted continuously from the very beginning. Their tests on Liège cores were stopped after 20.8 and 62.5 d (without seeing accelerated creep).

3.8 Effluent Analysis of the Flooded Cores

In the NaCl flooding experiments, the produced concentrations of Cl⁻ and Na⁺ were the same as injected (not shown), implying negligible chemical interaction from these ions. Figure 8a shows that significant concentrations of Ca²⁺ were produced: Initial transient peaks (KA6: 0.002 mol/L; MO12: 0.007 mol/L; LI2: 0.014 mol/L; AA21: 0.009 mol/L; SK2: 0.004 mol/L) were observed. After 2–3 PVs injection, steady concentrations of Ca²⁺ followed (KA6: 0.001 mol/L; MO12: 0.001 mol/L; LI2: 0.003 mol/L; AA21: 0.004 mol/L; SK2: 0.002 mol/L). The peaks were 2–7 times the stable values. We note that the measurements were near or below the detection limit (see Sup. Mat. 1.7). These transient (peak) and steady state observations indicate desorption and mineral dissolution processes (Madland et al. 2011; Andersen et al. 2012).

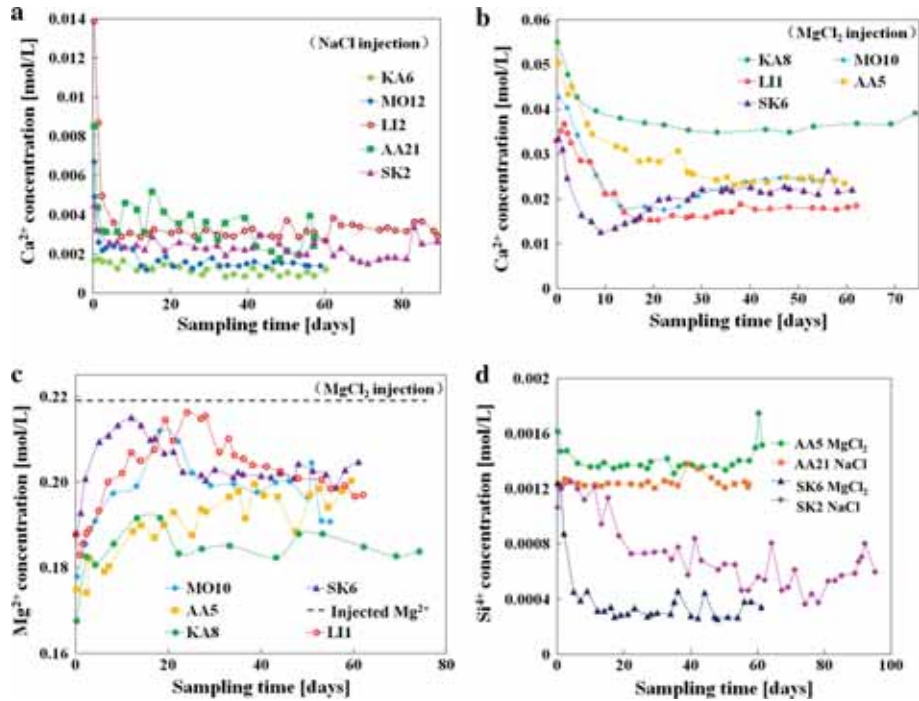


Fig. 8 Effluent analysis of the flooded cores. **a** Ca^{2+} concentration profiles in the effluent of NaCl-flooded cores, **b** Ca^{2+} concentration profiles in the effluent of MgCl_2 -flooded cores, **c** Mg^{2+} concentration profiles in the effluent of MgCl_2 -flooded cores, **d** Si^{4+} concentration profiles in the effluent of the cores AA5, SK6 (flooded with MgCl_2), AA21 and SK2 (flooded with NaCl)

Figure 8b shows the Ca^{2+} effluent measurements for MgCl_2 -flooded cores. Concentration peaks between 0.033 mol/L (for SK6) and 0.055 mol/L (for KA8) are observed initially. KA8 and AA5 displayed a decreasing trend before stabilizing around and 0.036 mol/L and 0.024 mol/L, respectively. The cores MO10, LI1 and SK6 displayed Ca^{2+} concentration minima (Fig. 8b, MO10: 0.018 mol/L; LI1: 0.015 mol/L; SK6: 0.013 mol/L) before increasing again to stable levels (MO10: 0.027 mol/L; LI1: 0.017 mol/L; SK6: 0.022 mol/L). Mg^{2+} was retained inside all the tested cores, as seen in Fig. 8c with effluent Mg^{2+} concentrations clearly below the injected value (0.219 mol/L). This behaviour is equivalently opposite compared to the Ca^{2+} profile, i.e. the sum of produced Ca^{2+} and Mg^{2+} was stable and close to equal the injected concentration of 0.219 mol/L (not shown), consistent with (Madland et al. 2011; Megawati et al. 2015). As seen in Fig. 8c, KA8 and AA5 obtained increasing Mg^{2+} concentration trends initially which then stabilized around 0.184 mol/L and 0.195 mol/L, respectively, while the cores MO10, LI1 and SK6 showed Mg^{2+} concentration peaks (MO10: 0.205 mol/L; LI1: 0.216 mol/L; SK6: 0.215 mol/L) at the times when the Ca^{2+} concentrations reached their minima. Subsequently, the Mg^{2+} effluent concentrations decreased and stabilized (MO10: 0.192 mol/L; LI1: 0.197 mol/L; SK6: 0.202 mol/L).

In addition to the mentioned ions, the Si^{4+} concentration profiles of AA21 and SK2 (flooded with NaCl) and AA5 and SK6 (flooded with MgCl_2) were measured by ICP-AES (Fig. 8d). Si^{4+} was produced, indicating dissolution of Si-bearing minerals in the cores, with

effluent concentration ranging from 0.0003 mol/L to 0.0016 mol/L (low values compared with the Ca^{2+} concentrations). The Aalborg cores (which had high initial content of SiO_2 , see Table 6) consistently produced more (concentrations between 0.0012 mol/L and 0.0016 mol/L) Si^{4+} than the SK cores (concentrations between 0.0003 mol/L and 0.0013 mol/L). A slightly higher production of Si^{4+} was observed in AA5 (flooded with MgCl_2 , on average: ~ 0.0013 mol/L) compared with AA21 (flooded with NaCl , on average: ~ 0.0012 mol/L). The opposite was seen in SK cores where SK2 (flooded with NaCl , on average: ~ 0.0007 mol/L) produced some more Si^{4+} than SK6 (flooded with MgCl_2 , on average: ~ 0.0004 mol/L).

3.9 Solid Density Estimation

Table 9 shows the density values (ρ_{end}) from parts P1 and P2 and groups G1, G2 and G3 (see 2.2.1, Fig. 1b) together with the calculated difference $\Delta\rho$ between the end measurement ρ_{end} and the pycnometry measurements $\rho_{\text{o-pyc}}$ of unflooded material of same type (see Table 2).

In the NaCl -flooded cores, $\Delta\rho$ ranged between -0.01 and $+0.01$ g/cm^3 , except for two measurements (MO12, G1: $+0.02$ g/cm^3 ; AA21, G3: -0.02 g/cm^3). KA6, LI2 and AA21 saw a slight increase in P1 ($+0.01$ g/cm^3), while P2 in LI2 and AA21 stayed the same as unflooded material and P2 in KA6 decreased (-0.01 g/cm^3). The same trends were seen from the groups, although the absolute values were lower for AA21. The purest chalks MO12 and SK2 generally showed same density measurements as unflooded: for MO12 there was no response in P1 and P2, although the group measurements indicated an increase in G1 ($+0.02$ g/cm^3) and G3 ($+0.01$ g/cm^3) and no change in G2. SK2 displayed the same density as unflooded material in P1 with an increase in P2 ($+0.01$ g/cm^3), while the group measurements indicated no density change along the core.

The solid density of the MgCl_2 -flooded cores displayed a clearer trend towards increased density (compared to the NaCl -flooded cores). The measurements of P1 and P2 varied from zero to $+0.03$ g/cm^3 and were higher in P1 than P2 for the cores KA8, MO10, LI2 and SK6, while in AA5 they were the same (P1, P2: $+0.03$ g/cm^3). The group measurements showed stronger variation, with $\Delta\rho$ varying from zero to $+0.06$ g/cm^3 . Most noticeable, KA8 and SK6 had strong density peaks near the inlet (ρ in G1: $+0.06$ g/cm^3 and $+0.05$ g/cm^3 , respectively) and lower density towards outlet ($\Delta\rho$ in G3: $+0.00$ and $+0.01$ g/cm^3 , respectively). MO10 showed increased density in G1 ($+0.02$ g/cm^3) and G3 ($+0.01$ g/cm^3), but no change in G2 (similar behaviour as MO12). LI1 gained its highest increase in G1 ($+0.03$ g/cm^3) and a somewhat lower increase (by $+0.02$ g/cm^3) in G2 and G3. AA5 displayed the same increase in G1 and G2 ($+0.02$ g/cm^3), but slightly lower increase in G3 ($+0.01$ g/cm^3).

3.10 Specific Surface Area (SSA)

Measurements of specific surface area (SSA_{end}) from slices 1, 3 and 7 of all flooded cores are listed in Table 10 together with the difference between these measurements taken from the flooded and unflooded material (Table 2).

The SSA in the NaCl -flooded cores was either unchanged or reduced: the pure chalk cores SK2 and MO12 did not obtain any significant change compared to unflooded material. The more impure cores (KA6, LI2 and AA21) all saw a strong reduction (the average change varied from -0.5 to -1.3 m^2/g) towards values similar to the pure cores, ~ 2 m^2/g (Stevens Klint chalk, in Hjuler and Fabricius 2009). For LI2 the reduction (by -0.5 , -0.4 , -0.6

Table 9 Solid density measured by pycnometry after flooding (ρ_{end}) for partitions P1, P2 and groups G1, G2, G3 (see Fig. 1b), and the difference ($\Delta\rho$) between measurement (ρ_{end}) of NaCl and MgCl₂-flooded cores and original solid density (Table 2, $\rho_{0\text{-pyc}}$)

NaCl-flooded cores				MgCl ₂ -flooded cores			
Core	Group	ρ_{end} (g/cm ³)	$\Delta\rho$ (g/cm ³)	Core	Group	ρ_{end} (g/cm ³)	$\Delta\rho$ (g/cm ³)
KA6	P1	2.71	0.01	KA8	P1	2.73	0.03
	P2	2.69	- 0.01		P2	2.71	0.01
	G1	*	*		G1	2.76	0.06
	G2	2.69	- 0.01		G2	2.71	0.01
	G3	2.69	- 0.01		G3	2.69	0.00
MO12	P1	2.70	0.00	MO10	P1	2.71	0.01
	P2	2.70	0.00		P2	2.70	0.00
	G1	2.72	0.02		G1	2.72	0.02
	G2	2.70	0.00		G2	2.70	0.00
	G3	2.71	0.01		G3	2.71	0.01
LI2	P1	2.70	0.01	LI1	P1	2.70	0.02
	P2	2.69	0.00		P2	2.69	0.01
	G1	2.70	0.01		G1	2.71	0.03
	G2	2.70	0.01		G2	2.70	0.02
	G3	2.69	0.00		G3	2.70	0.02
AA21	P1	2.68	0.01	AA5	P1	2.70	0.03
	P2	2.67	0.00		P2	2.70	0.03
	G1	2.67	0.00		G1	2.69	0.02
	G2	2.67	0.00		G2	2.69	0.02
	G3	2.65	- 0.02		G3	2.68	0.01
SK2	P1	2.69	0.00	SK6	P1	2.71	0.02
	P2	2.70	0.01		P2	2.70	0.01
	G1	2.69	0.00		G1	2.74	0.05
	G2	2.69	0.00		G2	2.71	0.02
	G3	2.69	0.00		G3	2.70	0.01

* No valid measurement was obtained for G1 in KA6

m²/g along the core) was uniform, while for KA6 and AA21 the most significant reduction (- 1.0 and - 2.8 m²/g, respectively) was near the inlet.

In the MgCl₂-flooded cores the SSA increased strongly in all slices by 0.4–4.1 m²/g, except for KA8 which saw a reduction in slices 3 and 7 and LI1 which had a small increase + 0.1 m²/g in slice 7 (Table 10). The purest chalk SK6 had the same increase (by + 1.0 m²/g) in slices 1 and 3, with a smaller increase (+ 0.4 m²/g) in slice 7, while MO10, KA8 and LI1 saw decreasing values along the core with the highest SSA near the inlet (MO10: 4.0 m²/g; KA8: 3.5 m²/g; LI1: 4.0 m²/g;). That is, for these cores the inlet SSA increased the most (MO10: + 1.8 m²/g; KA8: + 0.5 m²/g; LI1: + 1.3 m²/g) and the outlet SSA increased the least (MO10: + 0.8 m²/g; LI1: + 0.1 m²/g) or even decreased (KA8: - 0.8 m²/g). Unlike the other cores, the SSA increased along AA5 from inlet to outlet with values ranging from 6.7 to 9 m²/g, higher than seen in any of the other MgCl₂-flooded core slices. The increase was also large compared to the other cores, ranging from 1.8 to 4.1 m²/g.

Table 10 Specific surface area (SSA) of NaCl and MgCl₂-flooded cores

NaCl-flooded cores				MgCl ₂ -flooded cores			
Core	Slice	SSA _{end} (m ² /g)	ΔSSA (m ² /g)	Core	Slice	SSA _{end} (m ² /g)	ΔSSA (m ² /g)
KA6	KA6-1	2.0	-1.0	KA8	KA8-1	3.5	0.5
	KA6-3	2.4	-0.6		KA8-3	2.4	-0.6
	KA6-7	2.6	-0.4		KA8-7	2.2	-0.8
MO12	MO12-1	2.3	0.1	MO10	MO10-1	4.0	1.8
	MO12-3	2.2	0.0		MO10-3	3.6	1.4
	MO12-7	2.1	-0.1		MO10-7	3.0	0.8
LI2	LI2-1	2.2	-0.5	LI1	LI1-1	4.0	1.3
	LI2-3	2.3	-0.4		LI1-3	3.5	0.8
	LI2-7	2.1	-0.6		LI1-7	2.8	0.1
AA21	AA21-1	2.1	-2.8	AA5	AA5-1	6.7	1.8
	AA21-3	4.0	-0.9		AA5-3	7.8	2.9
	AA21-7	4.6	-0.3		AA5-7	9.0	4.1
SK2	SK2-1	2.0	0.0	SK6	SK6-1	3.0	1.0
	SK2-3	1.9	-0.1		SK6-3	3.0	1.0
	SK2-7	1.9	-0.1		SK6-7	2.4	0.4

ΔSSA is the difference between the end measurement SSA_{end} and the measurement of SSA from unflooded material (Table 2)

4 Discussion

4.1 Petrography, Mineralogy, Chemistry and Isotope Geochemistry

During flooding with NaCl, there was minute dissolution of calcite (Fig. 8a) and Si-bearing minerals (AA21 and SK2, Fig. 8d) as detected by whole-rock geochemistry analyses, effluent analysis and FEG-SEM (Sup. Mat. Fig. 2). No new mineral precipitation was observed by XRD (Table 4, Sup. Mat. Fig. 5) or MLA (Table 5, Sup. Mat. Fig. 8a–c), which agrees with previous studies (Madland et al. 2011; Megawati et al. 2015). Only some crystals showed smoothed edges and corners in FEG-SEM studies.

In contrast, the cores that were flooded with MgCl_2 experienced strong geochemical alterations. Generally, during the MgCl_2 injection, dissolution of calcite and Si-bearing minerals and precipitation of Mg-bearing minerals took place (Fig 4c, Sup. Mat. Fig. 3, 6, 9). In all cores magnesite was detected by XRD and FEG-SEM images. This has also been observed and reported in the previous studies by Madland et al. (2011), Megawati et al. (2015) and Zimmermann et al. (2013, 2015). MLA indicated formation of dolomite, but it was not verified by XRD. In all samples, increase in MgO and decrease in CaO could be observed in the geochemical analysis, but the MgO enrichment varied between chalks (Table 6): the cores KA8 and AA5 gained more MgO than the other cores, starting from 0.2 wt% and 0.4 wt% and ending at average values of 2.3 wt% and 3.0 wt%, respectively. This change is supported qualitatively by XRD (3.2.3) and quantitatively by the effluent measurement (Fig. 8b, c) where the Mg^{2+} -ion concentrations in the effluent of KA8 and AA5 were lower than for the other cores (Fig. 8c). This corresponds to Mg^{2+} retention of 1.49 g in KA8 and 1.56 g in AA5. The other cores, SK6, MO10 and LI1, retained 1.29 g, 1.23 g and 0.93 g of Mg^{2+} , respectively. Both magnesite (3.0 g/cm^3) and Mg-rich calcite have higher density than calcite (2.71 g/cm^3), which was reflected in the measured increase of solid densities after flooding (Table 9). The SSA also increased due to the formation of nano-sized magnesite, Mg-rich calcite crystals and clay minerals, with smaller grain sizes than the former calcite crystals and because of the growth position on surfaces of the host mineral (Table 10, Sup. Mat. Fig. 3). The reactive variations between the chalk types may be attributed to differences in their depositional setting, original mineralogy and the consequently higher or lower intra-fossil porosity, more or less abundant fossil debris etc. As seen from MLA in Fig. 5c, mineral precipitation occurred to large extent in open pores spaces of microfossils.

The MgO content profiles along the cores also varied, with peaks at different locations. KA8 experienced the most changes in slice 1, from 0.2 wt% (unflooded sample) to 6.5 wt% (after flooding) and rapidly decreasing content towards the outlet slice (0.8 wt%). The cores MO10 and LI1 had peaks in MgO (2.5 and 3.2 wt%, respectively) in slice 3 (not as strong as KA8), as confirmed by magnesite peaks in XRD. SK6 had a decreasing MgO content from slice 3 (2.9 wt%) to 7 (0.6 wt%). (Data from slices 1 and 2 were not available.) XRD and SEM-EDS indicated a peak in slice 2. Finally, AA5 indicated a high content of MgO in slice 2 (3.6 wt%), but with very uniform distribution with values of MgO content between 2.6 wt% and 3.6 wt% (also confirmed by SEM-EDS). This implies that the chalk type can affect the MgO distribution, most likely due to differences in primary non-carbonate content, thus the type and distribution of secondary phases, but also distribution of pores and microfossils. For comparison, in recent long-term tests on Liège chalk (Zimmermann et al. 2015) and related modelling results (Hiorth et al. 2013), most of the precipitated MgO accumulated near the inlet, with amounts decreasing rapidly towards the outlet.

Silica dissolution and re-precipitation (during MgCl_2 injection) as well as a significant concentration of Si^{4+} in the effluent could be observed in the chalk samples from Aalborg (Table 6, Fig. 8d). For the remaining chinks, the changes in SiO_2 composition after testing were less significant with SiO_2 content after flooding close to original (Table 6).

On several occasions, we saw that the analysis procedures had different detection limits. Most of the newly grown minerals had very small grain sizes, far below the spot size of the EDS of the FEG-SEM and the MLA. XRD can only detect a certain minimum amount of minerals, and slices with several wt% MgO or SiO_2 did not always result in positive identification of Mg - or Si -bearing minerals by XRD. The limited change in C–O isotope values (Sup. Mat. Table 2) may also be explained by the relatively low net formation of new secondary minerals from the hot fluid, which would not change the isotope composition significantly. In longer lasting tests, $\delta^{18}\text{O}_{SMOW}$ reflected the injection temperature when nearly the entire slice of a specific flooded chalk had been changed from calcite to magnesite (Zimmermann et al. 2013).

4.2 Significance of Opal-CT in the Aalborg Chalk Cores

As seen, the Aalborg chalk stood out from the other types. A main characteristic is that Aalborg had both the most considerable fraction of SiO_2 , and that it was in the form of opal-CT ($\text{SiO}_2 \cdot n\text{H}_2\text{O}$). In the other chinks the SiO_2 fraction was dominantly quartz, e.g. FEG-SEM images of unflooded material detected opal-CT in Aalborg (Fig. 3b, yellow square), but not in the other chalk types. The extraordinary shape of this crystal results in a high SSA ($4.9 \text{ m}^2/\text{g}$) compared to the rest ($2\text{--}3 \text{ m}^2/\text{g}$) and a low solid density (Table 2).

During flooding AA21 ($\sim 0.0012 \text{ mol/L}$) and AA5 ($\sim 0.0013 \text{ mol/L}$) displayed higher effluent concentrations of Si^{4+} than SK2 ($\sim 0.0007 \text{ mol/L}$) and SK6 ($\sim 0.0004 \text{ mol/L}$). Although such ICP-AES measurements were not made for the other cores, the whole-rock geochemistry indicated negligible alterations of the SiO_2 amount and spatial profiles apart from in the Aalborg cores (Table 6): AA21 displayed strong geochemical alteration after NaCl flooding (Table 6, Fig. 9a–c). The distribution of SiO_2 had a strong gradient from low values in slice 1 and 2 (2.4 wt%) to a plateau of more similar values (between 4.4 and 6.1 wt%) in slices 3 to 7. FEG-SEM images from AA21 after flooding could not detect opal-CT in slice 1 (Fig. 9a), but in slices 3 and 7 (Fig. 9b–c), corresponding to the locations where the SiO_2 content was low and high, respectively. The solid density changes (P1 (inlet): $+0.01 \text{ g/cm}^3$, P2 (outlet): $+0.00 \text{ g/cm}^3$) support the dissolution of a lighter mineral phase in the near inlet region. Furthermore, the SSA ($2.1 \text{ m}^2/\text{g}$) of AA21 in slice 1 after flooding (where the SiO_2 content was reduced from initially 4.9 to 2.4 wt%) is close to that of pure Stevns Klint chalk ($1.7 \text{ m}^2/\text{g}$) (Hjuler and Fabricius 2009). The other chalk types saw no significant changes in SiO_2 content or distribution (but a trend in reduction of SSA towards pure chalk). It is natural to conclude both that opal-CT is reactive, much more so than quartz and that it was mainly opal-CT that dissolved in AA21. Also, the SiO_2 profile combined with the locations of observed opal-CT grains (only in slices towards the outlet) suggests that the dissolution process occurs very fast, i.e. the brine becomes saturated (and less reactive) towards this mineral just after very short time in the core.

After flooding, our findings suggest that the reactive presence of opal-CT in Aalborg chalk plays a crucial role. The high Si^{4+} concentration obtained by dissolution of opal-CT allows interaction with Mg^{2+} in the brine, resulting in re-precipitation of new minerals, see FEG-SEM images of slice 1, 3 and 7 of AA5 in Fig. 9d–f. It is possible that talc was part of the new phase as indicated by MLA only for this core, but it was not verified by XRD. The formation of these new minerals (along with other Mg -bearing minerals) resulted in increased

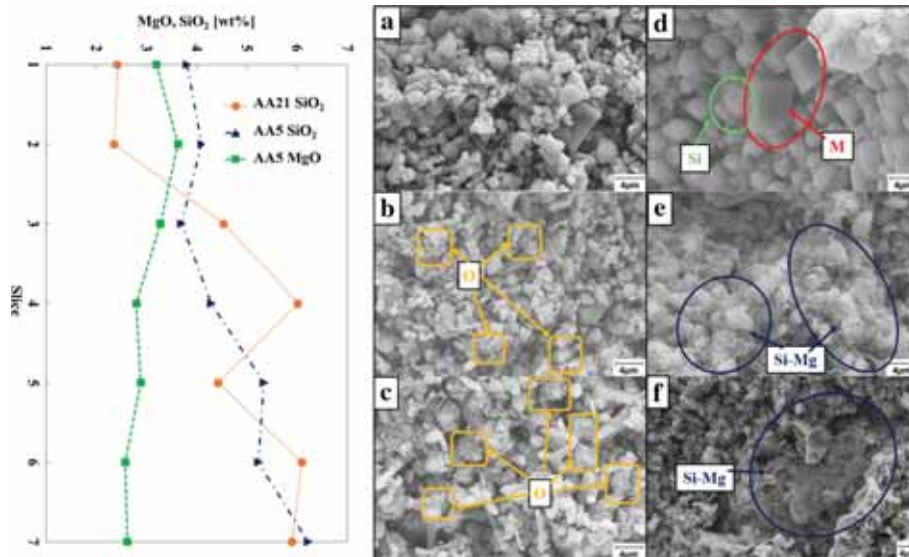


Fig. 9 Distribution (wt%) of SiO₂ and MgO along the core (left) are shown, along with FEG-SEM images from AA5 and AA21 (right): **a** AA21-1 (inlet), **b** AA21-3, **c** AA21-7 (outlet) and **d** AA5-1 (inlet), **e** AA5-3 and **f** AA5-7 (outlet). In AA5-1 we observe Si-bearing minerals (green circle) formed on top of a newly formed magnesite crystal (red circle). 'M': Magnesite was observed; 'Si-Mg': Si-Mg-bearing mineral was found in slices AA5-3 and AA5-7 as a thin coating (blue circles). The inlet slices AA5-1 and AA21-1 both display rounded grains indicative of dissolution. 'O': Opal-CT (yellow square) was detected in slices AA21-3 and AA21-7, but not in the inlet slice AA21-1. The SiO₂ content had been much reduced in the first two slices of this core

SSA. Particularly, the SSA (4.99 m²/g in unflooded material, as shown in Table 2), increased towards the outlet, in range 7–9 m²/g, consistent with the distribution of SiO₂ and the slices where the newly formed Si-Mg-bearing minerals were detected. The other MgCl₂-flooded cores (KA8, MO10, LI1, SK6), which did not indicate formation of such minerals, did not obtain higher SSA than 4 m²/g.

4.3 Modelling with PHREEQC

Flooding experiments of Aalborg chalk, including NaCl brine (AA21) and MgCl₂ brine (AA5), were replicated in a 1D advection dispersion reaction (ADR) model set-up in PHREEQC v3 (Parkhurst and Appelo 2013), a geochemical software. Similar modelling of core flooding tests considering more complex brines into pure chalk was performed in Madland et al. (2011) and Andersen et al. (2012), while modelling of MgCl₂ injection in a fracture–matrix context was considered by Andersen and Evje (2016). The current analysis was performed in order to investigate the role of Si⁴⁺-ions in the physicochemical interplay in light of the experimental observations.

Variables of minerals, brine ions and surface ions are represented by concentrations C_i given in mol per L pore volume. As initial rock composition, we apply the average composition of Aalborg chalk given in Table 6a, assuming SiO₂ belongs to opal-CT and MgO to magnesite, while the rest is calcite. A porosity of $\varphi = 47\%$ (see Table 2) was assumed. Opal-CT consists of cristobalite and tridymite; for simplicity the properties of cristobalite were taken as representative (Table 11). The conversion from mineral mass fraction p_i to mineral concentration C_i was made as follows:

Table 11 Parameters used in simulation

Mineral i	Dissolution reaction*	$\log K_i$ at 130 °C (-)	ρ_i (g/cm ³)	MW _{i} (g/mol)	Initial p_i (-)	Initial C_i (mol/L)	RF _{i} (-)
Calcite	$\text{CaCO}_3(\text{s}) \leftrightarrow \text{Ca}^{2+} + \text{CO}_3^{2-}$	0.39	2.71	100.09	0.935	28.09	4.75e-7
Magnesite	$\text{MgCO}_3(\text{s}) \leftrightarrow \text{Mg}^{2+} + \text{CO}_3^{2-}$	0.04	3.10	84.31	0.009	0.32	1.43e-4
Opal-CT**	$\text{SiO}_2 \cdot n\text{H}_2\text{O}(\text{s}) \leftrightarrow \text{SiO}_2 + n\text{H}_2\text{O}$	-2.46	2.33	66.76	0.056	2.53	8e-2
Talc	$\text{Mg}_3\text{Si}_4\text{O}_{10}(\text{OH})_2(\text{s}) \leftrightarrow -6\text{H}^+ + 3\text{Mg}^{2+} + 4\text{H}_2\text{O} + 4\text{SiO}_2$	13.27	2.71	379.27	0.000	0	1.0e-9

K_i : solubility constant, ρ_i : mineral density, p_i : mineral weight fraction, C_i : mineral concentration, RF _{i} : rate reduction factor

* Solid species (s) on left side, aqueous species on right side

** For opal-CT the density and solubility of cristobalite is assumed, along with a molar weight based on 10% hydration

$$C_i = \frac{\frac{P_i}{MW_i} (1 - \varphi)}{\sum_{j:\text{minerals}} \frac{P_j}{\rho_j} \varphi}, \quad (4)$$

where MW_i is mineral molar weight and ρ_i is mineral density (see values in Table 11). The initial brine is DW equilibrated with calcite and opal-CT. The injected brine is either 0.657 mol/L NaCl or 0.219 mol/L $MgCl_2$ with carbon concentration corresponding to what dissolves at atmospheric conditions ($P_{CO_2} = 10^{-3.5}$ atm); roughly 1.3×10^{-5} mol/L. The core is 7 cm in length, the injection rate 1 PV/d, and the temperature 130 °C. Thirty-five grid cells were used. Equilibrium calculations predicted that opal-CT and calcite could dissolve in NaCl brine and that re-precipitation of quartz could occur. As newly formed quartz could not be detected or significantly improve the modelling, it was not included. Further, $MgCl_2$ saturated with calcite and opal-CT could precipitate several Mg- or Si-bearing minerals such as brucite, dolomite, monticellite, quartz and talc. As magnesite and talc were indicated from the geological analysis, they were included in the model, in addition to calcite and opal-CT.

We include mineral dissolution and precipitation reactions (see Table 11) using kinetic rates of the following form (Palandri and Kharaka 2004; Appelo and Postma 2005):

$$\frac{dC_i}{dt} = -RF_i \left(\frac{A}{V}\right) \left(\frac{m}{m_0}\right)^{r_i} (k_{1,i} + k_{2,i} a_h^{n_i}) \text{sign}(1 - \Omega) |1 - \Omega_i^{p_i}|^{q_i}, \quad (5)$$

for the minerals i = calcite, magnesite, opal-CT and talc, where $\Omega_i = \frac{IAP_i}{K_i}$ represents the saturation state (ratio of the ion activity product IAP_i and solubility constant K_i) for each mineral. That is, if a mineral is oversaturated it precipitates, while if it is under-saturated (and its concentration is positive) it dissolves. $\left(\frac{A}{V}\right) = 14580 \text{ m}^2/\text{L}$ represents the original ratio of surface area to fluid volume based on average parameters from the two Aalborg cores. The factor $\left(\frac{m}{m_0}\right)^{r_i}$ is the ratio of current and initial moles, representing reduction in available surface area for a dissolving mineral. This factor was only used for opal-CT with $r_i = \frac{2}{3}$. a_h is the activity of H^+ , while $k_{1,i}$, $k_{2,i}$, p_i , q_i are mineral and/or temperature specific parameters collected from Palandri and Kharaka (2004). The reference assumption was that the full surface area of the rock was available for precipitation and dissolution, while a reduction factor $RF_i < 1$ was included to account for less available area. Ion exchange of Na^+ , Ca^{2+} and Mg^{2+} was included to capture the early Ca^{2+} peak and delay of Mg^{2+} observed in the effluent profiles (Fig. 6a, b). For treatment of charge balance, carbon speciation, complexes, etc., we refer to Parkhurst and Appelo (2013), Appelo and Postma (2005) and Andersen et al. (2012).

The four reaction rate coefficients RF_i and three ion exchange parameters [cation exchange capacity and two equilibrium constants, see Andersen et al. (2012)] were tuned in order to match the effluent time profiles and geochemistry spatial profiles after flooding. The parameters were uniquely matched and applied with same values in both the NaCl and $MgCl_2$ tests; AA21 and AA5. It was necessary to reduce the rates significantly varying from a factor of $RF = 0.08$ (for opal-CT) to 10^{-9} for talc (see Table 11). For opal-CT the RF was very close to the initial content (5.6 wt%). It is possible that the great oversaturation of talc and magnesite at high temperature and the fact that they were precipitating and not dissolving exceeded the validity of the literature rates, hence the need to reduce their magnitude. It is also possible that the available area for precipitation is less than the full surface area of the rock.

4.3.1 NaCl Flooding Tests

There was a discrepancy between the measured changes in SiO₂ composition (Table 6b) and the measured effluent Si⁴⁺ concentration (~ 0.001 mol/L, see Fig. 8d) from AA21. It was assumed that the geochemistry measurements were more accurate as they are cumulative, and some mismatch of the Si⁴⁺ effluent concentration was accepted (Fig. 6a). The amount of dissolved SiO₂ and the spatial profile were then well matched (Fig. 6b) using the literature rate (normalized to initial content). The observed SiO₂ wt% profile can be explained by rapid dissolution of opal-CT: the brine gets saturated after 3–4 cm with little dissolution downstream. Matching towards the effluent would give less dissolution and a more uniform profile.

The literature rate of calcite dissolution was sufficiently high to achieve full saturation ($\Omega_{\text{calcite}} = 1$) after flooding. Any tuning of RF_{calcite} maintained this property. The predicted effluent Ca²⁺ concentration was 0.00092 mol/L at steady state. That is roughly a factor of 4 lower than measured values, but within the range of uncertainty. (The measurements were near or below the detection limit, see Sup. Mat. 1.7.) Ca–Si complexes were evaluated to have negligible effect on the dissolution process, contrary to the statements in Fabricius and Borre (2007); the predicted production of Ca²⁺ was the same ($\sim 1\%$ difference) whether Si⁴⁺ was present in the system or not (reasonable for SK2 and MO12). On the other hand, much of the Si⁴⁺-ions were bound in complexes with Na⁺, effectively increasing the solubility by $\sim 15\%$ compared to DW (seen by the increasing Si⁴⁺ concentration the first PVs in Fig. 6a). Ion exchange parameters of Na⁺ and Ca²⁺ were tuned to give a peak 2–3 times higher than the steady state level.

Mass rates $\frac{dM}{dt}$ (g/mol) were calculated based on the injected and effluent concentrations C_i (mol/L) of the aqueous species, using their molar weight (g/mol) and injection rate Q (L/d) (see Table 2) as follows:

$$\frac{dM}{dt} = Q \sum_{i:\text{aq}} C_i^{\text{inj}} - C_i^{\text{eff}} \text{ MW}_i. \quad (6)$$

First, only considering the production of Ca²⁺ and CO₃²⁻ (assuming non-reactive Si⁴⁺), we obtain a mass rate of -0.0033 g/d, which is in the range of mass rate for the pure cores MO12 (-0.010 g/d) and SK2 (-0.002 g/d), but also the impure chalks with quartz; KA6 (-0.008 g/d) and LI2 (-0.006 g/d), see also Table 7. Adding the contribution from predicted SiO₂ (aq) production (effluent concentration 0.0044 mol/L), we obtain a mass rate of -0.013 g/d which is larger than the mentioned cores and more close to the measured mass rate of AA21 (-0.025 g/d). For this case the production of SiO₂ accounts for 74% of the mass loss.

4.3.2 MgCl₂ Flooding Tests

Also for the core AA5 there was a discrepancy between the effluent measurements of Si⁴⁺ and the whole-rock geochemistry for SiO₂: (1) the effluent Si⁴⁺ measurements (0.0013 mol/L) were ~ 2.5 times lower than the production required (0.0032 mol/L) to produce the measured changes in SiO₂ (as for AA21). Also, (2) the effluent measurements suggested a higher production of SiO₂ from AA5 (MgCl₂) than AA21 (NaCl), see Fig. 6d. On the other hand the geochemistry measurements suggested a greater loss of SiO₂ from AA21 (MgCl₂) than AA5 (NaCl). The model predicts that even without precipitation of secondary minerals, MgCl₂ dissolves less opal-CT than NaCl, further supporting to match the geochemistry also for this test.

The dissolution of calcite and precipitation of magnesite are closely coupled and is more or less a substitution process on core scale for wide ranges of their rate parameters. (The mass is, however, reduced since Mg weighs less than Ca.) Increasing the magnitude of either calcite or magnesite reaction rates led to more substitution (more production of Ca^{2+} and retention of Mg^{2+}), while altering the ratio of the two rates while keeping a fixed production affected the magnesite precipitation profile in the core. The dissolution rate of opal-CT was kept from the simulation of AA21. The predicted dissolution of opal-CT then resulted in higher Si^{4+} production than indicated by the geochemical changes in SiO_2 (Table 6), suggesting significant re-precipitation of Si-bearing minerals in the core, and the difference was eliminated by tuning the reaction rate of talc. Further, precipitation of talc affected the produced sum of Ca^{2+} and Mg^{2+} (i.e. making it no longer a substitution). These measurements were thus also an indirect observation of the extent of talc precipitation.

The effluent profiles of Ca^{2+} and Mg^{2+} were matched, see Fig. 10c, where the early transient phase was modelled by ion exchange of Ca^{2+} and Mg^{2+} . The simulated time frame of the ion exchange period was limited to the first ~ 15 PV, while transient effects were seen until ~ 25 PV. This could be better captured by a time-dependent increase in ion exchange capacity: as observed in Table 10, the SSA increased significantly during the AA5 test. A closer view of the low concentration effluent profiles is seen in Fig. 10d, especially comparing the predicted and measured Si^{4+} effluent profiles. The order of magnitude is well captured. Measured spatial profiles of MgO and SiO_2 describe quantitatively the local amount of an element in the rock, but not how it is distributed into different minerals. It was therefore decided to tune the model such that the total contribution of different species matched those measurements. The result is given in Fig. 10e for Mg^{2+} -species with a good match of both magnitude (indicative of consistency with effluent measurements) and spatial profile. Notably, magnesite is distributed evenly except for low concentrations at the inlet. A magnesite peak is given between 2 and 3 cm from the inlet, which is consistent with the XRD measurements, indicating a magnesite peak in slices 2 and 3 (Fig. 4c). Some Mg^{2+} is retained to the surface by adsorption with higher concentrations near the inlet (where the $\text{Mg}^{2+}/\text{Ca}^{2+}$ concentration ratio is higher). Talc is predicted to be distributed along the entire core, in agreement with the MLA (Table 5). The simulated talc profile was, however, not in complete accordance with experimental measurements which indicated increasing amounts of talc towards the outlet (Fig. 9d, e, f), while the simulations indicated the opposite trend. As talc was not positively verified by XRD (Fig. 4c) (merely indicated by MLA, see Fig. 5c and Table 5), other geologically relevant Si-Mg minerals, such as monticellite CaMgSiO_4 , were simulated, but also yielding same trend, decreasing in concentration from the inlet towards the outlet. This mismatch indicates that some mechanisms are yet not accounted for in the model. We note that changes in permeability, porosity, surface area could be such factors, but also solids transport or a more complex precipitation mechanism than applied here. The calculated and measured spatial Si profiles after flooding AA5 are given in Fig. 10f, again displaying good agreement between the SiO_2 measurements and the total Si concentration profile. Opal-CT was heterogeneously distributed in unflooded Aalborg chalk (ranging between 4 and 6 wt% SiO_2 , see Table 6a or Sup. Mat. Table 1), which can explain some of the variations along the core. A noticeable fraction of the initial opal-CT has been dissolved and converted into talc. The re-precipitation effect has led to a higher degree of opal-CT dissolution as seen by comparing Fig. 10f with Fig. 10b (NaCl-flooded AA21). Opal-CT has been significantly dissolved along the entire core in the case of AA5, unlike AA21 where only half the core was affected. We further note that the precipitation mechanism of talc induced a higher dissolution of calcite: the predicted steady state effluent Ca^{2+} concentration from AA5 when setting the talc and opal-CT reaction rates to zero (only calcite and magnesite minerals accounted for)

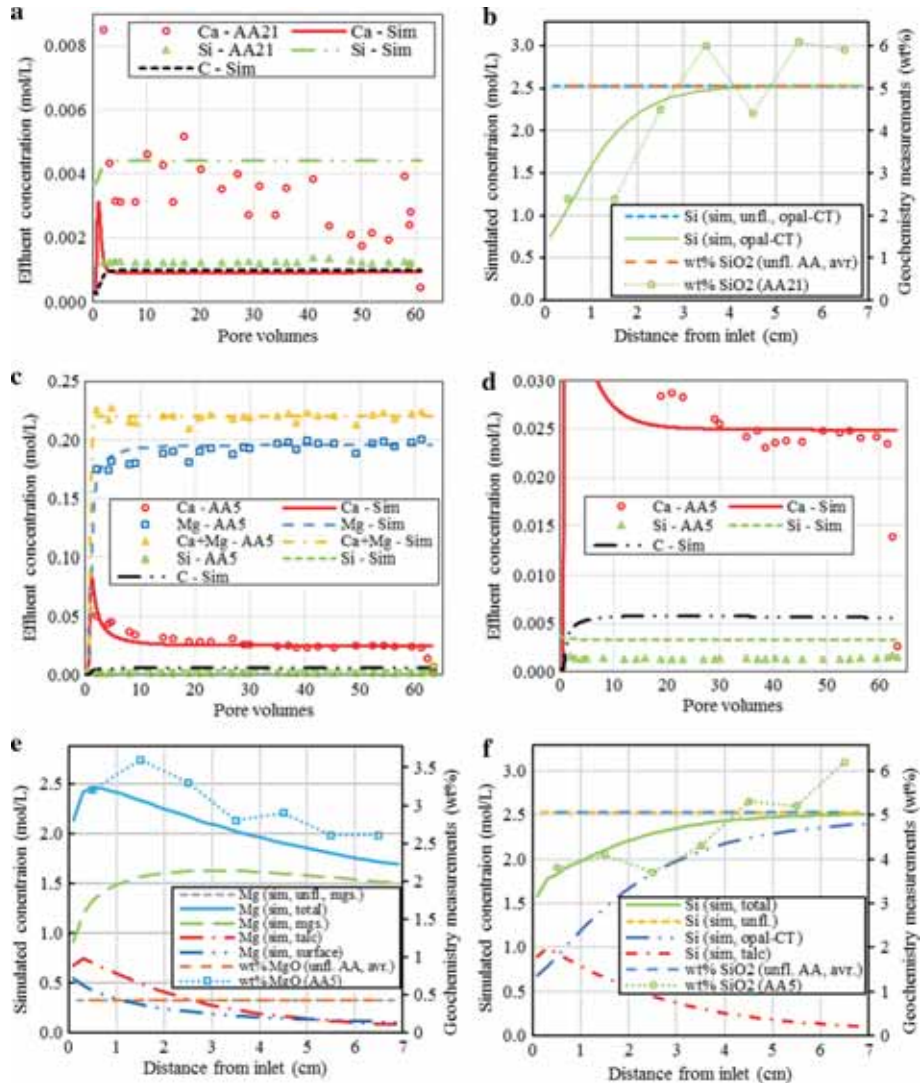


Fig. 10 Simulation (Sim) results from PHREEQC compared with experimental data (marked by core name). **a** Effluent from AA21; **b** spatial Si profiles from AA21; **c** effluent from AA5; **d** effluent from AA5 with focus on small concentrations; **e** spatial Mg profiles from AA5; **f** spatial Si profiles from AA5. Initial composition (unfl.) is based on average composition of unflooded Aalborg (unfl. AA, avr.). Concentration variables are scaled to match wt% measurements initially. All variables given in mol/L (left axis) unless specified to wt% (right axis). Simulated element contribution from different minerals is indicated

was 0.006 mol/L lower (originally 0.025 mol/L, see Fig. 10d). As expected, the measured average MgO content in AA5 (3.00 wt%) was the highest of all the cores, see Table 6c, while the originally pure cores MO10 and SK6 obtained the lowest values (1.49 and 1.54 wt%, respectively). Similarly, AA5 (-4.15 g) had the highest mass loss, while MO10 (-1.57 g) and SK6 (-1.11 g) lost the least mass, see Table 7. The high dissolution of calcite corresponds well the high compaction of AA5 and AA1, seen in Fig. 7b, compared to the other cores.

4.4 Compaction and Chemistry

As presented, NaCl flooding is typically performed to produce baseline results from which one can reduce or eliminate the impact of chemical effects. Considering the creep compaction profiles in Fig. 7a, we note that cores with higher content of SiO₂, experienced less deformation. Apparently, Si-bearing minerals can add to the strength of chalk during the creep phase. The most impure cores AA21 and LI2 produced the most Ca²⁺ among these cores (on average 0.0036 and 0.004 mol/L, respectively) (Fig. 8a), but of such a small amount (near the detection limit) that it likely did not impact the weakening of the chalk. In SK2 the production of Si⁴⁺ was also very low (~ 0.0007 mol/L). AA21 saw a more significant dissolution (0.0012 mol/L) in SiO₂ content (Fig. 8d, Table 6), but still contained after flooding higher SiO₂ content than the other chalk cores, and compacted the least.

For the MgCl₂-flooded cores, the trend was opposite. The two most impure cores AA5 and AA1 clearly compacted the most (AA5: 5.47 %, AA1: 6.55%, Fig. 7b). The other cores showed less, but roughly similar compaction (KA8: 2.99%; MO10: 3.2%; LI1: 3.57%; SK6: 3.58%; SK1: 3.22%). SK1, SK6, MO10 and LI1 showed creep acceleration (Fig. 7b). In particular, for the pure chalks SK1, SK6 and MO10 a delay period of low compaction rate was observed, followed by creep acceleration and higher compaction rate. KA8 saw a slight increase in compaction rate (up to 40 days), while LI1 saw a more clear, but gradual transition from slow (5–22 days with creep strain from 1.41 to 1.57%) to faster compaction (~ 23 days with creep strain 1.75%). From the performed tests, we note that if acceleration happened at later times it also occurred at higher strain (see Fig. 7b, Table 12). Considering the chalk types, these parameters mostly increase with amount of non-carbonates (mainly SiO₂), although KA8 breaks this trend, showing a slight compaction rate increase at an early time, but its low original porosity may be a factor. Although there could be a correlation between the onset of creep acceleration and chalk impurity, reliable prediction requires a more fundamental understanding.

The compaction behaviour was also reflected in the effluent concentration profiles. The cores having continuous compaction development (AA5 and KA8) also produced a monotonously decreasing effluent Ca²⁺ concentration before stabilizing, see Fig. 8b. The pure chalk cores MO10 and SK6 and the more impure core LI1, which experienced creep delay and accelerated creep, produced decreasing Ca²⁺ effluent concentrations to a minimum value (MO10: 0.018 mol/L; LI1: 0.015 mol/L; SK6: 0.013 mol/L). Then, roughly at the time of creep acceleration, the Ca²⁺ production increased significantly and reached a stable state (MO10: 0.024 mol/L; LI1: 0.018 mol/L; SK6: 0.022 mol/L). Accordingly, the Mg²⁺ effluent concentration obtained peaks before stabilizing, see Fig. 8c. These observations indicate once more the coupled nature of chemistry and compaction, by displaying increased chemical interaction at higher compaction rates. Comparing with previous studies (Madland et al.

Table 12 Data for cores, which exhibited creep acceleration: SiO₂ (wt%), time of acceleration and axial strain in delay period

Core	SiO ₂ (wt%)	Onset of creep acceleration (d)	Strain in delay phase (%)
SK1	0.35	7	0.3
SK6	0.33	15	0.5
MO10	0.92	26	0.8
KA8	1.7	9	0.4
LI1	2.2	32	1.5

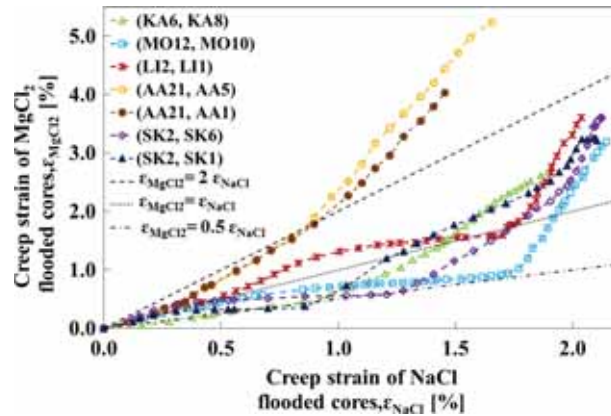


Fig. 11 Axial creep strain comparison between MgCl_2 and NaCl -flooded cores. The strain data $\varepsilon_{\text{MgCl}_2}$ of each MgCl_2 -flooded core are plotted vs. the strain $\varepsilon_{\text{NaCl}}$ of the NaCl -flooded core of same chalk type. The graph label reads '(NaCl-flooded core, MgCl_2 -flooded core)'. Lines indicating equal, half (0.5) and double (2) deformation with MgCl_2 , compared to NaCl , are indicated

2011) a Liège core injected with MgCl_2 at same conditions displayed continuous compaction (like the Aalborg cores), i.e. no delay phase or acceleration, and the effluent Ca^{2+} profile was monotonously decreasing. In addition, also common with the Aalborg cores, significant concentrations of Si^{4+} were detected in the effluent (~ 0.0025 mol/L) and re-precipitation of Si-bearing mineral was observed. These common features seen for two different chalk types (Liège and Aalborg) could suggest that an active Si chemistry affects both mineralogical alterations, effluent profiles of the divalent ions and the compaction behaviour.

To see the effect of brines on compaction, the axial creep strain of the MgCl_2 -flooded cores ($\varepsilon_{\text{MgCl}_2}$) is plotted versus the axial creep strain of the NaCl -flooded cores ($\varepsilon_{\text{NaCl}}$) of the same chalk type in Fig. 11. For data following $\varepsilon_{\text{MgCl}_2} = \varepsilon_{\text{NaCl}}$ (dotted line in Fig. 11) there are no significant effects from the rock-brine chemistry. Most of the chalk types followed this trend initially, but deviated more for creep strains > 0.5 %. Considering Fig. 7, this corresponds to 1–5 injected PVs, indicating brine sensitivity very early. The purest chalk cores MO10, SK1, SK6 and KA8 at first experienced less deformation with MgCl_2 than their corresponding cores MO12, SK2 and KA6 injected with NaCl brine, for $\varepsilon_{\text{NaCl}} < 1.5$ %. The ratio between the strains, $\varepsilon_{\text{MgCl}_2}/\varepsilon_{\text{NaCl}}$, did not reach below 0.5. The two LI cores compacted with similar magnitude for strains < 1.8 %. In long term, however, all these chalks eventually obtained more deformation with MgCl_2 than with NaCl (the ratio $\varepsilon_{\text{MgCl}_2}/\varepsilon_{\text{NaCl}}$ stayed below 2 during the test period). For Aalborg, the chalk with highest non-carbonate content, this effect was observed from the start: AA5 and AA1 (MgCl_2 -flooded) both displayed consistently higher strains than for AA21, and the difference increased gradually with time.

The mineralogical processes initiated by Mg^{2+} seem to inhibit compaction in pure chalk types (MO, SK and KA) compared to NaCl during the initial creep phase, but in the long run the compaction will be more significant, regardless of chalk type. Also Zhang et al. (2011) observed that MgCl_2 can inhibit creep compaction compared to NaCl in milled limestone (> 99 wt% calcite) at 150 °C. In this study, we could also observe acceleration in creep following the mentioned delay/inhibition period (Fig. 7).

The impact brines had on compaction which is represented in Fig. 11 and corresponds well with the mineralogical changes. As seen in Zimmermann et al. (2013), it is assumed that dissolution of the chalk matrix, triggered by the non-equilibrium fluids, can enhance the

precipitation of Mg-bearing minerals. The extent of increased compaction (compared with NaCl flooding) correlated well with the amount of MgO in the cores after flooding (KA8: 2.3 wt%; AA5: 3.0 wt%; SK6: 1.5 wt%; MO10: 1.5 wt%; LI1: 1.8 wt%, the cores had similar initial content of MgO, 0.2–0.4 wt%, Table 6). As exception, KA8 obtained a high MgO content and low compaction, but it is likely related to its lower porosity.

4.5 Application of the Results

In recent years ‘smart water’ brines, which typically involve modifying the natural set-up of ions in seawater (Ca^{2+} , Mg^{2+} , SO_4^{2-} , Na^+ , Cl^-), have been more and more investigated to increase oil recovery by attempting to change wettability, avoid scaling, but also predicting or controlling the extent of compaction. Our work, together with the Si-bearing minerals finding by Madland et al. (2011), demonstrates that the original mineralogy, especially the non-carbonate content, the newly formed minerals caused by dissolution and formation of secondary minerals in addition to re-precipitation of new minerals, can control the chemo-mechanical interactions and should be taken into account when predicting reservoir behaviour from laboratory studies [i.e. the Ekofisk field contains considerable amounts of non-carbonate minerals (Van den Bark and Thomas 1981)].

Chalk–fluid interactions at field scale is still a great challenge. In particular, fractured reservoirs in the North Sea have high porosity (up to 45%), low matrix permeability (3–4 mD) and small matrix block size. In order to understand the complex mechanisms and dynamics, a mathematical interpretation of the geochemical interaction was performed, capturing the main trends and observations. Taking the results to predicting performance during brine injection at field scale, the systematic laboratory analysis of chalk–brine interactions in this study can be helpful in bridging the gap when it comes to the effect of non-carbonate mineralogy in chalk. Potentially, the results can be used for predicting the extent of mineralogical changes and transformation of reservoir properties in fracture and matrix, e.g. our measurements show that the mineralogical alterations significantly affected the specific surface area, which is an indicator of permeability in chalks (Hjuler and Fabricius 2009; Megawati et al. 2015). The experimental results presented in this paper were made at a constant high temperature (130 °C representative of Ekofisk conditions). Both multiphase flow properties and reaction kinetics are strongly temperature dependent. In a producing field, cold water is normally injected, and thus, temperature-dependent reaction kinetics and compaction models should be developed or predicted and up-scaled before industrial application.

5 Conclusions

This study has considered five types of outcrop chalks (Kansas, Mons (Trivières Fm.), Liège, Aalborg and Stevns Klint, sorted from old to young), with similar age and high porosity, exposed to identical core flooding–compaction tests at 130 °C in creep state. Dual tests were performed where chalk cores were injected with 0.219 mol/L MgCl_2 or 0.657 mol/L NaCl at 1 PV/d over a period of 2–3 months to simulate reservoir conditions of some hydrocarbon reservoirs in the North Sea.

In this study, extensive analysis of unflooded and flooded material was made to systematically interpret mineralogical and chemical changes along the core samples (sliced in seven equal slabs) by means of XRD, SEM-MLA, SEM-EDS, whole-rock geochemistry, stable isotope geochemistry and BET (N_2). These methods are sensitive to alterations of the core and showed that non-carbonate chemistry (mainly Si-bearing minerals) does affect

rock mechanical parameter and processes. The diagenetic variations may help in establishing useful guidelines in searching for the best substitute analogous to the North Sea reservoir chalk with respect to mechanical and mineralogical properties. The measurements were also interpreted by mathematical modelling supporting the interpretation of the mechanisms in the Aalborg chalk: opal-CT dissolves very reactively both with NaCl and MgCl₂ brines. The released Si⁴⁺-ions can interact with injected Mg²⁺- and Ca²⁺-ions and re-precipitate as new mineral phases such as talc, consistent with experimental observations. The formation of these new minerals can trigger enhanced dissolution of calcite, which can explain the high compaction rate seen in the Aalborg cores (Fig. 7b) flooded with MgCl₂.

Mg-bearing minerals, mainly magnesite and Mg-rich calcite, are precipitated in the MgCl₂-flooded cores (KA8, MO10, LI1, AA5, and SK6). The cores KA8 and AA5 obtained more retention of Mg²⁺ than other cores (MO10, LI1 and SK6) in the geochemical measurement, which is also supported by the effluent analysis. This is reflected in the measured increased solid densities and increased SSA. The MgO distributions along the cores behave differently. The sample KA8 obtained the MgO peak near the inlet, while in AA5 a uniform pattern was observed. In the other three chalk types, the highest values occurred near the centre along the flooding direction of the cores. This implies that the MgO precipitation is not only time dependent, but also chalk type dependent, hence influenced by the genesis of the rock. In addition, Aalborg chalk contained abundant opal-CT, which was significantly dissolved with both NaCl and MgCl₂ brines. Si-Mg-bearing minerals (interpreted as talc by MLA) was detected as newly grown phase in MgCl₂-flooded Aalborg chalk and could be related to a significantly increased specific surface area. The other chalks, where SiO₂ was bound mainly in quartz, did not see strong alterations in SiO₂ distribution after flooding. These findings suggest opal-CT plays an important role.

In creep phase, NaCl-flooded cores with higher SiO₂ content compacted less, while cores exposed to MgCl₂ compacted more with increasing SiO₂ content. The cores flooded with MgCl₂ compacted more than that with NaCl given sufficient time; however, for a period MgCl₂ inhibited compaction in pure chalks compared to NaCl.

The study concludes that precipitation of new minerals not originally present, triggering enhanced matrix dissolution of original minerals is the key driving force for chemical creep compaction in these core flooding experiments. In future studies, we plan to assess the contribution of mechanisms and parameters such as pressure solution, porosity and creep stress which in this study are considered less important.

Acknowledgements The authors thank the Faculty of Science and Technology for the PhD grant for W. Wang. Thanks are due to the SEM work (AA5) done by Tania Hildebrand-Habel. The authors thank COREC for financial support for this research study and acknowledge the Research Council of Norway and the industry partners: ConocoPhillips Skandinavia AS, BP Norge AS, Det Norske Oljeselskap AS, Eni Norge AS, Maersk Oil Norway AS, DONG Energy A/S, Denmark, Statoil Petroleum AS, ENGIE E&P NORGE AS, Lundin Norway AS, Halliburton AS, Schlumberger Norge AS, Wintershall Norge AS of The National IOR Centre of Norway for support. The research presented is integral part of the PhD thesis of W. Wang at UiS.

References

- Andersen, P.Ø., Evje, S., Madland, M.V., Hiorth, A.: A geochemical model for interpretation of chalk core flooding experiments. *Chem. Eng. Sci.* **84**, 218–241 (2012). <https://doi.org/10.1016/j.ces.2012.08.038>
- Andersen, P.Ø., Evje, S.: A model for reactive flow in fractured porous media. *Chem. Eng. Sci.* **145**, 196–213 (2016). <https://doi.org/10.1016/j.ces.2016.02.008>
- Appelo, C.A.J., Postma, D.: *Geochemistry, Groundwater and Pollution*. Taylor & Francis Group, Boca Raton (2005)

- Bertolino, S.A.R., Zimmermann, U., Madland, M.V., Hildebrand-Habel, T., Hiorth, A., Korsnes, R.I.: Mineralogy, geochemistry and isotope geochemistry to reveal fluid flow process in flooded chalk under long term test conditions for EOR purposes. In: XV International Clay Conference, Brasil, vol. 676 (2013)
- Bjørlykke, K., Høeg, K.: Effects of burial diagenesis on stresses, compaction and fluid flow in sedimentary basins. *Mar. Petrol. Geol.* **14**, 267–276 (1997). [https://doi.org/10.1016/s0264-8172\(96\)00051-7](https://doi.org/10.1016/s0264-8172(96)00051-7)
- Bjørlykke, K.: Relationships between depositional environments, burial history and rock properties. Some principal aspects of diagenetic process in sedimentary basins. *Sediment. Geol.* **301**, 1–14 (2014). <https://doi.org/10.1016/j.sedgeo.2013.12.002>
- Brindley, G.W., Brown, G.: Crystal structure of clay minerals and their X-ray identification. In: Brindley, G.W., Brown, G. (eds.) *Mineralogical Society Monograph*, vol. 5, pp. 361–410. Mineralogical Society, London (1980)
- Collin, F., Cui, Y.J., Schroeder, C., Charlier, R.: Mechanical behaviour of Lixhe chalk partly saturated by oil and water: experiment and modelling. *Int. J. Numer. Anal. Methods* **26**, 897–924 (2002). <https://doi.org/10.1002/nag.229>
- Engstrøm, F.: Rock mechanical properties of Danish North Sea chalk. In: *Proceedings of 4th North Sea Chalk Sym*, Deauville (1992)
- Fabricius, I.L.: Compaction of microfossil and clay-rich chalk sediments. *Phys. Chem. Earth Part A* **26**, 59–62 (2001). [https://doi.org/10.1016/S1464-1895\(01\)00023-0](https://doi.org/10.1016/S1464-1895(01)00023-0)
- Fabricius, I.L., Borre, M.K.: Stylolites, porosity, depositional texture, and silicates in chalk facies sediments. Ontong Java Plateau–Gorm and Tyra fields, North Sea. *Sedimentology* **54**, 183–205 (2007). <https://doi.org/10.1111/j.1365-3091.2006.00828.x>
- Fabricius, I.L., Hoier, C., Japsen, P., Korsbech, U.: Modelling elastic properties of impure chalk from South Arne field, North Sea. *Geophys. Prospect.* **55**, 487–506 (2007). <https://doi.org/10.1111/j.1365-2478.2007.00613.x>
- Fjær, E., Holt, R.M., Horsrud, P., Raaen, A.M., Risnes, R.: *Petroleum Related Rock Mechanics*, 2nd edn, pp. 491–492. Elsevier, Amsterdam (2008)
- Frykman, P.: Spatial variability in petrophysical properties in Upper Maastrichtian chalk outcrops at Stevns Klint, Denmark. *Mar. Petrol. Geol.* **18**, 1041–1062 (2001). [https://doi.org/10.1016/S0264-8172\(01\)00043-5](https://doi.org/10.1016/S0264-8172(01)00043-5)
- Gaviglio, P., Vandycke, S., Schroeder, C., Coulon, M., Bergerat, F., Dubois, C., Pointeau, I.: Matrix strains along normal fault planes in the Campanian white chalk of Belgium: structural consequences. *Tectonophysics* **309**, 41–56 (1999). [https://doi.org/10.1016/s0040-1951\(99\)00131-6](https://doi.org/10.1016/s0040-1951(99)00131-6)
- Hart, M.B., Feist, S.E., Price, G.D., Leng, M.J.: Reappraisal of the K–T boundary succession at Stevns Klint, Denmark. *J. Geol. Soc. Lond.* **161**, 885–892 (2004). <https://doi.org/10.1144/0016-764903-071>
- Hart, M.B., Feist, S.E., Håkansson, E., Heinberg, C., Price, G.D., Leng, M.J., Watkinson, M.P.: The Cretaceous–Palaeogene boundary succession at Stevns Klint, Denmark: foraminifers and stable isotope stratigraphy. *Palaeogeogr. Palaeoecol.* **224**, 6–26 (2005). <https://doi.org/10.1016/j.palaeo.2005.03.029>
- Havmøller, O., Foged, N.: Review of rock mechanical data for chalk. In: *Proceedings of 5th North Sea Chalk Sym*, Reims (1996)
- Hellmann, R., Renders, P., Gratier, J., Guiguet, R.: Experimental pressure solution compaction of chalk in aqueous solutions Part 1. Deformation behavior and chemistry. In: Hellmann, R., Wood., S.A. (eds.) *Water–Rock Interactions, Ore Deposits, and Environmental Geochemistry: A Tribute to David A. Crerar*, vol. 7, pp. 129–152 (2002). <https://www.geochemsoc.org/publications/sps/v7/waterrockinteractionsore/>
- Hermansen, H., Thomas, L.K., Sylte, J.E., Aasboe, B.T.: Twenty five years of Ekofisk reservoir management. In: *SPE Annual Technical Conference and Exhibition San Antonio, Texas*, vol. 873–885 (1997). <https://doi.org/10.2118/38927-ms>
- Hermansen, H., Landa, G.H., Sylte, J.E., Thomas, L.K.: Experiences after 10 years of waterflooding the Ekofisk Field, Norway. *J. Petrol. Sci. Eng.* **26**, 11–18 (2000). [https://doi.org/10.1016/s0920-4105\(00\)00016-4](https://doi.org/10.1016/s0920-4105(00)00016-4)
- Hiorth, A., Jettestuen, E., Cathles, L.M., Madland, M.V.: Precipitation, dissolution, and ion exchange processes coupled with a lattice Boltzmann advection diffusion solver. *Geochim. Cosmochim. Acta* **104**, 99–110 (2013). <https://doi.org/10.1016/j.gca.2012.11.019>
- Hjuler, M.L.: Diagenesis of upper cretaceous onshore and offshore chalk from the North Sea area. PhD thesis, Technical University of Denmark, pp. 11–23 (2007)
- Hjuler, M.L., Fabricius, I.L.: Engineering properties of chalk related to diagenetic variations of Upper Cretaceous onshore and offshore chalk in the North Sea area. *J. Petrol. Sci. Eng.* **68**, 151–170 (2009). <https://doi.org/10.1016/j.petrol.2009.06.005>
- Jarvis, I.: The Santonian–Campanian phosphatic chalks of England and France. *Proc. Geol. Assoc.* **117**, 219–237 (2006). [https://doi.org/10.1016/S0016-7878\(06\)80011-8](https://doi.org/10.1016/S0016-7878(06)80011-8)

- Korsnes, R.I., Strand, S., Hoff, Ø., Pedersen, T., Madland, M.V., Austad, T.: Does the chemical interaction between seawater and chalk affect the mechanical properties of chalk? In: The International Symposium of the International Society for Rock Mechanics (2006a). <https://doi.org/10.1201/9781439833469.ch61>
- Korsnes, R.I., Madland, M.V., Austad, T.: Impact of brine composition on the mechanical strength of chalk at high temperature. In: The International Symposium of the International Society for Rock Mechanics. Liège, Belgium (2006b). <https://doi.org/10.1201/9781439833469.ch18>
- Korsnes, R.I., Madland, M.V., Austad, T., Haver, S., Røslund, G.: The effects of temperature on the water weakening of chalk by seawater. *J. Petrol. Sci. Eng.* **60**(3), 183–193 (2008)
- Madland, M.V., Midtgarden, K., Manafov, R., Korsnes, R.I., Kristiansen, T., Hiorth, A.: The effect of temperature and brine composition on the mechanical strength of Kansas chalk. In: International Symposium SCA (2008)
- Madland, M.V., Hiorth, A., Omdal, E., Megawati, M., Hildebrand-Habel, T., Korsnes, R.I., Evje, S., Cathles, L.M.: Chemical alterations induced by rock-fluid interactions when injecting brines in high porosity chalks. *Transp. Porous Med.* **87**, 679–702 (2011). <https://doi.org/10.1007/s11242-010-9708-3>
- McLennan, S.M., Taylor, S.R., Hemming, S.R.: Composition, differentiation, and evolution of continental crust: constraints from sedimentary rocks and heat flow. In: Brown, M., Rushmer, T. (eds.) *Evolution and Differentiation of the Continental Crust*, pp. 92–134. Cambridge Univ Press, Cambridge (2006)
- Megawati, M., Andersen, P. Ø., Korsnes, R.I., Evje, S., Hiorth, A., Madland, M.V.: The effect of aqueous chemistry pH on the time-dependent deformation behaviour of chalk experimental and modelling study. In: Pore2Fluid International Conference. Paris, France (2011)
- Megawati, M., Madland, M.V., Hiorth, A.: Mechanical and physical behavior of high-porosity chalks exposed to chemical perturbation. *J. Petrol. Sci. Eng.* **133**, 313–327 (2015). <https://doi.org/10.1016/j.petrol.2015.06.026>
- Molenaar, N., Zijlstra, J.J.P.: Differential early diagenetic low-Mg calcite cementation and rhythmic hard-ground development in Campanian–Maastrichtian chalk. *Sediment. Geol.* **109**, 261–281 (1997). [https://doi.org/10.1016/S0037-0738\(96\)00064-4](https://doi.org/10.1016/S0037-0738(96)00064-4)
- Nagel, N.B.: Compaction and subsidence issues within the petroleum industry: from Wilmington to Ekofisk and beyond. *Phys. Chem. Earth. Part A* **26**, 3–14 (2001). [https://doi.org/10.1016/S1464-1895\(01\)00015-1](https://doi.org/10.1016/S1464-1895(01)00015-1)
- Nermoen, A., Korsnes, R.I., Hiorth, A., Madland, M.V.: Porosity and permeability development in compacting chalks during flooding of nonequilibrium brines: insights from long-term experiment. *J. Geophys. Res. Solid Earth* **120**, 2935–2960 (2015). <https://doi.org/10.1002/2014JB011631>
- Nermoen, A., Korsnes, R.I., Aursjø, O., Madland, M.V., Kjørslevik, T.A.C., Østensen, G.: How stress and temperature conditions affect rock-fluid chemistry and mechanical deformation. *Front. Phys.* **4**, 1–19 (2016). <https://doi.org/10.3389/fphy.2016.00002>
- Neveux, L., Grgic, D., Carpentier, C., Pironon, J., Truche, L., Girard, J.P.: Experimental simulation of chemo-mechanical processes during deep burial diagenesis of carbonate rocks. *J. Geophys. Res. Solid Earth* **119**, 984–1007 (2014). <https://doi.org/10.1002/2013JB010516>
- Newman, G.H.: The effect of water chemistry on the laboratory compression and permeability characteristics of some North Sea chalks. *J. Petrol. Technol.* **35**, 976–980 (1983). <https://doi.org/10.2118/10203-pa>
- Palandri, J.L., Kharaka, Y.K.: *A Compilation of Rate Parameters of Water–Mineral Interaction Kinetics for Application to Geochemical Modeling*. U. S. Geological Survey, Menlo Park (2004)
- Parkhurst, D.L., Appelo, C.A.J.: Description of input and examples for PHREEQC version 3—a computer program for speciation, batch-reaction, one-dimensional transport, and inverse geochemical calculations. *U.S. Geological Survey Techniques and Methods*, Chap. A43 (2013)
- Paterson, M.S.: Nonhydrostatic thermodynamics and its geologic applications. *Rev. Geophys. Space Phys.* **11**, 355–389 (1973). <https://doi.org/10.1029/RG011i002p00355>
- Putnis, A.: Mineral replacement reactions: from macroscopic observations to microscopic mechanisms. *Miner. Mag.* **66**, 689–708 (2002). <https://doi.org/10.1180/0026461026650056>
- Risnes, R., Flaageng, O.: Mechanical properties of chalk with emphasis on chalk-fluid interactions and micromechanical aspects. *Oil Gas Sci. Technol.* **54**, 751–758 (1999). <https://doi.org/10.2516/Ogst:1999063>
- Risnes, R., Madland, M.V., Hole, M., Kwabiah, N.K.: Water weakening of chalk—mechanical effects of water-glycol mixtures. *J. Petrol. Sci. Eng.* **48**, 21–36 (2005). <https://doi.org/10.1016/j.petrol.2005.04.004>
- Ruiz-Agudo, E., Putnis, C.V., Putnis, A.: Coupled dissolution and precipitation at mineral-fluid interfaces. *Chem. Geol.* **383**, 132–146 (2014). <https://doi.org/10.1016/j.chemgeo.2014.06.007>
- Rutter, E.H.: The kinetics of rock deformation by pressure solution. *Philos. Trans. R. Soc. Lond.* **283**, 203–219 (1976)

- Schroeder, C., Gaviglio, P., Bergerat, F., Vandycke, S., Coulon, M.: Faults and matrix deformations in chalk: contribution of porosity and sonic wave velocity measurements. *Bull. Acad. Vet. Fr.* **177**, 203–213 (2006). <https://doi.org/10.2113/gssgfbull.177.4.203>
- Strand, S., Standnes, D.C., Austad, T.: Spontaneous imbibition of aqueous surfactant solutions into neutral to oil-wet carbonate cores? Effects of brine salinity and composition. *Energy Fuels* **17**, 1133–1144 (2003). <https://doi.org/10.1021/ef030051s>
- Strand, S., Hjuler, M.L., Torsvik, R., Pedersen, J., Madland, M.V., Austad, T.: Wettability of chalk: impact of silica, clay content and mechanical properties. *Petrol. Geosci.* **13**, 69–80 (2007). <https://doi.org/10.1144/1354-079305-696>
- Tang, G.Q., Firoozabadi, A.: Effect of pressure gradient and initial water saturation on water injection in water-wet and mixed-wet fractured porous media. *SPE Res. Eval. Eng.* **4**, 516–524 (2001). <https://doi.org/10.2118/74711-Pa>
- Van den Bark, E., Thomas, O.D.: Ekofisk-1st of the giant oil-fields in Western Europe. *AAPG Bull.* **65**, 2341–2363 (1981)
- Wang, W., Madland, M.V., Zimmermann, U., Neramoen, A., Korsnes, R.I., Bertolino, S.A.R., Hildebrand-Habel, T.: Evaluation of porosity change during chemo–mechanical compaction in flooding experiments on Liège outcrop chalk. In: Armitage, P.J., Butcher, A.R., Churchill, J.M., Csoma, A.E., Hollis, C., Lander, R.H., Omma, J.E. Worden, R.H. (eds.) *Reservoir Quality of Clastic and Carbonate Rocks: Analysis, Modelling and Prediction*. Journal of the Geological Society London. Special Publications, vol. 435 (2016). <https://doi.org/10.1144/SP435.10>
- Zhang, X., Spiers, C.J., Peach, C.J.: Compaction creep of wet granular calcite by pressure solution at 28 °C to 150 °C. *J. Geophys. Res.* **115**, 1–18 (2010). <https://doi.org/10.1029/2008jb005853>
- Zhang, X., Spiers, C.J., Peach, C.J.: Effects of pore fluid flow and chemistry on compaction creep of calcite by pressure solution at 150 °C. *Geofluids* **11**, 108–122 (2011). <https://doi.org/10.1111/j.1468-8123.2010.00323.x>
- Zimmermann, U., Madland, M.V., Bertolino, S.A.R., Hildebrand-Habel, T.: Tracing fluid flow in flooded chalk under long term test conditions. In: 75th EAGE Conference & Exhibition Incorporating SPE. London (2013)
- Zimmermann, U., Madland, M.V., Neramoen, A., Hildebrand-Habel, T., Bertolino, S.A.R., Hiorth, A., Korsnes, R.I., Audinot, J.N., Grysan, P.: Evaluation of the compositional changes during flooding of reactive fluids using scanning electron microscopy, nano-secondary ion mass spectrometry, X-ray diffraction and whole rock geochemistry. *AAPG Bull.* **99**, 791–805 (2015). <https://doi.org/10.1306/12221412196>

Paper VI: Tools to Determine and Quantify Mineralogical Changes During EOR Flooding Experiments on Chalk

Zimmermann, U., Madland, M.V., Minde, M.W., Borromeo, L. and Egeland, N. (2017).
Abu Dhabi International Petroleum Exhibition & Conference. Society of Petroleum Engineers, Abu Dhabi, UAE



NOT AVAILBLE IN THE BRAGE REPOSITORY

Paper VII: Quick, Easy, and Economic Mineralogical Studies of Flooded Chalk for EOR Experiments Using Raman Spectroscopy

Borromeo, L., Egeland, N., Minde, M.W., Zimmermann, U., Andò, S., Madland, M.V. and Korsnes, R.I. (2018).
Minerals 8 (6)

Article

Quick, Easy, and Economic Mineralogical Studies of Flooded Chalk for EOR Experiments Using Raman Spectroscopy

Laura Borromeo ^{1,2,*} , Nina Egeland ^{1,2}, Mona Wettrhus Minde ^{1,2}, Udo Zimmermann ^{1,2}, Sergio Andò ³ , Merete Vadla Madland ^{1,2} and Reidar Inge Korsnes ^{1,2}

¹ Department of Energy Resources, University of Stavanger, 4036 Stavanger, Norway; nina.sivertsen@gmail.com (N.E.); mona.w.minde@uis.no (M.W.M.); udo.zimmermann@uis.no (U.Z.); merete.v.madland@uis.no (M.V.M.); reidar.i.korsnes@uis.no (R.I.K.)

² The National IOR Centre of Norway, 4036 Stavanger, Norway

³ Department of Earth and Environmental Sciences, University of Milano-Bicocca, 20126 Milano, Italy; sergio.ando@unimib.it

* Correspondence: laura.borromeo@uis.no; Tel.: +39-338-600-8504

Received: 6 February 2018; Accepted: 17 May 2018; Published: 23 May 2018



Abstract: Understanding the chalk-fluid interactions and the associated mineralogical and mechanical alterations on a sub-micron scale are major goals in Enhanced Oil Recovery. Mechanical strength, porosity, and permeability of chalk are linked to mineral dissolution that occurs during brine injections, and affect the reservoir potential. This paper presents a novel “single grain” methodology to recognize the varieties of carbonates in rocks and loose sediments: Raman spectroscopy is a non-destructive, quick, and user-friendly technique representing a powerful tool to identify minerals down to 1 μm . An innovative working technique for oil exploration is proposed, as the mineralogy of micron-sized crystals grown in two flooded chalk samples (Liège, Belgium) was successfully investigated by Raman spectroscopy. The drilled chalk cores were flooded with MgCl_2 for ca. 1.5 (Long Term Test) and 3 years (Ultra Long Term Test) under North Sea reservoir conditions (Long Term Test: 130 $^\circ\text{C}$, 1 PV/day, 9.3 MPa effective stress; Ultra Long Term Test: 130 $^\circ\text{C}$, varying between 1–3 PV/day, 10.4 MPa effective stress). Raman spectroscopy was able to identify the presence of recrystallized magnesite along the core of the Long Term Test up to 4 cm from the injection surface, down to the crystal size of 1–2 μm . In the Ultra Long Term Test core, the growth of MgCO_3 affected nearly the entire core (7 cm). In both samples, no dolomite or high-magnesium calcite secondary growth could be detected when analysing 557 and 90 Raman spectra on the Long and Ultra Long Term Test, respectively. This study can offer Raman spectroscopy as a breakthrough tool in petroleum exploration of unconventional reservoirs, due to its quickness, spatial resolution, and non-destructive acquisition of data. These characteristics would encourage its use coupled with electron microscopes and energy dispersive systems or even electron microprobe studies.

Keywords: flooded chalk; Raman spectroscopy; Enhanced Oil Recovery; carbonates; calcite; magnesite

1. Introduction

Injection of seawater-like brines is one of the most successful Improved Oil Recovery (IOR) methods on the Norwegian Continental Shelf (amongst many others: [1,2]). The mechanical strength of chalk is weakened by seawater at reservoir temperatures, and as a consequence, compaction and loss in porosity occur, affecting the oil recovery factor of carbonate fields [3–10]. It is important to understand how fluids interact with rocks, because textural and chemical/mineralogical changes in the pore space affect the way water will adsorb and expel oil from the rock [3,8,11–17]. Previous research on fluid

injection has been carried out [5,8,17–21], and three ions have been proven to play important roles when chalk is exposed to seawater at elevated temperatures: Ca^{2+} , Mg^{2+} , and SO_4^{2-} . The injected seawater triggers several mechanisms such as precipitation, dissolution, ion exchange, adsorption, and desorption, to interplay at the same time, with different relative significance depending on the position in the reservoir (nearby to the injector or to the producer). It is therefore beneficial to simplify the system and study each ion individually. With MgCl_2 brines, which represent simplified aqueous chemistry of seawater, the role of Mg^{2+} is specifically studied.

The two cores investigated in this study (see Figure 1) were flooded with MgCl_2 for 1.5 (Long Term Test, LTT) and 3 years (Ultra Long Term Test, ULTT) under reservoir conditions (LTT: 130 °C, 1 PV/day, 9.3 MPa effective stress, ULTT: 130 °C, varying between 1–3 PV/day, 10.4 MPa effective stress), in order to reach a mineralogical insight of the basic processes that happen during long time brine injection.

The analyses are carried out by Raman spectroscopy, which is a quick and versatile technique gaining a wide range of information; it can easily be applied to almost all substances (gases, liquids, solids, organic, and inorganic), with only the exception of metals. In the last decades, Raman spectroscopy has proven to be an easy way to obtain mineral identification (see Figure 2) [22–27], as every Raman spectrum is like a fingerprint that can provide various types of information such as crystallinity, phase, intrinsic stress/strain, and polymorphism [28–31]. Furthermore, mineral phases can be identified down to a few microns [32], a possibility of paramount importance in chalk investigation. By applying Raman to flooded chalk, a “grain by grain” methodology was developed to obtain a better understanding of its mineralogy.

2. Materials and Methods

2.1. Samples

The samples studied in this project are all chalk, fine-grained carbonate rocks, built primarily of the skeletal debris of micro- and nano-organisms, mainly coccoliths, shed from coccolithophores (see SEM images in Figure 3). The cores were sampled at the Lixhe outcrop (Gulpen Formation, Campanian to late early Maastrichtian) [33] near Liège in Belgium, in particular from the Zeven Wegen Member [34] with an age of 75.5–78.0 Ma. The chalk shows clear signs of recrystallization, contact cements, and particle interlocking. Nevertheless, coccoliths are still well preserved, and the rock presents intrafossil porosity [35]. The chalk from Liège shows a clean compositional nature, as the main mineral component is calcite (CaCO_3), together with minor abundances of non-carbonate material (between 3 wt % and 5 wt % in total) [21,36] that mainly consist of quartz, smectite/mixed smectite-illite layer, mica, kaolinite, and clinoptilolite, and minor amounts of zeolite, apatite, opal, feldspar, pyroxene, pyrites, and titanium oxide [36,37].

The porosities lie in the range of 40–45% [12,21,33,35,38,39]. More information about mineralogy, petrography, and rheological characteristics of these chalk successions can be found in literature [12,33,35,38,39]. Onshore chalk successions are used as analogues for North Sea reservoir chalk in several studies [8,17,20,21,35].

2.2. Flooding Experiments

For this study, an unflooded chalk core and two long-term tests (length: ~70 mm, diameter: ~38 mm) were analyzed. Both test cores were flooded with MgCl_2 in reservoir conditions and mounted into triaxial cells that allow for measurements of axial strains while flooding of reactive fluids at elevated pressures, stresses, and temperatures. Each triaxial cell was equipped with a heating jacket and a regulation system that kept the temperature constant at 130 ± 0.1 °C throughout the experiment. To avoid boiling at temperatures above 100 °C, a pore pressure of 0.7 MPa was applied prior to the heating of the system. While distilled water was injected to ensure a clean pore system and to clean the sample, the confining pressure and pore pressure were simultaneously increased from 0.5 and 0 MPa to 1.2 and 0.7 MPa, respectively, with a constant effective stress equal to 0.5 MPa. Then, the confining

pressure was increased to 10.0 MPa (LTT) and 11.1 MPa (ULTT). A 0.219 M MgCl_2 brine, which has an ionic strength similar to that of seawater, was injected with a flooding rate of 1 pore volume per day (PV/day) for the LTT and varying between 1–3 PV/day for the ULTT. The effective stress was 9.3 MPa and 10.4 MPa for the LTT and the ULTT, respectively. After the experiment was finished, the two flooded cores were cleaned at 130 °C by injecting a minimum of three pore volumes of distilled water, without affecting the mineralogy of the samples. For more information about flooding experiment and cleaning procedure refer to Madland et al., 2011 [8]. After drying, the two test cores were cut into slices with thicknesses of about 10 mm (LTT; to the left in Figure 1) and of about 35 mm (ULTT; to the right in Figure 1); the samples were then investigated with different methods. For a thorough description of the performed tests, the reader is referred to Zimmermann et al., 2015 [36] for the LTT and Nermoen et al., 2015 [40] for the ULTT, since a detailed report on the experiments would have been out of focus in this mineralogical study.

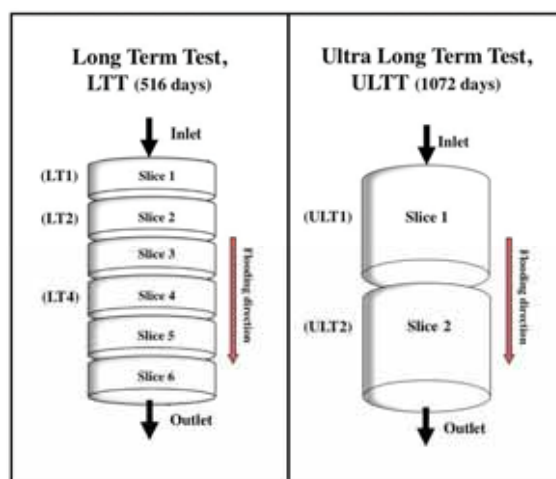


Figure 1. Schematic drawings of how the two cores were cut after the flooding experiment: Long Term Test (LTT) to the left (modified from Zimmermann et al., 2015 [36]) and Ultra Long Term Test to the right.

2.3. Field Emission Gun-Scanning Electron Microscopy with Energy-Dispersive Spectroscopy

Field Emission Gun-Scanning Electron Microscopy with Energy-Dispersive Spectroscopy (FEG-SEM) analyses were performed at the University of Stavanger using a Zeiss Supra VP 35. Freshly chipped off pieces of slices from the two core samples were analyzed together with chips of unflooded chalk from the end-pieces of the same cores. The samples were coated with palladium, ensuring a steady flux of electrons. The microscope parameters were set at an acceleration voltage between 12 to 15 kV, 30 μm aperture, and a working distance between 10 and 12 mm. The high current setting was used. To perform qualitative and semi-quantitative analyses of the chemical composition of the imaged areas, an EDAX energy dispersive X-ray spectroscopy (EDS) system was used. To optimize the quantification results, and because the chalk predominantly consists of calcite, an Iceland spar calcite crystal was used to calibrate the system [36].

2.4. Raman Spectroscopy

During this study, most of the spectra (465 of 557; reported with “H” in Figure 2) were collected with a Horiba XploRA Raman spectrometer (Kyoto, Japan) equipped with an Olympus microscope (Tokyo, Japan) with maximum magnification of 100 \times , and a motorized x–y stage. Calibration of

spectra was obtained using a silicon wafer with a main peak at 520.7 cm^{-1} as reference and maintained during the analysis with a constant checking of the position of a sharp neon lamp emission line at 476.8 cm^{-1} . Other spectra (92 of 557; LTT slice 1: p1_G and I; p2_D and E; slice 4: C and D; reported with “R” in Figure 2) were obtained using a high-resolution Renishaw inVia Reflex confocal Raman microscope, equipped with a Leica DM2500 polarizing microscope (Wetzlar, Germany) (maximum magnification of $100\times$) and motorized x–y stages. With both spectrometers, spectra were collected with a 532 nm line, solid-state lasers (10 mW at the sample); laser spot; and x, y, z spatial resolution around $1\text{ }\mu\text{m}$ with $100\times$ enlargement, spectral resolution of $\pm 1\text{ cm}^{-1}$, and acquisition time of 1–2 min. Microscope pictures were taken for each beamed grain or cluster of grains. The spectral region found to be the most important and convenient to our study was the low-medium one; setting the XploRA spectrometer with a 2400 lines/mm grating in back-scattering configuration allowed us to collect in the spectral range $100\text{--}1200\text{ cm}^{-1}$. Using a grating of 1800 lines/mm with the inVia spectrometer instead allowed us to collect in the range of $140\text{--}1900\text{ cm}^{-1}$. In order to try to detect the occurrence of hydrated silicates, the region between 2900 and 4200 cm^{-1} was investigated, collecting 200 spectra with the Renishaw inVia Reflex confocal Raman microscope at $100\times$ of magnification.

Determination of the position of the peaks was performed through the Gaussian–Lorentzian (Pseudo Voight) deconvolution method, with an accuracy of 0.2 cm^{-1} , using the software *Labspec 5*, utilized also for baseline subtraction that helped to eliminate the occasional fluorescence and background noise. Chalk cores were not analyzed directly on the rock surface, which can be done if the importance of the sample requires it. A very small amount of powder was scraped off with a needle from the rock, and placed and spread on a glass slide. In this way, it was possible to better focus on the sub-micrometric grains, and to obtain a consequent enhancement of the Raman signal. No specific preparation is needed to perform these analyses. The procedure allows for further investigation with other instrumentation on the rock sample (since there is no visible alteration after the scraping) or on the very same grains placed on the glass slide, which were not be destroyed during the Raman analysis.

2.5. Raman Spectroscopy on Carbonates

For their large diffusion and good Raman signal, carbonates have been investigated in detail, with particular attention to thermodynamic properties and their vibrational spectra [23,25,41–46]. Their Raman peaks positions are influenced by the magnesium content and crystallographic structure, and allow one to distinguish calcite from Mg-calcite, aragonite, magnesite, huntite, dolomite, and hydrated magnesium carbonates (such as artinite, nesquehonite, and hydromagnesite) [32,42,44,46–48]. Carbonate minerals show comparable spectra, as their structure is quite similar; a consistent increase in Raman shifts according to their Mg content occurs between calcite and magnesite, as a consequence of increased inter-atomic distances following the substitution of Ca^{2+} with the smaller Mg^{2+} ion in the cell [23,42,49]. This shift assists in distinguishing between the different carbonates.

Carbonate group minerals spectra (see Figure 2) present four main peaks, which can be divided into internal vibrations of the $(\text{CO}_3)^{2-}$ group (symmetric stretching, $600\text{--}1200\text{ cm}^{-1}$, and asymmetric stretching, $1200\text{--}1700\text{ cm}^{-1}$) [38,42,48,50,51] and into lattice vibrations involving translation and librations of the $(\text{CO}_3)^{2-}$ group relative to the Ca^{2+} or Mg^{2+} ions ($100\text{--}500\text{ cm}^{-1}$). The strongest and sharpest peak (ν_1 , *symmetric stretching mode* of the carbonate ion) is present around $1086\text{--}1095\text{ cm}^{-1}$ (calcite–magnesite, respectively), along with other subsidiary bands at $150\text{--}215\text{ cm}^{-1}$ (T, *translational mode*), $280\text{--}330\text{ cm}^{-1}$ (L, *librational mode*), and $712\text{--}738\text{ cm}^{-1}$ (ν_4 , *in-plane bending* of the $(\text{CO}_3)^{2-}$ group) [28,42,52].

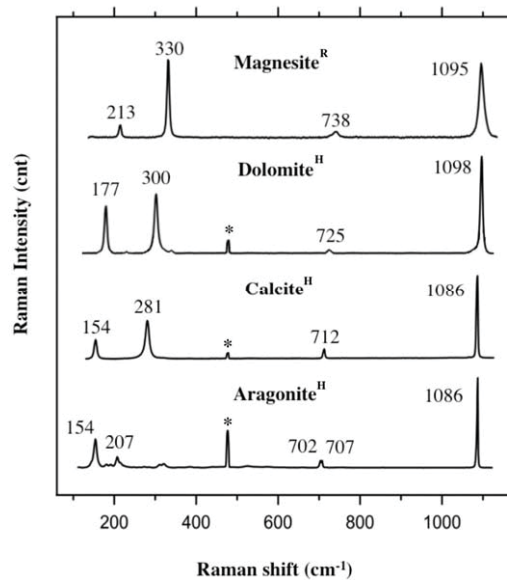


Figure 2. Raman spectra of calcium and magnesium carbonates: magnesite (Micro-Analysis Consultants certificated standard), dolomite (UNIMIB standard sample, Selvino, Italy), calcite (UNIMIB standard sample, Chihuahua, Mexico, ~0 mol % MgCO_3), and aragonite (UNIMIB—University of Milano Bicocca—standard sample, Val Formazza, Italy). Spectra with “R” were analyzed by the Renishaw inVia confocal Raman microscope and spectra with “H” by Horiba XploRA. Stars represent the neon lamp emission line at 476.8 cm^{-1} used for calibration with the Horiba XploRA spectrometer. Peak positions are reported without decimals.

2.6. Earlier Studies and Characterisation of the Sample Material

Various high-resolution methods were used to study mineralogical alteration in flooded chalk: field emission gun scanning electron microscopy, energy-dispersive X-ray spectroscopy (FEG-SEM-EDS) [3,5,8,14,36,37,53], nano secondary ion mass spectrometry (NanoSIMS) [36,47,54], X-ray diffraction (XRD) [36], whole-rock geochemistry techniques [21,36]. Tip-Enhanced Raman Spectroscopy-Atomic Force Microscopy (TERS-AFM) [55,56], Transmission Electron Microscopy (TEM) [53,57], and Mineral Liberation Analysis (MLA) [53]. The authors (Zimmermann et al., 2015 for the LTT, and Nermoen et al., 2015 for the ULTT) determined a loss of Ca^{2+} and a gain in Mg^{2+} , demonstrating a precipitation of new Mg-minerals in the core. FEG-SEM and TEM images have shown magnesite crystals with a grain size between 100 nm and $1 \mu\text{m}$ [53,57].

Based on geochemical methods, Zimmermann et al., 2015 [36] could calculate that 20% of the mass of the core had been dissolved during a 1.5 years long experiment. The core experienced axial shortening of 18% (in length) and a porosity reduction of 20%.

In the Long Term Test (LTT), using X-ray diffraction (XRD) [36], one could detect the presence of magnesite, chrysotile (slice 1–3), tillite (only in slice 4), quartz, and anthophyllite, as well as gypsum (the latter only in the unflooded chalk). Following a geochemical model [14], talc should precipitate, but this mineral could not be detected by XRD. Furthermore, magnesite could only be detected when it was rather abundant, and showed the limits of XRD as a detection method for traces of minerals. NanoSIMS 50 was the only analytical method that could detect positively with an image proof magnesite and very tiny new grown quartz of micron- and sub-micron sizes [36]. When analyzed by MLA, the shorter of the two tests, LTT, displayed a rather sharp ($\sim 1.5 \text{ mm}$) transition between two

areas with different mineralogy [53]. Closest to the inlet of the core, the rock material is completely altered into magnesite with minor contents of calcium along with clay minerals. In the area furthest away from the inlet, the mineralogy is still dominated by calcite, with occurrences of magnesite and clay, indicating only partial dissolution of calcite and precipitation of magnesite opposed to the complete substitution at the inlet. In the ULTT, the whole core showed similar composition, magnesite with the mentioned calcium impurities, and clay.

Nermoen et al. 2015 [40] describes the flooding experiment of the three years test (ULTT) in detail, and documents how dissolution and precipitation of the solid volume may alter significantly the porosity and permeability evolution during compaction.

The solid density increased from 2.68 to 2.90 g/cm³ throughout the experiment; simultaneously, the core has lost 22.93 g, which exemplifies that solid volume changes occur during flooding of MgCl₂ brines.

It is common for the two tests that compaction alone cannot explain the changes in permeability and porosity over time. For the ULTT [40], the permeability and calculated porosity are lowered during the start of the experiment in which compaction is the controlling mechanism, while throughout the experiment, the permeability and porosity starts to increase again. This is believed to be caused by processes that involve mineralogical transformation through dissolution of primary and precipitation of secondary minerals. These changes in mineralogy are therefore an important factor for both qualifying and quantifying to understand geomechanical alteration, as also seen in Wang et al., 2016 [21].

3. Results

3.1. FEG-SEM-EDS

The composition of the two cores after flooding has been affected by the nature of the fluid flow paths. This is often only visible at microscale, has a specific geometric form, and is composed of several compositional trends [53], and therefore awaits a detailed study and is not of relevance here. Hence, a quick and thorough investigation of the mineralogical composition prior to detailed FEG-SEM-EDS studies or further meticulous electron- and ion-beam-based analyses would be helpful.

When studied by FEG-SEM-EDS, both the texture and the chemical composition of the chalk is significantly altered compared to the unflooded material (Figure 3). The newly precipitated crystals are found in massive parts of the core (inlet part), with a homogenous high-magnesium carbonate composition, as well as single crystals within the calcite dominated areas. The grains are no longer rounded, but show a rhombic crystal shape, with grain-size mostly below 1 μm. In the completely altered areas, coccoliths and other micro/nano-fossils are no longer observed, while in parts where the calcite is still present, clear signs of dissolution is visible [36,53]. Additionally, significant amounts of clay-minerals are present, with main constituents being Mg and Si, which could be interpreted to be talc.

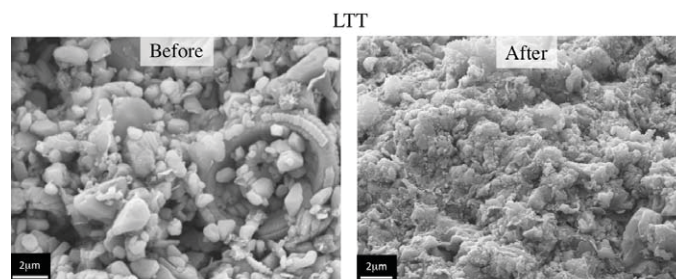


Figure 3. Cont.

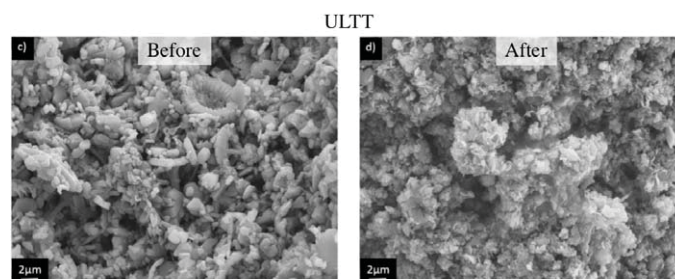


Figure 3. (a) SEM-micrograph of the LTT core before flooding; main components are coccoliths and fragments with a calcitic composition. (b) SEM-micrograph of the altered slice 4 of the LTT core after flooding with $MgCl_2$; coccoliths and other fossils are no longer visible, only magnesite crystals mainly below 1 μm in size are present. (c) SEM-micrograph of unflooded chalk of the ULTT with main components as observed in (a). (d) SEM-micrograph from slice 2 close to the outlet of the core, after $MgCl_2$ flooding; a deep and pervasive secondary growth of sub-micrometric and rhombic magnesite crystals is visible.

3.2. Raman Spectroscopy

3.2.1. Generals

Raman spectroscopy has proven to be easy to use, but it requires an experienced operator to decide the setting of the instrument and how to interpret the spectra (see below). The mineralogical changes due to fluid injection were quickly evaluated: in few tens of seconds it was possible to distinguish the carbonate minerals present in the chalk (see Table 1). 664 spectra were collected on an unflooded Liège chalk sample, on LTT and ULTT; only 5 could not be identified, as they were not present in databases or literature. In LTT core, 557 low region spectra were collected, 226 in slice 1 (120 in fragment 1, LT1_p1; 106 in fragment 2, LT1_p2), 220 in slice 2 (LT2), and 111 in slice 4 (LT4). In ULTT, 90 spectra were collected in 9 different areas of the core. Raman analyses were carried out in locations where previous studies have shown a change in composition or a change in color of the sample, which might indicate precipitation.

Calcite was the only mineral detected in the unflooded Liège chalk sample (Figure 4). In both ULTT and LTT cores, calcite and magnesite were present but no dolomite, aragonite, huntite, high magnesium-calcite, or hydrated minerals such as artinite, nesquehonite, and hydromagnesite were detected. As calcite Raman peaks positions reflect the magnesium content present in its lattice [46], it is possible to determine that the calcites present in ULTT and LTT always contain a low magnesium content (0–10 mol % \approx 4 wt %; [46]) in the mineral.

Table 1. Mineral composition of the two cores: amounts and percentages of Raman spectra collected for each mineral in the Long Term Test (LTT) and in the Ultra Long Term Test (ULTT). When a two minerals spectrum was found, both components were counted to obtain the calcite/magnesite percentages. For sample identification, see Figures 7 and 10.

	Calcite		Magnesite		Unknown		Other	
	Spectra	%	Spectra	%	Spectra	%	Spectra	%
LT1_p1A	20	77%	6	23%				
LT1_p1B	3	13%	20	87%				
LT1_p1C	20	87%	3	13%				
LT1_p1D	10	31%	19	63%	2	6%		
LT1_p1E	7	26%	20	74%				
LT1_p1F	18	60%	12	40%				
LT1_p1G	0	0%	25	100%			1 Brookite	4%
LT1_p1H	0	0%	25	100%				

Table 1. Cont.

	Calcite		Magnesite		Unknown		Other	
	Spectra	%	Spectra	%	Spectra	%	Spectra	%
LT1_p1I	0	0%	25	100%				
LT1_p2A	18	82%	4	18%				
LT1_p2B	2	10%	18	90%				
LT1_p2C	13	39%	20	61%				
LT1_p2D	16	53%	14	47%				
LT1_p2E	4	82%	16	18%				
LT2_A	70	92%	6	8%				
LT2_B	49	86%	7	12%	1	2%		
LT2_C	48	61%	31	39%				
LT2_D	30	41%	43	58%			1 Rutile	1%
LT4_A	19	79%	5	21%				
LT4_B	18	69%	6	23%	2	8%		
LT4_C	20	100%	0	0%				
LT4_D	20	100%	0	0%				
ULT1_1	1	9%	10	91%	1			
ULT2_4	1	9%	10	91%				
ULT2_5	0	0%	10	100%				
ULT2_5B	1	9%	10	91%				
ULT2_6	1	9%	10	91%				
ULT2_7	2	17%	10	83%				
ULT2_8	1	9%	10	91%				
ULT1_9	0	0%	10	100%				
ULT1_10	1	9%	10	91%	3			

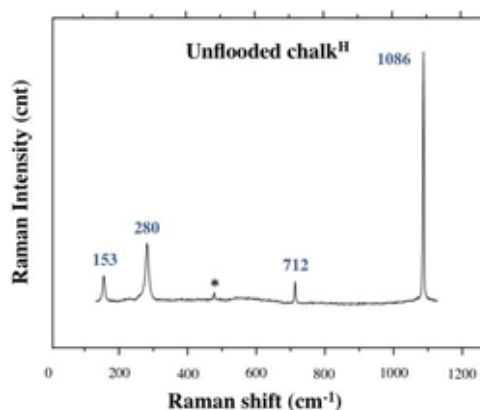


Figure 4. Raman spectrum collected on an unflooded Liège chalk core. Calcite is the only mineral detected, and its peaks are reported in blue/bold. The spectrum was collected with the Horiba XploRA spectrometer; the star represents the neon lamp emission line at 476.8 cm^{-1} used for calibration with the Horiba XploRA spectrometer. Peak positions are reported without decimals.

An important issue regarding the results presented in this study (Table 1) that are shown as a percentage mineral/total is that we need to consider these % not as weight % or volume %, as the data express the presence of the signal of a mineral compared to the total of the collected spectra. When vibrational modes of both calcite and magnesite were detected simultaneously in one spectrum, both minerals were counted. In fact, occasionally, peaks of both calcite and magnesite were present in the same spectrum: this can happen when the analyses are performed on overlapped or very closely spaced fine grains (dimension of 1–2 μm), when the laser beams both grains at the same time and the laser diameter is too large. In this case, the detector collects photons scattered from the two minerals, resulting in a spectrum that is the mathematical sum of the two spectra of the two minerals

(see Figure 5). Consequently, the strong and sharp ν_1 peak (*symmetric stretching mode* of the carbonate ion) of both calcite and magnesite is present in one spectrum, respectively, around 1086 and around 1095 cm^{-1} [25,44,45,48], depending on the intensity, sharpness, and nearness of these two peaks; *shoulders* (asymmetric peaks) or *double peaks* (peaks with two edges) can be present (examples in Figure 5). However, of importance is the fact that this can be detected. Another clear result of the simultaneous presence of calcite and magnesite signals in the same spectrum is given by the occurrence of the L (*librational mode*) peaks of the two carbonates at 280 and 330 cm^{-1} , respectively. When a two mineral spectrum was found, both components were counted to obtain the calcite/magnesite percentages for each slice (see Table 1). It is important to point out that, as Raman spectroscopy can differentiate between the carbonate species, the spectrum collected in cases such as the one described above (a magnesite and a calcite beamed at the same time, resulting in a combined spectrum) would be different from high Mg-calcite [46] or a dolomite spectrum (compare spectra shown in Figure 2 and the ones presented in Figure 5).

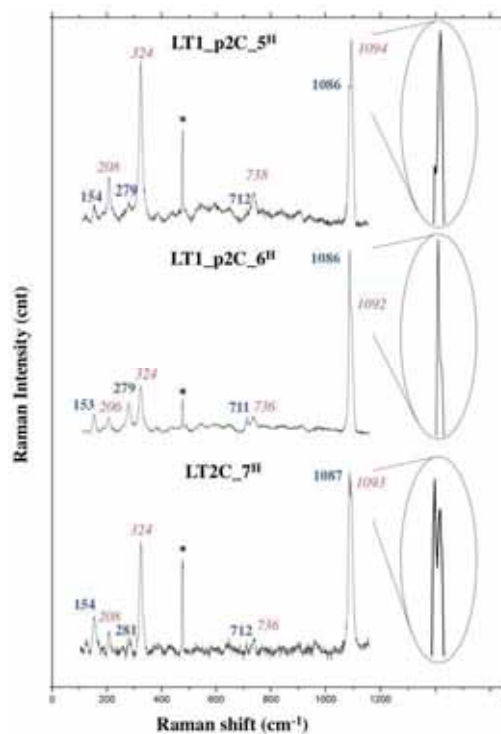


Figure 5. Raman spectra showing magnesite and calcite peaks in the same spectrum. This happens when grains of 1–2 μm in size and different mineralogy are overlapped or placed very close: the laser beams both grains at the same time, and, as a consequence, the instrumentation detects the vibrational modes of both minerals. In LT1_p2C_5, the signal from magnesite is stronger than the calcite one; in LT1_p2C_6 it is weaker. The main peaks (ν_1 , *symmetric stretching mode* of the carbonate ion) of the two minerals are very close, generating a high peak with a “shoulder”. In the third example shown, LT2C_7, the ν_1 of the two grains is so sharp and strong that a double peak is present. Calcite peaks are reported in blue/bold, magnesite peaks in red/italic. All the spectra were collected with the Horiba XploRA spectrometer; stars represent the neon lamp emission line at 476.8 cm^{-1} used for calibration. Peak positions are reported without decimals.

In order to detect the occurrence of hydrated silicates, the presence of diagnostic vibrational modes in the high frequencies region ($2900\text{--}4200\text{ cm}^{-1}$) of the Raman spectra was used, where the $(\text{OH})^-$ vibrational modes are located [25,58,59]. The signal of phyllosilicates is quite weak and, in the $0\text{--}1200\text{ cm}^{-1}$ region, it is easily covered by the calcite and magnesite stronger intensity. As these two carbonates are anhydrous, they do not show peaks in the high region of the spectra. More than 200 high region spectra were collected in slice one, LT1_p2_B, where an intense recrystallization of magnesite was already registered by Raman spectroscopy. The platy and very thin habit of phyllosilicates and clay minerals makes them really challenging to be detected, as it is very difficult to focus the laser inside their crystals and distinguish their weak scattering. Also, camera resolution and laser wavelength limit the analysis, and can lower the capability of focusing on the sample surface (under $1\text{--}2\text{ }\mu\text{m}$ in size).

3.2.2. Long Term Test

Raman spectroscopy could identify the presence of recrystallized magnesite along the core of the Long Term Test up to 4 cm from the injection surface (see Figures 5–7), which is also supported by Zimmermann et al., 2015 [36]. As predictable, the average alteration of the core is more pervasive close to the inlet surface, showing a decreasing amount of newly grown minerals with flooding direction (60% of magnesite in slice 1-LT1, 30% in in slice 2-LT2, and 10% in slice 4-LT4; see Table 1 and Figure 7). In Zimmermann et al., 2015 [36] positive XRD proof for magnesite could not be given in slice 4; however, geochemical data highlighted ca. 3.9% of MgO present in this slice, in comparison to 0.3% of MgO in the unflooded material. In this study, only two non-carbonate crystals out of 664 Raman spectra were detected in LTT: brookite in LT1_p1_G and rutile in LT2_D (see Table 1 and Figure 8).

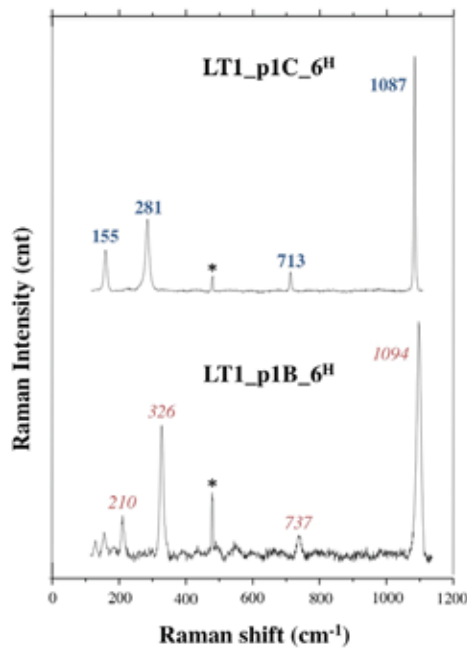


Figure 6. Raman spectra collected on the first slice of the Long Term Test. Raman showing the occurrence of the original calcite (LT1_p1C_6) and the presence of recrystallized magnesite (LT1_p1B_6). Calcite peaks are reported in blue/bold, magnesite peaks in red/italic. All the spectra were collected with the Horiba XploRA spectrometer; stars represent the neon lamp emission line at 476.8 cm^{-1} used for calibration with the Horiba XploRA spectrometer. Peak positions are reported without decimals.

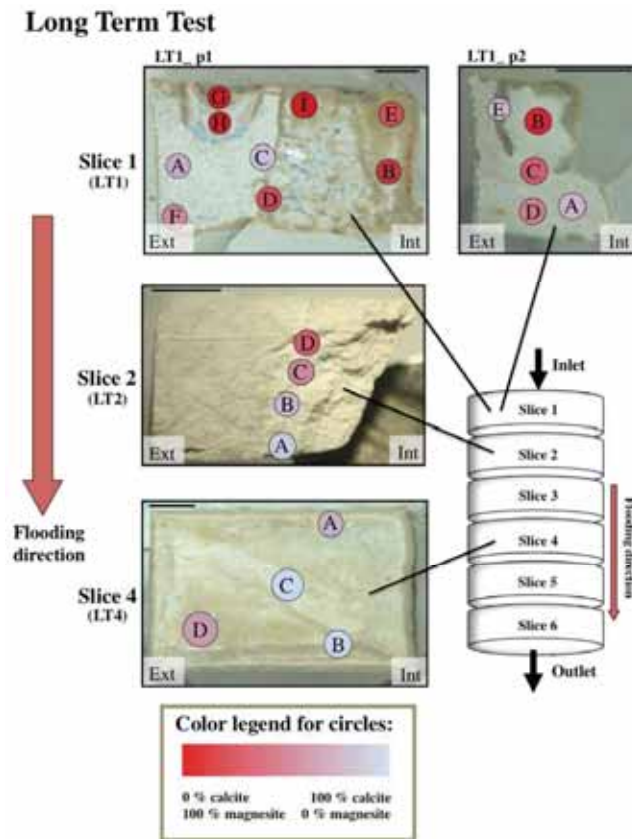


Figure 7. Mineralogical composition of the LTT core: 10 to 70 spectra have been collected in each of the area shown (9 areas in LT1_p1, 4 in LT1_p2, 4 in LT2, and 4 in LT4). Color legend reflects the percentage of calcite and magnesite spectra collected in each area of the sample. See Table 1 for calcite and magnesite amounts and percentages obtained for each area. Flooding direction is indicated. Inner (core) end external (rim), parts of the samples are marked. The scales represent 0.25 cm. A schematic drawing (modified from Zimmermann et al., 2015 [36]) of how the cores were cut after the flooding experiment is shown to the right.

Two pieces of Slice 1 (LT1_p1 and LT1_p2, LTT; see Figure 7) were analyzed, with a total of 14 areas, and 226 Raman spectra (Table 1; Figures 6 and 7).

In fragment 1 (LT1_p1), intense magnesite regrowth is present in the inner portion of the core (LT1_p1 E and B 74, and 87%, respectively, see Table 1 and Figure 7), which becomes less pervasive close to the external rims (LT1_p1 A, F: 23, 40%, respectively). In LT1_p1, a brown/ocre flow semi-circular structure is present and clearly visible to naked eye in the external part of the core; here, a complete recrystallization to magnesite is present, reaching 100% (LT1_p1 G and H, see Figure 7). However, in this region, also a crystal of brookite (TiO_2) was detected (see Table 1 and Figure 8). The average recrystallization of LT1_p2 is 47%, and another textural element has been observed, a grey vein of calcite (CaCO_3 82%, LT1_p2 E, see Figure 7). In order to try to detect hydrated minerals in LT1_p2, 210 high region spectra were collected. Unfortunately, no signal of clay minerals or talc was registered in any of them.

In Slice 2 (LT2; LTT), a longitudinal gradient in Mg content is perfectly detectable along flooding direction with a major magnesite recrystallization in the nearest areas to the inlet surface (from 58 (in LT2_D) to 8 (in LT2_A) %, see Table 1 and Figure 7). Four areas were investigated in slice 2, with a total amount of 220 Raman spectra. A rutile spectrum was collected in LT2_D (see Table 1 and Figure 8).

In Slice 4 (LT4; LTT), the recrystallization is less pervasive in the core than in the others (LT1 and LT2, LTT), as is the furthest from the inlet surface (Table 1; Figure 7). A diagonal deep and pale grey structure crosses the LT4 slice (see Figure 7) with a pure calcitic composition (111 spectra, 100% of CaCO_3 no magnesite spectra were detected in this area). Some MgCO_3 spectra have been collected in a brownish area near the rim of the core (23% of magnesite).

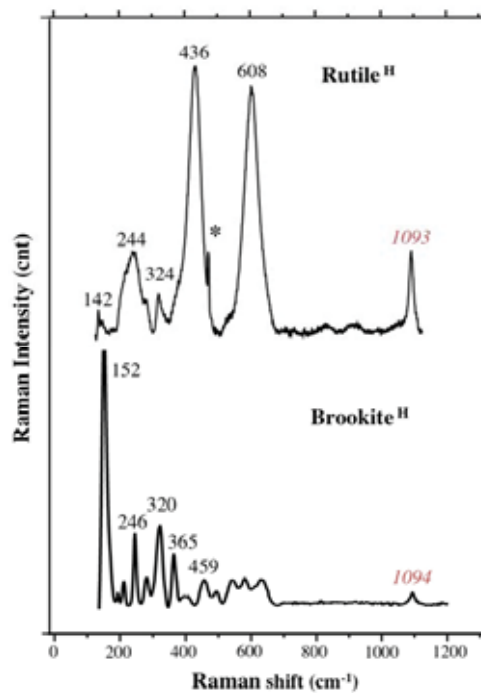


Figure 8. A brookite spectrum (identified in LT1_p1G) and one for rutile as identified in LT2_D (see Table 1). The main peak of magnesite (labelled in red) is present in both of them at 1093 and 1094 cm^{-1} , since the two minerals are surrounded by carbonates, which have a strong signal. Both spectra were collected with the Horiba Xplora spectrometer; the star represents the neon lamp emission line at 476.8 cm^{-1} used for calibration. Peak positions are reported without decimals.

3.2.3. Ultra Long Term Test

The Ultra Long Term Test presents a widespread recrystallization of magnesite (MgCO_3) in the range of 77–100% (see Table 1 and Figures 9 and 10) along the entire core, and no alteration front was detectable anymore with Raman spectroscopy [40,60].

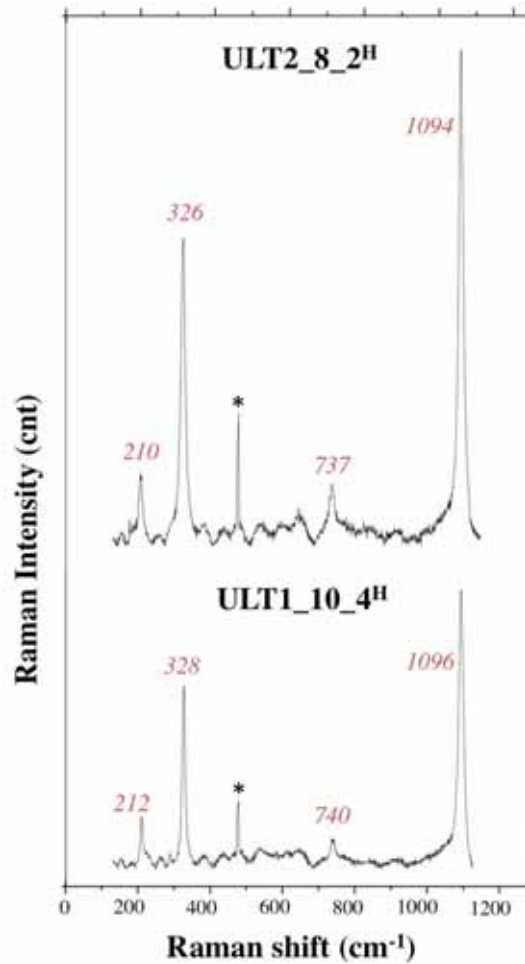


Figure 9. Raman spectra collected on the Ultra Long Term Test Raman showing the presence of recrystallized magnesite. Both spectra were collected with the Horiba XploRA spectrometer; stars represent the neon lamp emission line at 476.8 cm^{-1} used for calibration with the Horiba XploRA spectrometer. Peak positions are reported without decimals.

Raman spectra were collected in 9 different areas situated along the 7 cm core (90 spectra in total, see Table 1 and Figure 10). No structures or patterns are visible to the naked eye, and the core seems to be quite mineralogically homogeneous. Another study [54], made using ICP-MS (induced coupled plasma mass spectrometry), confirmed our data, as average of 4% of CaO was detected on the bulk sample, with no great difference in composition in the different portions of the sample.

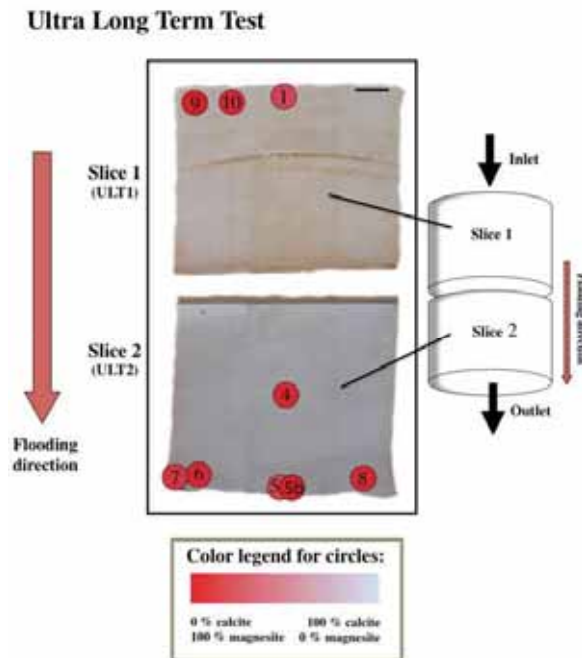


Figure 10. Mineralogical composition of the ULTT core: 10 spectra have been collected in each of the 9 areas shown. Color legend reflects the percentage of calcite and magnesite spectra collected in each area of the sample. See Table 1 for calcite and magnesite amounts and percentages obtained for each area. Flooding direction is indicated. The scale represents 0.5 cm. A schematic drawing of how the cores were cut after the flooding experiment is shown to the right.

4. Discussion

This study represents the first attempt to apply Raman spectroscopy to chalk mineralogy with a single grain approach on micron scale. The very fine-grained and soft texture of this sedimentary rock made detailed analysis quite challenging with common methods, and for this reason, in recent years, several high performing techniques have been included in Enhanced Oil Recovery (EOR) research. The purpose of this methodology paper is to demonstrate that Raman spectroscopy, thanks to its quickness, low cost, and micrometric resolution, is very suitable for these studies as, in few seconds and without any sample preparation, a mineralogical identification and a semi-quantitative compositional evaluation can be provided. It is perfectly complementary to methods such as SEM-EDS or XRD.

The major alteration front in LTT was previously suggested between LT3 and LT4 [36]; however, by the use of Raman spectroscopy, it was possible to detect magnesite even in slice 4 (Table 1; Figure 7), when XRD studies could not be positive in this regard [36]. The calcite dissolution and magnesite recrystallization were massive in the first 2 cm of the core (slice 1 and 2 of LTT; Figure 7). LTT5 and LTT6 were not studied in this investigation, as in a previous study [36], these slices were found to be the least altered slices by the flooding unable to provide further information when applying the used methods. Raman spectroscopy confirmed that such an alteration front was no longer present within the ULTT, which means that in three years of $MgCl_2$ injection, a sufficient quantity of Mg^{2+} was flooded into the core [40], permitting the substitution of almost all the Ca^{2+} to take place (92% of magnesite Raman spectra; see Table 1 and Figure 10).

The only precipitated mineral species that could be detected after flooding was magnesite. No dolomite, Mg-calcites, or hydrated minerals (such as hydromagnesite, artinite, and nesquehonite) were detected. As already seen with other techniques (SEM, XRD) applied in a previous study [36], it was not possible to identify clay-minerals in the two cores using Raman spectroscopy. It is very difficult to find a technique that could provide a resolution high enough to spot $< 1 \mu\text{m}$ crystals and simultaneously have the capability to cover a portion of the sample wide enough to detect a $\leq 5\%$ component, in a quick way, and image it at the same time. A principle technique would be a Mineral Liberation Analyser (MLA) with a nanometer-small spot size, which is still technically challenging using electron-beams on such small scales, or a Nano-scale Secondary Ion Mass Spectrometer (nano-SIMS) [36] or nanoRaman (TERS, Tip Enhanced Raman Spectroscopy) [55,56] application coupled with an Atomic Force Microscope (AFM), which allows in collecting topography and mineralogical maps at the nano-scale but is very time-consuming. In the LTT sample, nano-crystals of quartz have been detected only by nano-SIMS [36], which is a very time-consuming and destructive methodology, is extraordinarily expensive, and is not quantitative. Another technique would be TEM-EDS (Transmission Electron Microscopy), with has the same drawbacks besides the fact that the latter reveals quantitative data along with mineral-identification through diffraction analysis [57]. Raman spectroscopy could be the tool to use but with the known limits of 1–2 micron spotsizes and the impossibility of imaging the analyzed area with an optical microscope. An advance would be to scan an area, which is still a technical issue. A very low abundance of a mineral may be challenging to detect unless collecting a really huge number of spectra, which in turn would be time consuming. Furthermore, the identification of small and thin hydrated minerals is quite difficult to achieve in the $0\text{--}1200 \text{ cm}^{-1}$ region of the Raman spectra, since their signal is weak and easily covered by the higher carbonate peaks. For this reason, we tried to detect them with a different setting of the instrumentation, moving the analyses to the high region of the Raman spectra, around 3500 cm^{-1} , where the OH^- vibrational modes are present. Anhydrous minerals such as calcite and magnesite do not show peaks in this region. Unfortunately, no signal from phyllosilicates has been detected, possibly as a consequence of these technical difficulties.

Despite the impossibility of recognizing such low-concentrated and platy minerals, since the set-up is relatively economical and rapid, the authors think that Raman spectroscopy represents a very helpful methodology that could and should be used on hydrocarbon drilling rigs, possibly even as a drilling steering tool, because carefully investigations could show that positive and useful results were generated. This can lead to well-developed methodologies in the future for different approaches, like the petroleum industry.

5. Conclusions

The mineralogical and textural changes that follow dissolution, precipitation, and compaction in brine-injected chalk affect the permeability, porosity, reservoir potential, and oil flow pathways (e.g., [8,21,36,53]). For this reason, a deep investigation of secondary mineral recrystallization is of paramount importance in EOR research.

This study demonstrates that Raman spectroscopy is a robust, cheap, user-friendly point-analysis technique that, with a non-destructive sample preparation, allows one to quickly obtain semi-quantitative mineralogical and chemical information. This method has been applied to micron-sized chalk samples, giving an advantage in comparison to time consuming methods like SEM, thin section studies, nano-Raman or EMPA, and ion-probe analysis. An estimation of the magnesite recrystallization could be performed on two chalk cores that were flooded under reservoir conditions with MgCl_2 : Long Term Test (1.5-years-test, LTT) and Ultra Long Term Test (3-years-test, ULTT). In the LTT, the average recrystallization is more pervasive close to the inlet surface and varies with flooding direction. ULTT is, on the other hand, quite homogeneous, as the alteration front is no longer visible, and the whole core predominantly consists of magnesite.

However, not all reservoir rocks contain minerals and/or phases as small as those in chalk, which would make the here shown methodology very attractive. Anyway, when spectrometers with better analysis resolution and autofocus become available, Raman maps will be possible even on chalk cores samples, permitting to collect compositional maps and quantitative data analyses. Raman spectroscopy can, together with other research methods, provide a full range of information on flooded chalk cores leading to a broader understanding of chemical and mineralogical changes in those samples during the mentioned EOR experiments.

Until today, Raman spectroscopy has been only occasionally applied in the oil industry [61–64], and it is time for it to become a routine analysis.

Author Contributions: L.B. made a substantial contribution to every step of the study, such as the acquisition (with the fundamental help of N.E.) and interpretation of the data and writing of the paper. U.Z., L.B., M.W.M., and S.A. contributed to design and conception of the present publication. M.V.M. and R.I.K. designed and performed the long-term tests on the chalk cores. All the co-authors performed a critical revision of the intellectual content of the paper.

Acknowledgments: The authors acknowledge the Research Council of Norway and the industry partners ConocoPhillips Skandinavia AS, Aker BP ASA, Eni Norge AS, Maersk Oil Norway AS, Statoil Petroleum AS, ENGIE E&P NORGE AS, Lundin Norway AS, Halliburton AS, Schlumberger Norge AS, Wintershall Norge AS, and DEA Norge AS of The National IOR Centre of Norway for support. This study is a central part of the PhD thesis of L.B., who thanks the NIOR Centre of Norway for a grant to carry out the research, and Eduardo Garzanti and the group of Provenance Studies (University of Milano-Bicocca) for their advice.

Conflicts of Interest: The authors declare no conflict of interest. The funding sponsors had no role in the design of the study; in the collection, analyses, or interpretation of data; in the writing of the manuscript; or in the decision to publish the results.

References

- Hermansen, H.; Landa, G.H.; Sylte, J.E.; Thomas, L.K. Experiences after 10 years of waterflooding the Ekofisk Field, Norway. *J. Pet. Sci. Eng.* **2000**, *26*, 11–18. [[CrossRef](#)]
- Nagel, N.B. Compaction and subsidence issues within the petroleum industry: From Wilmington to Ekofisk and beyond. *Phys. Chem. Earth A* **2001**, *26*, 3–14. [[CrossRef](#)]
- Risnes, R.; Madland, M.V.; Hole, M.; Kwabiah, N.K. Water weakening of chalk—Mechanical effects of water-glycol mixtures. *J. Pet. Sci. Eng.* **2005**, *48*, 21–36. [[CrossRef](#)]
- Heggheim, T.; Madland, M.V.; Risnes, R.; Austad, T. A chemical induced enhanced weakening of chalk by seawater. *J. Pet. Sci. Eng.* **2005**, *46*, 171–184. [[CrossRef](#)]
- Korsnes, R.I.; Strand, S.; Hoff, Ø.; Pedersen, T.; Madland, M.V.; Austad, T. Does the chemical interaction between seawater and chalk affect the mechanical properties of chalk? In *Multiphysics Coupling and Long Term Behaviour in Rock Mechanics*; Cotthem, A.V., Charlier, R., Thimus, J.F., Tshibangu, J.P., Eds.; Taylor & Francis: London, UK, 2006; pp. 427–434.
- Korsnes, R.I.; Madland, M.V.; Austad, T.; Haver, S.; Rosland, G. The effects of temperature on the water weakening of chalk by seawater. *J. Pet. Sci. Eng.* **2008**, *60*, 183–193. [[CrossRef](#)]
- Madland, M.V.; Midtgarden, K.; Manafov, R.; Korsnes, R.I.; Kristiansen, T.; Hiorth, A. The Effect of Temperature and Brine Composition on the Mechanical Strength of Kansas Chalk. In Proceedings of the International Symposium of the Society of Core Analysts, Abu Dhabi, UAE, 29 October–2 November 2008.
- Madland, M.V.; Hiorth, A.; Omdal, E.; Megawati, M.; Hildebrand-Habel, T.; Korsnes, I.R.; Evje, S.; Cathles, M.L. Chemical alterations induced by rock-fluid interactions when injecting brines in high porosity chalks. *Transp. Porous Med.* **2011**, *87*, 679–702. [[CrossRef](#)]
- Zangiabadi, B.; Korsnes, R.I.; Hildebrand-Habel, T.; Hiorth, A.; Surtarjana, I.K.; Lian, A.; Madland, M.V. Chemical water weakening of various outcrop chalks at elevated temperature. In *Poromechanics IV*; Ling, H.I., Smyth, A., Betti, R., Eds.; DEStech Publications, Inc.: Lancaster, UK, 2009; pp. 543–548.
- Andreassen, K.A.; Fabricius, I.L. Biot critical frequency applied to description of failure and yield of highly porous chalk with different pore fluids. *Geophysics* **2010**, *75*, E205–E213. [[CrossRef](#)]
- Zhang, P.; Tweheyo, M.T.; Austad, T. Wettability alteration and improved oil recovery by spontaneous imbibition of seawater into chalk: Impact of the potential determining ions Ca^{2+} , Mg^{2+} , and SO_4^{2-} . *Colloids Surf. A Physicochem. Eng. Aspects* **2007**, *301*, 199–208. [[CrossRef](#)]

12. Strand, S.; Hjuler, M.L.; Torsvik, R.; Pedersen, J.I.; Madland, M.V.; Austad, T. Wettability of chalk: Impact of silica, clay content and mechanical properties. *Pet. Geosci.* **2007**, *13*, 69–80. [[CrossRef](#)]
13. Austad, T.; Strand, S.; Madland, M.V.; Puntervold, T.; Korsnes, R.I. Seawater in chalk: An EOR and compaction fluid. *SPE Reserv. Eval. Eng.* **2008**, *11*, 648–654. [[CrossRef](#)]
14. Hiorth, A.; Cathles, L.; Madland, M. The Impact of Pore Water Chemistry on Carbonate Surface Charge and Oil Wettability. *Transp. Porous Med.* **2010**, *85*, 1–21. [[CrossRef](#)]
15. Fathi, S.J.; Austad, T.; Strand, S. “Smart Water” as a Wettability Modifier in Chalk: The Effect of Salinity and Ionic Composition. *Energy Fuels* **2010**, *24*, 2514–2519. [[CrossRef](#)]
16. Ali, A.Y.; Salah Hamad, A.S.; Abdulaziz, A.K.; Mohammed Saleh, A.J. Laboratory Investigation of the Impact of Injection Water Salinity and Ionic Content on Oil Recovery from Carbonate Reservoirs. *SPE Reserv. Eval. Eng.* **2011**. [[CrossRef](#)]
17. Megawati, M.; Hiorth, A.; Madland, M.V. The impact of surface charge on the mechanical behavior of high-porosity chalk. *Rock Mech. Rock Eng.* **2013**, *46*, 1073–1090. [[CrossRef](#)]
18. Zhang, P.; Tweheyo, M.T.; Austad, T. Wettability Alteration and Improved Oil Recovery in Chalk: The Effect of Calcium in the Presence of Sulfate. *Energy Fuels* **2006**, *20*, 2056–2062. [[CrossRef](#)]
19. Andersen, P.Ø.; Evje, S.; Madland, M.V.; Hiorth, A. A geochemical model for interpretation of chalk core flooding experiments. *Chem. Eng. Sci.* **2012**, *84*, 218–241. [[CrossRef](#)]
20. Megawati, M.; Madland, M.V.; Hiorth, A. Mechanical and physical behavior of high-porosity chalks exposed to chemical perturbation. *J. Pet. Sci. Eng.* **2015**, *133*, 313–327. [[CrossRef](#)]
21. Wang, W.; Madland, M.V.; Zimmermann, U.; Neremoen, A.; Reidar, I.; Korsnes, R.; Bertolino, S.R.A.; Hildebrand-Habel, T. Evaluation of porosity change during chemo-mechanical compaction in flooding experiments on Liege outcrop chalk. In *Reservoir Quality of Clastic and Carbonate Rocks: Analysis, Modelling and Prediction*; Armitage, P.J., Butcher, A.R., Churchill, J.M., Csoma, A.E., Hollis, C., Lander, R.H., Omma, J.E., Worden, R.H., Eds.; Geological Society: London, UK, 2016; p. 435.
22. Raman, C.V. A new radiation. *Indian J. Phys.* **1928**, *2*, 387–398.
23. Krishnamurti, D. Raman spectrum of magnesite. *Proc. Indian Acad. Sci. Sect. A* **1956**, *43*, 210.
24. Griffith, W.P. Raman spectroscopy of minerals. *Nature* **1969**, *224*, 264–266. [[CrossRef](#)]
25. Kuebler, K.; Wang, A.; Abbott, K.; Haskin, L.A. Can we detect carbonate and sulfate minerals on the surface of Mars by Raman spectroscopy? In Proceedings of the 32nd Annual Lunar and Planetary Science Conference, Houston, TX, USA, 12–16 March 2001.
26. Downs, R.T. The RRUFF Project: An integrated study of the chemistry, crystallography, Raman and infrared spectroscopy of minerals. In Proceedings of the 19th General Meeting of the International Mineralogical Association, Kobe, Japan, 23–28 July 2006.
27. Andò, S.; Garzanti, E. Raman spectroscopy in heavy-mineral studies. In *Sediment Provenance Studies in Hydrocarbon Exploration and Production*; Scott, R.A., Smyth, H.R., Morton, A.C., Richardson, N., Eds.; Geological Society: London, UK, 2013; p. 386.
28. Gillet, P.; Biellmann, C.; Reynard, B.; McMillan, P. Raman spectroscopic studies of carbonates Part I: High-pressure and high-temperature behaviour of calcite, magnesite, dolomite and aragonite. *Phys. Chem. Miner.* **1993**, *20*, 1–18. [[CrossRef](#)]
29. Bendel, V.; Schmidt, B.C. Raman spectroscopic characterisation of disordered alkali feldspars along the join KAlSi_3O_8 – $\text{NaAlSi}_3\text{O}_8$: Application to natural sanidine and anorthoclase. *Eur. J. Miner.* **2008**, *20*, 1055–1065. [[CrossRef](#)]
30. Noguchi, N.; Abduriyim, A.; Shimizu, I.; Kamegata, N.; Odake, S.; Kagi, H. Imaging of internal stress around a mineral inclusion in a sapphire crystal: Application of micro-Raman and photoluminescence spectroscopy. *JRS* **2013**, *44*, 147–154. [[CrossRef](#)]
31. De La Pierre, M.; Carteret, C.; Maschio, L.; André, E.; Orlando, R.; Dovesi, R. The Raman spectrum of CaCO_3 polymorphs calcite and aragonite: A combined experimental and computational study. *J. Chem. Phys.* **2014**, *140*, 164509. [[CrossRef](#)] [[PubMed](#)]
32. Del Monte, B.; Paleari, C.I.; Andò, S.; Garzanti, E.; Andersson, P.S.; Petit, J.R.; Crosta, X.; Narcisi, B.; Baroni, C.; Salvatore, M.C.; et al. Causes of dust size variability in central East Antarctica (Dome B): Atmospheric transport from expanded South American sources during Marine Isotope Stage 2. *Quat. Sci. Rev.* **2017**, *168*, 55–68. [[CrossRef](#)]

33. Molenaar, N.; Zijlstra, J.J.P. Differential early diagenetic low-Mg calcite cementation and rhythmic hardground development in Campanian-Maastrichtian chalk. *Sediment. Geol.* **1997**, *109*, 261–281. [[CrossRef](#)]
34. Robaszynski, F.; Dhondt, A.V.; John, W.M. Cretaceous lithostratigraphic units (Belgium). *Geol. Belg.* **2001**, *4*, 121–134.
35. Hjuler, M.L.; Fabricius, I.L. Engineering properties of chalk related to diagenetic variations of Upper Cretaceous onshore and offshore chalk in the North Sea area. *J. Pet. Sci. Eng.* **2009**, *68*, 151–170. [[CrossRef](#)]
36. Zimmermann, U.; Madland, M.V.; Nermo, A.; Hildebrand-Habel, T.; Bertolino, S.A.R.; Hiorth, A.; Korsnes, R.I.; Audinot, J.N.; Grysan, P. Evaluation of the compositional changes during flooding of reactive fluids using scanning electron microscopy, nano-secondary ion mass spectroscopy, X-ray diffraction, and whole-rock geochemistry. *AAPG Bull.* **2015**, *99*, 791–805. [[CrossRef](#)]
37. Hjuler, M.L. Diagenesis of Upper Cretaceous Onshore and Offshore Chalk from the North Sea Area. Ph.D. Thesis, Department of Civil Engineering, Arctic Technology Centre, Technical University of Denmark, Kongens Lyngby, Denmark, 2007.
38. Felder, R.M.; Spence, R.D.; Ferrell, J.K. A method for the dynamic measurement of diffusivities of gases in polymers. *J. Polym. Sci.* **1975**, *19*, 3193–3200. [[CrossRef](#)]
39. Slimani, H. New species of dinoflagellate cysts from the Campanian-Danian chalks at Hallembaye and Turnhout (Belgium) and at Beutenaken (The Netherlands). *J. Micropalaeontol.* **2001**, *20*, 1–11. [[CrossRef](#)]
40. Nermo, A.; Korsnes, R.I.; Hiorth, A.; Madland, M.V. Porosity and permeability development in compacting chalks during flooding of nonequilibrium brines: Insights from long-term experiment. *JGR Solid Earth* **2015**, *120*, 2935–2960. [[CrossRef](#)]
41. Rutt, H.N.; Nicola, H.J. Raman spectra of carbonates of calcite structure. *Phys. C Solid State Phys.* **1974**, *7*, 4522. [[CrossRef](#)]
42. Bischoff, W.D.; Sharma, S.K.; MacKenzie, F.T. Carbonate ion disorder in synthetic and biogenic magnesian calcites: A Raman spectral study. *Am. Miner.* **1985**, *70*, 581–589.
43. Herman, R.G.; Bogdan, C.E.; Sommer, A.J.; Simpson, D.R. Discrimination among carbonate minerals by Raman spectroscopy using the laser microprobe. *Appl. Spectrosc.* **1987**, *41*, 437–440. [[CrossRef](#)]
44. Edwards, H.; Villar, S.; Jehlicka, J.; Munshi, T. FT-Raman spectroscopic study of calcium-rich and magnesium-rich carbonate minerals. *Spectrochim. Acta A* **2005**, *61*, 2273. [[CrossRef](#)] [[PubMed](#)]
45. Korsakov, A.; De Gussem, K.; Zhukov, V.P.; Perraki, M.; Vandenabeele, P.; Golovin, A.V. Aragonite-calcite-dolomite relationships in UHPM polycrystalline carbonate inclusions from the Kokchetav Massif, northern Kazakhstan. *Eur. J. Miner.* **2009**, *21*, 1301. [[CrossRef](#)]
46. Borromeo, L.; Zimmermann, U.; Andò, S.; Coletti, G.; Bersani, D.; Basso, D.; Gentile, P.; Schulz, B.; Garzanti, E. Raman spectroscopy as a tool for magnesium estimation in Mg-calcite. *JRS* **2017**, *48*, 983–992. [[CrossRef](#)]
47. Dandeu, A.; Humbert, B.; Carteret, C.; Muhr, H.; Plasari, E.; Bossoutrot, J.M. Raman Spectroscopy—A Powerful Tool for the Quantitative Determination of the Composition of Polymorph Mixtures: Application to CaCO₃ Polymorph Mixtures. *Chem. Eng. Technol.* **2006**, *29*, 221–225. [[CrossRef](#)]
48. Sun, J.; Zeguang, W.; Hongfei, C. A Raman spectroscopic comparison of calcite and dolomite. *Spectrochim. Acta A* **2014**, *117*, 158. [[CrossRef](#)] [[PubMed](#)]
49. Purgstaller, B.; Mavromatis, V.; Immenhauser, A.; Dietzel, M. Transformation of Mg-bearing amorphous calcium carbonate to Mg-calcite—In situ monitoring. *Geochim. Cosmochim. Acta* **2016**, *174*, 180–195. [[CrossRef](#)]
50. Krishnan, R.S. Raman spectra of the second order in crystals; part. I: Calcite. *Proc. Math. Sci.* **1945**, *22*, 182.
51. White, W.B. *Infrared Spectra of Minerals*; Farmer, V.C., Ed.; Mineralogical Society Monograph 4; Mineralogical Society: London, UK, 1974; pp. 87–110, 227–284.
52. Urmos, J.; Sharma, S.K.; Mackenzie, T. Characterization of some biogenic carbonates with Raman spectroscopy. *Am. Miner.* **1991**, *76*, 641–646.
53. Minde, M.W.; Haser, S.; Korsnes, R.I.; Zimmermann, U.; Madland, M.V. Comparative Studies of Mineralogical Alterations of Three Ultra-long-term Tests of Onshore Chalk at Reservoir Conditions. In Proceedings of the IOR 2017-19th European Symposium on Improved Oil Recovery 2017, Stavanger, Norway, 24–27 April 2017.
54. Minde, M.W.; Zimmermann, U.; Madland, M.V.; Korsnes, R.I. *Submicron Investigations—What Can We Learn? IOR*; Stavanger, Norway, 2016; Available online: http://www.uis.no/getfile.php/13300942/IOR-senter/IOR_16_MMinde%20-%20dag%202_theme%205.pdf (accessed on 18 May 2018).

55. Borromeo, L.; Minde, M.; Toccafondi, C.; Zimmermann, U.; Andò, S.; Ossikovski, R. A New Frontier Technique for Nano-analysis on Flooded Chalk-TERS (Tip Enhanced Raman Spectroscopy). In Proceedings of the IOR 2017—19th European Symposium on Improved Oil Recovery, Stavanger, Norway, 24–27 April 2017.
56. Borromeo, L.; Toccafondi, C.; Minde, M.; Zimmermann, U.; Andò, S.; Madland, M.V.; Korsnes, R.I.; Ossikovski, R. Application of Tip Enhanced Raman Spectroscopy in the nanoscale characterization of flooded chalk. *JRS* **2018**. submitted.
57. Egeland, N.; Minde, M.W.; Kobayashi, K.; Ota, T.; Nakamura, E.; Zimmermann, U.; Madland, M.W.; Korsnes, R.I. Quantification of Mineralogical Changes in Flooded Carbonate under Reservoir Conditions. In Proceedings of the IOR 2017—19th European Symposium on Improved Oil Recovery, Stavanger, Norway, 24–27 April 2017.
58. Frezzotti, M.L.; Tecce, F.; Casagli, A. Raman spectroscopy for fluid inclusion analysis. *J. Geochem. Explor.* **2012**, *112*, 1–20. [[CrossRef](#)]
59. Wang, A.; Freeman, J.J.; Jolliff, B.L. Understanding the Raman spectral features of phyllosilicates. *JRS* **2015**, *46*, 829–845. [[CrossRef](#)]
60. Egeland, N. Raman Spectroscopy Applied to Enhanced Oil Recovery. Master's Thesis, University of Stavanger, Stavanger, Norway, 2015, unpublished.
61. Gorelik, V.S.; Chervyakov, A.V.; Kol'tsova, L.V.; Veryaskin, S.S. Raman Spectra of Saturated Hydrocarbons and Gasolines. *J. Russ. Laser Res.* **2000**, *21*, 323–334. [[CrossRef](#)]
62. Costa, J.C.S.; Sant'Ana, A.C.; Corio, P.; Temperini, M.L.A. Chemical analysis of polycyclic aromatic hydrocarbons by surface-enhanced Raman spectroscopy. *Talanta* **2006**, *70*, 1011–1016. [[CrossRef](#)] [[PubMed](#)]
63. Sebek, J.; Pele, L.; Potma, E.O.; Gerber, R.B. Raman spectra of long chain hydrocarbons: Anharmonic calculations, experiment and implications for imaging of biomembranes. *PCCP* **2011**, *13*, 12724–12733. [[CrossRef](#)] [[PubMed](#)]
64. Andrews, A.B.; Wang, D.; Marzec, K.M.; Mullins, O.C.; Crozier, K.B. Surface enhanced Raman spectroscopy of polycyclic aromatic hydrocarbons and molecular asphaltene. *Chem. Phys. Lett.* **2015**, *620*, 139–143. [[CrossRef](#)]



© 2018 by the authors. Licensee MDPI, Basel, Switzerland. This article is an open access article distributed under the terms and conditions of the Creative Commons Attribution (CC BY) license (<http://creativecommons.org/licenses/by/4.0/>).